Doctoral Dissertation

Doctoral Program
in
Sustainable Materials, Processes and Systems for Energy Transition (38th Cycle)

Advanced Catalytic Pyrolysis of Biomass and Plastic Waste in Multi-Stage Reactors

Biagio Ciccone
* * * * * *

Supervisors
Dr. Giovanna Ruoppolo, Supervisor
Dr. Massimo Urciuolo, Dr. Maria Elena Russo, Co-Supervisors

Referees:
Prof. P. Salatino, Referee, University of Naples "Federico II"
Prof. P. Bareschino, Referee, University of the Studies of "Sannio"

Politecnico di Torino
October 31, 2025

This thesis is licensed under a Creative Commons License, Attribution - Noncommercial - NoDerivative Works 4.0 International: see www.creativecommons.org. The text may be reproduced for non-commercial purposes, provided that credit is given to the original author.

I hereby declare that the contents and organisation of this dissertation constitute my own original work and does not compromise in any way the rights of third parties, including those relating to the security of personal data.

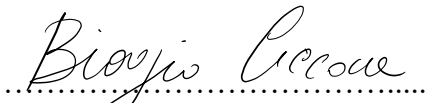

Biagio Ciccone
Turin, October 31, 2025

Abstract

The global transition towards a less fossil-dependent, circular economy demands innovative technologies for the alternative production of fuels and industrially-relevant chemicals. This should be done in complementarity with the management of persistent waste streams, primarily end-of-life plastics and lignocellulosic biomass. *Ex-situ* catalytic fast pyrolysis (CFP) presents a flexible platform for the valorization of biogenic and non-biogenic carbon sources. This study investigates the potential for upgrading pyrolysis vapours derived from waste polyolefins and olive stone biomass using a dual spouted-bed/fixed-bed pyrolysis unit. It provides insights in the understanding of how these chemically distinct feedstocks behave under comparable process conditions. The influence of key process parameters on product distribution, catalyst performance and deactivation was examined, highlighting the specific challenges and opportunities associated with each material.

This work begins with a detailed state-of-the-art providing a comprehensive overview of the potential roles of biomass and plastic waste in the transition towards a sustainable and circular economy and of catalytic cracking of pyrolysis volatiles as a strategy for upgrading raw pyrolysis products. The mechanisms of catalytic fast pyrolysis (CFP) are explored, including the role of different catalyst types (zeolites, metal oxides, and basic materials) in reducing oxygen content, and improving fuel quality. Particular attention is given to the challenges posed by the chemical diversity of biomass- and plastic-derived vapours, and how catalyst design and process conditions can be tailored to address these issues. Subsequently, the materials and methods used in the experimental investigation are described in detail. This includes the characterization of feedstocks (a polyolefin mixture and olive stone biomass), the selection and preparation of catalysts, the design and realization of a dual spouted-bed/fixed-bed pyrolysis

reactor and the experimental procedures used to quantify product yields, assess catalyst performance, and evaluate deactivation phenomena.

The results obtained can be synthesized as reported. For the upgrading of olive stone, the effect of space-time, primary pyrolysis temperature and cracking temperature on product yields and quality and on catalyst deactivation was investigated. The primary pyrolysis temperature was identified as the dominant parameter controlling the initial composition of the bio-oil precursors. Space-time and cracking temperature increase led to lower oil yield and higher yield of gases and water. Deactivation was consistently more severe compared to the case of polyolefin pyrolysis, with a coke content of ≈10 wt.% after 45 minutes of continuous operation due to the presence of highly reactive phenolic and oxygenated compounds in the biomass-derived vapours, which act as potent coke precursors. Deactivation was also confirmed by the evident reduction in surface area and micropore volume of the zeolite.

A screening of seven catalysts—including zeolites (HZSM-5, HY), metal oxides (γ-Al_2O_3), basic catalysts (dolomite), and homemade iron-based and waste-derived materials—established that catalyst functionality must be tailored to the specific upgrading objective. While HZSM-5 remained the benchmark for aromatization and reduction of light oxygenated compounds, calcined dolomite proved exceptionally effective for bio-oil deacidification, reducing organic acid content from 15.1% to just 0.5% via its basic sites. Other γ-Al_2O_3-based catalysts and Fe/dolomite did not exhibit remarkable performances, and more work is needed to explore their potential.

The investigation into polyolefin upgrading over a HZSM-5 zeolite revealed a trade-off between the production of light olefins and BTX aromatic hydrocarbons. The catalyst is able to completely crack heavy waxes, and a clear optimum was identified for light olefins (C_2-C_4) production, achieving a maximum yield of 77.1 wt.% at a space-time of 10 g_{cat} min/$g_{plastic}$. Increasing the space-time beyond this point led to secondary reactions, consuming olefins to produce a higher yield of BTX aromatics. Deactivation studies suggested that while higher cracking temperatures (500°C) ensured catalyst stability, lower temperatures (450°C) yielded slightly more BTX despite causing more severe and rapid deactivation due to coking from uncracked wax precursors, resulting in 18.1% loss in BET surface area. Moreover, space-time had a limited effect on deactivation when the temperature was kept at 500°C. Coke content on the catalyst was always lower than 3 wt.% even after 4 h of continuous operation and was higher for the portion of the catalyst bed immediately in contact with pyrolysis vapour.

This highlights that different catalysts are required to solve the distinct problems posed by biomass-derived vapours (acidity and oxygen content) versus plastic-derived vapours (molecular weight distribution). Ultimately, a “feedstock-aware” approach is essential since the chemical nature of the waste stream, rather than the reactor technology alone, dictates the choice of catalyst and process strategy for effective chemical recycling.

Acknowledgments

The completion of this doctoral thesis marks the culmination of a challenging yet profoundly rewarding period of research and personal growth. I wish to express my deepest gratitude to all those who have contributed to this result.

First, I wish to thank my scientific supervisor, Dr. Giovanna Ruoppolo, for her exceptional guidance, unwavering support, and intellectual rigor during my PhD. Her guide and continuous feedback were fundamental in shaping the scope and quality of this research. I am equally indebted to my co-supervisor, Dr. Massimo Urciuolo, whose expertise in thermochemical conversion processes provided invaluable perspectives and technical assistance, significantly enhancing the methodological framework of this work. I also wish to acknowledge Dr. Paola Brachi and Dr. Gianluca Landi, who, although not formally appointed, provided crucial mentorship and shared their expertise. I found in all of them not only supervisors and mentors, but a second supportive family. I extend my sincere thanks to the members of my Thesis Committee and Referees, Prof. P. Salatino, Prof. P. Bareschino, for their thoughtful review and constructive suggestions that greatly improved the final manuscript. The research presented here was made possible by the supportive environment of the STEMS institute of the National Research Council and by the administrative support provided by Politecnico di Torino.

My gratitude goes to all my colleagues of the research group from STEMS and from the DICMaPi of the University of Naples “Federico II”, who made the long hours in the lab both productive and enjoyable. Thanks to Andrea C. and Luigi S. for the support in the characterization of materials and catalysts. Thanks to Antonio C. for his fundamental support during the experimental campaign.

A special note of thanks is reserved for the colleagues and friends I met during my research stay at Euskal Herriko Unibertsitatea (EHU) of Bilbao. The experience of working in an international environment, sharing ideas, and building lasting professional and personal relationships was an enriching chapter of my doctoral studies. I thank Katrin, Gartzen, Maider, Maite, Enara, Prof. Martin Olazar and all the people I met there for their hospitality and collaboration. Thanks to Davide for making those months unforgettable. Eskerrik asko, laster arte!

I wish to acknowledge my girlfriend, Velia, whose patience, encouragement, and thoughtful understanding have accompanied every stage of this research,

offering both the emotional steadiness and the practical perspective that allowed me to complete this dissertation with determination and focus.

To my friends, Roberto, Nicola M., Gaetano, Nicola Z., Virginia, thank you for the much-needed distractions and enjoyable time together.

Finally, and most importantly, I thank my family for their unwavering love, patience, and encouragement. My father and my mother have been a constant source of strength and belief and supported me during all my years of studying. Thanks to my brother for sharing enjoyable time together and for often distracting me from overworking.

To all those who have contributed, directly or indirectly, to the completion of this work, I extend my deepest gratitude.

This Thesis is dedicated
to Nonna Pasqualina.

Table of contents

List of Tables

List of Figures

Chapter 1

Introduction and state of the art: steps towards Energy Transition

1.1 Trends in present and future energy systems

The global energy landscape is undergoing a deep and multidimensional transformation. Driven by the urgent need to mitigate climate change, improve energy security, and ensure access to affordable and reliable energy sources, current and future energy systems are shifting away from centralized, fossil-based infrastructures toward more decentralized, diversified, and low-carbon configurations (Montagnaro, 2024). This transition is being shaped by policy imperatives—such as the Paris Agreement and national net-zero targets—technological advances, market dynamics, and societal pressures. In 2024, fossil fuels satisfied the 81.2% of global energy needs, accounting for 142,420.89 TWh of a total of 175,271.75 TWh coming from oil, coal and gas (Energy Institute - Statistical Review of World Energy (2025)).

In this developing context, few macro-trends are emerging that redefine how energy is produced, converted, stored, and consumed. The most important is decarbonization effort, which is leading to a rapid expansion of renewable energy sources whose global installed capacities have grown significantly in the recent years (with global primary energy consumption by hydropower, wind, solar and other renewables being 10.86, 6.12, 5.15 and 2.47 PWh in 2024). In the same year, the global demand for biofuels rose by 3% to 2.2 Mbbloe/d[1] (Energy Institute - Statistical Review of World Energy (2025)). At the same time, the electrification of end-use sectors, including transport and heating, is increasing electricity demand and requiring more flexible and resilient grid architectures.

[1] Million barrels of oil equivalents per day, where 1 BOE (barrel oil equivalent) ≈ 1.7 MWh.

Despite advances in digitalization and decentralization, significant challenges are still present (e.g., the impossibility of easy electrification or decarbonization of some "hard-to-abate" sectors with renewables alone). Heavy industry, shipping, and aviation are example of energy-intensive sectors that require alternative energy carriers and carbon sources. Simultaneously, the environmental burden associated with waste streams—including plastics and biomass residues—continues to grow, posing both a challenge and an opportunity in the context of energy system transformation.

In this context, the role of bioenergy in future decarbonized, multi-commodity energy systems has been widely recognised. These systems are capable of providing a programmable renewable energy source that does not rely on the use of critical raw materials. Bioenergy can potentially be implemented in negative carbon emission conversion schemes and integrated—following a cascading use approach—into material recovery and valorisation processes typical of the circular economy. On the other hand, plastic residues have been also introduced as source of carbon for fuel production. In fact, the delegated Regulation (EU) 2023/1185 — which supplements the RED III Directive[2] — explicitly includes fuels derived from plastic waste (and other non-renewable waste) in the category of Recycled Carbon Fuels (RCFs), defined as liquid or gaseous fuels produced from solid or liquid waste streams of non-renewable origin, not suitable for material recovery according to Directive 2008/98/EC, or from process gases and exhaust gases of non-renewable origin generated as an unavoidable consequence of industrial processes.

Biological and thermochemical process can be used to transform biomasses in energy and fuels while only thermochemical route can be chosen to transform inorganic residues such as plastic.

Among thermochemical conversion technologies, pyrolysis represents a versatile pathway to valorise carbon-rich waste materials—such as lignocellulosic biomass and end-of-life plastics—by converting them into energy carriers (e.g., syngas, bio-oil) and carbonaceous solids (e.g., biochar), which may serve as fuels, chemical feedstocks, or carbon sinks, depending on the process configuration and downstream integration (Bridgwater, 2012). In this way, integration between waste management and valorization can be achieved.

From a systems perspective, pyrolysis technologies offer several strategic advantages:

- Feedstock-flexibility, accommodating a wide range of organic residues.
- Scalability, allowing both centralized industrial deployment and decentralized applications near waste sources.

[2] EU directive 2023/2413 with regard to the promotion of energy from renewable sources, available at http://data.europa.eu/eli/dir/2023/2413/oj.

- Integration across different sectors, enabling coupling between energy, waste management, and materials production.

In this work, the possibility to valorise olive stone and polyolefins - two different primary feedstocks–, the first a lignocellulosic biomass and the second end-of-life plastics, using the fast pyrolysis process has been investigated. More specifically the analysis has been focalized on the ex-situ catalytic fast pyrolysis as the most flexible and promising platform.

An overview on biomass and plastics as energy sources is initially given, together with a detailed state of the art on catalytic cracking of pyrolysis volatiles as upgrading strategy. The description of materials, catalysts and experimental procedures used for the investigation are then presented. Finally, results from the catalytic fast pyrolysis of a polyolefin mixture and olive stone will be discussed.

1.2 Biomass and plastics as energy sources

1.2.1 Biomass: characteristics and valorization routes

The term *biomass* refers to organic matrices directly or indirectly related to plants and to the photosynthesis process (Jacobsson and Johnson, 2000). In fact, biomass is formed by fixing incoming solar energy into the stable and noble form of chemical bonds in the presence of CO_2 and H_2O (Montagnaro, 2024).

Biomass resources on Earth are several, but a convenient classification (see Figure 1) among woody biomass, herbaceous and agricultural biomass, aquatic biomass, animal and human biomass waste, industrial biomass waste and biomass mixtures has been proposed by Vassilev et al. (2012). Woody biomass is the principal source of renewable energy in the world (Tursi, 2019).

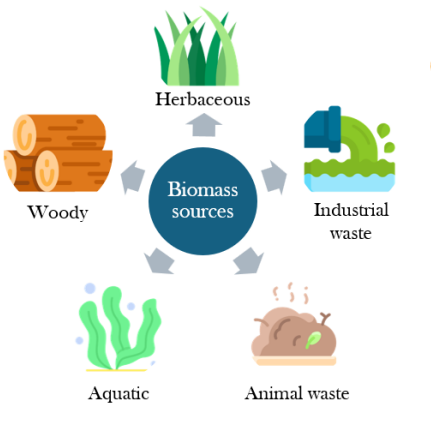

	C	O	H	VM	FC	M	A
	49-57	32-45	5-10	30-80	6-25	5-63	1-8
	42-58	34-49	3-9	41-77	9-35	4-48	1-19
	27-43	34-46	4-6	42-53	22-33	8-14	11-38
	57-61	21-25	7-8	43-62	12-13	3-9	23-34
	45-71	16-46	6-11	41-79	0-15	2-38	3-43

Figure 1: Biomass sources and their typical chemical characteristics. C, H, O stand for carbon, hydrogen and oxygen (wt.% on a *dry, ash-free* basis); VM=volatile matter, FC= fixed carbon, M= moisture and A=ash. Data from Vassilev et al. (2010).

The chemical composition and structure of biomass are of outstanding importance for their thermal treatment. Despite being a complex mixture of organic and – to a lesser extent – inorganic matter, the main constituents of biomass are cellulose, hemicellulose and lignin. Cellulose is a linear high-molecular weight biopolymer made up of D-pyran glucose subunits interlinked by β-(1,4)- glycosidic bonds. Its abundance is about 25-50% (wt.) of the biomass structure, of which up to 80% is in crystalline form. It has a structural function in plant cell walls.

Hemicellulose is a combination of different polysaccharides, among which sugars with five carbon atoms (arabinose, xylose) and six carbon atoms (glucose, mannose and galactose). Its structure is branched and disordered, with polymer chains being shorter than those found in cellulose, making hemicellulose an amorphous polymer. It represents 20-30% (wt.) of the biomass mass. Lignin is a mixture of amorphous, heterogeneous, high molecular weight aromatic compounds made up of phenolic units. It is responsible for the plant robustness and resistance. The lignin monomers (p- hydroxyphenyl (H), guaiacyl (G) and syringyl (S) units) are characterized by many polar groups which result in a strong intermolecular stability through the establishment of hydrogen bonds. Its abundance is 15-40% (wt.) of the biomass structure.

Among other components, lignocellulosic biomass retains moisture (from few percent -almost dry biomass- up to 90% in aquatic residues), and can contain minor organic compounds (e.g., proteins, nuclei acids, acetyls, extractives, resins) (Vassilev et al., 2012) and inorganic compounds such as a mixture of elemental metals, chlorides, sulphates, nitrates and many others (Tursi, 2019).

The relative amounts of cellulose, hemicellulose, and lignin vary depending on the specific biomass species (Crocker, 2010).

Biomass can be converted into fuels and/or chemicals of industrial interest following different paths. Its valorisation is considered environmentally more convenient than fossil fuels because biomass is virtually carbon-neutral, i.e., its combustion does not result in a net positive emission into the atmosphere. Specifically, during complete combustion of C and H, biomass releases the same amount of CO_2 previously fixed via photosynthesis during its growth, though emissions from processing and transportation must also be considered (Tursi, 2019; Montagnaro, 2024). Besides energy crops, valorization should prioritize residual biomass coming from industry, which would otherwise represent a waste.

After cultivation, harvesting and collection phase, biomass is pretreated, transported to the facility and/or stocked for future utilization. The main biomass conversion paths include physico-chemical conversion, thermochemical conversion and biochemical conversion (Figure 2).

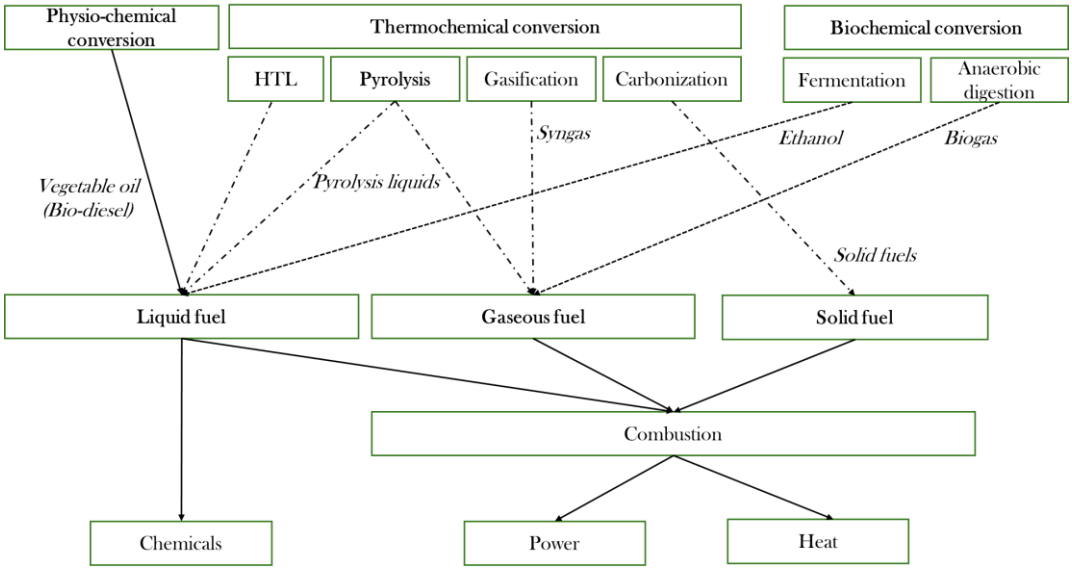

Figure 2: Biomass conversion technologies and products (adapted from Adams et al., 2018).

The physico-chemical route is limited to lipid-rich feedstocks and cannot process abundant lignocellulosic biomass. For instance, through the transesterification processes, biomass (especially vegetal oil and animal fats, which are constituted of triglycerides) is converted into a valuable *biodiesel.* The process includes the transformation of heavy oil triglycerides into fatty acids and glycerol, according to the following reaction (Tursi, 2019):

$$\text{Vegetable Oil} + \text{MeOH/EtOH} \rightarrow \text{Biodiesel} + \text{Glycerol} \qquad [1]$$

The transesterification process requires low temperatures (55-70°C) and pressure (1 atm) and high residence time (1-2 h), as reported by Shahid and Jamal (2011). After separation of biodiesel from glycerol, biodiesel is a renewable, non-toxic energy source composed of fatty acid methyl esters (FAMEs) of fatty acid ethyl esters (FAEEs). Its characteristics are similar to those of fossil diesel (Shahid & Jamal, 2011).

Biochemical conversion of biomass involves the use of bacteria, fungi, or enzymes to convert carbohydrates (hexoses and pentoses) to fuels and chemicals (Tursi, 2019). Before the biochemical treatment, there is a pretreatment step which converts biopolymers into smaller molecules (simple sugars), which is called *enzymatic hydrolysis*. After that, biomass can be valorised through the fermentation process or via anaerobic digestion (Figure 3), which are the most used biochemical routes (Brethauer and Studer, 2015).

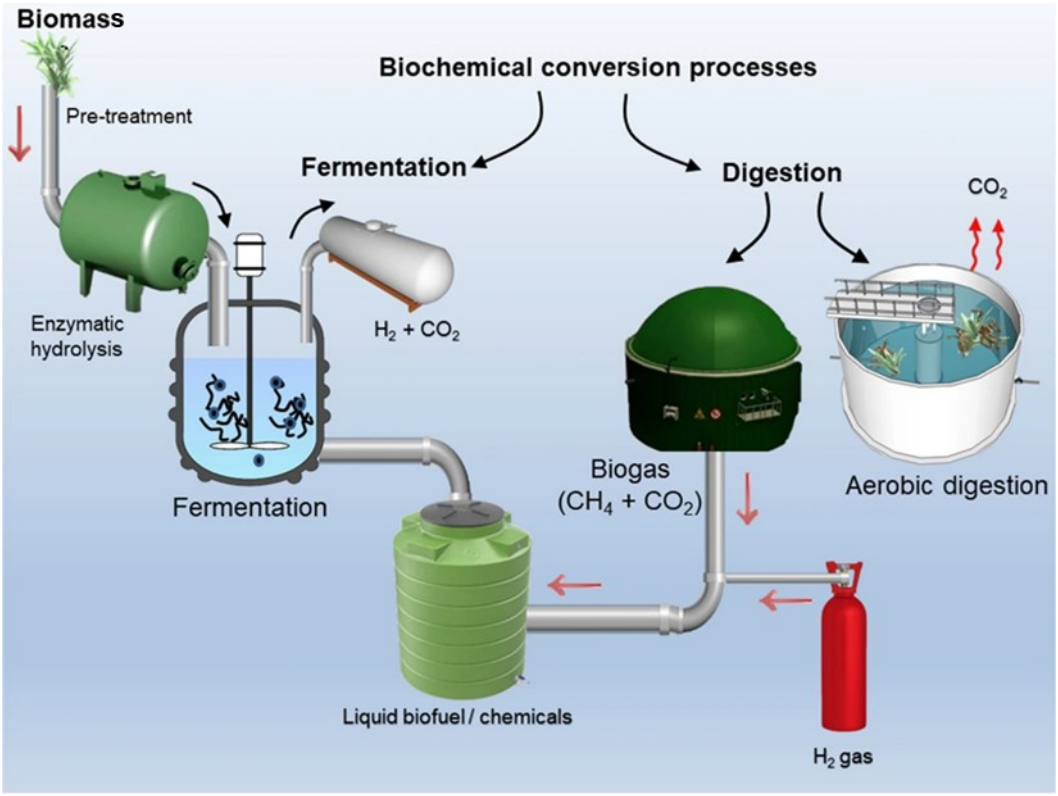

Figure 3: Schematic representation of fermentation and anaerobic digestion (Osman et al., 2021).

Fermentation is a process in which the simple sugars of biomass are converted into ethanol and carbon dioxide by yeasts. The product – a dilute aqueous solution of ethanol and biomass residues- is then distilled to recover ethanol in high purity. This can lead to low energy efficiencies, as low as 450 L/ton of dry corn (McKendry, 2002). Sugarcane and corn are the most used biomass for bio-ethanol production in Brazil and in the US (Adams et al., 2018).

Anaerobic digestion consists of a network of biochemical metabolic reactions in which bacteria degrade organic matter in an oxygen-free environment, leading to the production of biogas (mainly CO_2 and CH_4) and a residual digestate. The process is commercially proven and can be used to valorise high-moisture waste biomass while producing electricity and a valuable fertilizing agent (McKendry, 2002). In general, biochemical processes are not able to process as-received lignin-rich biomass, limiting the carbon efficiency and increasing the pre-treatment costs of the process; moreover, they are significantly slower compared to thermochemical routes.

Thermochemical conversion of biomass involves the use of heat to degrade bio-polymers and to generate gaseous, liquid and solid products. Combustion, pyrolysis, gasification and hydrothermal liquefaction are the most important thermochemical processes for biomass valorization (Tursi, 2019; Adams et al., 2018).

In the case of combustion, the energy stored within the biomass is released as radiative heat directly, while in the case of gasification, pyrolysis and liquefaction

a novel energy vector is produced. Thermochemical processes are faster and more efficient in degrading organic matter compared to biochemical processes (Adams et al., 2018; Leibbrandt et al., 2011). Regardless of the specific process, a commune heating path (a sequence of thermal events) involving drying, volatiles release (pyrolysis), volatile combustion, char combustion (or gasification)is at the basis of thermochemical processes. A schematic representation of the process is illustrated in Figure 4:

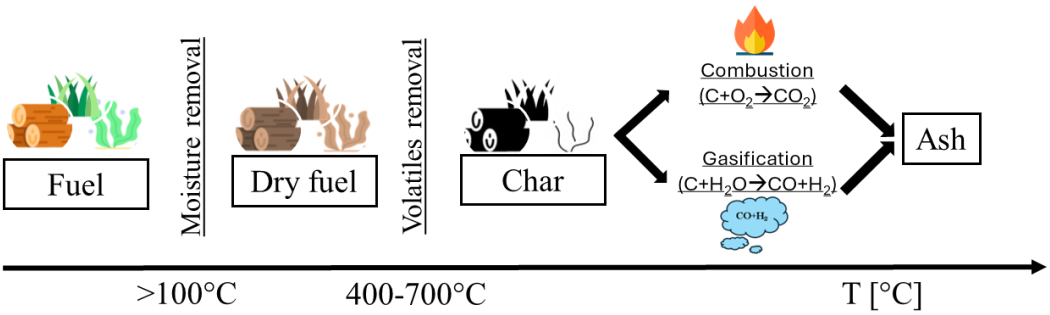

Figure 4: The heating path of a solid fuel particle. Adapted from Montagnaro (2024).

The fuel particle first loses its moisture (T>100°C), then - between 400 and 700°C - there is the pyrolysis step, during which biomass releases volatiles. These can burn around the flame until a char particle (made up of carbon and ash) is left behind. Char can then burn (if there is oxygen available) or be gasified to produce syngas, i.e., a mixture of CO and H_2.

During combustion the organic matter is completely oxidised under stoichiometric or excess oxygen conditions, which results in the production of carbon dioxide (CO_2) and water vapour (H_2O), along with the release of heat and the overall process is exothermic. Typical working temperatures within furnaces and combustion chambers range between 800-1000°C at atmospheric pressure.

The efficiency of the process is strongly dependent on the biomass properties, e.g., biomass with low moisture content (<50%) must be used in the process for stable combustion (Tursi, 2019), and particle size, on temperature and combustion environment. Moreover, the main challenge in the field of combustion is represented by emissions, specifically the control and abatement of particulate matter, NOx, CO, hydrocarbons (HC) and SO_2 (Adams et al., 2018). The technology is commercially available, and plants range from small to industrial scale (up to 100-3000 MW) (McKendry, 2002).

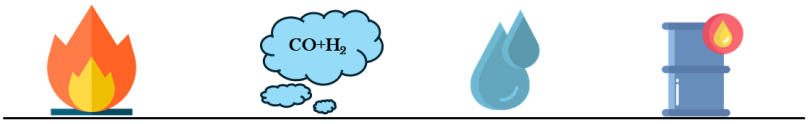

	Combustion	*Gasification*	*HTL*	*Pyrolysis*
Operating conditions	800-1000°C, atmospheric pressure, air	700-1500°C, 1-5 MPa, sub-stoichiometric O_2 or steam	280-370°C, 10-25 MPa, presence of water	300-900°C, atmospheric pressure, inert environment
Advantages	• High energy recovery as heat or power. • Direct and simple process.	• High efficiency of conversion to syngas. • Versatile product usage (electricity, chemicals, liquid fuels). • Can handle low-quality biomass.	• Efficient for wet biomass (no need for drying). • Produces bio-crude similar to fossil crude. • Lower energy requirements than pyrolysis and gasification.	• Bio-oil can be upgraded. • Moderate operating conditions. • Can process diverse feedstocks. • Fast pyrolysis yields up to 75% liquid products.
Disadvantages	• High emissions of CO_2 and pollutants (NO_x, SO_x, particulate matter. • Inefficient for wet biomass.	• Tar and particulate formation. • High CAPEX and OPEX. • Challenging process control and scaling.	• High-pressure requirements increase costs. • Bio-crude needs further refining. • Corrosion issues in reactors.	• Bio-oil requires upgrading (high oxygen content). • Char is a low-value product.
Main products	Heat, electricity, flue gases.	Syngas, char, ash.	Bio-liquid, aqueous phase, solid char, gases.	Bio-oil, char, permanent gases.
TRL	9	9	3-6	6-9

Figure 5: Comparison of different biomass thermochemical conversion processes. Data from Tursi (2019), McKendry (2002), Barriero et al. (2013), Bridgwater (2012). TRL data from Shahbaz et al. (2022).

Gasification of organic matter can occur in two distinct ways: in presence of a sub-stoichiometric concentration of oxygen or in presence of another gasification agent (CO_2, steam). In the first case, the dominant reactions are those of partial oxidation of carbonaceous material to produce CO and H_2 (syngas). In the second case, the process is dominated by reforming reactions (e.g., $C + H_2O \rightarrow CO + H_2$).

The process is conducted within reactors called "*gasifiers*" at temperatures between 800-1100°C and typically produces 85% gas, 10% solid char and 5% liquid tars (Bridgwater, 2012). After the gasification step, syngas is cleaned and purified to remove harmful compounds such as particulate matter (via filtration), tars (electrostatic precipitators, thermal or catalytic cracking), sulphur compounds (sorbent), nitrogen compounds, chlorides and alkali compounds (Woolcock and Brown, 2013). Cleaning and purification are a costly barrier to the widespread economic viability of gasifiers (Sharma et al., 2013). Then, syngas can be used as a fuel or can be upgraded to a plethora of chemicals of industrial interest, such as ethanol, methanol, ammonia, acetic acid, synthetic natural gas (SNG) and many others (Woolcock and Brown, 2013; You et al., 2018).

Hydrothermal liquefaction (HTL) is a thermochemical process that occurs at mild temperatures (280-370°C) and high pressure (10-25 MPa) in the presence of sub- or supercritical water as both solvent and reactant (Barreiro et al., 2013). HTL can process a wide variety of wet biomass, including algae, agricultural residues, sewage sludge, food waste, and other organic materials without the need for prior drying, making it especially suitable for water-rich materials. The primary product is bio-crude oil, a viscous, energy-rich substance that requires further processing before utilization (Yu et al., 2012). Other products include gases (e.g., CO_2, H_2), aqueous by-products rich in nutrients (which can be recycled), and solid residues (char). Figure 5 summarizes the main features of the thermochemical routes for biomass processing. Pyrolysis is the degradation of organic matter in the absence of oxygen at temperatures ranging between 300-900°C. The process can be tuned to produce high yields of liquid product. A detailed description of pyrolysis will be given in Section 1.3.

1.2.2 Plastics: characteristics and valorization routes

The term “plastics” refers to a family of polymeric materials which usually contain other substances or additives to improve their properties (Vert et al., 2012). Global plastic production reached 460 million tons in 2019 (OECD, 2022) and projections show that 975 million tons will be produced in 2050 (https://ourworldindata.org/plastic-pollution).

The most important plastic materials produced on a global scale include polyethylene terephthalate (PET), high-density and low-density polyethylene (HDPE and LDPE), polypropylene (PP), polyvinyl chloride (PVC) and polystyrene (PS). In the European Union, polyolefins like PP and PE represent a significant share of the total annual plastic production. In 2022, PP accounted for 16.6% of the total plastic production, while PE (LDPE and HDPE) accounted for 24% (Figure 6-A). It is noteworthy that only 10.1% of the plastic has been recycled, and that the extensive application of bio-based plastics is far from being significant. Packaging alone requires the 39.1% of all the produced plastic in a year, with the other “plastic-intensive” sectors being the building and construction, automotive and electronics (Figure 6-B).

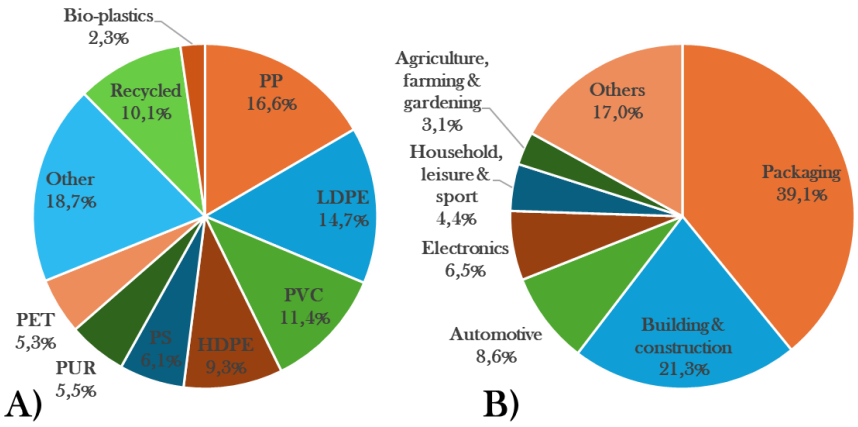

Figure 6: Plastic production in the European Union (EU27+3) in 2022 according to the type of polymer (a) and application (b); data from plasticseurope.org.

Except for PET, the most used polymers are characterized by carbon and hydrogen, with only traces of oxygen and other elements, as shown in Figure 7 where the proximate and ultimate analyses of different polymers are reported (Chang, 2023). The low ash content and the high volatile content of plastics favour the formation of liquid products during pyrolysis, with reduced solid residues (Yuan et al., 2022).

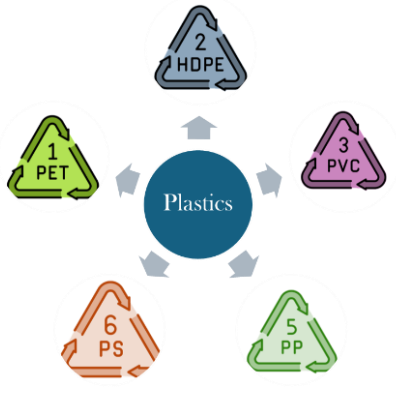

	C	O	H	VM	FC	M	A
1 PET	62.6-64.1	33.0-34.2	3.7-4.4	84.1-94.4	5.6 - 13.9	0.0	0.0
2 HDPE	85.5-86.5	0.0-0.2	14.2-15.1	97.2-99.6	0.0	0.0-0.2	0.2-0.8
3 PVC	38.3-38.7	0.0	4.5-4.8	94.9-95.8	4.2-5.1	0.0	0.0
5 PP	83.7-84.7	0.0-0.15	14.3-15-3	93.8-96.9	0.0-1.6	0.0 - 0.16	1.0-4.5
6 PS	90.4-91.6	0.18-0.45	7.8-8.6	99.6-99.8	0.2-0.4	0.0	0.0

Figure 7: Ultimate and proximate analysis of selected plastic wastes. C, H, O stand for carbon, hydrogen and oxygen (wt.% on a *daf* basis); VM=volatile matter, FC= fixed carbon, M= moisture and A=ash. Data from Chang (2023).

The valorization and recycling of polyolefin plastics, such as polyethylene (PE) and polypropylene (PP), represent a critical challenge and an area of intense scientific research, given their ubiquity in post-consumer waste and their inherent chemical inertness. Strategies for managing these materials can be broadly classified into three main categories: mechanical recycling, chemical recycling, and other valorization approaches.

Mechanical recycling is the most established and widespread approach for processing polyolefin waste. This process involves the collection, sorting, cleaning, and re-extrusion of plastic waste to produce pellets of recycled material, which can then be used to manufacture new products (Hassanian-Moghaddam et al., 2023). The primary advantage of this route lies in its lower cost and reduced

greenhouse gas emissions compared to other alternatives (Hassanian-Moghaddam et al., 2023). However, mechanical recycling has significant limitations. The process is highly sensitive to the purity of the incoming waste stream; contaminants such as other plastic types, organic residues, or additives can drastically compromise the properties of the recycled material (Faust et al., 2023). Furthermore, polyolefins undergo thermo-oxidative degradation during extrusion cycles, which leads to polymer chain scission, cross-linking, and the formation of oxygenated groups, with a progressive loss of mechanical properties, rendering the recycled material unsuitable for high-value applications and limiting its use to a finite number of cycles (Hassanian-Moghaddam et al., 2023; Westlie et al., 2022).

Chemical recycling refers to a set of technologies that decompose the polymeric structure of polyolefins into their basic molecular constituents or other valuable chemicals. This approach can handle more complex and contaminated plastic waste streams than mechanical recycling and can theoretically produce feedstocks of a quality comparable to virgin materials, enabling closed-loop recycling (Hassanian-Moghaddam et al., 2023). Among these technologies there are pyrolysis, gasification, hydropyrolysis and HTL.

One of the main chemical recycling technologies is pyrolysis, a thermal cracking process that occurs in the absence of oxygen at temperatures typically ranging from 300 to 700°C (Faust et al., 2023). The thermal pyrolysis of polyolefins produces a complex mixture of gaseous, liquid (pyrolysis oil), and solid hydrocarbons (waxes and char). The distribution of these products is highly dependent on operating conditions such as temperature and residence time (Lopez et al., 2017b). Catalytic pyrolysis employs acid catalysts, such as zeolites (e.g., HZSM-5) or Fluid Catalytic Cracking (FCC) catalysts, to enhance the process selectivity and lower the operating temperatures (Lopez et al., 2017b). The use of catalysts allows for a narrower product distribution, favouring the production of specific hydrocarbon fractions like gasoline or diesel. For instance, the HZSM-5 zeolite is particularly effective in producing light olefins and aromatic hydrocarbons, owing to its acidity and shape selectivity (Lopez et al., 2017b).

Other chemical recycling technologies include hydrocracking and hydrogenolysis, which utilize hydrogen and bifunctional catalysts (with metal and acid sites) to cleave polyolefin chains into saturated hydrocarbons at more moderate temperatures (Faust et al, 2023). These processes can yield high-quality liquid fuels, such as diesel and jet fuel, but require an input of hydrogen, which represents an additional cost (Faust et al., 2023).

Beyond mechanical and chemical recycling, other strategies exist for the valorization of polyolefins. Energy recovery through incineration is a common practice, especially for mixed and contaminated plastic waste that cannot be economically recycled by other means (Faust et al., 2023). Polyolefins have a high calorific value, comparable to that of fossil fuels, making them a good source

of energy. However, incineration is considered the least sustainable option as it involves the loss of material and the generation of greenhouse gas emissions and other pollutants.

Another emerging strategy is the integration of products derived from plastic pyrolysis, such as waxes, directly into refinery cracking units (e.g., FCC). This approach, termed co-processing, leverages existing and amortized infrastructure to convert plastic waste into fuels and chemicals, thereby reducing investment costs (Lopez et al., 2017b). Studies have shown that co-processing polyolefin waxes with vacuum gas oil (VGO) can improve conversion and gasoline yield, representing a promising route for large-scale valorization (Lopez et al., 2017b).

Polyolefins and biomass are both valuable resources that can be valorised to produce energy, fuels and chemicals. To have a clear understanding of the differences between these two classes of materials, this paragraph briefly describes the properties of polyolefins in comparison to those of lignocellulosic biomass. As shown in Figure 8, biomass is characterized by a wide range of C/H/O ratios, with H/C between 1-2, and O/C from 0.2 to 1.2. On the other hand, polyolefins occupy the upper-left region of the Van Krevelen diagram, as they show a low oxygen content (low O/C) and high hydrogen-to-carbon ratio. This is the result of the different chemical composition of biomass (40-50% C, 5-6% H, 40-50% O, <1% N, as illustrated in Figure 1) compared to PE and PP (83-85% C, 13-15% H, <1% O, as reported in Figure 7).

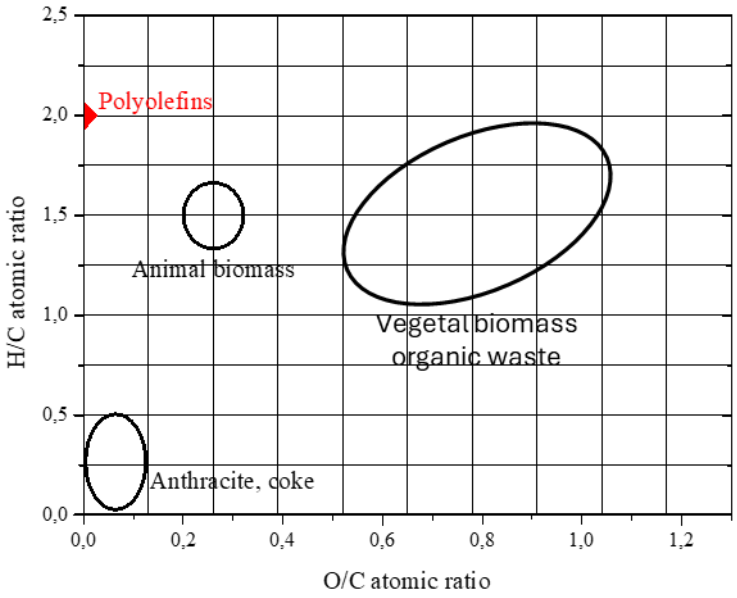

Figure 8: Van Krevelen diagram for different solid fuels (adapted from Montagnanaro, 2024).

As a result, the heating value of polyolefins is typically double (40-45 MJ/kg) than that of lignocellulosic biomass (16-20 MJ/kg). Moreover, the moisture content of biomass can reach 60%, leading to a reduced energy density compared to polyolefins, in which moisture is virtually absent (<1%).

Biomasses are easily degradable, while polyolefins are chemically more stable and resistant to degradation, making their disposal problematic in an environmental context. Thus, biomass is a non-polluting renewable resource, while polyolefins – although having a lower environmental impact compared to PVC or PET – are non-renewable, fossil-based materials.

1.3 Fast pyrolysis

As previously underlined, the valorization of residual biomass and plastic waste will play an increasingly important role in the transition toward a decarbonized world, progressively replacing fossil resources in the production of biofuels and platform chemicals, and only thermochemical routes are applicable at both biogenic and not biogenic carbon sources. In addition, thermochemical processes are capable of converting all the carbon present in the raw material, unlike biological processes which can only valorise the non-recalcitrant fraction of biomass, or mechanical processes for plastic residues, which allow to obtain a product with lower quality.

Among thermochemical processes, fast pyrolysis offers a direct route for producing liquid fuels and chemical products, with greater flexibility regarding feedstock characteristics and higher energy input efficiency compared to other thermochemical processes. Moreover, fast pyrolysis is well-suited for "long-chain" valorization pathways, based on the decentralized conversion of raw materials at collection sites into intermediate products (e.g., pyrolytic oil), which can subsequently be transported, upgraded and refined in biorefineries.

Pyrolysis is a thermal treatment during which a solid organic material is degraded in an inert atmosphere, i.e. in the absence of oxidizing agents (Bridgwater, 2012). Under these conditions, organic polymers are thermally decomposed to form three distinct products: a solid fraction called "biochar", a liquid product (bio-oil, bio-liquid, pyrolysis oil), and incondensable gases. In the case of biomass, it is common to refer to the pyrolysis liquid as "bio-oil". For non-biogenic carbon sources, the term "pyrolytic oil" appears more adequate.

The relative proportions of the products are determined by many factors, among which the operating conditions of the reactor (i.e., temperature, pressure, residence time of the solid and vapours), the heating rate of the solid fuel particles, and the reactor technology itself (Sharifzadeh et al., 2019; Bridgwater, 2012). Table 1 illustrates the typical product distribution from the pyrolysis of wood under different operating conditions:

Table 1: Product distribution from different modes of wood pyrolysis (d.b.) (adapted from Bridgwater, 2012)

Type	Conditions	Bio-oil [%]	Char [%]	Gas [%]
Fast	500°C, HVRT~1s	75	12	13
Intermediate	500°C, HVRT~10-30s	50	25	25
Slow	400°C, vapor residence time: hours-days	30	35	35
Gasification	750-900°C	5	10	85
Torrefaction	290°C, solid residence time: 10 -60 min	0-5	up to 80	20

HVRT= Hot Vapour Residence Time

When the process is characterized by low temperature and high residence time within the reactor, high char yields (up to 80% wt.) can be expected – especially in the case of biomass with high ash content. In the opposite case, when reaction temperature is very high (700-900°C), the main product is incondensable gas (up to 85%), with limited formation of solid and liquid products.

For processes aimed at producing liquid products, the optimal reaction temperature for many lignocellulosic biomasses is typically around 500°C (Kersten and Garcia-Perez, 2013). Additionally, it is essential to minimize the residence time of the hot vapours inside the reaction environment to prevent excessive cracking of products into incondensable gases.

Biomass chemical composition and physical structure are of outstanding importance for the design of thermochemical conversion processes because they deeply influence the product distribution and the chemical composition of the products themselves (Figueirédo et al., 2022; Tursi, 2019).

During pyrolysis, biomass particles undergo a complex reaction network involving heat and mass transfer within the reactive environment. Initially, the biomass releases its free moisture as water, and then, thanks to the rupture of OH-bonds within dehydration reactions involving alcohols, ethers and other oxygenated molecules in holocellulose and lignin, reaction water is also produced. At the same time, some incondensable gases such as CO and CO_2 are expelled from the biomass structure, which does not change substantially at this stage. Primary pyrolysis reactions occurring within the temperature range of 200-600°C convert large biopolymers into condensable vapours, which serve as precursors for the bio-oil fraction, along with the formation of solid char (Salatino et al., 2023).

This happens through a complex network of chemical reactions which break some bonds to form different molecules. The main steps of this process are:

- depolymerization of long-chain biopolymers and formation of volatiles monomers, dimers and trimers which can condense at ambient temperature.
- polymers and oligomers fragmentation with non-condensable gases expulsion from the biomass structure.

- char formation through intermolecular rearranging reactions with generation of water and incondensable gases.

The condensable vapours, comprising the bio-oil fraction, can undergo further breakdown into incondensable gases (CO, CO_2, H_2) if the residence time of vapours is prolonged. Therefore, efficient design of a fast pyrolysis unit necessitates precise control of the reactor temperature and prompt removal of pyrolysis condensable vapours from the system to prevent secondary cracking reactions catalysed by hot char particles. Indeed, char is characterized by a porous structure able to host metal active sites that can function as catalysts for the conversion of pyrolysis vapours into incondensable gases, thereby reducing the yield of bio-oil (Pienihäkkinen et al, 2022). Consequently, char should be promptly removed from the system, while the vapours are cooled and condensed to produce bio-oil. This design approach ensures the preservation of thermolabile desired molecules and prevents undesirable reactions that could compromise the quality of the product.

Biomass pretreatment plays a fundamental role in enhancing pyrolysis performance, encompassing both mechanical and chemical techniques. Mechanical methods, such as grinding and densification, improve heat transfer within the reactor and limit the formation of secondary polymerization products, thereby enhancing the quality of bio-oil. Chemical pretreatments, including acidic or alkaline treatments, focus on the removal of impurities, reduction of undesired reactions, and enhancement of biomass energy content, which collectively improve the yield and composition of pyrolysis outputs (Agbor et al., 2011).

Temperature is a critical variable in pyrolysis, as it provides the thermal energy necessary to cleave chemical bonds in biomass molecules. This, in turn, affects the yield and composition of pyrolysis products, particularly bio-oil (Bridgwater, 2012) Analytical techniques such as thermogravimetric analysis (TGA) and differential thermal analysis (DTA) are often used to investigate these thermal effects, identifying key stages in biomass decomposition—namely dehydration, devolatilization, and carbonization (e.g., Di Blasi et al., 2013). The optimal pyrolysis temperature is highly dependent on biomass type, revealing the complex interaction between thermal input, feedstock composition, and liquid product yield. Among the biomass constituents, hemicellulose is the most sensitive to temperature increase. Its decomposition starts at relatively low temperature (200-300°C) and produces mainly light organic molecules such as aldehydes, alcohols, acids (e.g., formic, acetic) and water. Cellulose decomposes at higher temperatures (300-400°C) and, together with hemicellulose, contributes to the formation of monomeric anhydro-sugars (e.g., levoglucosan), heterocyclic compounds (e.g., furfural and HMFU), hydroxy-aldehydes, ketones, and alcohols (methanol, ethanol) (Figueiredo et al., 2022). Finally, lignin is characterized by higher resistance to temperature, and decomposes in a wide range of temperatures, from 200°C up to 900°C. Aromatic hydrocarbons (benzene, toluene),

methoxyphenols (guaiacols, syringols, catechols), and pyrolytic lignin oligomers are the main decomposition products (Arnold et al., 2017).

Biomass particle size also influences the pyrolysis process, particularly in catalytic systems. Smaller particles enhance internal heat transfer and increase the uniformity of thermal decomposition, while larger particles can cause uneven heating and reduce bio-oil yield. Empirical studies consistently report an inverse relationship between particle size and liquid product yield, highlighting the importance of particle size optimization in reactor design and operation (e.g., Shen et al., 2009b).

The heating rate is another major factor in pyrolysis, significantly impacting the decomposition kinetics and the distribution of products. The optimum heating rate is specific to each feedstock and is crucial for maximizing process efficiency and product quality.

Finally, moisture content in the biomass feedstock must be carefully controlled, with optimal levels typically below 10%. High moisture levels lead to increased water content in the resulting bio-oil, including both intrinsic and reaction-generated water, which can result in undesirable phase separation and reduced fuel quality. Proper drying and moisture management are therefore essential to ensure stable and high-quality pyrolysis products (Bridgwater, 2018; Oasmaa et al., 2015). Fast pyrolysis can also be effectively applied to non-biogenic materials such as waste plastics. In this case, the absence of oxygen and the high heating rates similarly promote polymer chain scission, leading to the formation of liquid hydrocarbons, waxes, and gaseous products. The process parameters, particularly temperature and residence time, influence the distribution of these products, with higher temperatures favouring gas production and lower temperatures enhancing liquid yield. Unlike biomass pyrolysis, no significant char formation occurs, and the resulting pyrolytic oil generally contains fewer oxygenated compounds, exhibiting a composition closer to conventional fossil-derived fuels.

1.3.1 Reactors for fast pyrolysis

Many technologies have been developed for the fast pyrolysis of biomass and plastic materials. Reactors are often classified according to the final targeted product (such as pyrolytic oil, syngas, or biochar), the type of heat source utilized (direct or indirect heating), construction materials, whether the reactor operates continuously or in batch mode, the pressure conditions (such as atmospheric, vacuum, or pressurized) or the heating rate (Slezak et al., 2023; Garcia-Nunez et al., 2017). This section will explore fast pyrolysis reactors in detail, followed by a discussion of alternative technologies, highlighting both their operational mechanisms and their advantages within various pyrolysis applications.

Bubbling fluidized-bed reactors (Figure 9-A) are widely used for the thermochemical conversion of biomass and plastic materials, leveraging high

heating rates for effective pyrolysis. In these systems, feedstock particles are heated rapidly using a solid inert heat carrier—typically sand—and a carrier gas (usually nitrogen) to fluidize the particles, ensuring they mix thoroughly with the sand bed. Due to the inherently low thermal conductivity of biomass particles (Cai et al., 2017), the feedstock must be finely ground to a particle size of less than 2-3 mm (Bridgwater, 2012). This promotes high heat transfer rates, minimizes thermal gradients, and helps prevent clogging within the reactor.

The reactor's fluidizing gas is introduced from the bottom and distributed evenly by a distribution plate, ensuring a uniform bubbling regime. During continuous operation, the feedstock undergoes pyrolysis, releasing volatile compounds that flow through a solid capture system (cyclone separators, filter), where elutriated char particles are captured. The volatile stream then is sent to a condensation stage, where pyrolysis oil is collected, achieving yields of up to 70% on a dry-feed basis in optimal conditions (Bridgwater, 2012).

Bubbling fluidized-bed reactors are advantageous due to their mature technology, ease of scale-up, and excellent temperature control, making them one of the preferred technologies for biomass conversion. However, they require relatively high flow rates of the fluidizing gas—usually 1.5 to 2 times the minimum fluidization velocity—to maintain a stable bubbling regime (Slezak et al., 2023).

Spouted-bed reactors are a class of gas-solid contactors characterized by a unique pattern of solid and gas flow. As described by Mathur & Epstein (1974), spouted regime is obtained when a jet of gas is injected vertically from the bottom of the reactor through a small nozzle. When the gas velocity is increased to a certain extent, the momentum of the gas jet is sufficient to overcome the gravitational and frictional forces of the packed bed, thus hurling particles upwards to form a *fountain*. These particles then, subject to the gravitational force, return to the annular region of the solid bed, and slowly move downward until reaching the bottom of the vessel (Figure 9-B). In that moment, the particle is sucked again into the spouting region and the process repeats. It is common in the literature to schematise the spouted-bed as the composition of two distinct regions: a central region called *spout*, characterized by an extremely low solid fraction and high velocity; on the other hand, the *annulus*, which is characterized by higher solid concentration and a void fraction typical of a loose packed bed. The solid velocity within the annulus is much lower compared to the spouting region. Thanks to this system, a cyclic pattern for the solid particles is obtained, which can be extremely useful in certain applications in which the solid residence time inside the reactor must be properly controlled.

In ablative pyrolysis (Figure 9-C), biomass particles are pressed against a hot surface, typically kept below 600°C (Bridgwater, 2012) where thermal decomposition occurs at the interface between the biomass and the surface. As the biomass particles are in direct contact with this heated surface, pyrolysis reactions are triggered, producing an oil film and incondensable gases. The oil film acts as a

lubricant for incoming particles, while the movement of the hot surface brings fresh areas into contact with new biomass particles, increasing the pyrolysis rate.

The efficiency of ablative pyrolysis depends on several factors, including the surface temperature, applied pressure, and the rate at which biomass contacts the heated surface (Bridgwater, 2012). A unique advantage of this technology is that it operates without a carrier gas, which enables the production of a non-diluted volatile stream and allows for efficient condensation with small-size equipment (Uddin et al., 2018). Oil yields in ablative pyrolysis can reach up to 70%, similar to yields in fluidized-bed reactors (Garcia-Nunez et al., 2017; Bridgwater, 2012).

However, there are notable challenges associated with ablative pyrolysis. Due to the absence of a carrier gas, pyrolysis products are more challenging to separate, often leading to high solid concentrations in the resulting oil (Slezak et al., 2023; Bridgwater et al., 1999). Additionally, the reactor requires precise control of the heated surface area and involves moving parts at high temperatures, which increases system complexity, wear, and maintenance needs over time (Garcia-Nunez et al., 2017; Bridgwater, 2012). After the fundamental studies conducted by CNRS in Nancy (France) on the mechanism of ablative pyrolysis and the effects of operating parameters on ablation rate (Lédé et al., 1985), different configurations of ablative reactors have been developed by NREL (Diebold and Scahill, 1988), Aston University (Peacocke and Bridgwater, 1994) and by PyTec in Germany – with a size up to 250 kg/h (Meier et al., 2004).

In rotating cone reactors (Figure 9-D), a mixture of biomass particles and hot sand is introduced at the base of the reactor, where centrifugal forces generated by a heated rotating cone (operating up to 10 Hz) ensure thorough mixing and heat transfer (Bridgwater, 2012). Char is typically separated and burned externally, while the heated sand is recirculated back into the reactor, maintaining the necessary thermal conditions. This design promotes bio-oil yields of 60-70 wt.% (dry basis) due to its efficient heat transfer (Wagenaar et al., 2001).

One of the key advantages of rotating cone reactors is that they do not rely on a large volume of carrier gas, making the system more compact and reducing operating costs (Slezak et al., 2023). The lower carrier gas requirement also facilitates the condensation of pyrolysis vapours, improving the pyrolytic oil recovery process compared to fluidized bed reactors. A successful example of scale-up for this technology is the 50-ton-per-day demonstration plant established in Malaysia (Garcia-Nunez et al., 2017).

Screw reactors (Figure 9-E) represent a robust and scalable solution for continuous pyrolysis, particularly of biomass and plastic waste. Their design enables precise control over residence time and heating rate, critical for optimizing product distribution (Bridgwater, 2012). Material is conveyed by a rotating screw through a heated tube, typically under inert atmosphere, allowing for thermal decomposition into oil, gas, and char (Mohan et al., 2006). These reactors are mechanically simple, have low maintenance requirements, and are well-suited for handling solids with heterogeneous particle sizes. Heat transfer

efficiency, however, is often limited by conduction through the screw and walls, requiring external heaters or heat carrier solids (Bridgwater, 2012).

Circulating fluidized-bed (CFB) reactors are more complex than fluidized and spouted-bed reactors and are designed to optimize heat transfer and treat high amounts of biomass. A typical CFB system includes a fluidized-bed reactor and a separate combustor (see Figure 9-F). In this configuration, biomass feedstock is introduced at the base of the reactor, where it is rapidly mixed with hot sand, facilitating pyrolysis. Due to the elevated gas velocities in CFB systems, the vapor residence time is limited to about 0.5–1 second, and the solids are moved from or to the reactor, depending on the configuration (Sharifzadeh et al., 2019).

The pyrolysis process produces char, which, along with the hot sand, is transported to the combustor. Here, the char is combusted, releasing heat that reheats the sand, which is then recycled back to the reactor to sustain the endothermic pyrolysis reactions. A solid-gas separation system, typically a cyclone, cleans the volatile stream, allowing it to be directed to the condensation stage for bio-oil recovery, while separating it from particulate matter. As in bubbling bed reactors, biomass should be shredded before feeding and the high nitrogen flowrates produce a diluted gas (Slezak et al., 2023).

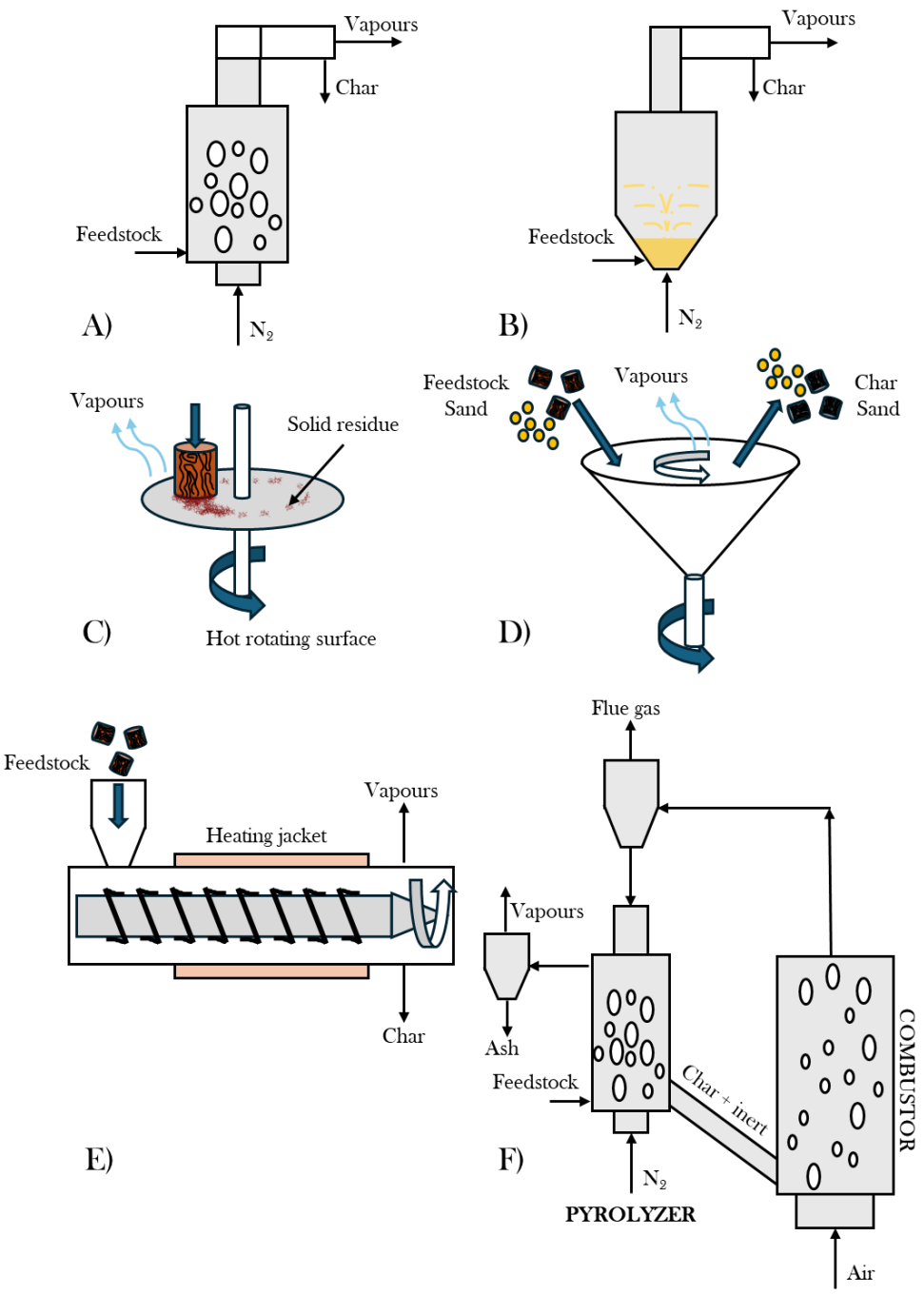

Figure 9: Selected pyrolysis reactor technologies. Bubbling fluidized bed reactor (A), spouted-bed reactor (B), ablative pyrolysis (C), rotating cone reactor (D), auger reactor (E) and circulating fluidized bed reactor (F). Pictures adapted from Vamvuka et al. (2011) and Perkins et al. (2018).

1.3.2 Fast pyrolysis products

As mentioned before, pyrolysis always yields three products (biochar, pyrolytic oil, incondensable gases), but their relative amount is dependent on the conditions of the process and on the characteristics of the feedstock.

Biochar is a solid residue which consists of fixed carbon and ash from the original biomass and can contain up to 25% of the initial biomass energy content (Bridgwater, 2012). Its formation is promoted in low-temperature, low-heating

rates pyrolytic processes. Its physical and chemical characteristics are dependent on the feedstock and the operating conditions of the pyrolysis process (Saravanan and Kumar, 2022). Biochar has been extensively studied in the recent decades, and it was shown that it can be used for adsorption, as activated carbon, for soil amendment and fertilization or as support for metal catalysts (Saravanan and Kumar, 2022). More specifically, the specific surface area of biochar was found to be larger in the case of steam or CO_2 pyrolysis atmosphere (Lee et al., 2017). Other applications of biochar include co-feeding in boilers (Liu et al., 2013) and synthesis of carbon nanotubes (Titirici et al., 2012).

Integrated biomass pyrolysis systems can involve a section for char combustion or gasification which exploits its energy to dry the biomass feedstock or to sustain the thermicity of the process. It is worth mentioning that in the case of plastic materials, solid residue is typically low due to the high volatile fraction between 90-99 wt.% (Mansor et al., 2022).

The incondensable gas produced during the fast pyrolysis of biomass is mainly composed of CO, CO_2, H_2, CH_4 and light hydrocarbons such as ethane (C_2H_6), ethylene (C_2H_4), propane (C_3H_8), propylene (C_3H_6) and butane (C_4H_{10}), with a heating value of 6.4-9.8 MJ/kg (Varma et al., 2018). Gas yield can be promoted by increasing reaction temperature and residence time within the reactor, so that volatiles can undergo cracking, decarboxylation, decarbonylation and other secondary reactions (Kan et al., 2016). Nevertheless, in the case of fluidized-bed reactors, this gas is heavily diluted in N_2, which is used as fluidization agent and can represent up to 99% of the total gas flow. For this reason, incondensable gases are of limited interest and are generally burned to help the heat integration within the pyrolysis system (Hoang et al., 2021). In the case of plastic materials (e.g., HDPE), the gas fraction is characterized by C_1-C_4 hydrocarbons (e.g., methane, ethane, ethylene, propane, propylene, butanes and butenes) and hydrogen, with their proportions being dependent on the operating parameters of the process (Elordi et al., 2011a).

The primary product obtained from fast pyrolysis is a dense organic liquid - known as *pyrolytic oil*. In the case of biomass feedstocks, bio-oil is a complex mixture of compounds resulting from the decomposition of biomass macro components, namely cellulose, hemicellulose, and lignin. It can be considered as a micro-emulsion comprising a pyrolytic lignin phase dispersed within an aqueous solution of cellulose and hemicellulose decomposition products (Bridgwater, 2018). The physical and chemical properties of bio-oil can significantly differ depending on the feedstock. Table 2 shows some properties of bio-oil and of HDPE-derived oil.

Table 2: Comparison between biomass- and plastic-derived pyrolysis oil.

Parameter	Bio-oil [a]	Plastic oil (HDPE) [b]
Carbon [wt%]	56	85
Hydrogen [wt%]	6	14.5
Oxygen [wt%]	38	0.27
Nitrogen [wt%]	0-0.1	0.27
Moisture [%]	25	0
pH	2.5	5.5
Specific gravity	1.2	0.78
HHV [MJ/kg]	17	42.9
Viscosity @40°C [mPa s]	40-100	1.3

[a] Data adapted from Bridgwater (2018)
[b] Data adapted from Hasan et al. (2023)

Examination of Table 2 and Figure 10 helps to clarify the difference between plastic-derived pyrolysis oils and bio-oils. Bio-oil is characterized by high acidity, with pH levels as low as 2-3. This is caused by the presence of organic carboxylic acids coming from the depolymerization of cellulose and hemicellulose (Bridgwater, 2018). As a consequence, bio-oil is corrosive and can pose challenges to storage. Moreover, due to the high concentration of oxygenated molecules susceptible to polymerization reactions during storage or handling, bio-oil can undergo an "aging" process, which increases viscosity and water content of the oil with time. The aging rate depends on the chemical composition of the oil and on the storage temperature, which can accelerate etherification and esterification of oxygenated compounds (Oasmaa and Czernik, 1999), often leading to phase separation (Oasmaa et al., 2015). The significant water content (up to 30%) in bio-oil, coming both from the moisture of the feed and from dehydration pyrolysis reactions, reduces viscosity and acidity but also diminishes combustion properties and heating value, making bio-oil difficult to ignite.

Some impurities can be found in bio-oil, such as chlorine, sulphur, alkali metals, nitrogen compounds and char particles. This depends on poor solid separation and on biomass contamination. The presence of impurities can significantly hinder the upgrading of pyrolysis vapour (Bridgwater, 2018).

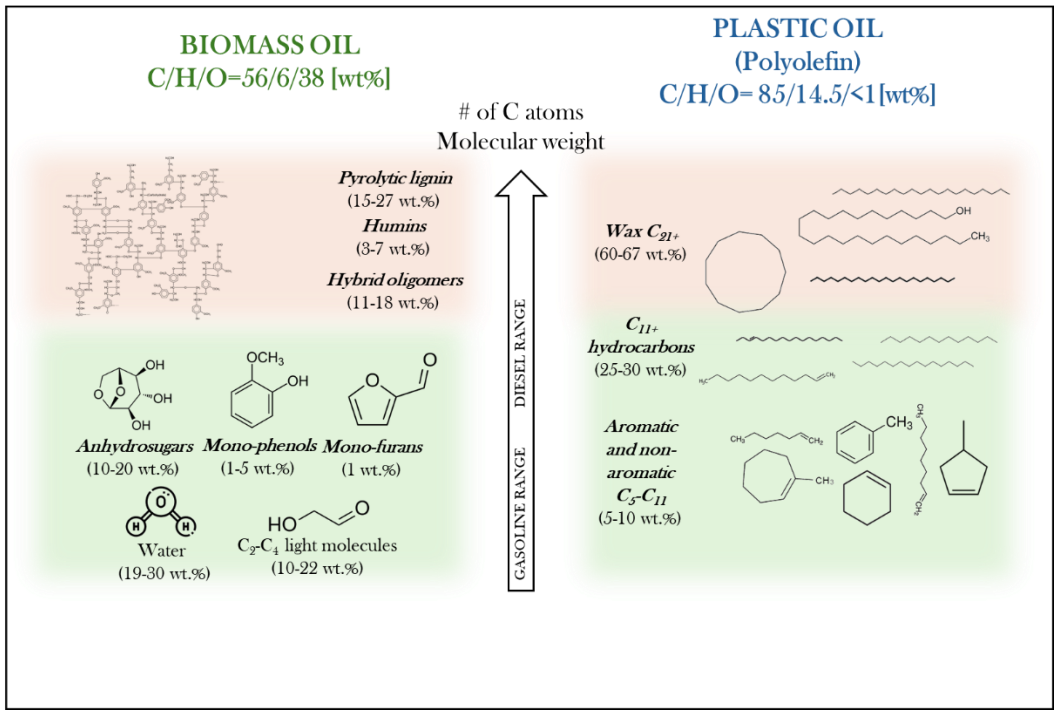

Figure 10: Typical composition of plastic-oil and bio-oil. Data from Pinheiro Pires et al. (2019) and Arabiourrutia et al. (2017).

The case of plastic-derived oils is, on the other hand, more favourable to upgrading and direct utilization. Considering the example of polyolefins (HDPE) as feedstock, Figure 10 illustrates the typical product distribution within the oil. This oil is typically composed of various types of hydrocarbons, including alkanes, alkenes, aromatic compounds, and cycloalkanes, each contributing distinct properties to the oil's overall chemical profile. Almost two thirds of the mass is characterized by waxes, high molecular-weight paraffinic or olefinic hydrocarbon compounds (C_{21+}) which are solids at ambient temperature. Hydrocarbons in the diesel range (C_{12}-C_{20}) represent 25-30%, while those in the gasoline range (C_5-C_{11}) are only 5-10 %wt, with both aromatic and non-aromatic molecules.

1.4 Catalytic vs. non catalytic pyrolysis: focus on mechanism

As discussed in Section 1.3, pyrolysis is the thermal decomposition of a feedstock—either biomass or plastic waste—in the absence of oxygen. The process can be described as an initial primary pyrolysis stage, in which the feedstock decomposes into macromolecules, oligomers, and heavy species, followed by secondary and tertiary pyrolysis stages (Evans & Milne, 1987). During these latter stages, (i) large molecules are cracked into lighter compounds and permanent gases through C–C and C–O bond cleavage, and (ii) light vapor-phase species undergo further reactions producing secondary products such as aromatics and olefins, either among themselves or with reactive solid surfaces; iii) formation of tertiary products such as PAHs. In the absence of a catalyst, secondary and tertiary reactions are governed predominantly by thermal effects, whereas in the presence of a catalyst, vapor–solid interactions strongly influence reaction pathways and product distribution.

1.4.1 Pyrolytic conversion of lignocellulosic biomass

The identification of single reaction pathways in the pure thermal and in the catalytic pyrolysis of lignocellulosic materials is a relevant matter in the scientific community, but also highly complex due to the heterogeneous starting composition of biomass. Cellulose, hemicellulose and lignin follow specific decomposition reactions with increasing temperature and operating conditions, but their interaction has also been acknowledged (e.g., Usino et al, 2021).

Mechanism of primary biopolymer decomposition

The mechanism of primary pyrolysis of biopolymers is reported to be not significantly affected by the presence of catalysts, meaning that the effect of molecular-scale interaction is easily overshadowed by the macro-scale bulk mixing of biomass and catalyst (Liu et al., 2014a). The effect of the catalyst should therefore result from the subsequent interaction of primary pyrolysis vapours with active sites, promoting the conversion into desired high-value compounds through selective secondary reaction pathways (Zhou et al., 2011).

Thermal decomposition of single biopolymers has received considerable attention in the literature since the pioneering work by Evans & Milne (1987). Cellulose depolymerization (starting at around 300°C) proceeds with cracking of glycosidic bonds and the formation of anhydrosugars (among which levoglucosan is the most abundant), free radicals and light molecules (Dai et al., 2020). Some competing reactions involve molecular rearrangement, ring opening, aromatization and others, which convert anhydrosugars into light oxygenates (hydroxyacetaldehyde, formic and acetic acid, acetone, furfural) – see Luo et al. (2004) - and incondensable gases. Levoglucosan is produced in liquid form during

pyrolysis of cellulose and then evolves as primary vapour, leading to further reactions to form pyrans and light oxygenates (Liu et al., 2014a). Along with this reaction pathway, secondary reactions of primary vapours can favour the production of char especially when the vapour residence time is increased (Antal & Varhegyi, 1995).

Hemicellulose decomposes at lower temperature (<250°C) compared to cellulose (Yang et al., 2007). Considering xylan as model representative of hemicellulose, decomposition starts with dehydroxylation, decarboxylation and production of CO_2 via radical mechanism (Shen et al., 2010). As evidenced in the literature (Patwardhan et al., 2011) some of the typical products of hemicellulose depolymerization include water, light organic acids (formic, acetic), ketones and furans (2-methylfuran, 2-furfuraldehyde and others). When the reaction temperature is sufficiently high, xylose units are released as a consequence of the breaking of glycosidic bonds within the structure (Dai et al., 2020). At higher temperature (400°C) cyclization and aromatization reactions produce aromatic rings, which can then evolve towards polycyclic aromatic hydrocarbons (PAHs) and condensed structures in the char.

The thermal decomposition of lignin is believed to occur via free-radical reactions (Zakzeski et al., 2010; Antal et al., 1998). Lignin, composed of phenylpropanoid units (guaiacyl, syringyl, p-hydroxyphenyl), exhibits the most complex thermal behavior. Decomposition occurs over a wide temperature range (150–800 °C) due to the presence of various ether and C–C linkages. Initial reactions include cleavage of β-O-4 and α-O-4 bonds around 250–350 °C (Chu et al., 2013), releasing methoxyphenols like vanillin, guaiacol and dimethoxy-acetophenone. At higher temperatures, breaking of C-C bonds between lignin units is achieved and repolymerization and crosslinking reactions dominate, forming char and polyaromatic structures. Figure 11 summarizes the mechanism of thermal decomposition of single biopolymers.

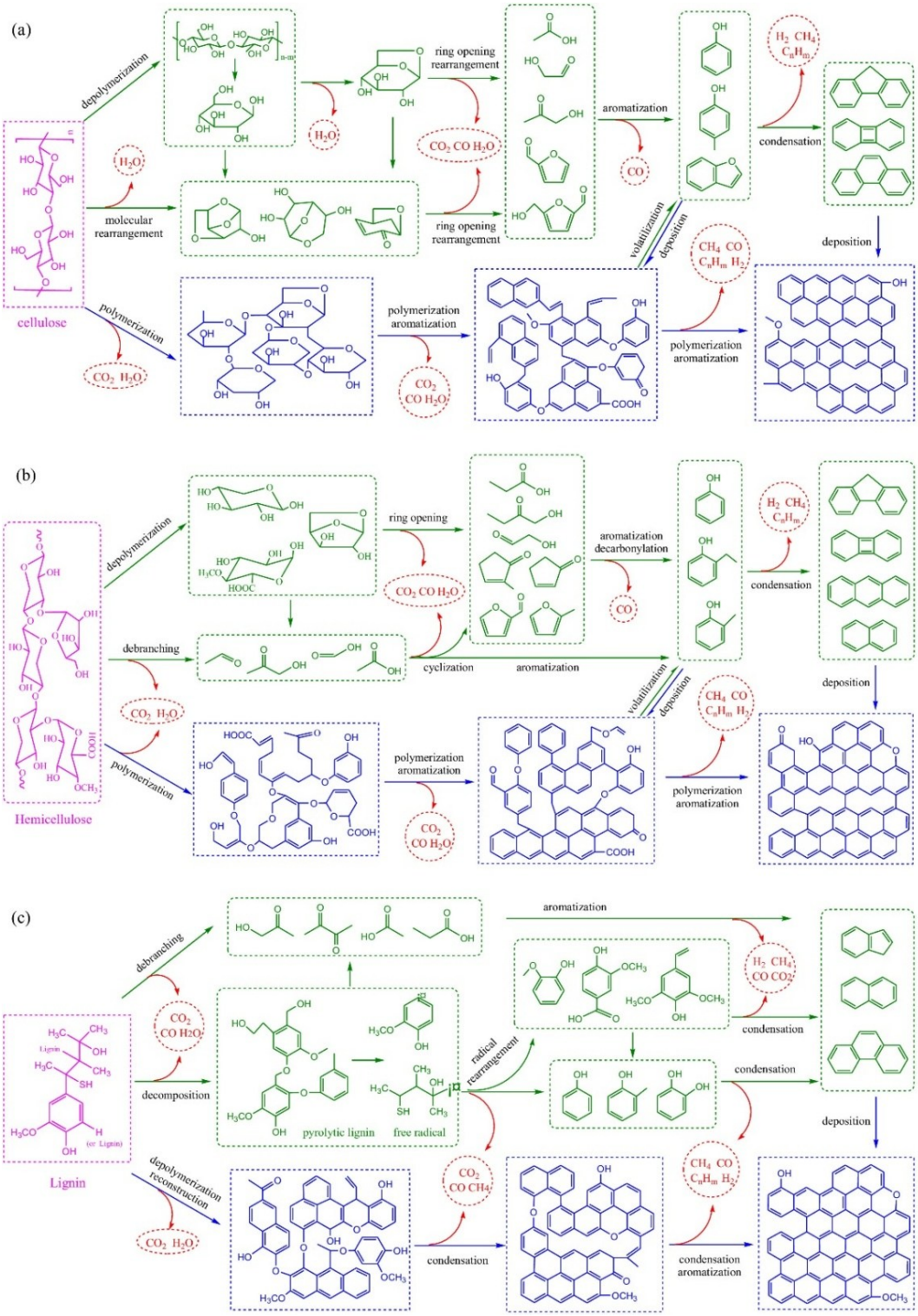

Figure 11: Proposed mechanism of cellulose, hemicellulose and lignin thermal decomposition (Chen et al., 2022).

Mechanism of secondary and tertiary pyrolysis of vapours: thermal vs. catalytic

The reaction chemistry during catalytic fast pyrolysis of lignocellulosic biomass is also a complex topic, involving several reaction routes such as cracking, aromatization, ketonization and aldol condensation (Liu et al., 2014a). A simplified mechanism of catalytic fast pyrolysis of biomass volatiles in the presence of acid ZSM-5 catalyst is illustrated in Figure 12. Catalytic cracking of oxygenated molecules can produce aromatic species and olefins (Rezaei et al., 2014) in addition to other smaller molecules. The main reactions involved are hereby listed (Liu et al., 2014a):

1. Protolytic cracking of C-C bonds
2. Hydrogen transfer
3. Isomerization
4. Aromatic side-chain scission
5. Decarbonylation
6. Decarboxylation
7. Dehydration

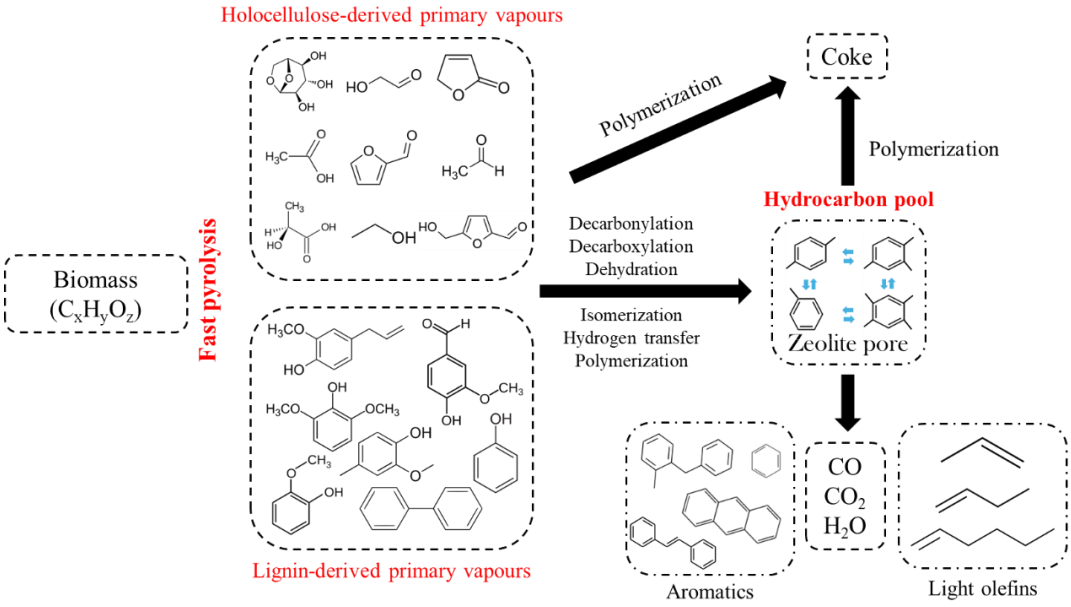

Figure 12: Simplified mechanism of catalytic pyrolysis of biomass pyrolysis volatiles on ZSM-5 zeolite catalyst (adapted from Dai et al., 2020).

Decarbonylation and decarboxylation reactions remove carbonyl and carboxyl functionalities in the form of CO and CO_2, thus reducing the oxygen content of bio-oils. Dehydration is responsible for the formation of dehydrated molecules with simultaneous ejection of water. Olefins, paraffins and coke can be the result of several dehydration steps of polyols, as suggested by Corma et al. (2007). Also dehydrated species can react with olefins via Diels-Alder and condensation reactions to produce aromatics (Corma et al., 2007).

Lignin-derived primary vapours are susceptible to $C_{aromatic}$-O bond cleavage to form aromatic hydrocarbons. In addition, $C_{aromatic}$-alkyl group bond cleavage can be responsible for the production of benzendiols and benzentriols from substituted phenols and methoxyphenols (Liu et al., 2014a).

It is known that in presence of acidic catalysts (e.g., HZSM-5), light oxygenated molecules such as furans, acids, aldehydes and ketones can be converted to produce valuable aromatics via "hydrocarbon pool mechanism" (Carlson et al., 2010). This aromatization reaction pathway has been confirmed for a variety of model compounds such as methanol, ethanol (Johansson et al., 2009), cyclopentanone, acetic acid and propanoic acid.

Given the high complexity of the reaction mechanism, it is likely that other reactions such as ketonization of carboxylic acids, aldol condensation of aldehydes and ketones can also be involved in the process. Moreover, steam reforming of small oxygenates (Wang et al., 1996; Wang et al., 1998) and water-gas shift reaction can contribute to producing CO, CO_2 and H_2, which can be used in hydrogenation reactions. Further details on the reaction mechanism of pyrolysis volatiles during catalytic cracking in the presence of HZSM-5 and other catalysts have been deferred to specific sections discussing the effect of the catalyst and operating conditions on the composition of the resulting bio-oil.

1.4.2 Survey of integrated thermal/catalytic processes for olive-derived biomass conversion

The catalytic pyrolysis of olive-derived biomass has been explored through various approaches, with each study contributing specific insights into catalyst performance and process optimization. A summary of the relevant literature – mostly using in-situ configuration in laboratory-scale reactors - has been included in Table 3. A foundational comparison by Recio-Ruiz et al. (2023) between thermal and catalytic pyrolysis confirmed that acidic catalysts like γ-Al_2O_3 enhance deoxygenation primarily through decarbonylation. However, the work by Brachi et al. (2022) on in-situ catalytic pyrolysis of olive stone and LDPE/OS mixtures highlighted a significant challenge, demonstrating that under their in-situ fluidized-bed conditions, neither γ-Al_2O_3 nor increased temperature substantially improved bio-oil quality, and co-pyrolysis with plastics led to undesirable PAH formation, especially naphthalene derivatives.

To address feedstock quality, Ganda et al. (2022) successfully demonstrated the benefit of torrefaction as a pre-treatment, showing that it could be coupled with an acidic ZSM-5 catalyst to selectively enhance the yield of valuable lignin-derived phenols. This finding was nuanced by Trubetskaya et al. (2023), who argued that process temperature and feedstock type ultimately have a more dominant impact on product distribution than torrefaction severity itself. Further exploring pre-treatment, Sánchez & San Miguel (2016) employed a rotary reactor to define

optimal torrefaction conditions for improving the energy density of olive stones and to optimize char and bio-oil production in the 400-900°C range.
Exploration into novel catalytic systems has also been a key focus. Ahmadi et al. (2025) introduced an innovative approach using a eutectic molten salt catalyst based on sodium, potassium and lithium carbonate (Li_2CO_3:Na_2CO_3:K_2CO_3=1:1:1), proving its effectiveness in degrading undesirable light oxygenates, although high temperatures (>700°C) were required to produce aromatics and alkylphenols. In a comprehensive catalyst screening using a fixed-bed reactor, Christoforou et al. (2018) established a crucial functional distinction: basic catalysts like MgO were superior for deoxygenation via ketonization and aldol condensation reactions (CO_2 removal), whereas acidic ZSM-5 was unmatched for its selectivity towards aromatic hydrocarbons, clearly framing the "catalyst-for-purpose" challenge.

Parallel research has focused on the fundamental thermal behavior of olive stone. Its kinetic advantages in co-pyrolysis mixtures with PVC and microalgae were identified via thermogravimetric analysis by Rasam et al. (2022), while Al-Farraj et al. (2017) highlighted the importance of reactor choice by comparing TGA data from different systems. The influence of biomass structure was investigated by Magalhães et al. (2021), who studied the pyrolysis of fractionated olive stone constituents (cellulose, hemicellulose and lignin) via organosolv and subsequent pyrolysis in a wire mesh reactor. The effect of process parameters on the product yields has also been mapped: Petrov et al. (2008) demonstrated that vacuum conditions favor higher liquid yields and lower solid yields due to enhanced volatile evacuation, and Lopez et al. (2002) characterized the evolution of permanent gases as a function of pyrolysis temperature in a Gray-king type furnace, providing a baseline for gas-phase analysis. The formation of methane and light hydrocarbons is believed to be related to methoxy groups release from lignin structure and consequent C-C bond breaking via hydrogen transfer reactions (Jakab et al., 1997). Collectively, these studies have built a comprehensive understanding of the material's intrinsic pyrolytic properties, creating the foundation upon which advanced catalytic strategies can be developed.

The valorization of other olive-derived biomasses, such as olive pomace (OP) and olive mill wastewater sludge (OMWWS), has been extensively investigated, with a strong focus on innovative catalytic strategies and process configurations. Table 4 summarized the relevant literature in this field. A significant trend is the use of low-cost, waste-derived materials as catalysts. Yel et al. (2025) introduced the use of marble sludge for the co-pyrolysis of OP and plastics (PET/PP), demonstrating its potential for mixed waste valorization. Similarly, Agblevor et al. (2017) successfully employed red mud, another industrial residue, to produce a high-quality, low-viscosity, and neutral-pH bio-oil from OMWWS, mostly composed of aliphatics.

The modification and screening of functional catalysts have been central to this research. Inaloo and Saidi (2023) demonstrated that modifying natural zeolites with basic metal oxides (NiO, Co_3O_4, MgO, CaO) could significantly increase aromatic hydrocarbon content in the final oil, despite reducing its yield. The importance of catalyst functionality was further detailed by Iliopoulou et al. (2023), who conducted a comprehensive screening for OMWWS upgrading, establishing that acidic ZSM-5 promotes cracking and aromatization while basic MgO enhances aliphatic hydrocarbon production. The role of catalyst structure was explored by Karadağ et al. (2022), who found that nanostructured MgO was superior to its bulk counterpart for producing syngas from olive oil residue, yielding less CO_2 and tars. The effectiveness of different microporous catalysts was also highlighted by Farah et al. (2022), who identified SAPO-34 and its Ni- and Fe-modified forms as a promising catalyst for enhancing gas production from olive cake.

Process intensification and alternative energy sources have also been explored. Kostas et al. (2020) introduced microwave-assisted pyrolysis as an energy-efficient method to process olive pomace, concluding that despite negligible effects on chemical composition, microwave power influenced the textural properties of bio-char, and the resulting oils were acetic acid-rich, while bio-chars exhibited high surface area. Caballero et al. (2020) demonstrated a novel pathway for producing hydrogen-rich syngas by coupling slow pyrolysis of "orujillo" (olive solid waste) with subsequent volatiles treatment at 800°C using thermal, thermal-alumina, and Ni-catalysed methods. The optimization of process parameters remains a crucial aspect, as shown by Hani and Hailat (2016), who optimized catalytic pyrolysis of olive oil-cake in a batch reactor, identifying 10% catalyst loading as ideal for maximizing bio-oil yield and quality. The resulting oils showed high H/C ratios, reduced oxygen content, and saturated hydrocarbon profiles (C_{10}–C_{29}), with distillation ranges comparable to diesel and kerosene.

Finally, the effectiveness of established catalysts in two-stage systems has been confirmed. Encinar et al. (2008) demonstrated the high stability and tar-cracking efficiency of dolomite in a two-stage reactor, and Demiral et al. (2008) compared the deoxygenation performance of activated alumina and sodium feldspar. Pütün et al. (2005) evaluated the pyrolysis of olive residue under varying process conditions in a fixed-bed setup, emphasizing the role of temperature, gas flow, and particle size on product distribution, helping define the operational envelope for olive waste valorization and highlighting its potential as a dual-purpose fuel and chemical feedstock

Collectively, these studies reflect the maturation of catalytic pyrolysis as a platform for olive biomass and mixed waste valorization. The consistent emphasis on deoxygenation, aromaticity, and H_2 enrichment—via tailored catalyst design and novel reactor configurations (e.g., microwave, nano-catalysts, dual-stage setups)—underlines the technological evolution toward cleaner and more selective

thermochemical conversion. Notable innovations include the application of industrial residues as catalysts (marble sludge, red mud), systematic catalyst comparisons (zeolite-metal oxide systems, dolomite, feldspar), and pioneering thermal strategies for hydrogen recovery. The literature on biomass catalytic pyrolysis underscores a persistent trade-off between deoxygenation and liquid yield. While acidic zeolites (e.g., HZSM-5) are effective in producing aromatics, they often do so at the cost of significant gas and coke formation. The field is thus evolving towards multifunctional catalysts and process configurations (e.g., torrefaction pre-treatment, ex-situ staging) to decouple primary pyrolysis from catalytic upgrading, thereby preserving carbon while enhancing product quality.

Table 3: Catalytic pyrolysis of olive stone in the literature.

Catalyst (Si/Al)	Feed	Reaction conditions	Mode	Product distribution (wt.%)	Reference
Li_2CO_3:Na_2CO_3:K_2CO_3 salt	Olive stone	500-800°C, Py-GCMS, different catalyst-to-biomass ratios.	In-situ	N.A.	Ahmadi et al., 2025
γ-Al_2O_3	Olive stone	500°C, fixed bed reactor under nitrogen flow. B/C=15.	In-situ	Gas:25.3; Oil: 55.1; Solid:19.6.	Recio-Ruiz et al., 2023
OS-derived activated carbon	Olive stone	500°C, fixed bed reactor under nitrogen flow. B/C=15.	In-situ	Gas:33.3; Oil: 45.7; Solid:21.0.	
Zr/AC	Olive stone	500°C, fixed bed reactor under nitrogen flow. B/C=15.	In-situ	Gas:34.7; Oil: 46.7; Solid:18.6.	
None	Olive stone	500°C, fixed bed reactor under nitrogen flow. B/C=15.		Gas:13.1; Oil: 67.6; Solid:19.3.	
ZSM-5 (38)	Torrefied and as-received olive stone	500°C, bench-scale fluidized-bed reactor.	In-situ	N.A.	Ganda et al., 2022
γ-Al_2O_3	Olive stone & LDPE	500-600°C, bench-scale fluidized-bed reactor.	In-situ	OS/500°C/non-catalytic: Gas:18.3; Oil: 41.0; Solid:12.8; Water: 10.4. OS/500°C/γ-Al_2O_3: Gas:20.8; Oil: 16.4; Solid:17.9; Water: 20.7.	Brachi et al., 2022
None	As-received olive stone	Lab-scale fluidized bed reactor at 500 and 600°C		At 500°C: Gas: 19.8; Oil: 42.0; Solid: 20.8.	Trubetskaya et al., 2023
None	Torrefied olive stone	Lab-scale fluidized bed reactor at 500 and 600°C		At 500°C: Gas: 24.1; Oil: 35.3; Solid: 24.3.	
10%Ni/ZSM-5	Torrefied olive stone	Lab-scale fluidized bed reactor at 500 and 600°C	In-situ	At 500°C: Gas: 24.3; Oil: 35.2; Solid: 24.4.	
None	OS/PVC/*Spirulina* blends	Thermogravimetric analyzer.			Rasam et al., 2022
None	Torrefied and as-received live stone	Mesh wire reactor (800-1150°C).		Only char yields available.	Magalhães et al., 2021
None	Olive stone	Packed-bed bench-scale system, 500°C.		Gas:14.0; Oil: 44.3; Solid:37.1.	Di Blasi et al., 2019
None	Olive husks and kernels	Fluidized-bed reactor (thermal pyrolysis).		Olive kernel at 500°C: Gas: 16.99; Oil: 53.62; Solid: 21.02.	Christoforou et al., 2018
ZSM-5	Olive husks and	Fixed-bed reactor (in-situ upgrading).	In-situ	Olive kernel at 500°C: Gas: 23.71; Oil: 47.03;	

	kernels			Solid: 29.26.	
MgO	Olive husks and kernels	Fixed-bed reactor (in-situ upgrading).	In-situ	Olive kernel at 500°C: Gas: 23.47; Oil: 46.72; Solid: 29.82.	
5%Co/ZSM-5	Olive husks and kernels	Fixed-bed reactor (in-situ upgrading).	In-situ	Olive kernel at 500°C: Gas: 23.87; Oil: 48.51; Solid: 27.63.	
5%Co/MgO	Olive husks and kernels	Fixed-bed reactor (in-situ upgrading).	In-situ	Olive kernel at 500°C: Gas: 23.23; Oil: 43.96; Solid: 32.81.	
None	Olive stone	Fixed-bed and Fluidised-bed thermogravimetric pyrolysis reactors.		N.A.	Al-Farraji et al., 2017
None	Olive stone	Slow pyrolysis in lab-scale rotary reactor, 3 rpm, 200-900°C, 10°C/min.		At 500°C: Gas: 20.2; Oil: 50.3; Solid: 29.5.	Sánchez et al., 2016
None	Olive stone and olive pulp	Laboratory-scale reactor, 60°C/min up to 800°C for 10 min.		Olive stone atmospheric pyrolysis: Gas: 21.3; Oil: 59.0; Solid: 19.7.	Petrov et al., 2008
None	Olive stone and olive pulp	Laboratory-scale reactor, 60°C/min up to 800°C for 10 min.		Olive stone vacuum pyrolysis: Gas: 22.1; Oil: 60.7; Solid: 17.2.	
None	Olive stone	Gray-King type furnace, 15°C/min up to 600°C for 15 min.		Gas:20.9; Oil: 45.4; Solid:33.7.	Lopez et al., 2002

Table 4: Catalytic pyrolysis of other olive-derived biomass in the literature.

Catalyst (Si/Al)	Feed	Reaction conditions	Mode	Product distribution (wt.%)	Reference
Marble sludge ($CaCO_3$)	PP/PET+Olive Pomace	Fixed bed catalytic co-pyrolysis at 500°C.	In-situ	Mixture 70%PP, 15%OP, 15%Catalyst: Gas: 24.57; Oil: 56.12; Solid: 19.31. Mixture 70%PET, 15%OP, 15%Catalyst: Gas: 60.6; Oil: 13.39; Solid: 26.02	Yel et al., 2025
None	Olive pomace	Quartz fixed bed reactor at 500°C, different C/B ratios.		At 500°C: Gas: 21.8; Oil: 55.9; Solid: 22.3	Inaloo et al., 2023
Natural zeolite (NZ)	Olive pomace	Quartz fixed bed reactor at 500°C, different C/B ratios.	In-situ	At 500°C and C/B=5: Gas: 21.8; Oil: 55.9; Solid: 22.4	
NiO/NZ	Olive pomace	Quartz fixed bed reactor at 500°C, different C/B ratios.	In-situ	At 500°C and C/B=5: Gas: 34.8; Oil: 34.6; Solid: 30.6	
Co_3O_4/NZ	Olive pomace	Quartz fixed bed reactor at 500°C, different C/B ratios.	In-situ	At 500°C and C/B=5: Gas: 34.9; Oil: 33.3; Solid: 31.8	
MgO/NZ	Olive pomace	Quartz fixed bed reactor at 500°C, different C/B ratios.	In-situ	At 500°C and C/B=5: Gas: 37.8; Oil: 32.2; Solid: 30.0	
CaO/NZ	Olive pomace	Quartz fixed bed reactor at 500°C, different C/B ratios.	In-situ	At 500°C and C/B=5: Gas: 39.0; Oil: 31.7; Solid: 29.3	
None	OMWS	Bench-scale stainless-steel fixed bed tubular reactor.	In-situ	At 500°C and C/B=0: Gas: 12.5; Oil: 61.4; Solid: 26.1	Iliopolou et al., 2023
ZSM-5	OMWS	Bench-scale stainless-steel fixed bed tubular reactor.	In-situ	At 500°C and C/B=3: Gas: 30; Oil: 43; Solid: 27	
Co/ZSM-5	OMWS	Bench-scale stainless-steel fixed bed tubular reactor.	In-situ	N.A.	
MgO	OMWS	Bench-scale stainless-steel fixed bed tubular reactor.	In-situ	At 500°C and C/B=3: Gas: 21; Oil: 51; Solid: 28	
Co/MgO	OMWS	Bench-scale stainless-steel fixed bed tubular reactor.	In-situ	N.A.	
Al_2O_3	OMWS	Bench-scale stainless-steel fixed bed tubular reactor.	In-situ	At 500°C: Gas: 18; Oil: 52; Solid: 30	
SiO_2	OMWS	Bench-scale stainless-steel fixed bed tubular reactor.	In-situ	At 500°C: Gas: 16; Oil: 57; Solid: 17	
20%Fe/Al_2O_3	OMWS	Bench-scale stainless-steel fixed bed tubular reactor.	In-situ	At 500°C and C/B=3: Gas: 22; Oil: 50; Solid: 28	
20%Fe/SiO_2	OMWS	Bench-scale stainless-steel fixed bed tubular reactor.	In-situ	At 500°C and C/B=3: Gas: 17; Oil: 54; Solid: 29	
20%Fe/MgO	OMWS	Bench-scale stainless-steel fixed bed tubular reactor.	In-situ	At 500°C and C/B=3: Gas: 19; Oil: 55; Solid: 26	
20%Mn/Al_2O_3	OMWS	Bench-scale stainless-steel fixed bed tubular reactor.	In-situ	At 500°C and C/B=3: Gas: 22; Oil: 54; Solid: 24	

20%Mn/SiO_2	OMWS	Bench-scale stainless-steel fixed bed tubular reactor.	In-situ	At 500°C and C/B=3: Gas: 21; Oil: 55; Solid: 24	
20%Mn/MgO	OMWS	Bench-scale stainless-steel fixed bed tubular reactor.	In-situ	At 500°C and C/B=3: Gas: 21; Oil: 57; Solid: 22	
RFCC	Olive pomace	Quartz fixed bed reactor at 500°C, different C/B ratios.	In-situ	At 500°C and C/B=0.5: Gas:44.0 ; Oil: 31.1; Solid: 24.9	Inaloo et al., 2022
B-MgO	Olive oil residue	Tubular furnace 3g biomass + 2% catalyst. T=400-600-800°C.	In-situ	At 400°C: Gas: 7.0; Oil: 12.0; Solid: 81.0	Karadağ et al., 2022
N-MgO	Olive oil residue	Tubular furnace 3g biomass + 2% catalyst. T=400-600-800°C.	In-situ	At 400°C: Gas: 2.0; Oil: 8.0; Solid: 85.0	
B-ZnO	Olive oil residue	Tubular furnace 3g biomass + 2% catalyst. T=400-600-800°C.	In-situ	At 400°C: Gas: 8.0; Oil: 13.0; Solid: 79.0	
N-ZnO	Olive oil residue	Tubular furnace 3g biomass + 2% catalyst. T=400-600-800°C.	In-situ	At 400°C: Gas: 10.0; Oil: 12.0; Solid: 78.0	
None	Olive cake	Quartz tube reactor. C/B=0.3. T=500°C for 35 min.		At 500°C: Gas: 39.5; Oil: 39.5; Solid: 21.0	Farah et al., 2022
SAPO-34	Olive cake	Quartz tube reactor. C/B=0.3. T=500°C for 35 min.	Ex-situ	At 500°C: Gas: 62.5; Oil: 12.5; Solid: 25.0	
Ni-SAPO-34	Olive cake	Quartz tube reactor. C/B=0.3. T=500°C for 35 min.	Ex-situ	At 500°C: Gas: 51.6; Oil: 22.2; Solid: 26.2	
Fe-SAPO-34	Olive cake	Quartz tube reactor. C/B=0.3. T=500°C for 35 min.	Ex-situ	At 500°C: Gas: 66.7; Oil: 9.95; Solid: 23.35	
None	Olive pomace	Microwave-assisted pyrolysis reactor.		Optimal MW pyrolysis with high specific energy (3.6 kJ/g) produced 26-30% bio-oil, rich in acetic acid (66.5-71.9% area).	Kostas et al., 2020
None	"Orujillo"	Pyrolysis reactor + vapor treatment tubular reactor (batchwise). T=500-700°C.		At 500°C: Gas: 32.2; Oil: 35.5; Solid: 32.3	Caballero et al., 2020
Al_2O_3	"Orujillo"	Pyrolysis reactor + vapor treatment tubular reactor (batchwise). T=500-700°C.	Ex-situ	At 500°C: Gas: 38.8; Oil: 29.4; Solid: 31.8	
44% Ni/(CaO/Al_2O_3)	"Orujillo"	Pyrolysis reactor + vapor treatment tubular reactor (batchwise). T=500-700°C.	Ex-situ	At 500°C: Gas: 49.9; Oil: 17.8; Solid: 32.3	
None	OMWS	Bench-scale fluidized bed reactor.	In-situ	At 500°C: Gas: 36.2; Oil: 30.4; Solid: 24.4; Water: 8.8	Agblevor et al., 2017
Red mud	OMWS	Bench-scale fluidized bed reactor.	In-situ	At 500°C: Gas: 37.7; Oil: 29.5; Solid: 20.4; Water: 11.8	
None	Olive oil cake	Stainless steel reactor (in-situ) at 500°C. From 5% to 40% wt. Catalyst)	In-situ	At 500°C: Gas: 17.1; Oil: 36.1; Solid: 27.1; Water: 16.1.	Hani & Hailat, 2016
Natural zeolite (NZ)	Olive oil cake	Stainless steel reactor (in-situ) at 500°C. From 5% to 40% wt. Catalyst)	In-situ	At 500°C and C/B=0.4: Gas: 23.5; Oil: 34.0; Solid: 22.4; Water: 20.1	

None	Olive waste	Two cylindrical stainless-steel reactors connected in series. T=500-800°C. Different amounts of dolomite (0-100 g).		At 500°C: Gas: 23.36; Oil: 48.38; Solid: 28.26	Encinar et al., 2008
Dolomite	Olive waste	Two cylindrical stainless-steel reactors connected in series. T=500-800°C. Different amounts of dolomite (0-100 g).	Ex-situ	At 700°C: Gas: 49.39; Oil: 27.22; Solid: 23.39	
None	Olive bagasse	Fixed bed Heinze reactor. T=500°C, 10°C/min.	In-situ	At 500°C: Gas: 18.8; Oil: 38.0; Solid: 26.9; Water: 17.1	Demiral et al., 2008
Activated alumina	Olive bagasse	Fixed bed Heinze reactor. T=500°C, 10°C/min.	In-situ	At 500°C: Gas: 20.4; Oil: 34.7; Solid: 25.1; Water: 19.8	
Sodium feldspar	Olive bagasse	Fixed bed Heinze reactor. T=500°C, 10°C/min.	In-situ	At 500°C: Gas: 31.9; Oil: 31.5; Solid: 23.5; Water: 13.1	
Dolomite	Olive husks	Screw pyrolysis reactor (975 K) + cracking reactor (975-1175 K).	Ex-situ		Taralas & Kontominas, 2006
None	Olive residue	Fixed bed reactor, 7°C/min, T=400-700°C.		At 500°C: Gas: 20.0; Oil: 32.7; Solid: 28.0	Pütün et al., 2005

1.4.3 Pyrolytic conversion of plastics

Mechanism of primary decomposition of polyolefins

Pyrolysis of polyolefin is quite different from that previously reported for biomasses. There is agreement in the scientific community on that the thermal pyrolysis of polyolefins occurs via random radical scission of the polymeric chain, leading to a wide spectrum of products, from light hydrocarbons (C_1-C_4) when the temperature is higher than 800°C with low residence time, liquid hydrocarbons (aliphatic and aromatic C_5-C_{20}) to high molecular weight waxes at lower temperature (Lopez et al., 2017b; Dai et al., 2024). The production of aromatic hydrocarbons (BTX) is favoured at 650-800°C with moderate residence time, but the process has low selectivity (Lopez et al., 2017b). The process can be schematized in three different steps, namely, chain initiation, propagation and termination (Thangaraj and Lee., 2025).

During the initiation step, thermal energy coming from the reaction environment facilitates the homolytic cleavage of C-C bonds producing unstable primary free radicals which convert to stable secondary radicals. Primary radicals can undergo β-scission and produce shorter radicals and ethylene molecules. Secondary radicals' β-scission produces alkenes and shorter radicals during the propagation step. In the termination step, primary and secondary free radicals combine to form n-alkanes and iso-alkanes (Dai et al., 2024). Finally, isomerization and cyclization reactions can produce cyclic hydrocarbons and aromatics. A schematization of the process is reported in Figure 13:

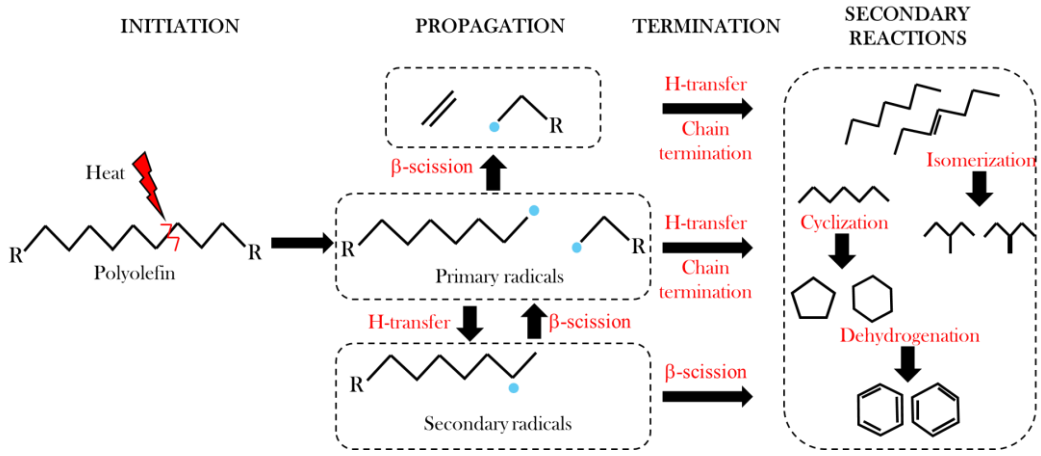

Figure 13: Postulated free-radical mechanism for the thermal cracking of polyolefins. The process is characterized by (a) initiation via homolytic C-C bond cleavage, (b) propagation via β-scission, and (c) termination via radical combination. Adapted from Dong et al. (2022).

Mechanism of catalytic cracking of polyolefin decomposition products

Catalytic cracking of polyolefins, such as polyethylene and polypropylene, on acidic zeolites enables selective production of high-quality fuel oils by leveraging the reactivity of Brønsted and Lewis acidic sites on the catalyst surface (Dai et al., 2024). The reaction mechanism begins when a polyolefin molecule interacts with a Brønsted acidic site, resulting in protonation that forms a carbonium ion—a pentavalent carbocation. Due to its inherent instability, the carbonium ion quickly decomposes to form alkanes and carbenium ions (see Figure 14).

Carbenium ions, which are trivalent carbocations, are more stable than carbonium ions due to stabilizing effects such as hyperconjugation and inductive effects from nearby alkyl groups (Corma and Orchillès, 2000). These carbenium ions can further isomerize, producing even more stable secondary and tertiary forms that facilitate the progression of catalytic cracking reactions. The formation and subsequent reactions of these stable tertiary carbenium ions represent a primary pathway for the catalytic breakdown of polyolefins into shorter hydrocarbon chains (Sadeghbeigi, 2020).

It should also be noted that carbenium ions rearrangement to form tertiary carbocations implies a higher degree of ramification of the products from the catalytic cracking compared to pure thermal pyrolysis (Artetxe, 2013). The main reaction occurring during the propagation step is the β-scission reaction, where the C–C bond in the β-position relative to the positively charged carbon is broken. This cleavage forms a lighter olefin and another reactive carbenium ion, allowing the reaction to continue.

The β-scission reaction can occur through different pathways, depending on the nature of the initial and resulting carbenium ions. In Type A β-scission, both the starting and resulting species are tertiary carbocations, which are highly stable due to hyperconjugation and inductive effects. Type B β-scission involves two possible pathways: Type B1, where a secondary carbocation undergoes β-scission to produce a more stable tertiary carbocation, and Type B2, where a tertiary carbocation undergoes β-scission to form a secondary carbocation, which is less favourable due to the resulting decrease in stability. In Type C β-scission, both the initial and resulting species are *tert*-carbenium ions (Corma and Orchillès, 2000; Dai et al., 2024). Secondary reactions of isomerization, Diels-Alder cycloaddition, cyclization, dehydrogenation and oligomerization take place among the carbenium ions and light products, with the overall process being endothermic and leading to a broad distribution of products.

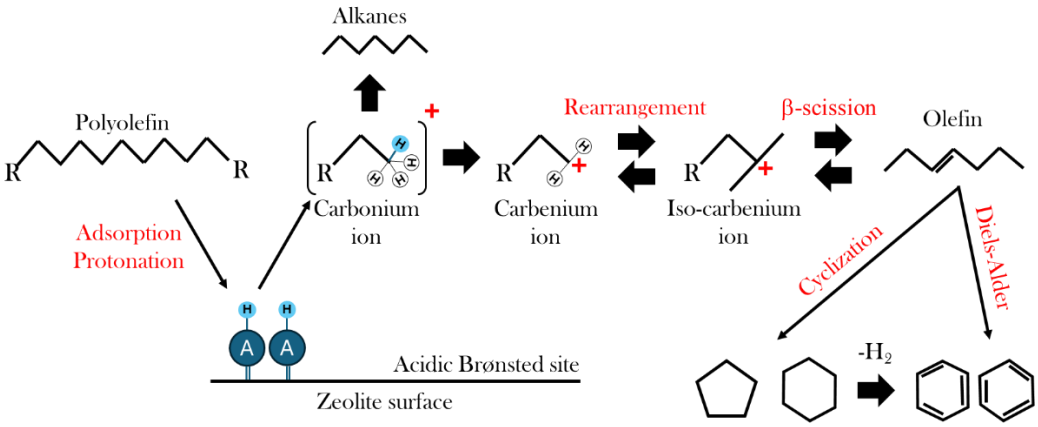

Figure 14: Reaction mechanism of catalytic cracking of polyolefins on acidic zeolite, adapted from Dong et al. (2022).

The mechanism of catalytic cracking explains why the product distribution is narrower compared to the case of pure thermal cracking, with selective production of light olefines and aromatic hydrocarbons, which are fundamental bulk chemicals. For instance, benzene is used as precursor for styrene, cumene and aniline, which are used for the production of polystyrene plastics, for the synthesis of phenol and acetone and other applications. Similarly, toluene has many applications as solvent in paints, coatings and adhesives. Xylenes, sold as mixture of isomers, are used as precursors of terephthalic acid (from which PET is produced) and phthalic anhydride (Farmer & Mascal, 2015).

The real mechanism of formation of aromatics is not yet fully understood, and different pathways have been proposed (see Figure 15): i) Diels-Alder cycloaddition of a conjugated diene to an alkene with further dehydrogenation (Dorado et al., 2015); ii) cyclohexane formation and aromatization (Dai et al., 2024); iii) "hydrocarbon pool" mechanism (Ilias and Bhan, 2013). Given the complexity of the catalytic reaction network, it is likely that all three mechanisms make their contribution in the formation of aromatic hydrocarbons (especially BTX).

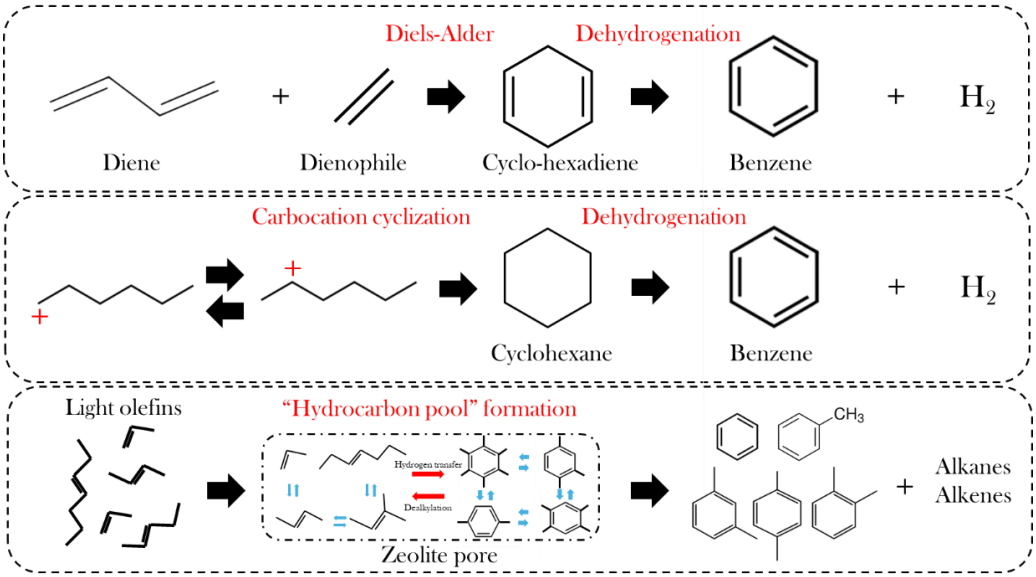

Figure 15: Possible mechanisms for aromatics formation during catalytic cracking of polyolefins.

1.4.4 Survey of in-situ and ex-situ catalytic cracking of polyolefins

Transitioning from oxygenated, heterogeneous biomass to hydrocarbon-based, homogeneous polyolefins, the focus of catalytic cracking shifts fundamentally from deoxygenation to selective C-C bond scission and molecular reshaping. The underlying carbocation chemistry, while sharing principles with some biomass conversion pathways, proceeds without the complexities introduced by oxygen atoms, leading to a different product slate and distinct catalytic challenges. Zeolite-based catalysts are extensively utilized in the catalytic pyrolysis of polyolefins due to their unique structural and chemical properties. Zeolites are crystalline aluminosilicate materials composed of a framework of interconnected tetrahedral units, where each tetrahedron consists of a silicon or aluminum atom surrounded by four oxygen atoms. This highly ordered and repeating structure creates a porous material with well-defined pore sizes and shapes (Dai et al., 2024).
The most important zeolites used in the context of catalyst cracking of polyolefins are ZSM-5 (MFI) and Y (FAU) zeolites. Other catalysts include FCC catalysts, aluminosilicates, carbon-based catalysts and metal oxides (Dai et al., 2024).

A summary of the extensive literature experimental work on catalytic pyrolysis of HDPE in the “in-situ” configuration, i.e., with the catalyst directly located in the pyrolysis reactor, has been compiled in Table 5. Cen et al. (2024) recently used a batch reactor to investigate the performance of a layered self-pillared zeolite (Z100) for the conversion of HDPE into gasoline. The zeolite had a superior selectivity (99%) to gasoline when operated at 240°C for 4 h with a catalyst/plastic ratio of 0.2. Chen et al. (2024) explored the effect of different Fe-loaded USY zeolite catalysts on the pyrolysis of HDPE, concluding that the presence of iron increases oil yield (especially in gasoline and diesel range) and promotes the formation of more aromatics and alkenes. Metallic iron has greater catalytic activity compared to iron oxides.

Yu et al. (2020) synthetized six different ZSM-5-based catalysts with different acidity, of which three also included micro-crystalline cellulose (MCC) as co-template during hydrothermal synthesis. The experiments were conducted in a fixed-bed quartz tube reactor containing 1 g of plastics and 0.5 g of catalyst and operated at 550°C. The most acid catalyst with MCC (MZ-27) achieved the highest oil yield and the highest BTX selectivity due to the high density of acid sites and the increased mesopore volume. It was concluded that MCC can be a smart resource to tune the morphology, pore structure and acidity of zeolite catalysts.

Liu et al. (2014b) used HZSM-5 in a fixed-bed reactor operated at 430°C for 3 h with a plastic-to-catalyst ratio of 10 obtaining a significant gas yield (75.2%). Nevertheless, wax formation suggests that HDPE conversion was not complete during the experiment. They also compared the performance of the catalysts with

other materials (MCM-41, Al_2O_3, CaO and clay), concluding that HZSM-5 was the only catalyst able to convert most of HDPE to gas. MCM-41 produced the highest yield of liquid, while alumina and CaO yielded a lot of waxes. Clay, which does not have acidic sites and a porous structure, appeared to produce more alkanes in the oil, encouraging the investigation on cheap clay-based catalysts.

Marcilla et al. (2009) examined the thermal and catalytic pyrolysis of HDPE in dynamic conditions using a batch reactor and confirmed that the highest yield of gas was obtained with HZSM-5. The gas was mostly composed of olefins, 1-olefins, n-paraffins and iso-paraffins, while the liquid has a significant aromatic nature. Miskolczi et al. (2004) studied the thermo-catalytic conversion of HDPE in a lab-scale Pyrex batch reactor in the 400-450°C range, using a spent FCC catalyst, a commercial HZSM-5 and a clinoptilolite containing rhyolite tuff (NCM). Results showed that HZSM-5 produced the highest amount of gases in all temperature conditions, but the liquid product was always the most abundant together with the residue, probably due to the poor contact between catalyst and HDPE and the low temperature. The investigation of Miskolczi et al. (2009) also proved the efficacy of HZSM-5 catalyst for the catalytic cracking of PP and HDPE waste plastic in a 9 kg/h pilot-scale gas-heated tubular reactor.

A batch fluidized-bed reactor (500°C, HDPE/catalyst ratio of 1.41) has been used for the in-situ catalytic pyrolysis of HDPE on HZSM-5 and USY zeolite catalysts by del Remedio Hernández et al. (2007). Compared to the aromatic-free n-paraffinic liquid recovered during thermal pyrolysis, the oil produced in the presence of HZSM-5 contains mostly aromatics, followed by linear and branched paraffins, with the composition being significantly affected by the pyrolysis temperature.
Using a similar apparatus, Mastral et al. (2006) concluded that catalytic pyrolysis should not be carried out at low temperature (350-400°C) to avoid the incomplete degradation of the polymer with subsequent solid residue generation. On the other hand, temperature higher than 500°C resulted in partial thermal cracking effect on product distribution.
Other investigations with fluidized bed reactors were performed by Lin et al. (2004), Lin et al. (1998), Sharrat et al. (1997) and Ali et al. (2003).

The in-situ catalytic pyrolysis of HDPE was also studied in a spouted-bed reactor by Elordi et al. (2011a). Continuous reaction (up to 15 h) at 500°C with a 30 g catalyst bed was conducted with three different catalysts, namely HZSM-5 (Si/Al=30), HY and Hβ. High mass and heat transfer between fluidization gas and solid particles and the short residence time in the reaction environment contributed to a smooth, problem-free continuous operation. The three catalysts exhibited different product distribution at zero time, with HZSM-5 mainly producing C_2-C_4 olefins and paraffins. HY mainly produced non-aromatic gasoline range liquid and diesel liquid, while Hβ's behaviour was in between.

HZSM-5 was also characterized by the highest resistance to deactivation, with the product distribution remaining practically unchanged for 15 h of continuous operation. The pore structure and acidity of the catalyst deeply influence the product distribution. For instance, light olefin yield is inversely proportional to the pore size of the catalyst. Bigger pore size leads to compounds in the C_5-C_{11} range and C_{11+} hydrocarbons (Elordi et al., 2009). Catalysts with higher acidity promote the formation of monoaromatics (BTX). In general, "the higher the pore size, the heavier the fraction is" (Elordi et al., 2009).

In conclusion, other investigations to be reported are those of Eschenbacher et al. (2022) who studied a P/mesoZ55-ss catalyst in a micro-pyrolyser at 600°C with a plastic/catalyst ratio of 1/80. The catalyst was a phosphorus-modified mesoporous HZSM-5 zeolite which proved to be effective in the catalytic pyrolysis of a polyolefin mixture (LLDPE, LDPE, HDPE and PP), leading to 79% yield of light olefins and 5% aromatics. Moreover, P-modified zeolite showed high resistance to coke deposition compared to conventional HZSM-5.

Fresh and spent FCC catalysts have also been widely used for the catalytic conversion of polyolefins, as summarized in Table 6. Abbas-Abadi et al. (2013) used a semi-batch reactor operated at 420-510°C and with a HDPE/FCC ratio in the range of 1/60 to 1/20 to produce liquid fuels. The main product were always liquid oil and waxes, with non-condensable gases being <10%. Reaction temperature and catalyst load were the most important parameters of the process, and the highest oil yield was obtained at 450°C, with 10% of catalyst. Similar conclusions were reached by Lee et al. (2002, 2003) using a spent FCC catalyst.
Miskolczi et al. (2004, 2006) used FCC catalyst in a fixed-bed reactor for 1 h at 430°C and 2wt. % catalyst, obtaining 82% of liquid (oil + waxes) and low gas yield (5.8%).
Elordi et al. (2012b) used a continuous spouted-bed reactor at 500°C for the catalytic conversion of HDPE (1 g/min) over spent FCC catalyst agglomerated with bentonite (50%), achieving 28.3% of gas, 61.6% of liquid oil and 10.1% of wax. Given its use in reaction-regeneration cycles, spent FCC is characterized by weak acidity, which limits aromatization and condensation reactions (coke formation). Using the same experimental apparatus, Olazar et al. (2009) found that the production of diesel range liquid can be increased from 13 wt% (spent non-treated FCC at 500°C) to 38 wt% (FCC steamed for 5 h at 760°C, pyrolysis at 500°C) and to 69% (with severe steaming for 8 h at 816°C and pyrolysis at 475°C). Other experiments with spent FCC catalysts were conducted in a fluidized bed reactor by Ali et al. (2003) and by Salmiaton & Garforth (2011).

The use of silica-alumina and other mesoporous materials as catalysts for the catalytic cracking of polyolefins is well documented. Recently, Mondal et al. (2023) observed that the catalytic activity of ASA (sol-gel prepared amorphous silica-alumina) can be improved by reducing the Si/Al ratio and by doping it with titanium. Using a batch reactor with a plastic/catalyst ratio of 25, it was found that

Ti-doped ASA converted nearly 96% of the fed LDPE with high selectivity towards gasoline and – above all – with low temperature conditions (376°C). Lin et al. (2004) worked with MCM-41 and SAHA (Synclyst 25 silica−alumina, Crosfield Chemicals, Warrington, U.K.) in a fluidized bed reactor and observed that the catalytic degradation of HDPE was less pronounced compared to that found with HZSM-5, given the lower acidity and the larger pore structure of non-zeolite catalysts, which also contributed to their faster deactivation. Seo et al. (2003) had previously concluded that amorphous silica-alumina, despite showing activity in cracking heavy hydrocarbons towards lighter olefins, is inferior to zeolites in terms of aromatic production. Simple alumina powder yielded 82% of liquid (against the 84% of thermal pyrolysis of HDPE), but half of it was still in the C_{13}-C_{23} range.
Earlier investigations with non-zeolite catalysts – among which MCM-41, Silica-alumina and Silicalite- were carried out in stirred batch reactors (Van Grieken et al, 2001), fluidized bed reactors (Lin et al., 1998; Sharrat et al., 1997) or stirred semi-batch reactors (Sakata et al., 1997).

It is worth citing the work of Ahmad et al. (2013), who used $BaTiO_3$ and its modifications (4% Pb/$BaTiO_3$, 0.25% Co/$BaTiO_3$, 3.94-0.25% Pb-Co/$BaTiO_3$) to convert HDPE in a micro steel reactor operated at 350 °C. It was found that the best catalyst to maximize liquid yield was Pb-Co/$BaTiO_3$; all $BaTiO_3$-based catalysts enhanced the production of paraffins while reducing olefins and naphthenes. The concentration of aromatics was always zero for all catalysts and heavy hydrocarbons represented a significant part of the liquid samples, suggesting poor catalytic activity. Finally, Jan et al. (2010a and 2010b) explored the potential use of a basic catalysts (e.g., $BaCO_3$, $MgCO_3$) for the degradation of HDPE in a batch reactor. Compared to the thermal process (450°C, 2h), the presence of $MgCO_3$ (0.2 g_{cat}/g_{HDPE}) avoided wax production and 92% liquid product was obtained in the optimal conditions.

Table 5: In-situ catalytic cracking of HDPE on zeolite catalysts in the literature.

Catalyst (Si/Al)	Reaction conditions	Products distribution (wt.%)	Reference
Layered self-pillared zeolite (Z100)	240°C, 4 h, HDPE/catalyst=5, batch reactor	C_1-C_3=0.6; C_4-C_{12}=81.2	Cen et al., 2024
USY (10)	500°C, HDPE/catalyst=10, fixed bed quartz reactor	Liquid=56.5; Gas=42.6; Coke=0.9	Chen et al., 2024
HZ-27 (27)	550°C, fixed-bed quartz tube reactor, 1 g plastic/0.5 g catalyst	Liquid=20; Gas=77.66; Coke=1.6	Yu et al., 2020
MZ-27 (27)	550°C, fixed-bed quartz tube reactor, 1 g plastic/0.5 g catalyst	Liquid=21.5; Gas=77.3; Coke=1.2	
HZ-80 (80)	550°C, fixed-bed quartz tube reactor, 1 g plastic/0.5 g catalyst	Liquid=17.5; Gas=81.3; Coke=1.2	
MZ-80 (80)	550°C, fixed-bed quartz tube reactor, 1 g plastic/0.5 g catalyst	Liquid=18.8; Gas=80.4; Coke=0.8	
HZ-150 (150)	550°C, fixed-bed quartz tube reactor, 1 g plastic/0.5 g catalyst	Liquid=13.9; Gas=85.4; Coke=0.7	
MZ-150 (150)	550°C, fixed-bed quartz tube reactor, 1 g plastic/0.5 g catalyst	Liquid=14.3; Gas=85.2; Coke=0.5	
HY (5.5)	430°C, 3h, HDPE/catalyst=10, fixed bed reactor	Gas=18; Liquid=49; Residue=34	Kunwar et al., 2016
HZSM-5 (25)	430°C, 1h, HDPE/catalyst=10, fixed bed reactor	Gas=75.2; Liquid=14.3; Wax=10.5	Liu et al., 2014b
HZSM-5 (30)	500°C, 7.5 h, spouted-bed reactor (30 g catalyst bed), 1 g/min HDPE	C_2-C_4 olefins=57; C_4 paraffins=15; non-aromatic C_5-C_{11}=14; aromatics =12; C_{12}-C_{20}=1; Wax=1	Elordi et al., 2011a
HY (5.2)	500°C, 7.5 h, spouted-bed reactor (30 g catalyst bed), 1 g/min HDPE	C_2-C_4 olefins=37; C_4 paraffins=3.5; non-aromatic C_5-C_{11}=47; aromatics =4.5; C_{12}-C_{20}=2.5; Wax=5.5	
Hβ (75)	500°C, 7.5 h, spouted-bed reactor (30 g catalyst bed), 1 g/min HDPE	C_2-C_4 olefins=22.5; C_4 paraffins=3.5; non-aromatic C_5-C_{11}=44; aromatics =7.5; C_{12}-C_{20}=10.5; Wax=12	
HUSY	550°C, HDPE/catalyst=10, batch reactor	Liquid=41.0; Gas=39.5; Char=1.9	Marcilla et al., 2009
HZSM-5	550°C, HDPE/catalyst=10, batch reactor	Liquid=17.3; Gas=72.6; Char=0.7	
HZSM-5 (30)	500°C, spouted-bed reactor (30 g catalyst bed), 1 g/min HDPE	Gas=74 Liquid=25.5; Wax=0.5	Elordi et al., 2009
HY (5.2)	500°C, spouted-bed reactor (30 g catalyst bed), 1 g/min HDPE	Gas=36; Liquid=63; Wax=1	

Hβ (75)	500°C, spouted-bed reactor (30 g catalyst bed), 1 g/min HDPE	Gas=48; Liquid=50; Wax=2	
HZSM-5 (24.1)	520°C, 5 wt.% catalyst, horizontal tube reactor (continuous)	Gas=11; Liquid+Wax=89; Residue=0	Miskolczi et al., 2009
HZSM-5 (22.2)	500°C, HDPE/catalyst=1.41, fluidized bed reactor (batch)	Gas=88.3; Liquids=4.3; Wax=5.0; Residue=5.6	del Remedio Hernández et al., 2007
USY (4.8)	500°C, HDPE/catalyst=1.41, fluidized bed reactor (batch)	Gas=83.4; Liquids=9.7; Wax=1.0; Residue=10.9	
HZSM-5 (28.1)	430°C, 1h, 2 wt.% catalyst, fixed bed reactor	Gas=12; Liquid+Wax=82; Residue=6	Miskolczi et al., 2006
HZSM-5	500°C, HDPE/catalyst=1.41, fluidized bed reactor (batch)	Gas=78.48; Wax=21.52; Residue=0.0	Mastral et al., 2006
HZSM-5 (28.1)	450°C, 1h, 3 wt.% catalyst, pyrex batch reactor	Gas=15.1; Liquid=81.0; Residue=3.9	Miskolczi et al., 2004
HZSM-5	360°C, 15 min, HDPE/catalyst=0.4/1, fluidized bed reactor	Gas=64.1; Liquid=29.4; Residue=4.5	Lin et al., 2004
ZSM-5 powder	450°C, batch reactor, HDPE/catalyst=20, 30 min	Liquid=35 (99.9% C_{12}-C_{16}); Gas=63; Coke=1.5	Seo et al., 2003
Zeolite-Y powder	450°C, batch reactor, HDPE/catalyst=20, 30 min	Liquid=71.5 (96.9% C_{12}-C_{16}); Gas=27; Coke=1.5	
Mordenite pellet	450°C, batch reactor, HDPE/catalyst=20, 30 min	Liquid=78.5 (71.0% C_{12}-C_{16}); Gas=18.5; Coke=3	
HZSM-5 (17.5)	450°C, HDPE/catalyst=1/6, fluidized bed reactor	Gas=57.4; Liquid=28.28; Residue=11.9	Ali et al., 2003
USY (6.2)	450°C, HDPE/catalyst=1/6, fluidized bed reactor	Gas=25.4; Liquid=44.7; Residue=20.2	
HY (5.5)	450°C, 1 h, HDPE/catalyst=10, fixed bed reactor	Liquid=14.9; Gas=75.8; Residue=9.3	Park et al., 1999
HZSM-5 (22)	450°C, 1 h, HDPE/catalyst=10, fixed bed reactor	Liquid=10.4; Gas=88.4; Residue=0.7	
HZSM-5 (44)	450°C, 1 h, HDPE/catalyst=10, fixed bed reactor	Liquid=21.5; Gas=78.5; Residue=0	
H-Natural zeolite	450°C, 1 h, HDPE/catalyst=10, fixed bed reactor	Liquid=65.1; Gas=34.9; Residue=0	
H-Natural zeolite/Ni	450°C, 1 h, HDPE/catalyst=10, fixed bed reactor	Liquid=35.7; Gas=64.3; Residue=0	
HZSM-5 (17)	360°C, 20 min, HDPE/catalyst=0.4/1, fluidized bed reactor	Gas=93.2; Liquid=2.3; Residue=4.5	Lin et al., 1998

HUSY (6.0)	360°C, 20 min, HDPE/catalyst=0.4/1, fluidized bed reactor	Gas=89.7; Liquid=3.2; Residue=7.1	
HMOR (6.3)	360°C, 20 min, HDPE/catalyst=0.4/1, fluidized bed reactor	Gas=88.6; Liquid=2.5; Residue=8.9	
HZSM-5 (17)	360°C, 15 min, HDPE/catalyst=0.4/1, fluidized bed reactor	Gas=91.5; Liquid=4.0; Residue=4.5	Sharrat et al., 1997
HZSM-5 (17)	430°C,15 min, HDPE/catalyst=0.4/1, fluidized bed reactor	Gas=94.2; Liquid=2.1; Residue=3.7	
ZSM-5 (75.9)	430°C, HDPE/catalyst=10, stirred semi batch reactor	Liquid=49.8; Gas=44.3; Residue=5.8	Sakata et al., 1997
Fe-(O-550)/USY	500°C, HDPE/catalyst=10, fixed bed quartz reactor	Liquid=72.5; Gas=26.1; Coke=1.4	Chen et al., 2024
Fe-(R-300)/USY	500°C, HDPE/catalyst=10, fixed bed quartz reactor	Liquid=69.9; Gas=28.2; Coke=1.9	
Fe-(R-450)/USY	500°C, HDPE/catalyst=10, fixed bed quartz reactor	Liquid=66.7; Gas=31.2; Coke=2.1	
P/mesoZ55-ss (55)	600°C, HDPE/catalyst = 1/80, micro-pyrolizer	CH_4=0.3, C_2-C_4 olefins=82.8, C_4 alkane=0.9, Aromatic= 4.1, Aromatics free C_5-C_{11}= 9.9, C_{12}-C_{20}= 1.6, C_{21}-C_{35}=0.4	Eschenbacher et al., 2022
Nanocrystalline (55 nm) HZSM-5	340°C, 2 h, HDPE/catalyst=100, stirred batch reactor	C_1-C_5=100; C_{6+}=0%. Conversion 18.8%	Serrano et al., 2005
Nanocrystalline (20 nm) HZSM-5	340°C, 2 h, HDPE/catalyst=100, stirred batch reactor	C_1-C_5=100; C_{6+}=0%.Conversion 27.2%	
Nanocrystalline (12 nm) HZSM-5	340°C, 2 h, HDPE/catalyst=100, stirred batch reactor	C_1-C_5=100; C_{6+}=0%. Conversion 48.7%	

Table 6: In-situ catalytic cracking of HDPE on other catalysts in the literature.

Catalyst (Si/Al)	Reaction conditions	Products distribution (wt.%)	Reference
FCC	450°C, HDPE/catalyst=1/20, semi batch reactor	Liquid=91.2; Gas=4,1; Coke=4.7	Abbas-Abadi et al., 2013
FCC	420°C, HDPE/catalyst=1/20, semi batch reactor	Liquid=89.1; Gas=6.7; Coke=4.2	
FCC used	500°C, spouted-bed reactor (30 g catalyst bed), 1 g/min HDPE	Gas=28.3; Liquid=61.6; Wax=10.1	Elordi et al., 2012b
Used FCC	450°C, HDPE/catalyst=1/6, fluidized bed reactor	Gas=41.6; Liquid=34.1; Residue=24.3	Salmiaton & Garforth, 2011
FCC equilibrated	475°C, spouted-bed reactor (30 g catalyst bed), 0.5 g/min HDPE	Gas=8.2; Liquid=91,2; Wax=0	Olazar et al., 2009
FCC (16.4)	430°C, 1h, 2 wt.% catalyst, fixed bed reactor	Gas=5.8; Liquid+Wax=82; Residue=12.2	Miskolczi et al., 2006
FCC (16.4)	450°C, 1h, 3 wt.% catalyst, fixed bed reactor	Gas=6.3; Liquid=82.5; Residue=11.2	Miskolczi et al., 2004
Used FCC	450°C, HDPE/catalyst=1/6, fluidized bed reactor	Gas=29.2; Liquid=55.8; Residue=13.0	Ali et al., 2003
FCC used	430°C, HDPE/catalyst=20, stirred semi batch reactor	Liquid=79.7; Gas=19.4; Residue=0.9	Lee et al., 2003
FCC used	400°C, HDPE/catalyst=10, stirred semi batch reactor	Liquid=82; Gas=17; Residue<1%	Lee et al., 2002
Coconut Shell Activated Carbon	400°C, 45 min, HDPE/catalyst=1, batch microwave reactor	Liquid=36.6; Gas=62.6; Residue=0.8	Juliastuti et al., 2018
ASA (98.5)	405°C, LDPE/catalyst=25, batch reactor	Liquid=81.1; Gas=18.1; Residue=7.5	Mondal et al., 2023
ASA+ Ti (61.1)	376°C, LDPE/catalyst=25, batch reactor	Liquid=88.9; Gas=11.1; Residue=4.1	
MSM-41	430°C, 1h, HDPE/catalyst=10, fixed bed reactor	Gas=57.7; Liquid=42.3; Residue=0	Liu et al., 2014b
Silica alumina (2.6)	360°C, 15 min, HDPE/catalyst=0.4/1, fluidized bed reactor	Gas=31.2; Liquid=56.6; Residue=12.1	Lin et al., 2004
MCM-41 (17.5)	360°C, 15 min, HDPE/catalyst=0.4/1, fluidized bed reactor	Gas=26.4; Liquid=64.4; Residue=9.1	
Silica-Alumina powder	450°C, batch reactor, HDPE/catalyst=20, 30 min	Liquid=78(91.3% C_{12}-C_{16}); Gas=21; Coke=1.0	Seo et al., 2003

Alumina powder	450°C, batch reactor, HDPE/catalyst=20, 30 min	Liquid=82 (53% C_{12}-C_{16}); Gas=15.9; Coke=2.1	
MCM-41 (17.5)	380°C, 360 min, stirred batch reactor	Gas=35.9; Liquid=22.9; Residue=41.2	Van Grieken et al., 2001
F9	500°C, 1 h, fluidized bed reactor (batch)	Liquid=65; Gas=24; Residue=11	Luo et al., 2000
SA	500°C, 1 h, fluidized bed reactor (batch)	Liquid=86; Gas=8; Residue=6	
SAHA (2.6)	360°C, 20 min, HDPE/catalyst=0.4/1, fluidized bed reactor	Gas=84.5; Liquid=3.4; Residue=12.1	Lin et al., 1998
MCM-41 (17.5)	360°C, 20 min, HDPE/catalyst=0.4/1, fluidized bed reactor	Gas=84.8; Liquid=6.1; Residue=9.1	
Silicalite (>1000)	360°C, 60 min, HDPE/catalyst=0.4/1, fluidized bed reactor	Gas=4.1; Liquid=1.5; Residue=94.4	Sharrat et al., 1997
Silicalite (>1000)	430°C, 60 min, HDPE/catalyst=0.4/1, fluidized bed reactor	Gas=24.2; Liquid=1.8; Residue=74	
SA-1 (4.99)	430°C, HDPE/catalyst=10, stirred semi batch reactor	Liquid=67.8; Gas=23.7; Residue=8.5	Sakata et al., 1997
SA-2 (0.267)	430°C, HDPE/catalyst=10, stirred semi batch reactor	Liquid=74.3; Gas=13.4; Residue=12.3	
KFS-16	430°C, HDPE/catalyst=10, stirred semi batch reactor	Liquid=71.1; Gas=11.0; Residue=17.9	
Pb-Co/$BaTiO_3$	350°C, 1 wt.% catalyst, fixed bed reactor	Gas=10.1; Liquid=64.8; Wax=20.3; Residue=4.13	Ahmad et al., 2013
$BaCO_3$	450°C, 1 h, HDPE/catalyst=10, batch reactor	Liquid=29.60	Jan et al., 2010a
$MgCO_3$	450°C, 1 h, HDPE/catalyst=10, batch reactor	Liquid=33.60	
$CaCO_3$	450°C, 1 h, HDPE/catalyst=10, batch reactor	Liquid=32.20	
$MgCO_3$	450°C, HDPE/catalyst=5, batch reactor	Gas=18; Liquid=51; Wax=28; Residue=3.4	Jan et al., 2010b

The ex-situ catalytic cracking of HDPE pyrolysis vapours has been investigated by several authors by using different kind of catalysts, reactor combinations and operating conditions, as illustrated by the data reported in Table 7.

Dwivedi et al. (2021) investigated the process with a pyrolysis batch reactor followed by a fixed-bed catalytic cracking reactor operated at 350°C, with a plastic/catalyst ratio of 30. The feed was a mixture of PP, LDPE and HDPE. Compared to the simple thermal cracking (≈75% liquid product and ≈25% gases), regular HZSM-5 increased gas production (≈40%) while 5% Fe/HZSM-5 produced 76% of liquid, of which 66.4% was in the fuel range hydrocarbons (C_6-C_{20}). Moreover, Fe- doped HZSM-5 experienced lower deactivation and coke deposition.

Akubo et al. (2019) investigated the efficacy of various metal-doped Y zeolite catalysts in the catalytic pyrolysis of high-density polyethylene (HDPE) for the production of high-value fuels. Utilizing a two-stage (thermal followed by catalytic) fixed-bed pyrolysis system operating at 600 °C, the study demonstrated that the introduction of Y zeolite catalysts reduced the overall oil yield—from 69% under thermal pyrolysis conditions to 45%—while significantly enhancing product quality, achieving an aromatic hydrocarbon content of approximately 79%. The incorporation of transition metals (Ni, Mo, Ga, Fe, Ru, and Co) into the Y zeolite framework further increased the aromatic hydrocarbon yield, reaching values between 80 and 95 wt.% relative to the total oil fraction, when compared to the non-catalytic process. However, an increase in metal loading from 1% to 5% resulted in a decline in aromatic yield, indicating an optimal loading threshold. The aromatic fraction was predominantly composed of mono- and bi-aromatic hydrocarbons—such as toluene, xylene, and ethylbenzene—which accounted for 97–99% of the total aromatics produced with metal-doped Y zeolite catalysts. A noted drawback was that higher metal loadings also promoted carbon deposition on the catalyst surface, potentially reducing catalyst longevity and effectiveness.

Dai et al. (2021) conducted an extensive catalyst screening study for the catalytic cracking of high-density polyethylene (HDPE) using a microwave-assisted pyrolysis system coupled with two sequential fixed-bed catalytic reactors. The first reactor facilitated the catalytic cracking of pyrolysis volatiles, while the second reactor was designed for their hydrogenation and reforming into low-aromatic-content naphtha. This was achieved using an Al_2O_3-pillared metal-clay (M-clay) catalyst, which promoted olefin-to-paraffin conversion reactions. The experimental conditions included a pyrolysis temperature of 500 °C, a catalyst-to-plastic ratio of 1:1, and a catalytic cracking temperature of 450 °C.

The study evaluated a range of catalysts, including ZSM-5, ultra stable Y (USY), SBA-15, and metal-loaded SBA-15 variants (with metal loadings ranging from 1% to 10%). Among these, Zn/SBA-15 exhibited high cracking activity attributed to its acidic properties, though it yielded a low aromatic content (6.66%). In contrast, ZSM-5, USY, and Al/SBA-15 demonstrated the highest

selectivity towards C_5–C_{12} aromatic hydrocarbons, achieving yields of 84.15%, 81.07%, and 45.90%, respectively.

Ratnasari et al. (2017) investigated the impact of staged catalysis on the reforming of high-density polyethylene (HDPE) pyrolysis volatiles using a two-stage fixed-bed reactor system. The catalytic configuration employed a dual-layer bed combining mesoporous MCM-41 and microporous ZSM-5, aimed at enhancing selectivity towards gasoline-range hydrocarbons. Optimal performance was achieved with a 1:1 mass ratio of MCM-41 to ZSM-5 and a plastic-to-catalyst ratio of 1:2. Under these conditions, the process yielded 97.7% gasoline-range hydrocarbons, with an aromatic content of 95.8%, demonstrating the synergistic effect of combining meso- and microporous catalysts in a staged configuration.

Artetxe et al. (2012) examined the continuous catalytic pyrolysis of high-density polyethylene (HDPE) using a two-stage system comprising a spouted-bed pyrolysis reactor followed by a fixed-bed catalytic reactor. The study demonstrated that the spouted-bed reactor is well-suited for the continuous pyrolysis of plastic waste due to its superior heat and mass transfer characteristics and its ability to operate continuously without defluidization issues. The use of an HZSM-5 catalyst in the downstream fixed-bed reactor enabled the production of high yields of light olefins. The results indicated that increasing both the space-time and the cracking temperature enhanced the formation of light olefins—reaching a maximum yield of 62 wt.% at 550 °C and a space-time of 8 g_{cat} min g_{HDPE}^{-1}—as well as monoaromatics, which peaked at 13 wt.%. Furthermore, the acidity of the HZSM-5 catalyst was identified as a key parameter in modulating the product distribution during catalytic pyrolysis (Artetxe et al., 2013). Specifically, an increase in catalyst acidity was found to enhance the yield of light olefins, attributed to the catalyst's higher cracking activity, as well as the formation of monoaromatic compounds, due to the promotion of condensation and aromatization reactions.

Table 7: In line catalytic cracking of HDPE on different catalysts in the literature.

Catalyst (Si/Al)	Reaction conditions	Products distribution (wt.%)	Reference
HZSM-5 (30)	350°C, HDPE/catalyst=30, batch+fixed bed reactor	Liquid=60; Gas=40; Residue=N.D.	Dwivedi et al., 2021
ZSM-5	500°C, HDPE/catalyst=1, microwave reactor + tandem catalytic cracking+ reforming	C_5-C_{12} paraffins=0.45; C_5-C_{12} olefins=9.22; C_5-C_{12} aromatics=84.15; C_{13+} hydrocarbons=6.18	Dai et al., 2021
USY	500°C, HDPE/catalyst=1, microwave reactor + tandem catalytic cracking+ reforming	C_5-C_{12} paraffins=6.08; C_5-C_{12} olefins=3.53; C_5-C_{12} aromatics=81.07; C_{13+} hydrocarbons=9.08	
Zeolite Y	600°C, two-stage fixed bed reactor (thermal stage + catalytic stage), 2 g HDPE, 4 g catalyst.	Gas=36; Liquid=45; Coke=10	Akubo et al., 2019
ZSM-5 (20)	500°C, two-stage fixed bed reactor (thermal stage + catalytic stage), 2 g HDPE, 4 g catalyst.	Gas=21.4; Liquid=79.3	Ratnasari et al., 2017
HUSY (5.2)	470°C, 45 min, two-stage fixed bed reactor (thermal stage + catalytic stage). 10 g HDPE, 1 g catalyst.	Gas=93.2; Liquid+Wax=4.9; Solids=1.9	Zeaiter, 2014
Hβ (300)	470°C, 45 min, two-stage fixed bed reactor (thermal stage + catalytic stage). 10 g HDPE, 1 g catalyst.	Gas=95.7; Liquid+Wax=1.4; Solids=1.9	
HZSM-5 (80)	Spouted-bed (1g/min HDPE, 500°C)+ fixed bed (8 g of catalyst, 550°C)	C_2-C_4 olefins=43.9; C_1-C_4 paraffins=7; non-aromatic C_5-C_{11}=23.9; aromatics =3.4; C_{12}-C_{20}=22.5	Artetxe et al., 2013
HZSM-5 (280)	Spouted-bed (1g/min HDPE, 500°C)+ fixed bed (8 g of catalyst, 550°C)	C_2-C_4 olefins=35.6; C_1-C_4 paraffins=5.6; non-aromatic C_5-C_{11}=28.7; aromatics =1.7; C_{12}-C_{20}=28	
HZSM-5 (30)	Spouted-bed (1g/min HDPE, 500°C)+ fixed bed (8 g of catalyst, 550°C)	Gas=72.2; Liquid=27.8; Coke=0	Artetxe et al., 2012
5%Fe/HZSM-5	350°C, HDPE/catalyst=30, batch+fixed bed reactor	Liquid=76; Gas=24; Residue=N.D.	Dwivedi et al., 2021
1 wt% Ni-Y	600°C, two-stage fixed bed reactor (thermal stage + catalytic stage), 2 g HDPE, 4 g catalyst.	Gas=36; Liquid=36; Coke=22	Akubo et al., 2019
5 wt% Ni-Y	600°C, two-stage fixed bed reactor (thermal stage + catalytic stage), 2 g HDPE, 4 g catalyst.	Gas=36; Liquid=43; Coke=18	
1 wt% Mo-Y	600°C, two-stage fixed bed reactor (thermal stage + catalytic stage), 2 g HDPE, 4 g catalyst.	Gas=38; Liquid=31; Coke=24	

5 wt% Mo-Y	600°C, two-stage fixed bed reactor (thermal stage + catalytic stage), 2 g HDPE, 4 g catalyst.	Gas=36; Liquid=35; Coke=20	
1 wt% Fe-Y	600°C, two-stage fixed bed reactor (thermal stage + catalytic stage), 2 g HDPE, 4 g catalyst.	Gas=33; Liquid=40; Coke=14	
5 wt% Fe-Y	600°C, two-stage fixed bed reactor (thermal stage + catalytic stage), 2 g HDPE, 4 g catalyst.	Gas=38; Liquid=30; Coke=22	
1 wt% Ga-Y	600°C, two-stage fixed bed reactor (thermal stage + catalytic stage), 2 g HDPE, 4 g catalyst.	Gas=37; Liquid=36; Coke=18	
5 wt% Ga-Y	600°C, two-stage fixed bed reactor (thermal stage + catalytic stage), 2 g HDPE, 4 g catalyst.	Gas=37; Liquid=29; Coke=24	
1 wt% Ru-Y	600°C, two-stage fixed bed reactor (thermal stage + catalytic stage), 2 g HDPE, 4 g catalyst.	Gas=42; Liquid=34; Coke=18	
5 wt% Ru-Y	600°C, two-stage fixed bed reactor (thermal stage + catalytic stage), 2 g HDPE, 4 g catalyst.	Gas=31; Liquid=43; Coke=20	
1 wt% Co-Y	600°C, two-stage fixed bed reactor (thermal stage + catalytic stage), 2 g HDPE, 4 g catalyst.	Gas=36; Liquid=36; Coke=22	
5 wt% Co-Y	600°C, two-stage fixed bed reactor (thermal stage + catalytic stage), 2 g HDPE, 4 g catalyst.	Gas=40; Liquid=30; Coke=26	
SBA-15	500°C, HDPE/catalyst=1, microwave reactor + tandem catalytic cracking+ reforming	C_5-C_{12} paraffins=0.88; C_5-C_{12} olefins=12.13; C_5-C_{12} aromatics=2.18; C_{13+} hydrocarbons=84.81	Dai et al., 2021
Co-SBA-15	500°C, HDPE/catalyst=1, microwave reactor + tandem catalytic cracking+ reforming	C_5-C_{12} paraffins=4.60; C_5-C_{12} olefins=13.57; C_5-C_{12} aromatics=1.12; C_{13+} hydrocarbons=75.38	
Fe-SBA-15	500°C, HDPE/catalyst=1, microwave reactor + tandem catalytic cracking+ reforming	C_5-C_{12} paraffins=2.62; C_5-C_{12} olefins=31.32; C_5-C_{12} aromatics=6.28; C_{13+} hydrocarbons=59.55	
Ni-SBA-15	500°C, HDPE/catalyst=1, microwave reactor + tandem catalytic cracking+ reforming	C_5-C_{12} paraffins=0.91; C_5-C_{12} olefins=33.59; C_5-C_{12} aromatics=1.38; C_{13+} hydrocarbons=60.24	
ZnAl-SBA-15	500°C, HDPE/catalyst=1, microwave reactor + tandem catalytic cracking+ reforming	C_5-C_{12} paraffins=4.27; C_5-C_{12} olefins=38.24; C_5-C_{12} aromatics=12.15; C_{13+} hydrocarbons=45.34	
FCC	450°C, 17 min, two-stage fixed bed reactor (thermal stage + catalytic stage)	Gas=0.5; Liquid=38.5; Residue=61.0	Achilias et al., 2007
Spent FCC	Spouted-bed (1g/min HDPE, 500°C)+ fixed bed (6 g of catalyst, 450-550°C)	C_2-C_4 olefins=12-28; C_1-C_4 paraffins=3.5; non-aromatic C_5-C_{11}=34-52; aromatics =<3; Wax=36-1	Barbarias et al., 2015

MCM-41 (4)	500°C, two-stage fixed bed reactor (thermal stage + catalytic stage), 2 g HDPE, 4 g catalyst.	Gas=11.8; Liquid=88.2	Ratnasari et al., 2017

1.5 Upgrading strategies of pyrolysis liquids

As previously discussed, due to the inherent chemical complexity and low-quality characteristics of raw pyrolysis oil—including high oxygen content, acidity, instability, and impurities—the direct application of these products as fuels or chemical feedstocks is limited (Gollakota et al., 2016). Upgrading processes are therefore essential to transform pyrolysis oil into a higher-value, stable, and energy-dense product that meets the quality requirements for use in conventional fuel and chemical industries. Typically, a physical pre-treatment of bio-oil is necessary before the chemical upgrading.

Physical filtration can be a simple strategy to reduce the concentration of solid particles (char) in the oil, increasing its stability over time (Agblevor, 1994); nevertheless, recent studies have demonstrated that hot gas filtration – i.e., filtration of hot pyrolysis vapours coming from the reactor, before condensation – is able to decrease oil viscosity and reduce solid content in the oil more efficiently than liquid filtration (Brown, 2019), reaching 0.01% for char concentration and 10 ppm of alkali metals (Crocker, 2010).

Other physical processes that can be adopted to improve the quality of the pyrolytic oil include atmospheric distillation, extraction with supercritical fluids, liquid-liquid extraction and emulsification. Distillation of bio-oil is not straightforward as for crude oil. Thus, during the heating process, bio-oil oxygenated compounds tend to polymerize leaving behind 40-50 wt.% of the oil as solid residue (Lachos-Perez et al., 2023). To counter this phenomenon, vacuum distillation working at lower temperature has been proposed as an alternative, but its cost and energy intensity pose challenges for scale-up.

The use of supercritical fluids -especially $scCO_2$ because it is inert, non-toxic, inexpensive and easy to liquefy - has shown potential for selective extraction of target molecules from bio-oils (Feng and Meier, 2017; Wang et al., 2010). Nevertheless, the selectivity of the process is far from being satisfactory and the severe pressure conditions (>150 bar) make this technology expensive. A cheaper strategy to fractionate bio-oil is by simple liquid-liquid extraction (LLE) using solvents like toluene, ether, methanol. Alcohols, especially methanol, are able to dilute reactive oxygenates and to limit re-polymerization reactions (Brown, 2019).

Water can also be used as solvent, but its addition can cause phase separation of the oil (Lindfors et al., 2014) into a water-soluble phase (containing holocellulose -derived sugars and light organics) and a water-insoluble lignin-rich phase (Gollakota et al., 2016). Typically, multi-stage LLE has been performed to separate bio-oil into many selective fractions (Ren et al., 2017; Garcia-Perez et al., 2007).

Finally, bio-oil can be emulsified together with fossil fuels (diesel) or bio-based diesel by using appropriate surfactants (Lachos-Perez et al., 2023). By tuning the most important process parameters (i.e., temperature, bio-oil/diesel

ratio, surfactant concentration, mixing time and intensity) it is possible to produce stable, high- quality emulsions.

This section describes different techniques used to improve the characteristics of bio-oils, but some of them (namely, catalytic and thermal cracking, steam and dry reforming) proved to be effective to obtain hydrocarbon fuels or hydrogen from plastic oil too.

Hydrodeoxygenation is a widely investigated route to reduce the oxygen content of bio-oils. It operates at high temperatures (350-500°C) and pressures (5-15 MPa) in the presence of hydrogen and of an acidic catalyst able to cleave the C-O bond and to eject oxygen in the form of CO_2 and H_2O from the system (Dickerson and Soria, 2013; Nanda et al., 2021). Figure 16 illustrates the process:

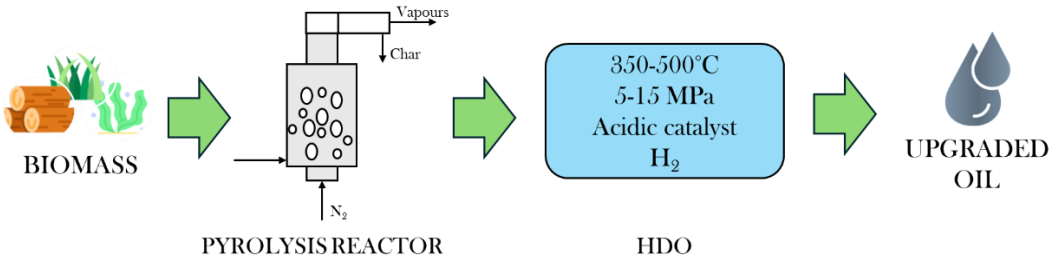

Figure 16: Schematic representation of bio-oil HDO.

The degree of HDO largely depends on the reaction conditions, specifically the temperature, pressure, hydrogen feed rate, and the choice of catalyst; but the process results in bio-oils with lower oxygen content, enhanced stability and improved calorific values. The main reactions occurring during the hydrotreating of bio-oil include hydrogenation, dehydration, decarbonylation, decarboxylation, cracking and hydrocracking (Zacher et al., 2014).

Different catalysts proved to be suitable for the HDO process, but five main catalyst groups have been investigated: sulphides, oxides, noble metals, phosphides and others, i.e. carbides and nitrates (Dabros et al., 2018).

Initially, sulfided CoMo and NiMo supported on alumina were tested as catalysts in conditions similar to those of traditional petroleum desulfurization process, but support's instability due to high concentration of water led to the development of novel catalysts over the past decades (Crocker, 2010; Elliot, 2007). Figure 17 shows the upgraded oil yield as a function of the degree of deoxygenation (DOD) for a selection of catalysts in both mild and harsh conditions (in Dabros et al., 2018 adapted from Wildschut et al., 2009):

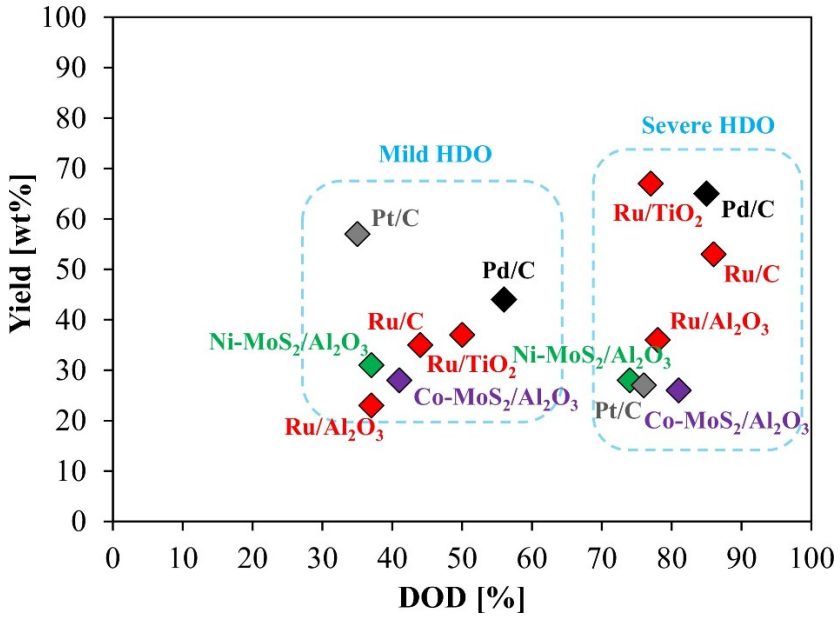

Figure 17: Oil yield as a function of the degree of deoxygenation (DOD) for different catalysts in mild (250°C and 100 bar) and severe (350°C, 200 bar) conditions. Picture from Dabros et al., (2018).

The primary advantage of HDO is its high carbon efficiency. By removing oxygen primarily as water, it preserves the carbon backbone of the organic molecules, which is crucial for maximizing the yield and energy density of the final hydrocarbon fuel. This carbon retention is crucial for achieving high energy density in the upgraded bio-oil, as carbon atoms are integral to calorific content. Nevertheless, high costs associated with continuous hydrogen supply (up to 490-710 L_{H2}/L_{oil}, as reported by Bunting and Boyd, 2012) and to high pressure conditions reduce economic viability on a large scale (Zacher et al., 2014).

This technique has a number of advantages, among which the feedstock versatility, the efficient and selective removal of oxygen from the bio-oil and the possibility to blend upgraded oil with fossil fuels to be processed in standard petroleum refineries. If coupled with renewable hydrogen sources and biomass feedstocks, HDO would have the potential to produce lower-carbon fuels. This contributes to greenhouse gas emission reduction goals and helps reduce dependence on fossil fuel sources.
Unfortunately, HDO relies heavily on hydrogen, which is often sourced from non-renewable methods, adding to both cost and environmental impact. The catalyst is also subject to fouling and deactivation (coking, sintering), thus reducing the process efficiency and requiring frequent catalyst regeneration (Li et al., 2017). The high temperature and pressure also increase the cost of the process (Zhang et al., 2021).

Steam reforming of bio-oil produces hydrogen (H_2) or syngas (a mixture of hydrogen and carbon monoxide). Being synthesized from a renewable energy resource, the produced gas is considered a clean and efficient energy carrier (Kumar et al., 2017). The process is similar to steam reforming of fossil fuels for hydrogen production. Steam and hydrocarbons react following a complex kinetic

scheme involving reforming, reverse water-gas shift, thermal decomposition of oxygenates (Kumar et al., 2017). A schematization of the process is given in Figure 18:

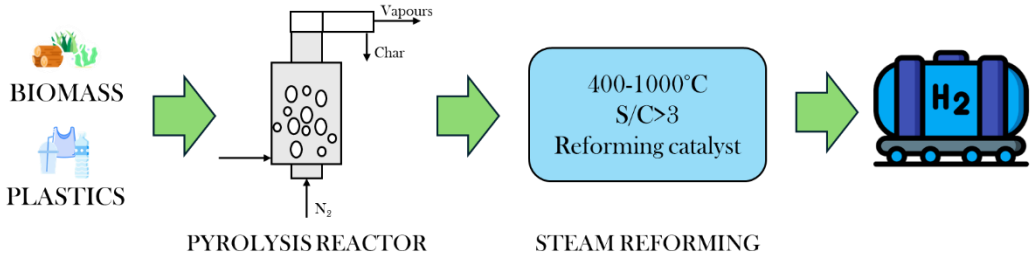

Figure 18: Schematic representation of bio-oil steam reforming process.

Steam reforming is typically conducted at high temperatures (400-1000°C), with high steam/carbon (S/C) ratios (>3) in the presence of a reforming catalyst and can produce hydrogen with yields up to 90% (Lachos-Perez et al., 2023). High bio-oil conversion is obtained at high temperature, low pressure and high S/C ratio. Catalysts need improved activity towards hydrogen production and resistance to coke formation and sintering to guarantee continuous operation. In this sense, high S/C ratio help reduce coke deposition by increasing carbon gasification rate at the catalyst's surface (Wang et al., 2007).

Catalysts based on Ni, Mg and noble metals have been synthesised for steam reforming of bio-oil. Nickel is preferred due to the lower cost compared to noble metals and its activity towards C-C bond cleavage (Lachos-Perez et al., 2023). Despite the higher activity and lower tendency to coke deposition of noble metals compared to Ni (Sehested, 2006), the high cost has limited practical applications. La and K promoters have been used to reduce coke formation on the catalyst surface (Davidian et al., 2007; Kumar et al., 2017).

Nevertheless, the main concern in steam reforming of bio-oil is represented by the thermal deactivation of the catalyst via sintering due to the severe operating temperature (Adeniyi et al., 2019).

The process has been successfully applied to biomass-derived volatiles (Fernandez et al., 2022a; Fernandez et al., 2022b; Santamaria et al., 2019) and to plastic-derived pyrolysis oil (Barbarias et al., 2018: Arregi et al., 2020; Li et al., 2023b); it can be carried out in different kinds of reactors, among which fixed-bed (Kechagiopoulos et al., 2006), fluidized-bed (Remiro et al., 2013) and spouted-bed reactors (Cortazar et al., 2023; Garcia et al., 2024; Suarez et al., 2024). Another viable alternative consists in the gasification of bio-oil to produce synthetic biofuels, such as kerosene, diesel, gasoline and synthetic natural gas (Crocker, 2010).

Esterification is a simple process used to convert polar, light, organic molecules present in the oil - in particular carboxylic acids - into the corresponding esters by reaction with alcohols, according to the general equation:

$$R_1OOH + R_2OH \rightarrow R_1OOR_2 + H_2O \quad [2]$$

With the conversion of organic acids into esters, the resulting bio-oil shows lower acidity, lower viscosity and improved stability over time (Lachos-Perez et al., 2023). The process can be carried out with or without a catalyst, with the catalytic process significantly improving the quality of the resulting oil. The significant water content in typical fast pyrolysis oils calls for innovative heterogeneous solid acid catalysts tailored for esterification.

These catalysts should possess robust hydrothermal stability and be designed with hydrophobic surfaces that can effectively push water away from the active sites. Sulphated zirconia, zeolites, mesoporous silica and carbon-based acidic catalysts have been developed and tested in the literature (Ciddor et al., 2015).

As an example, Liu et al. (2015) investigated the upgrading of bio-oil via catalytic esterification using a ZrO_2-TiO mixed oxide catalysts. They showed that 93.7% of the total acetic acid can be converted to esters using a 50% wt. ZrO_2 catalyst at 100°C, with a substantial increase in the calorific value of the oil (from 8.08 to 22.7 MJ/kg).

1.5.1 Upgrading via thermal and catalytic cracking

Cracking is a process that involves breaking down large molecules by cleaving C–O and C–C bonds to yield smaller, lighter molecules. The process can occur in the presence or the absence of a catalyst. In the thermal cracking process, pyrolysis vapours are sent to a bed of inert material at elevated temperatures, often reaching up to 900°C (Fagbemi et al., 2001). The high temperature promotes the cleavage of molecular bonds, producing smaller molecules. This method can effectively reduce oxygen content of bio-oil but also decreases bio-oil yield as a portion of the oil is converted into incondensable gas. The success of thermal cracking in deoxygenating compounds, enhancing selectivity toward desired hydrocarbons (such as aromatics, light alkanes, and light olefins), and controlling yield depends on optimizing key parameters—especially the temperature and residence time of the volatile compounds.

The use of a catalyst allows to improve selectivity and reduce operative temperatures. *Catalytic cracking* lowers the temperature requirements while enhancing control over product quality, allowing for more effective deoxygenation and fine-tuning of chemical composition in the resulting vapour.

More specifically, the main advantages of the catalytic process include: i) the reduction in the operating temperature due to the reduction of the activation energy in the C-C and C-O bond cleavage; ii) the reduction in the residence time of volatiles in the reactor; iii) increase the selectivity of the process towards specific classes of compounds (e.g., gasoline, diesel, light olefins in the case of plastic-derived bio-liquid) (Artetxe et al., 2013). For what concerns the last point, it should be noted that while cracking of pyrolysis volatiles derived from biomass pyrolysis generally aims at reducing the oxygen content of the resulting liquid – even though at the price of lower yields -, in the case of volatiles coming from the

pyrolysis of polyolefins there is more space for tuning the exact composition of the upgraded liquid.

The schematization of pure-thermal and catalytic cracking is depicted in Figure 19.

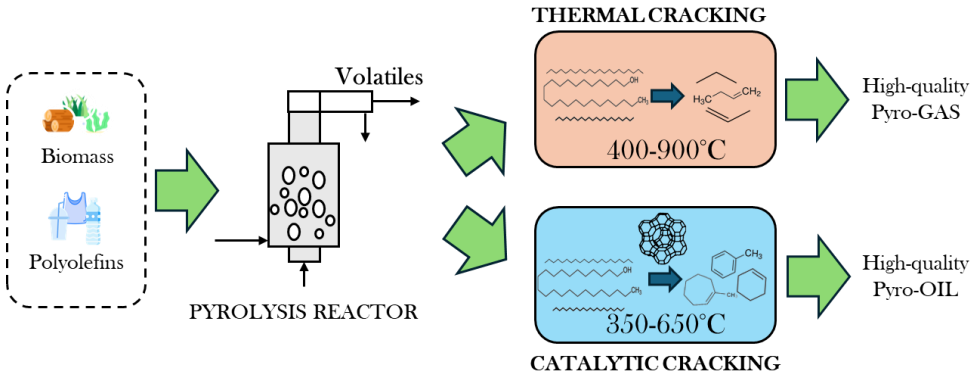

Figure 19: Thermal and catalytic cracking of pyrolysis volatiles.

Catalytic cracking is considered one of the most effective methods for upgrading pyrolysis oil due to its ability to produce high-quality, fuel-range hydrocarbons with improved stability and energy density. Compared to other upgrading strategies, catalytic cracking does not require external hydrogen, making it more cost-effective and environmentally favourable, especially when hydrogen supply is limited or derived from non-renewable sources. Moreover, operating conditions are milder, and cheaper catalysts can be used instead of noble-metals.

The method also benefits from compatibility with existing refinery infrastructure, allowing upgraded bio-oil to be co-processed with fossil fuels. Catalysts like zeolites offer high surface area and acidity, enabling efficient conversion and deoxygenation. Its flexibility in handling diverse feedstocks, including biomass- and plastic-derived pyrolysis volatiles, makes it suitable for large-scale applications. Overall, catalytic cracking offers a balanced combination of performance, scalability, and economic viability, positioning it as a leading technology for transforming pyrolysis oil into sustainable transportation fuels

In the catalytic process, the catalyst can be mixed with the feedstock in the reaction environment ("in-situ"); alternatively, a second reactor can be employed to crack pyrolysis vapours ("ex-situ" or "in-line"). Both configurations offer advantages and disadvantages, influencing their suitability depending on specific operational goals and economic considerations. (Figure 20).

Despite reducing equipment needs and minimizing vapour loss, the in-situ configuration limits control over cracking conditions, often leading to higher coke formation and rapid catalyst deactivation due to contaminant exposure, which compromises product quality and requires frequent reactor maintenance (Lopez et al., 2017b). Conversely, the "in-line" configuration provides precise control over cracking parameters (temperature and space-time) by separating the pyrolysis and cracking stages, thus enabling the production of higher-quality and more selectively targeted products (Wan and Wang, 2014). This approach also

facilitates easier catalyst replacement, but the additional reactor and vapor transfer system increase the complexity, operational costs, and energy requirements of the process.

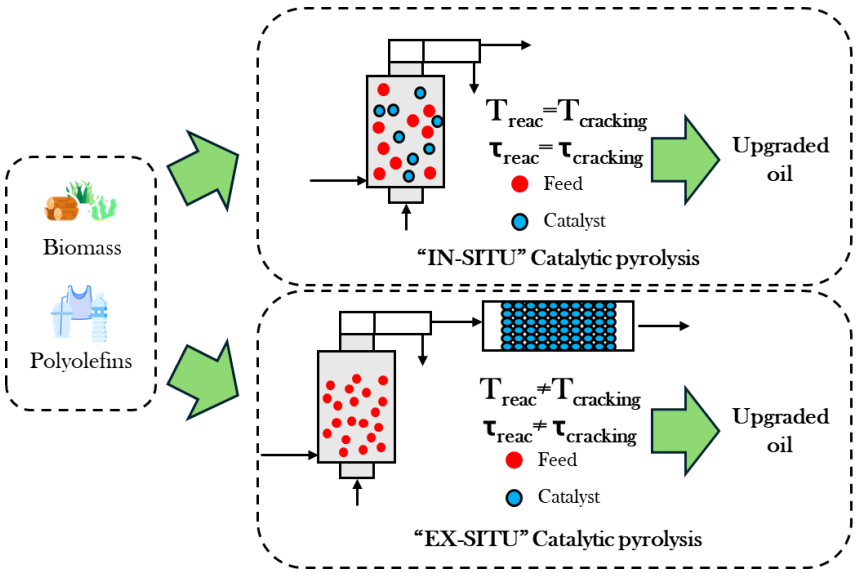

Figure 20: "In-situ" and "ex-situ" catalytic cracking configurations.

1.6 Properties of catalysts relevant to pyrolysis

The raw liquid products from fast pyrolysis are chemically complex and unstable; thus, catalytic upgrading is essential to transform them into valuable, drop-in fuels. This process fundamentally relies on heterogeneous catalysis, where a solid catalyst interacts with the reacting fluid phase (gas or liquid). A catalyst functions by selectively accelerating the reaction rate toward equilibrium by altering the reaction mechanism to favour lower-energy pathways, though it cannot overcome thermodynamic limitations. Given that most industrial chemical processes, including the cracking of pyrolysis volatiles in this work, employ solid catalysts, the focus is on heterogeneous systems.

The essential properties of a catalyst are its activity (the rate of reaction per unit weight), selectivity (the ability to kinetically favour desired reactions), and life (critical for industrial application, dictating reactor choice). The functionality of heterogeneous catalysts is predicated on maximizing the interphase contact between reactants and the catalyst surface, necessitating the use of highly porous materials with a high surface area. A typical supported catalyst is composed of three primary elements. The active phase is usually a metal or metal alloy (e.g., Pt, Fe, V) that possesses high intrinsic catalytic activity. Due to the high cost of noble metals (e.g., Pt, Pd, Ru), the active material is typically dispersed onto a support. The support is a high-surface-area material (e.g., silica, alumina, zeolites) that increases the accessibility and dispersion of the active phase, enhances the catalyst's stability against sintering, and provides mechanical resistance to attrition and fragmentation. Supports can also be multifunctional, participating in one step of the reaction (e.g., acidic supports in bifunctional catalysis). Promoters are substances added in small quantities during preparation to favourably influence

catalytic activity. Textural promoters improve surface area and porosity by hindering sintering, while structural promoters increase intrinsic chemical kinetics and enhance resistance to poisons.

The physio-chemical characteristics of the catalyst, such as surface area, pore structure, metal dispersion, and particle size, are critical in determining its performance. High metal dispersion and small particle sizes generally correlate with enhanced activity. The support material's properties—including acidity/basicity (defined by Lewis or Brønsted sites), thermal stability, and chemical inertness—significantly impact the active metal-support interaction. For instance, acidic supports like zeolites are crucial for bifunctional catalysis, providing sites for reactions like cracking, while the metal component facilitates hydrogenation. The final characteristics of the catalyst, including metal dispersion, textural properties, and mechanical resistance, are heavily influenced by the chosen synthesis method (Hutchings and Vèdrine, 2004). Common preparation techniques include:

- Precipitation. Involves forming a solid catalyst by inducing the precipitation of metal salts from a solution, typically by adding a base. Careful control of parameters like pH and temperature is necessary to manage the nucleation and agglomeration steps (Campanati et al., 2003; Satterfield, 1991). The precipitate is subsequently calcined to yield the active phase.
- Ion Exchange. A technique effective for uniform distribution of active species, where ions in a solid support (e.g., zeolite) are replaced by metal cations or anions from a solution until thermodynamic equilibrium is reached (Perego and Villa, 1997).
- Adsorption. Involves the attraction of ions from a solution to an electrically-charged solid surface (Campanati et al., 2003). It is preferred for low metal loading and is influenced by the nature of the support, precursor characteristics, temperature, and pH (Richardson, 1989; Santamaria Moreno, 2019).
- Impregnation. A method used for supported catalysts, detailed elsewhere in this work (Section 2.2.2).

One of the main bottlenecks in the use of catalysts both in the sin-situ and ex-situ configuration is the rapid deactivation due to coke deposition on the surface of the catalyst. Deactivation phenomena have been widely studied due to the impact on the performance of catalytic reactors and – consequently- on costs (Denny and Twigg, 1980; Richardson, 1989; Bartholomew, 2001; Boskovic and Baerns, 2004; Butt, 2012; Martìn et al., 2022).

The literature has identified many factors leading to deactivation of heterogeneous catalysts (Bartholomew, 2001), but they can be conveniently categorized according to the effect on the catalyst structure. Table 8 summarizes the most common deactivation phenomena:

Table 8: Mechanisms of catalyst deactivation, adapted from Bartholomew (2001).

Mechanism	Cause	Effect
Poisoning	Chemical	Active site blockage due to chemisorption of poison
Fouling/ coking	Chemical/mechanical	Carbon deposition with consequent pore plugging
Sintering	Thermal	Loss of surface area
Volatilization	Thermo-chemical	Reaction of active phase producing volatiles
Vapor-solid reaction	Thermo-chemical	Reaction of catalyst with gas to produce inactive compounds
Attrition	Mechanical	Loss of surface area and active sites due to attrition of particles

Catalyst deactivation can be due chemical, thermal or mechanical causes, but often a combination of the mechanisms is responsible for the loss of activity. The most relevant in the case of catalytic cracking of pyrolysis vapours coming from both biomass and plastics is coke deposition (Rezaei et al., 2014).

In general, when a catalytic process involves carbon-containing materials (e.g., biomass, plastics), the physical deposition of impurities from the reaction environment onto the catalytic surface - a typical deactivation phenomenon, called "coking"- occurs. Carbon deposition leads to the deactivation of the catalyst due to blocking the pores and the consequent reduction of the active surface area (Figure 21). While "carbon" refers to the product of CO disproportionation, the term "coke" is usually used to describe condensed heavy hydrocarbon deposits with no heteroatoms (Argyle and Bartholomew, 2015; Daligaux et al., 2021). According to the H/C ratio, which is related to the average chemical composition of the deposit, "soft" or "light" coke (constituted by aliphatic hydrocarbons, with high H/C ratios) and "heavy" coke (made up of polyaromatics with lower H/C ratio) can be distinguished (Daligaux et al., 2021).

The coking rate and the chemical structure of the deposits is intrinsically dependent on the catalyst properties (e.g., texture, acidity), but also on the reaction environment (e.g., feed rate, feed characteristics, operating conditions, presence of impurities, reactor materials) (Bartholomew, 2001).

The mechanism of fouling/coking is dependent on the chemical characteristics of the catalyst. For biomass, it is caused by the polymerization of reactive oxygenates (phenols and furans) on the catalyst's surface. For plastics, it stems from the oligomerization of olefins and aromatics on acid sites. Understanding these distinct coking pathways is central to developing robust catalysts.

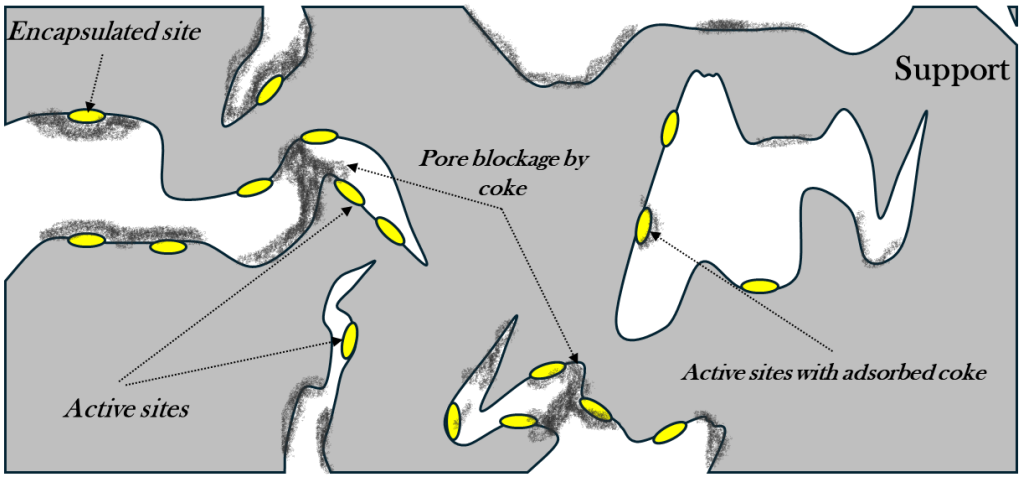

Figure 21: Effect of coke deposition on supported catalysts.

Zeolite catalysts can be deactivated by coke formation. Acidity and pore structure significantly influence the coking rate of zeolites (Guisnet et al, 1997; Boskovic and Baerns, 2004). More in detail, it has been observed that coke deposition is reduced when pore size is smaller at a fixed acidity (Bartholomew, 2001).

The mechanism of coke formation on metal oxides is both physical and chemical. On one hand, coke can be strongly adsorbed onto the acidic sites of the catalyst, reducing the activity; on the other hand, coke precursors (e.g., aromatics, olefins) can undergo condensation reaction leading to the formation of large polyaromatic molecules which can encapsulate acidic sites (Bartholomew, 2001). Pore size and shape in zeolites are the most relevant parameters determining the rate and the extent of deactivation by coking (Guisnet et al., 1997).

According to Guisnet et al. (1997), the deactivation of HZSM-5 can occur according to four different modalities:

i) coke is reversibly adsorbed on acidic sites.
ii) coke is irreversibly adsorbed on acidic sites, partly obstructing pores.
iii) Partial steric blockage of pores.
iv) Severe blockage of pores.

In the case of Modes 1 and 2, pore blockage is due to chemical reasons, while for Modes 3 and 4 it is promoted by steric reasons. Diffusion of reactants to the acidic sites in the inner sections of the pores is de facto limited or completely prevented.

Other deactivation phenomena include poisoning, where a molecule (reactant, product, or impurity) is strongly chemisorbed onto the active surface, irreversibly reducing the number of active sites and potentially causing structural modifications (Hegedus and McCabe, 1984); sintering, the loss of activity and surface area due to the thermal-induced growth and agglomeration of metal particles, which occurs via particle migration and coalescence or Ostwald Ripening (Hansen et al., 2013), with the rate drastically increasing near the Tamman temperature (Hughes, 1984); volatilization of the active phase, which

occurs at high temperatures (>800°C) through partial devolatilization or the formation of volatile species like metal carbonyls at moderate temperatures (Argyle and Bartholomew, 2015); and vapour-solid reactions, which lead to the formation of inactive species on the catalyst surface (Bartholomew, 2001; Argyle and Bartholomew, 2015). Mechanical deactivation is primarily due to attrition, which is the physical damage (friction, abrasion, crushing, or fragmentation) to the catalyst structure caused by mechanical stress from high temperature/pressure, turbulent flow, or improper handling in industrial settings (Argyle and Bartholomew, 2015).

1.7 Scope of the work

The scope of the present work is to overcome specific knowledge gaps into ex-situ catalytic fast pyrolysis of two different waste streams: polyolefins and lignocellulosic biomass. The overall research is structured into two distinct but complementary parts, each with its own specific objectives designed to address the unique challenges posed by the respective feedstock. Both campaigns were performed using dedicated two-stage pyrolysis systems (spouted-bed reactor + fixed-bed reactor), a configuration chosen to decouple the primary thermal effects from the secondary catalytic phenomena, allowing for a systematic analysis of key process variables. The specific objectives of this work are as follows:

For the Polyolefin Waste Stream:

1. To systematically investigate the effect of catalyst space-time on the product distribution from the upgrading of a model mixed polyolefin stream (HDPE/LDPE/PP) over an HZSM-5 catalyst.
2. To clarify the kinetic trade-off between the production of high-value light olefins and the secondary formation of BTX aromatics.
3. To analyse the catalyst deactivation mechanisms and severity under different operating conditions (cracking temperature and catalyst space-time) to understand the interplay between coking, activity, and selectivity.

As for olive stone valorization, this work aimed:

1. To investigate the influence of primary pyrolysis temperature (thermal decomposition) and secondary cracking temperature (catalytic upgrading) on the final product yields and bio-oil composition from olive stone.
2. To establish the role of distinct functionalities (acidic, basic, redox) of the catalyst in the performance of biomass vapor upgrading.
3. To develop new catalysts also evaluating the effectiveness of low-cost and waste-derived catalysts (dolomite, SCA/γ-Al_2O_3) as viable alternatives to conventional zeolites.

This work begins with a comprehensive overview of the potential roles of biomass and plastic waste in the transition towards a sustainable and circular economy and a state of the art of catalytic cracking of pyrolysis volatiles as a product upgrading strategy. An overview on the mechanisms of catalytic fast pyrolysis (CFP) in thermal and catalytic conditions is given, together with the analysis of the performance of different catalyst types (zeolites, metal oxides, and basic materials) in reducing oxygen content and improving fuel quality. Particular attention is given to the challenges posed by the chemical diversity of biomass- and plastic-derived vapours, and how catalyst design and process conditions can be tailored to address these issues. Subsequently, feedstock characterization (a mixture of polyolefins and raw olive stone biomass), catalyst selection and preparation, the design and operation of the pyrolysis plants (dual spouted-bed/fixed-bed pyrolysis reactor) are presented. Furthermore, the experimental procedures to quantify product yields and quality, assess catalyst performance, and evaluate deactivation phenomena have been described. Finally, the results of the experimental campaigns are reported and discussed.

Chapter 2

Materials and Methods

2.1 Lignocellulosic biomass and Polyolefins

Olive stone and a polyolefin mixture (50% wt. HDPE, 40% wt. LDPE and 10% wt. PP) have been chosen as reference materials for the experimental activity of this work.

Olive stone. In the Mediterranean basin, olive stones are an abundant byproduct of the olive oil industry, offering a consistent and geographically localized feedstock that aligns with circular economy principles. Europe produced over 1.5 million tonnes of olive oil in 2024 (*https://agriculture.ec.europa.eu/media/news/european-commission-launches-market-observatory-olive-oil-and-table-olives-sector-2024-11-11_en*), with countries such as Spain, Italy, Greece and Portugal contributing the vast majority, thus ensuring a stable and cost-effective supply of olive stone residues. It is estimated that for each hectare of olive grove, 3 tonnes of olives are obtained. From those, 0.6 tonnes of olive oil and 0.6 tonnes of olive stones are produced (García Martín et al., 2020). From a compositional standpoint, olive stones are characterized by high lignocellulosic content—typically around 40 % lignin, 28 % cellulose and 19 % hemicellulose—and low moisture, yielding a high calorific value (above 18 MJ/kg) and low ash content. These features translate into an efficient conversion into high-quality bio-oil, syngas and biochar under pyrolysis conditions (Ganda et al., 2022; Brachi et al., 2022; Christoforou et al., 2018) and made it possible the investigation of lignin-rich pyrolysis vapours with minimal interference from catalytic ash components. Furthermore, pyrolyzing olive stones provides a way to valorise an agro-industrial waste material that would otherwise incur disposal costs or environmental burdens.

Olive stone has been crushed and sieved in the range 0.45-2 mm and was dried at ambient conditions until reaching a low moisture content (below 14%). Operating with biomass particles smaller than 2 mm is beneficial to liquid production as it favours heat transfer and facilitates devolatilization; nevertheless,

extremely fine particles (<0.60 mm) can redirect towards gas production (Dada et al., 2023; Varma & Mondal, 2017).

Polyolefins. To address the investigation on catalytic fast pyrolysis of plastic waste, it was decided to start focusing on the valorization of pure polyolefins (POs). Polyolefins (e.g., HDPE, LDPE and PP) represented more than 40% of the EU plastic production in 2022 (see Figure 6). They are ubiquitous in packaging, textiles and consumer goods, and are among the most pervasive pollutants in the environment. Addressing polyolefin valorization provides the opportunity to tackle the largest fraction of the plastic waste stream in Europe. Unlike other plastics like PVC, which can release toxic byproducts during thermal processing, polyolefins' degradation is relatively clean and safe, thanks to their simple chemical structure. PET already has established recycling systems, but it has a lower overall production volume - about 5.4% of the global plastic waste production in 2019 (OECD, 2022) compared to olefins. Given the high market volume, the potential of polyolefins valorization into high-value products (i.e., fuels and chemicals) is immense and gives the opportunity to develop a waste-to-resource path on a larger scale.

The composition of the polyolefin mixture was selected to simulate a plausible composition of post-consumer polyolefin waste streams in municipal recycling facilities. This was done to ensure that the results regarding product yields, catalyst performance, and deactivation can serve as a preliminary reference for the practical challenges associated with processing heterogeneous plastic waste, rather than representing an idealized single-polymer system. HDPE, LDPE and PP were provided by Dow Chemical (Tarragona, Spain) in the form of chipping of 4 mm. The particle size was chosen to be compatible with the solid feeding systems of the two plants used in this study to guarantee smooth feeding without blocking and to avoid heat transfer limitations within the reaction environment. Both the materials were fed to the spouted-bed reactors without operational problems.

The two feedstocks have been characterized with several techniques as reported below.
Proximate and ultimate analyses were performed according to ASTM standards using a *LECO TG701* thermogravimetric balance (ASTM D5142), *LECO CS832* (ASTM D 4239) and a *LECO CHN 828* elemental analyser (ASTM D5373) for the proximate analysis, elemental analysis of CHN and S, respectively. More specifically, the ASTM D5142 standard requires a first heating in inert atmosphere (nitrogen) to 107°C for around 40 min to remove surface and inherent moisture. Then, the temperature of the sample is increased to 950°C with a rapid ramp (50°C/min) for 7 min in nitrogen atmosphere to volatilize combustible components excluding moisture. The carrier gas is subsequently changed to air, and the sample is first cooled to 600°C and then heated to 750°C at 15°C/min and held at constant temperature until sample mass is stabilized (around 60 min). This

step allows the burn off of fixed carbon, leaving behind ash residue. Fixed carbon is calculated by difference from moisture, volatile matter and ash.

In the ASTM D5373 is the standard test method of determination of carbon, hydrogen and nitrogen in solid fuels. A weighted amount of sample is burned in excess oxygen at high temperatures (950°C) and the resulting gases (CO_2 from carbon, H_2O from hydrogen and NO_x from nitrogen) are measured by infrared and TCD detectors and put in relation to the composition of the sample. In the ASTM D4239 for sulphur content determination, a definite amount of sample biomass is heated at 1350°C in excess of oxygen in order to completely burn all organic and inorganic S contained in it. An IR detector allows the measurement of SO_2 in the flue gas, which is then related to biomass sulphur content.

The calorific value was determined using a *PARR 6200* calorimeter equipped with a Mahler calorimeter bomb following the ASTM D5865 protocol. All measurements were repeated at least three times. In the procedure, a precisely weighed sample was placed in a crucible within a sealed metal bomb calorimeter. The bomb was filled with pure oxygen at a pressure of 20 bar and subsequently submerged in a water bath maintained at a uniform initial temperature. Combustion was initiated by an ignition system consisting of two electrodes and a tungsten ignition wire in contact with the sample. The resulting rapid and exothermic reaction led to an increase in the temperature of the surrounding water. The higher heating value (HHV) of the sample was then calculated based on an adiabatic heat balance, accounting for the measured temperature rise and system calibration parameters.

The standard methods reported above are commonly used for the characterization of woody biomass materials in the literature (e.g., Frau et al., 2015; Hennessy, 2010). Moreover, we chose to characterize both OS and polyolefins using the same procedures for easy direct comparison.

ICP-MS (Inductively Coupled Plasma–Mass Spectroscopy) has been performed on both olive stone and char samples obtained from the pyrolysis tests using an Agilent 7850 analyser. The samples have been mineralized to bring them in a homogeneous, solubilized form by mixing the sample (approximately 0.1-0.3 g) with 5 mL of HNO_3, 1 mL of H_2O_2, 0.5 mL of HF and 4 mL of ultra-pure water; the solutions are then heated up to 230°C for 20 minutes in a ETHOS UP high-performance microwave digestion system (Milestone Srl) before the ICP-MS analysis.

2.2 Catalyst selection and preparation

2.2.1 Catalyst selection

Most of the experimental work presented in this Thesis has been conducted using a commercial HZSM-5 catalyst based on alumina (HSZ-840HOD1A, TOSOH Chemicals, Japan). ZSM-5 (zeolite Socony Mobil-5) is a crystalline

aluminosilicate characterized by an MFI topology, with straight 10-membered ring channels (5.2 x 5.7 Å) with a mean pore size around 5.5 Å (Cai et al., 2020). Thanks to the 3-dimensional pore system and to the uniform diameter of its pores, ZSM-5 is suitable for shape selective processes, i.e. reaction in which the shape of reactants, products or intermediates is tuned by the internal structure of the catalyst. The catalyst is characterized by high acidity and has been employed in the form of white pellets with a 1.5 mm diameter. It is widely known that ZSM-5 catalyst is suitable for upgrading of pyrolysis vapours from biomass and plastics (Wang et al., 2022; Qiu et al., 2022b; Kan et al., 2020; Liu et al., 2014a; Liu et al., 2020). Other catalysts have been tested for the upgrading of pyrolysis vapours of olive stone biomass in a two-stage pyrolysis system, namely:

- HY zeolite catalyst with clay binder (HSZ-385HUD1C, TOSOH Chemicals, Japan)
- A homemade low-cost waste-derived catalyst (see Section 2.2.2)
- A homemade 3% Fe/ γ-Al_2O_3
- γ-Al_2O_3 (Sasol Chemicals)
- Calcined dolomite (Peroglio S.r.l)
- A homemade 3% Fe/dolomite catalyst.

2.2.2 Catalyst preparation

Two different Fe-based catalysts have been synthesized and their performance for the catalytic upgrading of biomass pyrolysis vapours has been tested. γ-Al_2O_3 (Sasol Chemicals, CAS 1344-28-1) and dolomite (Peroglio S.r.l, CAS 16389-88-1) have been used as support for the catalysts.

The two catalysts, 3%Fe/ γ-Al_2O_3 and 3%Fe/$CaMg(CO_3)_2$, were prepared by wet impregnation method. The process has been conducted using a *Laborota 4002,* which allows the continuous addition of a solution containing the salt precursor of the metal (Iron (III) nitrate nonahydrate, *Sigma Aldrich*, purity >98%) on to the support (Figure 22). In more detail, the precursor solution is put into the evaporation flask together with the support and, thanks to the rotation provided by the motor, it is well dispersed on it. The evaporation flask is partially immersed in a temperature-controlled water bath. With passing time, the solution completely impregnates the support and fills the pores by capillarity. The rotavapor operates at 60°C under vacuum conditions (70-160 mbar), allowing for a faster evaporation of the excess solution. The evaporated solvent vapor rises through the flask's neck and enters the condenser, which is cooled by circulating water. As the vapor comes into contact with the cooled surface of the condenser, it condenses back into liquid form and flows into the collection flask. This separation of solvent vapor and its subsequent condensation ensure a continuous and efficient solvent recovery process. Once the catalyst is impregnated, it needs a thermal treatment step (calcination in N_2 atmosphere up to 800°C at 10°C/min) to volatilize the nitrates the precursor and to obtain the catalyst in its final form.

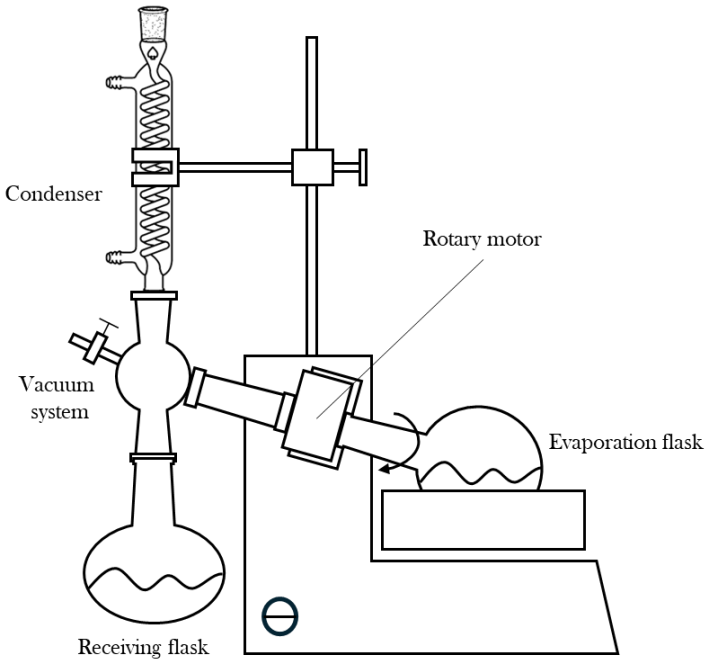

Figure 22: Schematic of Rotavapor equipment (Laborota 4002)

Before impregnation, dolomite was calcined in a fluidized-bed reactor at 800°C in inert atmosphere (N_2) until all the CO_2 was removed from its structure. This step was necessary to improve the catalytic activity of dolomite towards bulky organics in the pyrolysis vapours (Encinar et al., 2008). The catalytic activity of dolomite is closely related to its basicity and external surface area. Calcination of natural dolomite ($CaMg(CO_3)_2$) to form CaO and MgO significantly increases its surface area and porosity, thereby creating more active sites for catalysis (Chen et al., 2021; Xu et al., 2022). Studies have shown that calcined dolomite exhibits stronger basicity than pure CaO, which enhances its catalytic performance (Chen et al., 2021).

The process was completed within 15 minutes after reaching the set temperature with a yield of 47%. The CO_2 generation was monitored using a portable *MRU VarioLuxx Syngas analyser* (Section 2.6.5) and its profile during the calcination process is illustrated in Figure 23.

For the preparation of Fe/ γ-Al_2O_3 catalyst, 18.13 g of Fe $(NO_3)_3 \cdot 9H_2O$ have been dissolved in 250 mL of distilled water, while the support was 47.5 g of γ-Al_2O_3. For the Fe/ $CaMg(CO_3)_2$ catalyst, 18.14 g of Fe $(NO_3)_3 \cdot 9H_2O$ have been dissolved in 250 mL of distilled water, while the support was 47.5 g of dolomite. The results from Inductively Coupled Plasma Mass Spectrometry (ICP-MS) analysis confirmed that Fe was correctly deposited on the support (3.34% Fe on γ-Al_2O_3 and 2.74% Fe on dolomite).

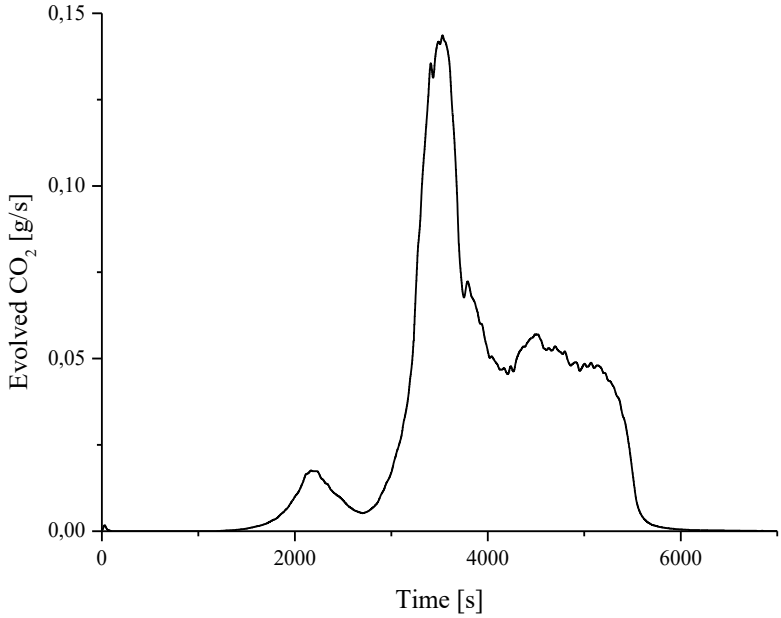

Figure 23: CO_2 evolution during calcination of dolomite.

A low-cost catalyst has been prepared from the ashes coming from sewage sludge combustion in fluidized-bed reactor (Coppola et al., 2015). The ashes from sludge combustion are characterized by high metal content (especially Fe, Ca and Mn), and it is possible to deposit these metals onto high surface-area γ-Al_2O_3 (Sasol Chemicals, 1 mm spheres). This catalyst will be addressed as SCA/γ-Al_2O_3 (Sludge Combustion Ashes over γ-Al_2O_3) in this Thesis.

2.3 Catalyst characterization

2.3.1 Surface area, pore volume and pore diameter

The physical characteristics of the fresh catalysts (namely the specific surface area, the pore size and pore volume distribution) have been determined according to the ASTM D3663-20 using a *Autosorb IQ* automated gas sorption analyzer *(*Quantachrome Instruments*)* working under the N_2 adsorption-desorption principle. The measurement requires complete degasification of the sample (a first step at low temperature and a second at 150°C for 8 h) to eliminate impurities, water and other chemisorbed species. The sample (typically 50-70 mg for zeolites) is loaded into the equipment, where is subject to several adsorption-desorption cycles using pure nitrogen (99.9995%) at its cryogenic point (77 K) until equilibrium is reached. The equipment is able to calculate the physical properties of the catalyst from the equilibrium isotherm data, based on the use of material balance and gas state equation together with pressure measurements. The calculation of surface area is made with the BET equation, while the pore size distribution is calculated by the BJH method.

2.3.2 Acidity and acidic sites' strength

The acidic properties of the catalysts employed in this study were characterized using a *Micromeritics AutoChem II* chemisorption analyser. This instrument was utilized to determine both the quantity and the relative strength of acidic sites on the catalyst surface—key parameters influencing catalytic cracking activity toward organic molecules. The analysis was conducted as follows:

1. Approximately 100 mg of catalyst sample was subjected to ammonia adsorption by flowing a gas mixture of 5% NH_3 in He at 50 cm^3/min for 1 hour at ambient temperature (20 °C).
2. The ammonia-containing gas was then replaced with pure helium (50 cm^3/min), and the system was allowed to stabilize until a baseline was established.
3. The sample was subsequently heated from ambient temperature to 550 °C at a ramp rate of 10 °C/min, followed by an isothermal hold at 550 °C for 1 hour. During this temperature-programmed desorption (TPD) phase, ammonia desorbed from the catalyst surface, with the temperature corresponding to the desorption peak providing an indication of the relative strength of the acidic sites.
4. Finally, the sample was cooled back to ambient temperature.

The equipment is also provided with a chemical KOH-based trap suitable for not interfering with the ammonia desorption. The same equipment is used for CO_2-based Temperature Programmed Desorption experiments to quantify basicity of dolomite-based catalysts in terms of mmol $CO_2/g_{catalyst}$.
An acid site classification according to the relative strength -i.e. to the peak desorption temperature – was established by Elordi et al. (2012a):

1. Weak acidity between 150-280°C
2. Average acidity between 280-420°C
3. Strong acidity between 420-550°C

2.3.3 Temperature programmed oxidation (TPO) of spent catalyst

The calculation of the amount of coke deposited on the catalyst was approached by using temperature programmed oxidation (TPO). A thermobalance (T.A. Instruments TGA Q5000) was used to measure coke content. The temperature program was as follows:

1. Sample stabilization by heating in inert atmosphere (N_2, 50 mL/min) up to 200°C at 10 °C/min for 20 min to remove any oxygen from the combustion chamber and to remove chemisorbed species from the sample (e.g., moisture)
2. Cooling down to 100°C and switch to air
3. Heating to 800°C in air (50 mL/min) at 5°C/min for complete coke combustion for 15 minutes.

4. Cooling down to 120°C

During the process the values of temperature, sample mass and mass loss rate are registered by the instrument. The amount of coke on the catalyst was calculated by difference between the initial and final mass of the sample before and after combustion similarly to what was explained in Section 2.6.6. Dolomite based catalysts were subjected to preliminary calcination at 800°C before the TPO analysis. Moreover, TG-MS analysis was performed to distinguish between coke and other desorbed species (CO_2, water).

2.4 Scanning Electron Microscopy

SEM characterization of fresh catalyst samples has been realized using a FEI INSPECT S50 Scanning Electron Microscope. The instrument has been used in high-resolution mode, with acceleration voltage between 500 and 1200 kV. Image acquisition was conducted in secondary electron (SE) mode using an Everhart-Thornley detector (ETD) to observe the superficial morphology of the samples. Non-conductive samples (e.g., zeolites) were coated with a thin gold film to improve image resolution and mounted on a metallic stub with a graphite-based adhesive. Images up to 30 μm resolution (magnification 3000x) were obtained to observe superficial details and defects. The data collected supported the interpretation of experimental results.

2.5 Total phenolic content (TPC)

The Folin-Ciocâlteu assay (FC) is the analytic method used to quantify the total amount of phenols in the bio-oil obtained from pyrolysis tests. This method does not allow to distinguish among different kind of phenols but also considers polyphenols and compounds with more than one chemical functionality. In the context of this Thesis, it was decided to employ the FC assay because of its simplicity, reproducibility and cost-effectiveness (Perèz et al., 2023) to give a preliminary estimation of the total content of phenolics in pyrolysis oils (see, for instance, Rover & Brown, 2013; Fardhyanti et al., 2020; Fardhyanti et al., 2024; Stankowskj et al., 2017a; Stankowskj et al., 2017b; Del Pozo et al., 2020).

The FC reagent has not been prepared according to the original protocol (Singleton & Rossi, 1965) but has been bought from VWR International Srl (Avantor). The Folin–Ciocâlteu reagent is a complex blend of phosphotungstic and phosphomolybdic acids that undergoes reduction during the assay, forming a blue metal complex chromophore with peak absorbance at 765 nm (Rosbash, 1949). Phenolic compounds are able to interact with the FC reagent according to a redox reaction, in which the phenolic group is the reducing agent while the FC reagent is the oxidizer (Figure 24).

Given the tendency of the FC reagent to interact with all reducing species, it can somehow overestimate the total phenol content of bio-oil samples.

Nevertheless, comparison between samples is straightforward. The result from the FC assay is usually reported in terms of equivalents of a standard compound, usually gallic acid (GA) in most applications (mg GAE/L oil or mg GAE/ g oil). Nevertheless, for application with pyrolysis oils, guaiacol has been used as a standard, therefore our results are expressed in mg of guaiacol equivalent per g of bio-oil (mg GUE/g oil). Guaiacol has a lignocellulosic origin and is more representative of the phenolic effect in pyrolysis oils compared to gallic acid. This also guarantees chemical coherence between the sample and the standard used for calibration. Finally, guaiacol has high solubility in organic solvents like acetone.

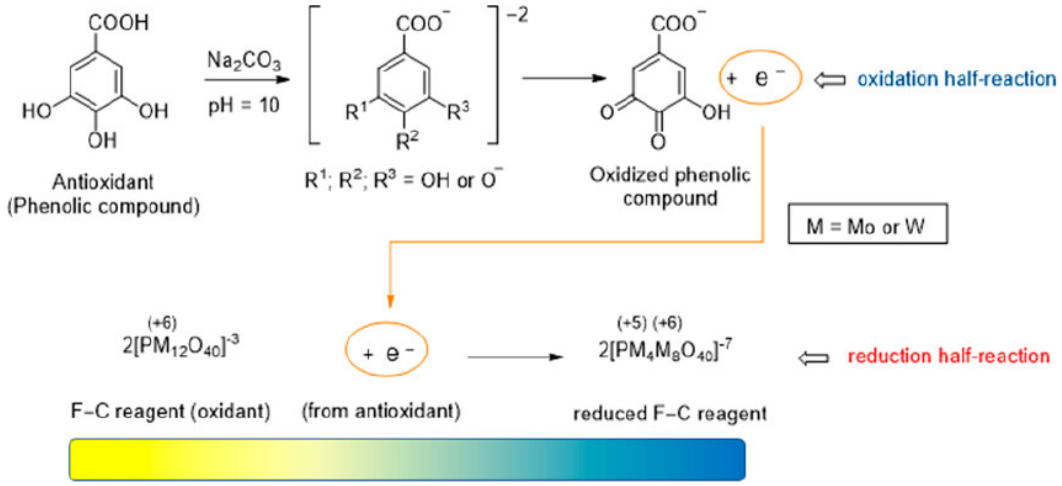

Figure 24: Redox reaction during FC assay (Pèrez et al., 2023).

The concentration of phenols in the sample is related to the absorbance of the sample according to the Lambert-Beer equation:

$$A = \varepsilon\, l\, c \qquad [3]$$

where A is the absorbance obtained by the spectrophotometer, ε is the molar extinction coefficient of the complex, l is the optical path, and c is the concentration. The measurements were conducted using an Agilent Cary 60 UV-Vis spectrophotometer operated at 765 nm.

The detailed laboratory protocol for the Folin-Ciocâlteu assay (Swita et al., 2022) has been reported in Appendix D.

2.6 Bench-scale plant @CNR-STEMS (Plant P1)

Two different experimental plants have been used to carry out the pyrolysis tests during the experimental campaign presented in this Thesis.

The experimental plant located @CNR-STEMS is illustrated in Figure 25. The plant consists of a flat-base spouted-bed reactor (FBSBR) followed by fixed-bed catalytic reactor and by a product condensation and recovery unit. The design of the system has been performed *ad hoc* for this thesis project and has been based on the relevant literature concerning spouted-bed reactors.

The plant is divided into different units, namely:

1) Solid feeding system
2) Pyrolysis reactor
3) Cracking reactor
4) Product condensation and recovery

Each section will be detailed and discussed in the following paragraphs.

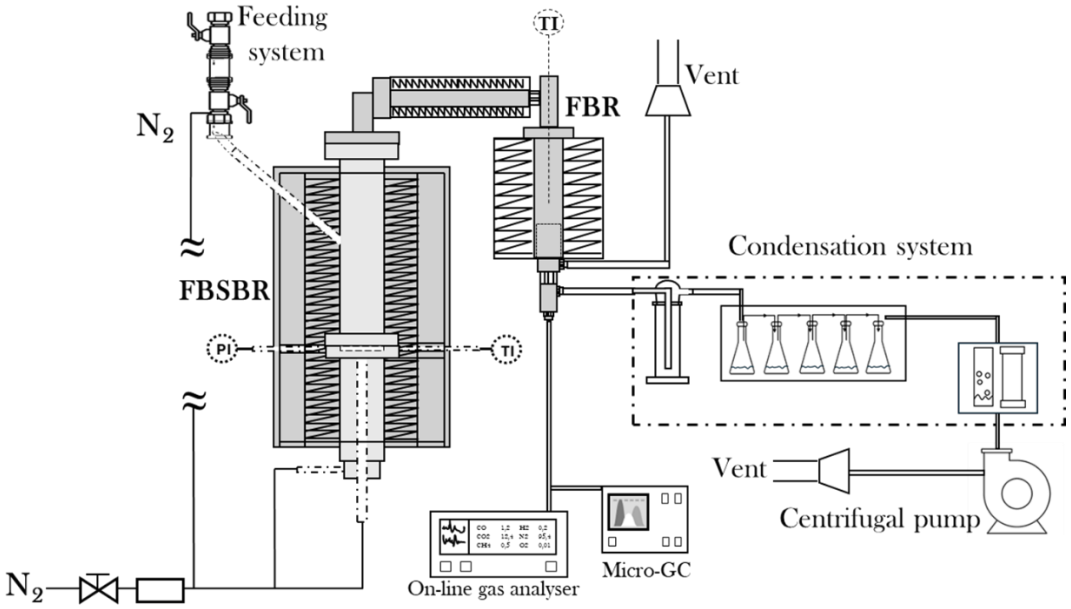

Figure 25: The laboratory-scale pyrolysis apparatus (CNR-STEMS).

2.6.1 Solid and gas feeding systems of plant P1

The solid feeding system employed in the plant is characterized by a double-valve unit which allows to feed the solid fuel (biomass) in semi-continuous regime (Figure 26). The globe valves (2" ID) are connected on each side of a tube. The outlet from the lower valve is connected to the side fuel inlet of the reactor through a flexible plastic tube. The system is completely sealed, and any leakage is prevented. A quick connector is used to supply a small nitrogen (N_2) flowrate into the feeding tube through a Teflon pipe (6 mm ID) to help solid particles motion and to prevent surface overheating and fuel melting, the uprising of pyrolysis vapours from the reaction chamber and condensation of heavy molecules.

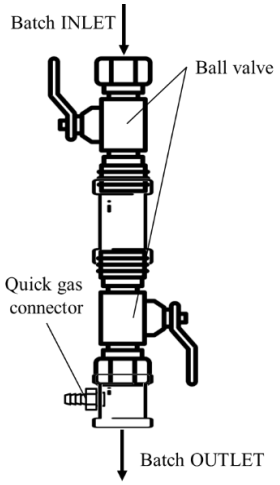

Figure 26: The semi-continuous solid feeding system used at CNR-STEMS.

During an experimental run, a batch of solid fuel (e.g., 1 g) is manually charged into the valve system at fixed time (e.g., 1 g every 30 s). This solution, despite being discontinuous, allows to regulate the feed rate up to 3 g min^{-1}. Higher feed rates might result in the partial or total blockage of the feeding tube. The gas lines are equipped with mass flow controllers (EL-FLOW Select, max. 900 L/h) which have been calibrated before the experimental campaigns.

2.6.2 Reactor units (plant P1)

Pyrolysis reactor

The flat-base spouted-bed reactor is illustrated in Figure 27. The reactor consists of a stainless-steel tube (41 mm ID) working as reaction chamber and a gas preheater, which are joint together by a pair of flanges. The bottom flange is provided with a housing for the fluidising gas distribution plate.

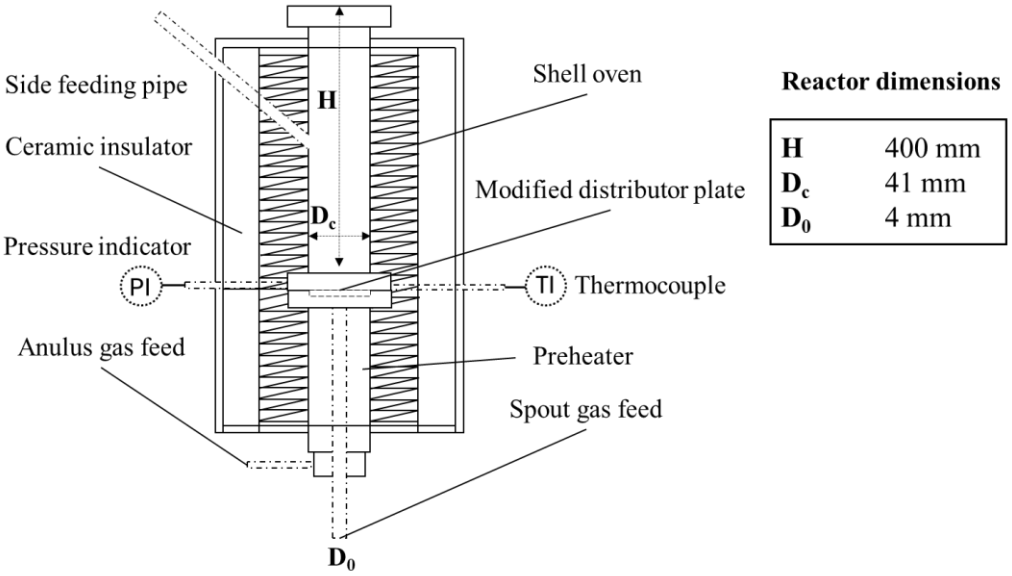

Figure 27: Flat-base spouted-bed reactor (CNR-STEMS).

The plate is made up of stainless steel and is characterized by the presence of a central hole (D_f =5 mm ID) and distributed holes in the annular region (each hole is d_h =0.5 mm ID), as represented in Figure 28.

Thanks to the design of the distribution plate, it is possible to obtain different hydrodynamic regimes within the solid bed. In particular, the reactor can operate under bubbling fluidization (when gas is only fed in the annular region of the distributor), under spouting regime (in the opposite case) and in spout-fluidized conditions[3]. The particle size distribution (PSD) of the solid bed material was chosen to be compatible with hole diameter of the distribution plate to avoid material loss.

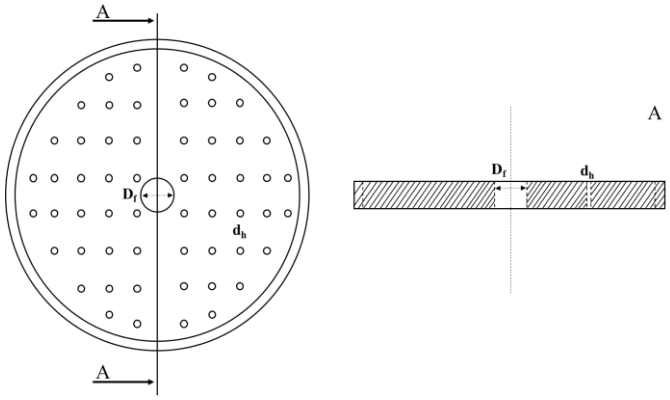

Figure 28: Gas distribution plate for fluidization and spouting regimes.

The reactor has a total height, H, of 400 mm, a column diameter of 41 mm and spout diameter of 4 mm ID. Two stainless steel tubes (one 8 mm ID and one 6 mm ID), staggered by 180°, are welded to the reactor and are used for the measurement and monitoring of the pressure drop across the equipment and of the

[3] Additional information on the stability of the spouted regime during biomass pyrolysis experiments can be found in Appendix F.

temperature within the solid bed material with a type K thermocouple. The reactor is equipped with two radiating half-shells with electrical resistances (Watlow model VS406J24S) which guarantee isothermal operation. In addition, the system is fully insulated with a ceramic fibre mat which in turn is covered with a steel plate. The spouted bed configuration was selected for the primary pyrolysis stage since it has demonstrated its effectiveness in the thermal treatment of biomass and plastic materials via fast pyrolysis. In the first place, spouted-beds promote vigorous mixing and circulation of solids and gases, facilitating heat and mass transfer (Makibar et al., 2011). The high gas-solid contact area allows for efficient heat transfer, leading to improved pyrolysis kinetics and faster conversion of solid fuels to the desired products. As for the fluidized bed reactors, the intense mixing helps maintain a uniform temperature distribution throughout the reactor, reducing the risk of hot spots and improving product quality and consistency.

The unique circulation pattern for the solid material helps the regulation of solid and gas residence time distribution inside the contactor, which are of outstanding importance in reactor design. Finally, spouted-bed reactors can handle irregularly shaped biomass, like wheat, without feeding clogging problems or instability; it is possible to employ particles greater than those normally used for bubbling beds (1 mm), helping reducing biomass pre-treatment costs (Fernandez-Akarregi et al., 2013).

Cracking reactor

The fixed-bed cracking reactor is located downstream and is connected to the spouted-bed reactor's head via a heated transfer line (maintained at 280°C to prevent vapor condensation). The length and the diameter of the reactor are 225 and 42 mm, respectively, as shown in Figure 29. A thin sintered stainless-steel sheet (mesh hole diameter 100 μm) is located at the bottom of the reactor as a support for the catalytic bed.

The mesh also serves as pre-filter, preventing fine solid particles from reaching the condensers. The reactor is kept at a constant temperature thanks to an electric heating jacket (Chromalox ISOPAD GmbH, 50 x 350 mm, 450 W, max 900°C).

At the exit of the fixed-bed rector, the pyrolysis vapour stream is divided into three sub-streams. A small fraction of the stream (ca. 60 L/h) is sent to the online gas analyser for the characterization of the incondensable fraction of the pyrolysis gas. A fraction of the stream (300 L/ h as set by the centrifugal pump) is sent to the condensation system, where the condensable vapours are cooled and collected as liquids (Section 2.6.4). The remaining part of the volatile stream is sent to the vent. At the end of each experimental run, the catalyst bed is recovered from the reactor and saved for further characterization. The sintered steel sheet is then soaked in acetone and cleaned before its reuse.

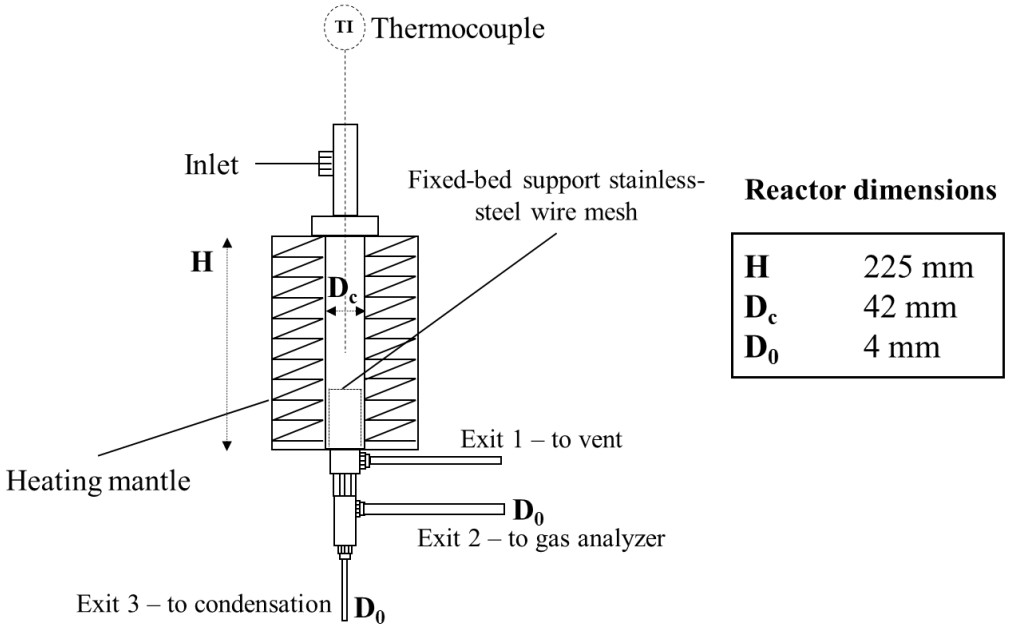

Figure 29: Fixed-bed catalytic cracking reactor

2.6.4 Product condensation and recovery

The condensing system consists of the following elements: an ambient temperature flask condenser (Pyrex, 500 mL, T≈ 20°C), a set of 5 flask condensers (Pyrex, 250 mL) kept at ≈0°C thanks to a chiller (Megasystem Cooling System, 230 V), a second ambient temperature condenser and a cotton filter to prevent liquid droplets reaching the centrifugal pump. The flow of pyrolysis vapours passing through the condensation system is set to 5 L/min by a centrifugal pump.

Before the remaining vapour/gas stream passes through the pump, it is necessary to remove any residual condensable material, which may affect the good functioning of the pump's rotor. For this reason, the system is equipped with a pump protection module consisting of a water bubbler followed by a silica gel dehumidifying bed. At the beginning and the end of each experiment, the condensers are weighed, and oil samples are retrieved for further analysis and characterization.

2.6.5 Product analysis and characterization

Analysis of permanent gases

The analysis of permanent gases (i.e., O_2, CO, CO_2, H_2, CH_4) has been conducted online using a portable *MRU VarioLuxx Syngas analyser*, with a measurement frequency of 1 s. The analyser is able to measure the volume concentration of the above-mentioned species by using dedicated sensors:

1. Long-life electrochemical sensor for O_2 (range 0-25% vol.)
2. TCD detector for H_2 (range 0-100% vol.)
3. IR sensors for CO, CO_2 and CH_4 (range 0-100% vol.)

The system is also equipped with an HPI industrial sampling unit with a heated handle (with glass wool prefilter), sampling line with hose heated to 120°C and interchangeable steel tip with K-thermocouple to assess the temperature of the line gas. The line is heated to 160°C during sampling operation, with a sampling flowrate of 60 L/h and a Peltier at 5°C. The N_2 concentration is calculated by difference (balance gas). As an example, Figure 30 shows permanent gas concentration profiles during ex-situ catalytic pyrolysis of olive stone using a commercial HZSM-5 catalyst (T_1=500°C, T_2=500°C, τ=20 g_{cat} min/g $_{OS}$). It can be appreciated that the process is continuous and stable.

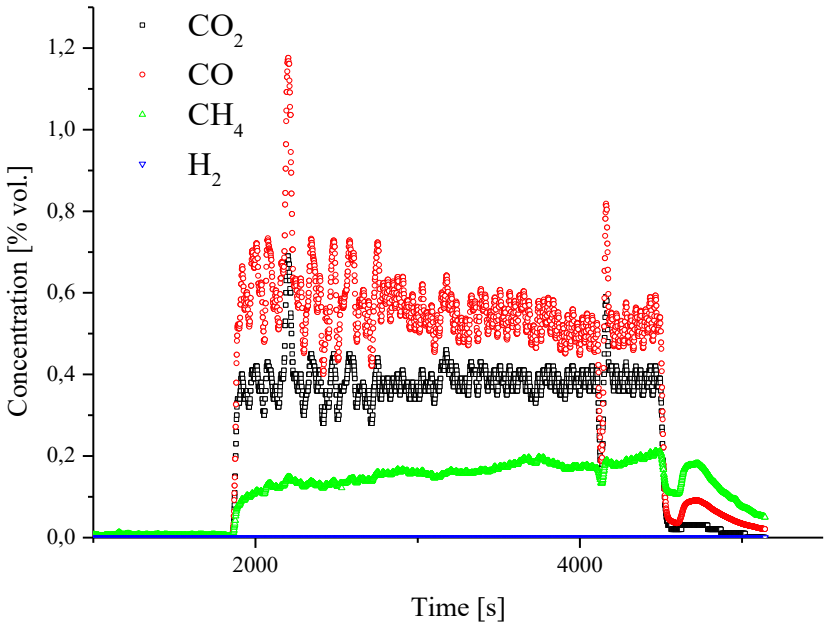

Figure 30: Permanent gas concentration profile during typical pyrolysis test (T_1=500°C, T_2=500°C, τ=20 g_{cat} min/g $_{OS}$)

Given the typical composition of gases produced during pyrolysis of biomass, different light hydrocarbons can be found with concentrations ranging between 0-3000 ppm. For this reason, the data obtained from the online gas analyser were supplemented by the information provided by an *Agilent 3000A* micro-GC. Also, since H_2 concentration during steady-state pyrolysis tests often ranged between 0.01 and 0.2 %, it was measured using micro-gas chromatography because its concentration was outside of the detection range on the online analyser.

The micro-GC is equipped with four detectors and four columns in total, arranged in four independent analytical channels as follows:

- Channel A: equipped with 1 OV1 column (14 m x 0.15 mm x 2 µm) and a TCD (Thermal Conductivity Detector), is optimized to detect C_1-C_7 hydrocarbons.
- Channel B: equipped with an alumina-based column (14 m x 0.15 mm x 2 µm) and a TCD (Thermal Conductivity Detector), is optimized for the detection light hydrocarbons.

- Channel C is equipped with a PLOTU column followed by (8 m x 0.32 mm x 10 µm) a TCD. The channel is configured to detect CO_2, and light alkanes and olefins.
- Channel D is equipped with a MS5Å (10 m x 0.32 mm x 30 µm) column followed by a TCD. The channel is configured to detect CO, H_2, CH_4 and N_2.

Table 9 reports the operating conditions for the analysis method of the Agilent 3000A Micro GC for the four channels, while the complete list of the response factors for each compound detected by the equipment is reported in Table 10:

Table 9: Operating conditions of the analytic channels of Micro-GC

Parameter	Ch-A	Ch-B	Ch-C	Ch-D
Column temperature, °C	65	90	80	100
Injection temperature, °C	70	70	70	70
Pressure, psi	25	30	25	25
Injection time, ms	250	250	250	20
Analysis time, min	3	3	3	3
Backflush time, s	-	30	-	13

Table 10: Compounds detected by micro-GC and relative analytical channel

Compound	Ch-A	Ch-B	Ch-C	Ch-D
Isobutene	X	X	-	-
Isobutane	X	X	-	-
Butene	X	X	-	-
Butane	X	X	-	-
3-methyl-butene	X	-	-	-
Isopentane	X	-	-	-
Pentene	X	-	-	-
Isohexane	X	-	-	-
Hexene	X	-	-	-
Hexane	X	-	-	-
Heptane	X	-	-	-
Propane	-	X	X	-
Propylene	-	X	-	-
Acetylene	-	X	X	-
CO_2	-	-	X	-
Ethylene	-	-	X	-

Ethane	-	-	X	-
H_2	-	-	-	X
O_2	-	-	-	X
N_2	-	-	-	X
CH_4	-	-	-	X
CO	-	-	-	X

Bio-oil characterization

The characterization of bio-oil samples has been carried out offline by means of Gas-Chromatography / Mass Spectrometry technique (GC/MS) using an Agilent 7890A Gas Chromatograph equipped with a 5975C-VLMSD Mass Spectrometer. The system is equipped with an Agilent J&W DB-624 column (mid-polar, 6% cyanopropyl/phenyl, 94% polydimethylsiloxane, 30 m x 320 µm x 1.8 µm), designed for the detection of organic volatile pollutants. The sample has been prepared by mixing equal amounts (1 mL) of acetone-diluted oil samples from the first condenser (ambient temperature, dense, carbon-rich liquid) and from the set of flask condensers in the chiller (at 0°C, more aqueous fraction). Then, approximately 0.5 mL of the resulting solution is diluted in acetone to get 1 mL sample. This was to make sure that all compounds were effectively detected in the sample.

During injection, 1 µL of sample diluted in acetone is injected into the column through a SS inlet operating at 230°C and 3.7 psi, with a total He flow of 13.8 mL/min and using a split ratio of 5:1 (split flow of 9 mL/min).

The GC method consists of holding the sample at 45°C for 4 min, then heating the oven to 235°C with a heating rate of 3°C/min and holding at isothermal temperature for 13 minutes. The maximum temperature for this column is 260°C. The gas flow in the column is set to 1.8 mL/min, with a mean velocity of 48.7 cm/s.

The mass spectrometer is equipped with an EI source operated at 230°C with a fixed electron energy of 70.3 eV. The quadrupole temperature is set to 150°C, and the scanning range is between 35 and 350 m/z.

Chromatographic peaks were identified using the NIST 11 mass spectral data library, based on their retention times. A semi-quantitative method was employed to estimate the relative abundance of each bio-oil component. This was achieved by internally normalizing the areas of all resolved (detected) peaks to calculate the percentage of each compound as commonly done in the literature (Masoum et al., 2013; Lazzari et al., 2016; Santos et al., 2015, Dyer et al., 2021). Hundreds of compounds found in bio-oil samples have been grouped into the following families: aldehydes, furans, guaiacols/syringols, ketones, organic acids, alkyl-phenols, sugars, aromatics (non-oxygenated and oxygenated), PAH (polycyclic aromatic hydrocarbons) and others (alcohols, ethers…).

An example of chromatogram from olive stone non-catalytic fast pyrolysis is illustrated in Figure 31. Based on the retention time (RT) of compounds, it is possible to distinguish a light fraction (RT<30 min), a middle fraction (30<RT<50 min) and a heavy fraction (RT>50 min). Then, a similar chromatogram in the case of catalytic fast pyrolysis (τ= 20 $g_{catalyst}$ min /g_{OS}) is reported in Figure 32.

Water concentration in bio-oil samples was measured by means of an Omnis Karl Fischer volumetric titrator (Metrohm, USA), while elemental composition in terms of C, H and N content was assessed by using a LECO CHN 828 as discussed in Section 2.1. Each measurement was done in triplicates to ensure reproducibility. Given the high viscosity and the limited amount of the dense-carbon rich oil obtained in the ambient-temperature condensation stage, raw bio-oil samples only included the aqueous fraction of bio-oil obtained in the 0°C condensation step. While this does not represent the entire bio-oil, it provides a consistent basis for comparing the elemental composition of the water-soluble fraction across different experiments.

A measure of the acidity of bio-oil samples produced in different conditions has been realized by measuring the pH in a pocket pH-meter (LAQUAtwin pH-33, VWR International Srl, Avantor) calibrated using buffer solutions at pH=1.68, 4.01, 7.00, 10.01 and 12.46, respectively.

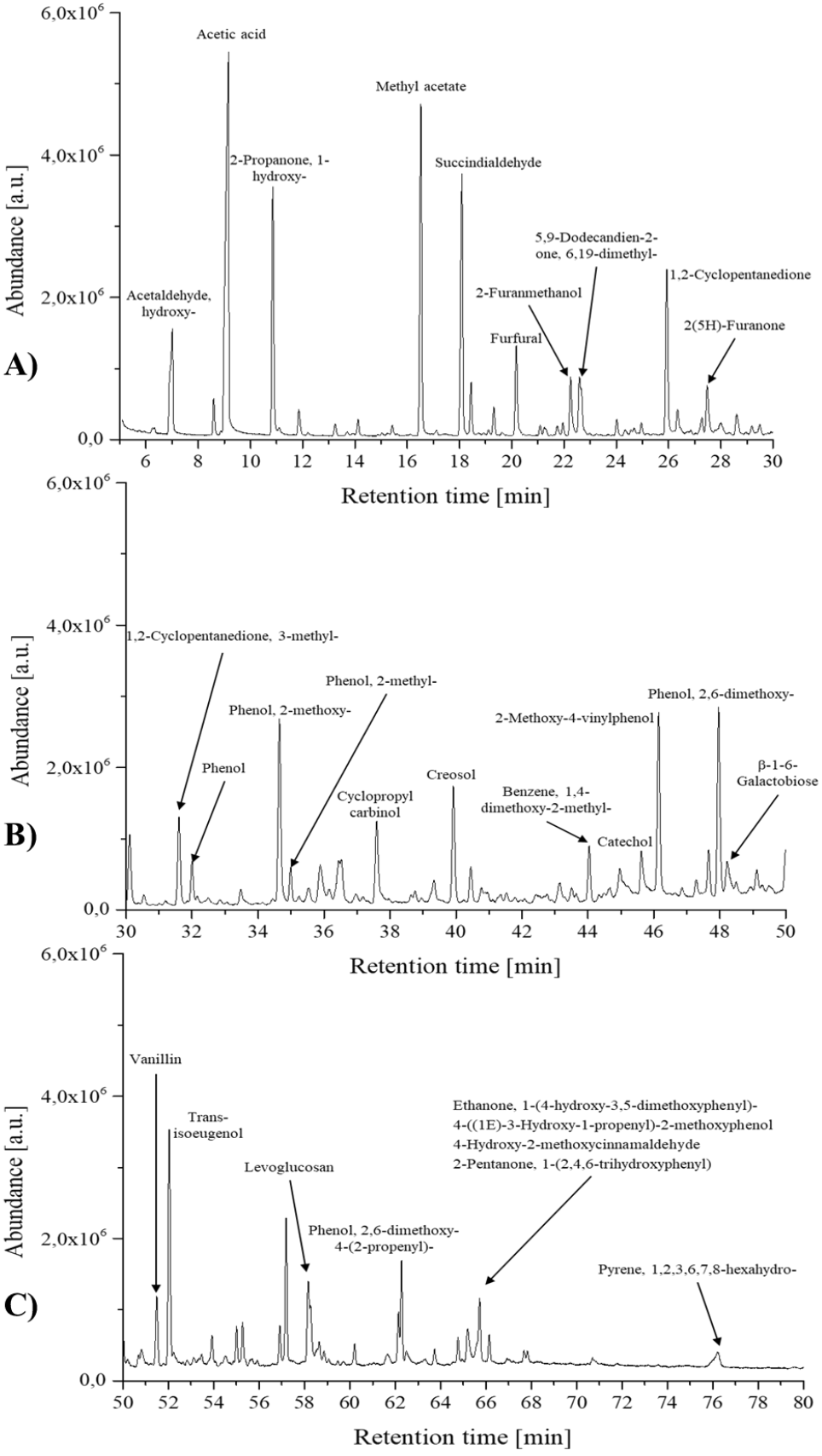

Figure 31: Chromatograms of pyrolysis oil in non-catalytic conditions. Light fraction (A), middle fraction (B) and heavy fraction (C). Temperatures in first and second reactor were both 500°C.

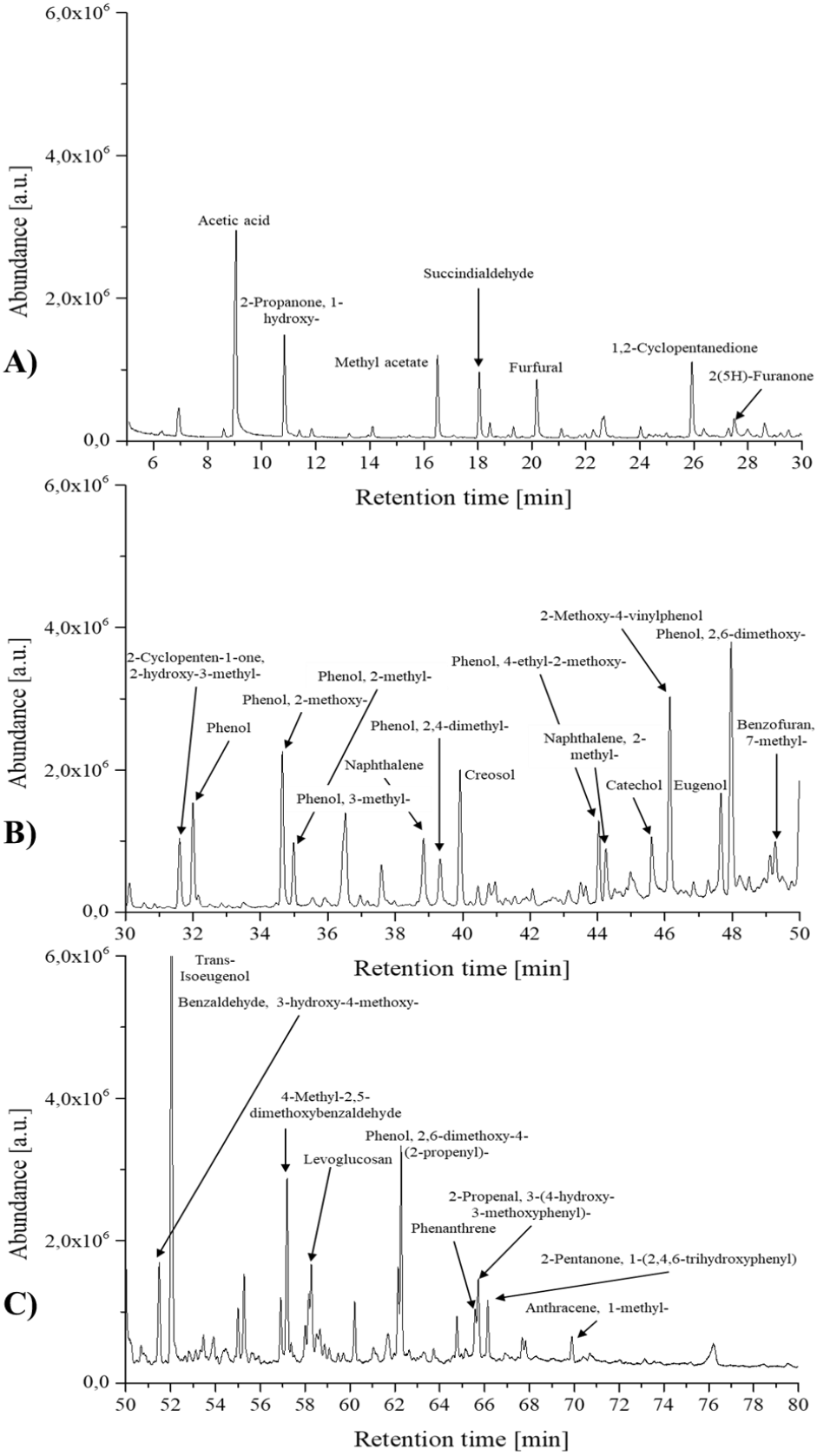

Figure 32: Chromatogram from catalytic fast pyrolysis of olive stone using commercial HZSM-5. Light fraction (A), middle fraction (B) and heavy fraction (C). Conditions were $T_{pyrolysis}$=$T_{cracking}$=500°C and τ= 20 $g_{catalyst}$ min /g_{OS}.

Analysis of the solid fraction

The solid fraction of the product consisted of the char produced during biomass devolatilization in the pyrolysis reactor (which is retained in the bed mixed with sand) and the fine carbonaceous residue deposited onto the catalyst's surface during catalytic cracking (coke). The char produced in the first reactor was separated from the sand bed and was characterized by elemental analysis (CHN), ICP-MS and porosimetry (N_2-adsorption/desorption).

Coke deposition on the catalyst's surface has been studied by temperature programmed oxidation (TPO) using a *Micromeritics AutoChem III Chemisorption Analyzer* with the same temperature program described in Section 2.3.3.

For the further characterization of spent catalyst samples, acidity deterioration was studied by NH_3-TPD, and physical properties deterioration was quantified by N_2 adsorption/desorption cycles.

2.6.6 Quantitative assessment of pyrolysis yields

After each pyrolysis test, the product yields were calculated on an as-fed feedstock basis using the mass of the recovered solid, liquid, and gaseous fractions. The char yield (η_{char}%) was determined by weighing the solid residue remaining in the first reactor after reaction and calculated as:

$$\eta_{char}\,[\%] = \frac{\dot{m}_{char}\,\left[\frac{g}{h}\right]}{\dot{m}_{biomass}\left[\frac{g}{h}\right]}100\% \qquad [4]$$

It was confirmed that the contribution of elutriated char was negligible relative to the amount of char recovered from the pyrolysis reactor, also thanks to the unique hydrodynamics of the spouted-bed reactor. Furthermore, because no char fines were detected in the condensation system and in the pump protection bubbler, it was assumed that all char remained within the primary reactor.

The coke content on the catalyst's surface has been measured by means of thermogravimetric analysis (TGA). A spent catalyst sample was heated at controlled temperature following the steps:

1. Heating to 200°C in nitrogen at 10°C/min to remove adsorbed species and moisture from the sample.
2. Cooling to 100°C at 10°C/min to stabilize the mass of the sample.
3. Heating to 800°C in air at 5 °C/min to burn carbon from the sample.

The coke content was calculated from the mass loss of the sample before and after combustion. Given the low amount of carbon deposited on coarse sand in the catalytic bed (always less than 1%), it was not considered in the calculation of coke yield except for the case of pure thermal cracking, where the bed was only made of coarse sand. Process coke yield (η_{coke}) was calculated by dividing the mass of coke produced in the process by the mass of biomass fed to the reactor.

$$Coke\ content\ [\%/g_{cat}] = \frac{m_{sample}(800°C) - m_{sample}(200°C)}{m_{sample,0}} \quad [5]$$

$$\eta_{coke}\ [\%] = \frac{Coke\ content\ \left[\frac{\%}{g_{cat}}\right] m_{cat}}{m_{biomass}} \quad [6]$$

Gas yield has been calculated from the volume concentrations obtained both from the portable analyser and from the micro-GC. First, the mean concentration of each compound was measured. CO, CO_2 and CH_4 concentrations were taken from the portable analyser, while H_2 and light hydrocarbons were taken from the micro-GC. The N_2 concentration was calculated by difference.

The total flowrate exiting from the second reactor was calculated by a mass balance on nitrogen, which does not undergo chemical reaction during the process:

$$\rho_{IN} Q_{IN} y_{N_2}^{IN} = \rho_{OUT} Q_{OUT} y_{N_2}^{OUT} \quad [7]$$

Where ρ_{IN} and ρ_{OUT} are the densities of the gas mixture [kg/m^3] before and after the pyrolysis + cracking system, Q_{IN} and Q_{OUT} are the relative volume flowrates [NL/h] and $y_{N_2}^{IN}$and $y_{N_2}^{OUT}$represent nitrogen mass-fraction before and after the process.

The density changes of the gas mixture before and after the reactor series is negligible because all the calculation is performed at STP (0°C, 1 atm) and the variation in gas composition resulting from pyrolysis is overshadowed by the high degree of nitrogen dilution.

Therefore,

$$Q_{OUT} = \frac{Q_{IN} y_{N_2}^{IN}}{y_{N_2}^{OUT}} > Q_{IN}\ as\ \frac{y_{N_2}^{IN}}{y_{N_2}^{OUT}} < 1 \quad [8]$$

From the volume concentration of each compound in the gas phase, it is possible to calculate the volume flowrate of component *i* as:

$$\dot{v}_i \left[\frac{NL}{h}\right] = Q_{OUT} y_i^{OUT} \quad [9]$$

The mass flowrate and the total mass of compound *i* produced in the test is then estimated using the ideal gas equation and test duration. Finally, gas yield (η_{gas}) is calculated as the ratio of total gas production rate [g/min] and the biomass feed rate:

$$\dot{m}_i \left[\frac{g}{min}\right] = \frac{P\ M_w \dot{v}_i}{RT}\ @STP \quad [10]$$

$$m_i[g] = \dot{m}_i\ \Delta t \quad [11]$$

$$\eta_{gas} = \frac{\sum_{i=1}^{N} \dot{m}_i}{\dot{m}_{biomass}} \quad [12]$$

Experimental liquid yield was initially obtained by collecting and weighing the condensates (organic phase + water) and normalizing the liquid condensate to the total flow coming from the catalytic reactor, as follows:

$$\eta_{liquid}[\%] = \frac{\dot{m}_{liquid}\left[\frac{g}{h}\right]}{\dot{m}_{biomass}\left[\frac{g}{h}\right]} \frac{Q_{OUT}\left[\frac{NL}{h}\right]}{Q_{Sampled}\left[\frac{NL}{h}\right]} \quad [13]$$

Finally, distinction between water and organics yield is obtained by including data from Karl Fischer titration.

Despite the accuracy in measurements, the total mass balance closure during the tests was in the range 78-86%. This deviation is a well-known limitation in laboratory-scale pyrolysis systems employing conventional condensers and is ascribed to the loss of light organic volatile compound.

We had the possibility to validate this assumption at the end of the experimental campaign, by installing, in series with the condensation system, a condenser cooled with liquid nitrogen (KFL 29-GL-A, 250 mL, UNIFO) operating at -196°C. The calculation of the liquid yield during this test showed an increase, confirming the presence of light compounds that normally escape condensation at 0°C. The liquid recovered in the liquid nitrogen-cooled condenser contained, in addition to the typical phenolic compounds derived from lignin, light aldehydes and ketones, BTX compounds, and furans. To provide a better estimate, the yield of organics has been alternatively calculated by difference as:

$$\eta_{organics}[\%] = 100 - \eta_{gas}\,[\%] - \eta_{coke}\,[\%] - \eta_{char}\,[\%] - \eta_{water}\,[\%] \quad [14]$$

Finally, water vapour was not included in the results about the gas-phase compounds, assuming it is all condensed.

The optimization of the condensation stage therefore emerges as a key aspect of the experimental work. Although this optimization falls outside the primary scope of the present thesis, several parallel studies and the implementation of different strategies to enhance oil recovery were carried out during preliminary experimental campaigns. These efforts led to the development of a more efficient condensation system, which will be adopted in future experiments. The system consists of a first ambient temperature condenser followed by a 0°C stage and a battery of liquid nitrogen-cooled condensers.

2.7 Pilot plant @UPV/EHU (Plant P2)

The scheme of the laboratory-scale plant used for plastic pyrolysis experiments is illustrated in Figure 33. The plant consists, also in this case, of two independent reactors: a conical spouted-bed reactor (CSBR) in which the pyrolysis process takes place, and a fixed bed reactor (FBR) for the subsequent catalytic cracking of pyrolysis volatiles.

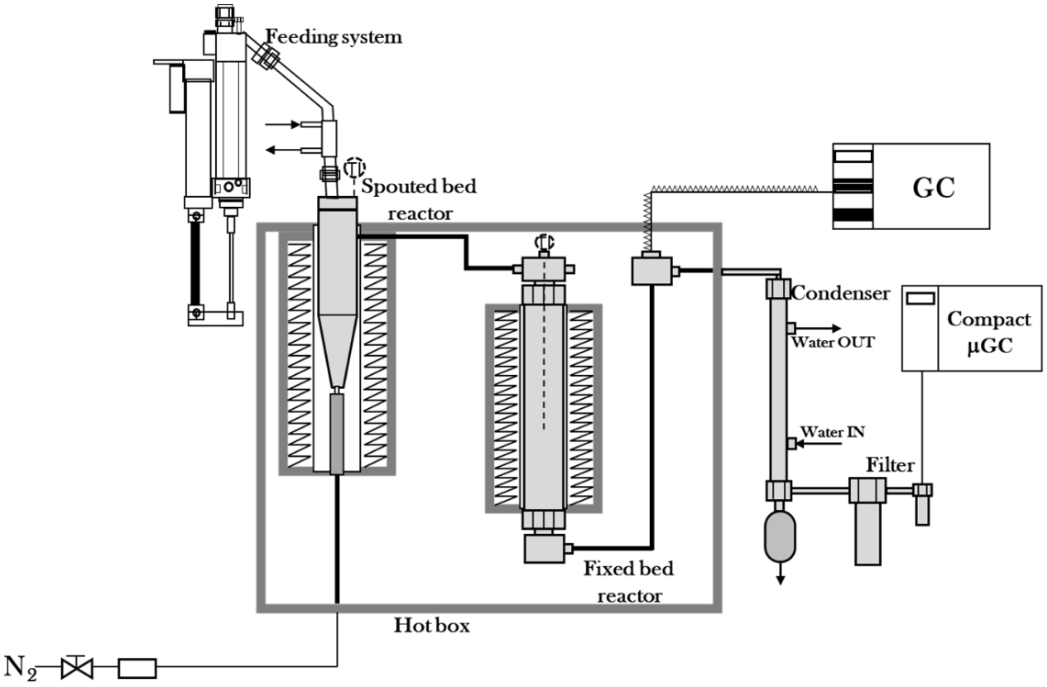

Figure 33: Laboratory-scale plant for plastic pyrolysis and catalytic cracking.

The construction and the operation of the plant were based on the experience matured by the research group on the technology of the conical spouted-bed reactor (CSBR), which was used in the context of hydrodynamic studies (e.g., Olazar et al., 1992), thermochemical conversion of biomass materials (Amutio et al., 2012; Alvarez et al., 2014;), pyrolysis of waste tyres (e.g., Lopez et al., 2010; Lopez et al., 2017a), thermochemical conversion of plastics (e.g., Elordi et al., 2009; Artetxe et al., 2012; Orozco et al., 2022) and innovative two-stage processes, e.g., pyrolysis followed by steam reforming of volatiles (e.g., Garcia et al., 2024). In this work, the system has been used for the pyrolysis of plastic materials followed by catalytic cracking of pyrolysis volatiles.

The plant can be conveniently divided into different components:

1. Solid feeding system
2. Gas feeding system
3. Reactor units
4. Product separation and recovery

In the following sections, a detailed description of the different units is given.

2.7.1 The solid feeding system (plant P2)

The solid feeding system has been developed to ensure a smooth continuous feeding of biomass or plastic materials in the reactor (Figure 34). It consists of a cylindrical vessel of 30 mm ID equipped with vertical shaft with a piston (60 cm long stroke). During normal operation, the piston slowly goes upwards pulling the biomass to the upper part of the equipment, where a vibration module is installed to provide the necessary motion for the solid particles to smoothly fall into the side feeding tube (3/4"). The vibrator can be controlled with a switch located on the control unit.

The feeding tube, which is connected vertically to the head of the pyrolysis reactor, is also refrigerated thanks to a cooling jacket with tap water. This ensures that biomass and plastic particles are not pyrolyzed before entering the reactor, thus obstructing the feeding system. Moreover, a small flowrate of nitrogen (N_2) is supplied through a 1/8" ID tube in order to avoid the rising of pyrolysis vapours from the reactor and to prevent the condensation of volatiles within the feeding tube. In addition, nitrogen also facilitates solid motion in the tube.

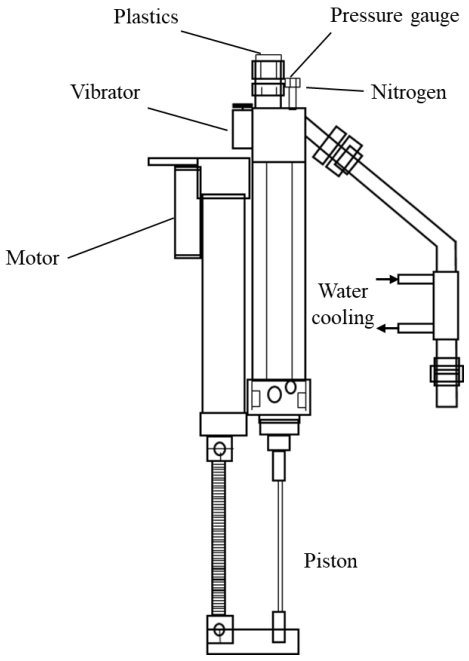

Figure 34: Schematic of the solid feeding system used in the plant. Adapted from Santamaria Moreno (2019).

The speed of the piston must be carefully regulated to keep a specific mass flowrate of solid fuel. This is ensured by a controller *Toho TTM-204*, which was programmed to modulate the piston speed between 0 and 80 mm/min, corresponding to a solid feed between 0 and 5 g/min. The feeding system should be calibrated before an experimental campaign to check that the fuel rate is correct and is kept stable over time. The pressure within the system is measured by a differential pressure tape located at the top of the feeding system.

2.7.2 The gas feeding system (plant P2)

The gases are supplied to the pyrolysis reactor thanks to a feeding system located at the bottom of the reactor itself. Although only nitrogen has been utilized in the present work as fluidization agent, the gas feeding system consists of three different lines, for nitrogen (N_2), air and hydrogen (H_2), respectively (only nitrogen shown in Figure 33). The lines are equipped with manual valves (*HOKE*), mass flow controllers (*Bronkhorst High-Tech*) and non-return valves (*HOKE*) to ensure a safe supply of gases to the system, avoiding any gas uprising into the lines. The mass flow controllers (inlet and outlet pressure of 4 and 1 bar) can guarantee a maximum flowrate of 20 L/min for nitrogen and air, and of 5 L/min for hydrogen.

2.7.3 Reactor units (plant P2)

The reactor unit includes a first conical spouted-bed reactor (CSBR) for the pyrolysis step and a fixed bed reactor (FBR) in line for the catalytic cracking of the volatiles produced. Both the reactors are located into a stainless-steel forced convection oven (80 x 80 x 80 cm). The oven is heated thanks to two 1500 W resistances and to two fans, which make possible the circulation of heat in the box, making the temperature homogeneous and constant during the operation. The oven is kept at a fixed temperature of 300°C to prevent the condensation of volatiles after the cracking reactor. In this way, it is possible to fully characterize the product stream (volatile molecules + incondensable gases) by chromatographic methods.

Pyrolysis reactor.
The core of the process is represented by the conical spouted-bed reactor (CSBR), whose schematic representation together with its the main dimensions is given in Figure 35. The reactor is characterized by a combination of a conical section (at the bottom) and a cylindrical section. The total height of the reactor, H_T, is 297 mm; the height of the conical section is 77 mm, and its tilt angle is γ=30°. The diameter of the cylindrical section of the reactor, D_c, is 54.8 mm, the diameter of the base of the conical section, D_i, is 12.5 mm, and the gas nozzle diameter, D_0, is 4.9 mm.

The geometry of the contactor (namely the height of the conical section, the diameters) has been selected as a result of previous extensive research in the context of spouted-bed hydrodynamic regimes conducted by the research group. The reactor differs from that developed @STEMS for its conical shape. The given dimensions can provide a stable spouting regime in the operating conditions of interest.

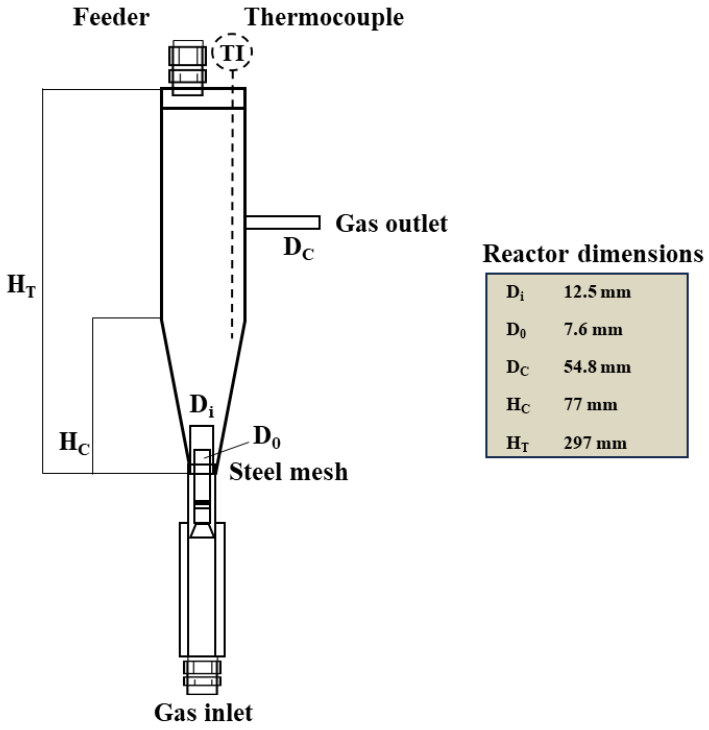

Figure 35: Conical spouted-bed reactor. Adapted from Artetxe, (2013).

At the top of the reactor, there is the inlet for the solid feeding system and a second inlet (1/8") where a thermocouple (type K) is installed to monitor the temperature within the bed material, in the conical section. The gas coming from the feeding system passes through a stainless-steel preheater (31 cm high, 2.7 cm ID) where efficient heat transfer to the fresh gas is ensure by a vertical tube bank.
The reactor is located inside a ceramic shell oven (52 cm long, 1250 W of power) covered with a steel sheet, which provides the necessary heat flow to keep the desired reaction temperature in the pyrolysis stage and to preheat the fresh fluidization gas.

Cracking reactor.

The cracking reactor is connected in line to the CSBR and is used for the catalytic cracking of pyrolysis vapours. A schematic representation of the fixed bed cracking reactor is shown in Figure 36. The reactor consists of a stainless-steel tube 440 mm long with an ID of 38.1 mm. The reactor is equipped with a thermocouple to monitor and control the temperature within the solid catalyst bed. The reactor heating is ensured by a shell oven similar to the one enclosing the CSBR (305 mm long, 550 W of power).

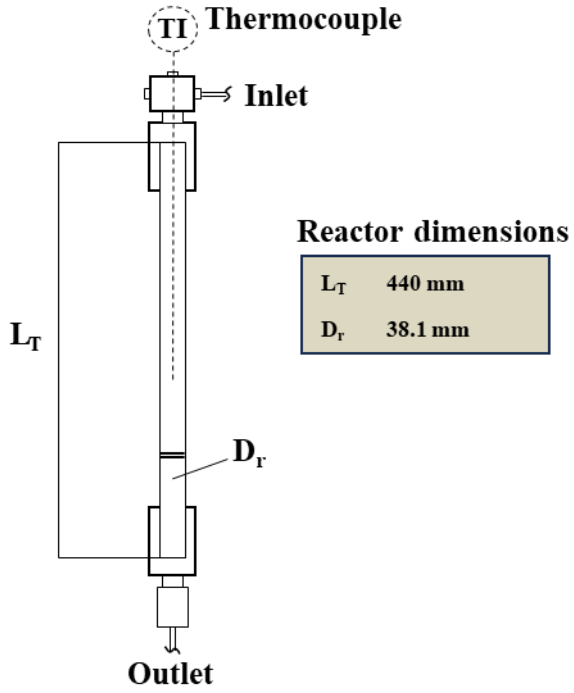

Figure 36: The fixed bed reactor used for catalytic cracking. Adapted from Artetxe, (2013).

Condensation section.

The volatile stream is then separated thanks to a T-shaped connector. A fraction is sent to the GC for analysis (through a thermal line), while the rest is sent to the condensation system, consisting of a tap water condenser and a coalescence filter. The condenser is made up of two coaxial pipes. The volatile stream coming from the reactor enters the inner pipe while tap water passes through the external jacket, ensuring the condensation of liquid in a 150 mL tank. The coalescence filter (maximum design pressure 10 bar) removes the remaining microdroplets from the gas stream.

2.7.4 Product characterization and analysis

The analysis of the condensable (volatiles) and incondensable gases has been performed in-line under steady-state conditions. A fraction of the volatile stream coming from the T-shaped connector after the cracking reactor is sent to the gas chromatograph through a heated line (280°C to prevent condensation). The permanent gases are analysed using micro-gas chromatography. Gas samples have been taken after the complete condensation and filtration of the product stream, and the measurement has been repeated several times to ensure reproducibility.

Analysis of pyrolysis volatiles

The qualitative and quantitative analyses of the volatile stream coming from the cracking reactor were performed using an *Agilent 8890 Gas Chromatograph*. The system uses a HP-PONA column (50 m x 0.2 mm, film thickness 0.5 μm, made in dimethylpolysiloxane), which can – among others -separate and identify paraffins, olefins, naphthene, and aromatics. This type of column is especially

useful in the petrochemical industry for analysing the composition of fuels, lubricants, and other hydrocarbon mixtures. The *Agilent 8890 Gas Chromatograph* is equipped with a FID detector, operated at 350°C. According to Harmanos (1997), FID detectors provide a proportional relationship between peak area and mass for hydrocarbons, for which the response factor has been set to 1.

The sampling valve used by the chromatograph to load the sample into the column is operated at 295°C, and it is schematized in Figure 37. When in the LOAD position, the sample is introduced in the loop and occupies the loop volume. The carrier gas flows normally in the column and to the detector. As it is switched to the INJECT position, the carrier gas starts flowing in the loop, carrying to the column the sample volume.

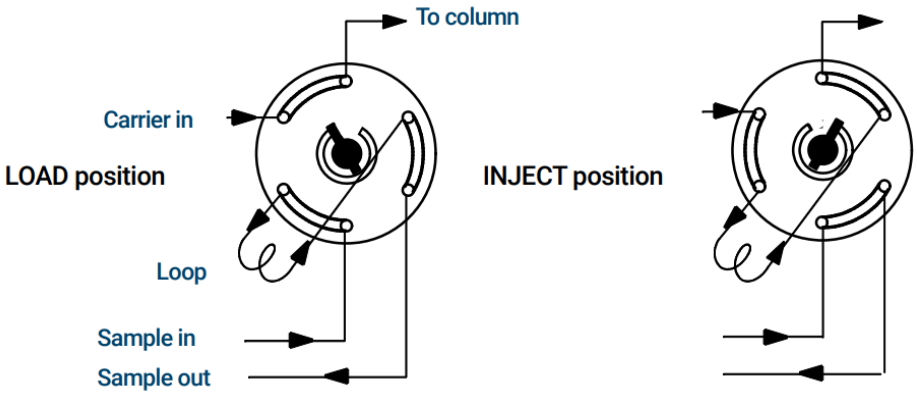

Figure 37: Sampling valve used in the gas chromatograph (Agilent 8890/8850 GC Operation Manual)

The injector (operated at 350°C) is a *split/splitless* (S/SL) type, which means that only a small fraction of the sample is finally injected into the column, while the rest is sent to the vent. The temperature program used in the chromatographic oven includes 2 min at 40°C, followed by a ramp of 15 °C/min up to 320°C and a 3 min isotherm at 320°C, as shown in Figure 38:

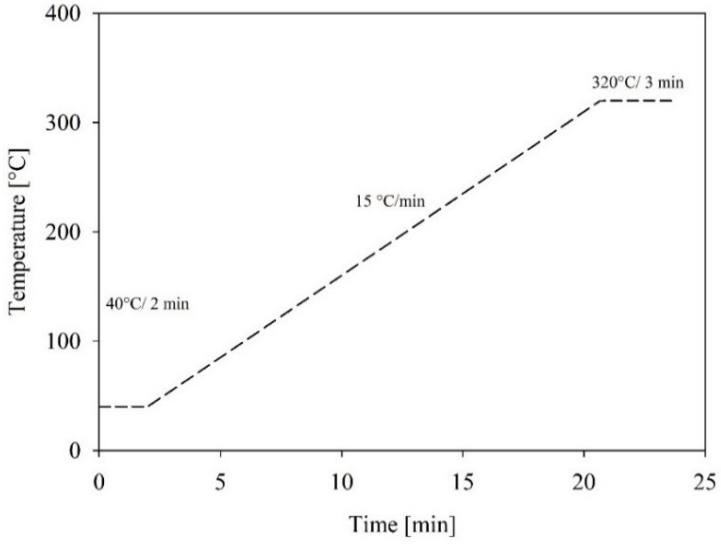

Figure 38: Temperature program for the GC analysis.

Table 11: Standard retention time of selected compounds.

Compound	Standard RT [min]
Methane	2.480
Ethane + ethylene	2.502
Propane + propylene	2.538
Butane	2.709
Butene	2.774
C_5	3.036
C_6	4.224
Benzene	4.896
C_7	5.544
Toluene	6.379
C_9	6.970
o-Xylene	7.707
p-Xylene	7.830
m-Xylene	8.131
C_{10}	8.312
C_{11}	9.536
C_{12}	10.657
C_{14}	11.694
C_{15}	18.719
C_{16}	20.224
C_{17}	21.545

In Figures 39-A, 39-B, and 39-C, the chromatograms illustrate the product distribution obtained from the catalytic cracking of volatiles derived from HDPE pyrolysis. The reaction was conducted at 500°C using a 1% Ni/(HZSM-5 + Al_2O_3 + bentonite) catalyst with a space-time of 10 g_{cat} min/g_{HDPE} after 30 minutes of operation.

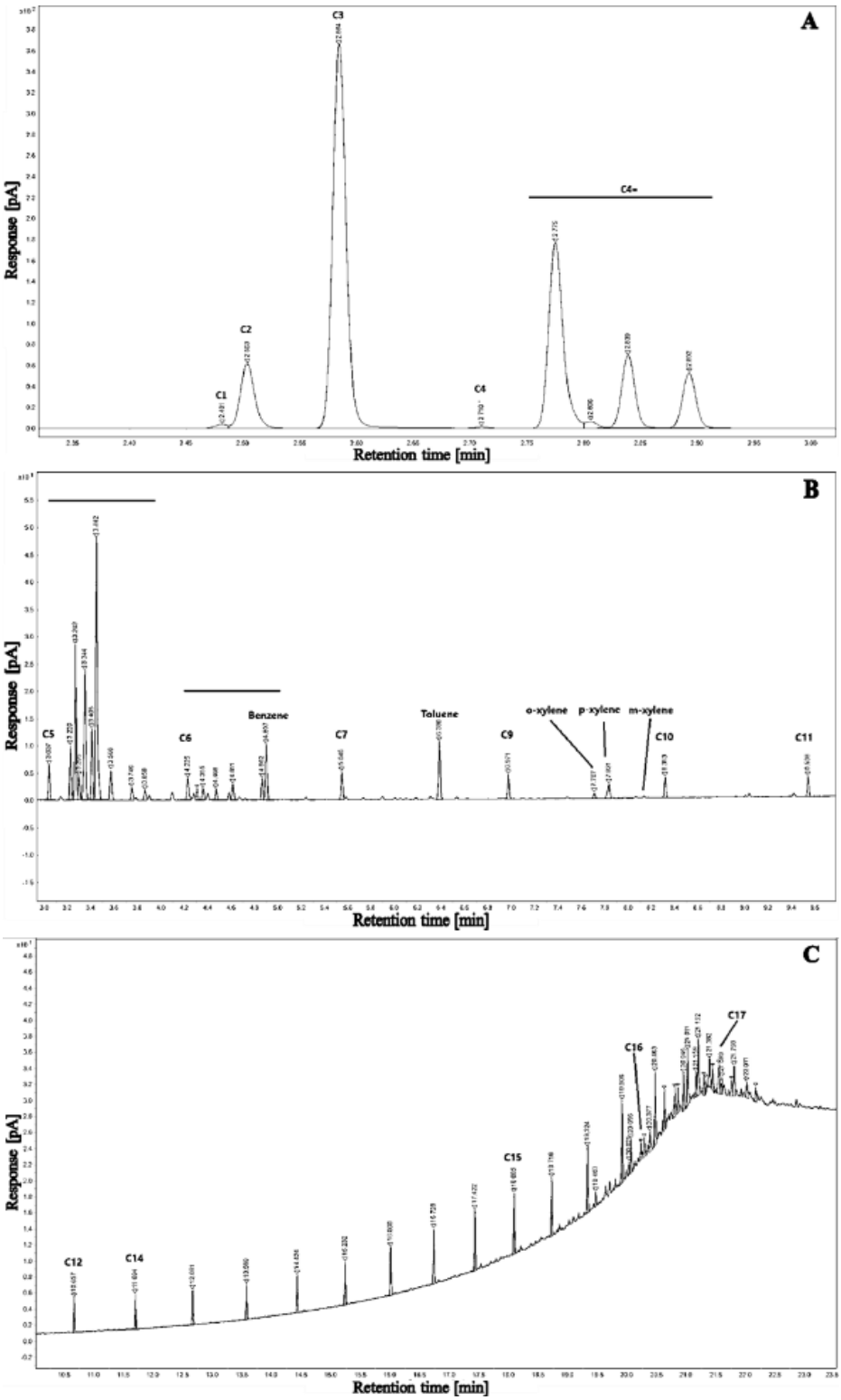

Figure 39: Chromatogram of cracking products from HDPE pyrolysis on 1%Ni/HZSM-5 at 500°C and τ=10 g_{cat} min/g_{HDPE}, after 30 min of operation. Light fraction C_1-C_4 (A), gasoline range hydrocarbons C_5-C_{11} (B) and heavy fraction C_{12+} (C).

Light hydrocarbons (fraction C_1-C_4) are observed to have retention times ranging from 2 to 3 minutes. The elution order begins with methane, followed by a combined peak for ethane and ethylene, and another combined peak for propane and propylene. C_4 hydrocarbons follow. This overlap necessitates the use of complementary micro-gas chromatography data to accurately quantify each

individual species, as the co-elution prevents precise peak separation in the primary chromatogram. The gasoline fraction (C_5-C_{11}) exits the column between 3 and 10 minutes; finally heavier hydrocarbons (C_{12+}) are found from minute 10 until the end of the analysis.

Analysis of permanent gases

The analysis of permanent gases has been conducted using a *G.A.S. Compact micro-GC*. The mass concentration of H_2, CH_4, CO, CO_2, ethane, ethylene, propane, propylene, butane and its isomers has been determined as a function of the peak area given as a response by the equipment. The use of the micro- gas chromatograph has been necessary to evaluate the ratio between ethane/ethylene and propane/propylene, as in the GC these compounds are merged in single peaks. The *G.A.S. Compact micro-GC* is equipped with two detectors and four columns in total, arranged in three analytical channels as follows:

- Channel 1: equipped with 2 capillary Rtx-1 columns (3 x 0.25 mm and 12 x 0.25 mm) and a FID (Flame Ionization Detector), is optimized to detect C_1-C_4 hydrocarbons.
- Channel 2: equipped with 2 capillary Rt-Q-Bond columns (3 x 0.32 mm and 10 x 0.32 mm) and a TCD (Thermal Conductivity Detector), is optimized for the detection of CO_2, CH_4, ethylene, ethane, propylene and propane.
- Channel 3: is equipped with a Rt-Q-Bond column followed by a Molecular Sieve column (5A, 10 x 0.53 mm) and a TCD. The channel is configured to detect CO, CO_2, H_2, CH_4 and N_2.

Table 12 reports the operating conditions for the analysis method of the *G.A.S. Compact micro-GC* for the three channels, while the complete list of the response factors for each compound detected by the equipment is reported in Table 13:

Table 12: Operating conditions for the G.A.S. Compact micro-GC.

Parameter	Ch1	Ch2	Ch3
Column temperature, °C	45	50	70
Injection temperature, °C	70	70	70
Pressure, kPa	40	90	35
Injection time, ms	50	25	25
Analysis time, min	4	4	4

Table 13: Response factors for G.A.S. Compact micro-GC.

Compound	FID	TCD-1	TCD-2
Hydrogen	-	-	1220
Methane	-	26	28
Carbon monoxide	-	-	26
Carbon dioxide	-	23	-
Ethylene	-	21	-
Ethane	-	20	-
Propylene	-	18	-
Propane	-	18	-
Butanes	0.11	-	-
Butenes	0.12	-	-

2.7.5 Spent catalyst characterization

Spent catalyst samples have been characterized in terms of surface area and other physical properties (via N_2 adsorption-desorption cycles), coke deposition and acidity. The measurements were done in according to the techniques discussed in Section 2.3

Chapter 3

Feedstocks and catalysts characterization

3.1 Feedstocks characterization

The results from the characterization carried out on both feedstocks (olive stone and polyolefins) are reported in Table 14 in terms of proximate analysis, ultimate analysis and high-heating value (HHV), while Figure 40 illustrates results of the thermogravimetric analysis. The polymers composing the polyolefin mixture (HDPE, LDPE and PP) are characterized by negligible moisture content (<0.2%) and no solid residue, as expected. An $(H/C)_{eff}$ of 0.11 has been obtained for olive stone (chemical formula $C_{1.24}H_{2.14}OS_{0.001}$) meaning that it is a hydrogen-deficient material, difficult to upgrade to high quality fuels (Qiu et al., 2022a; Chen et al., 1986). A very low concentration of ashes has been found for olive stone.

Table 14: Ultimate and proximate analysis of olive stone (OS) and polyolefin mixture (POM).

	OS	HDPE	LDPE	PP
Ultimate analysis (wt %, d.b.)				
C	45.05	85.19	85.69	85.47
H	6.50	14.81	14.31	14.53
N	-	-	-	-
O	48.34	-	-	-
S	0.11	-	-	-
Proximate analysis (wt %, a.r.)				
Volatile matter	66.44	99.83	99.81	99.80
Fixed carbon	19.50	-	-	-
Ash	0.33	-	-	-
Moisture	13.73	0.17	0.19	0.20
HHV, MJ/kg	18.02	46.5*	47.2*	46.7*

*Calculated by literature correlation (Channiwala & Parikh, 2002)

As found in the literature (García Martín et al., 2020), olive stone pyrolysis using thermogravimetric analysis clearly shows three different peaks associated with different weight losses (Figure 40-A). The first peak (at around 100-150°C) is associated with evaporation of inherent moisture from the biomass, while the second (at 300°C) and third peak (375°C) are commonly associated with devolatilization of hemicellulose and cellulose (Blanco-López et al., 2002; Martín-Lara et al., 2018). The weight loss related to lignin decomposition is spread on a wider temperature range and is responsible for the final tail in the dm/dt vs. temperature diagram.

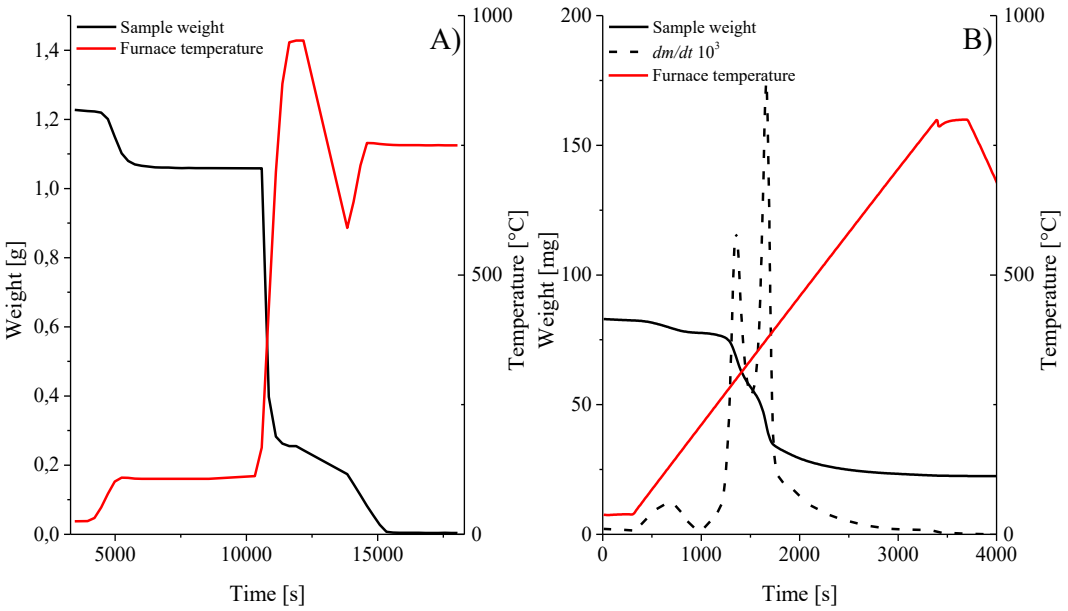

Figure 40: Proximate analysis of olive stone according to ASTM D5142 (A) and pyrolysis under N_2 at 15°C/min (B).

The ICP analysis performed on olive stone shows that the ash fraction (0.33 wt.%) contains catalytically active alkali and alkaline earth metals (AAEMs) that can modify the distribution of products by influencing the complex reaction network and favouring the yield of solid products during catalytic pyrolysis (Shen et al., 2011). More specifically, the results reported in Table 15 show that olive stone has a significant amount of potassium (≈1780 ppm) and calcium (≈780 ppm), minor amounts of Na, Mg, P, Fe and traces of other metals (<10 ppm). As previously mentioned, it is known that AAEMs favour fragmentation reactions by glycosidic bond ruptures prevailing over levoglucosan-producing reactions during cellulose pyrolysis, thus promoting light oxygenates formation and char production (Shen et al., 2011; Liu et al., 2014). These metals, present in the form of cations or salts, can thus act as a primary in-situ catalyst if vapours come in contact with AAEM-bearing biomass char accumulating in the reactor (Troiano et al., 2022). Nevertheless, as the ash fraction is extremely low, e.g., by proper management of char inventory in the reactor, it is reasonable to assume that the pre-catalytic effect is negligible compared to the extent of upgrading obtained in

the catalytic step. Some insights on the fate of these metals in pyrolysis products are given in Section 4.2.

Table 15: Metal content of olive stone (measured by ICP-MS).

Primary metals	Concentration [ppm]	Trace metals	Concentration [ppm]
Na	29	Mn	3
Mg	70	*Cd*	8
Al	12	*Cu*	1
P	90	*Zn*	3
K	1782	Pb	1
Ca	777	*Sr*	4
Fe	35	*Ba*	1

The results from Inductively Coupled Plasma Mass Spectrometry (ICP-MS) performed on the homemade iron-based catalysts confirmed that Fe was correctly deposited on the support (3.34% Fe on γ-Al_2O_3 and 2.74% Fe on dolomite). The low-cost waste-derived catalyst (SCA/γ-Al_2O_3) has been prepared from the ashes coming from sewage sludge combustion in fluidized-bed reactor (Coppola et al., 2015). The ashes from sludge combustion are characterized by high metal content (especially Fe, Ca and Mn). The ICP-MS confirmed the presence of high content of Fe (10470 mg/kg), Ca (4014 mg/kg) and K (1423 mg/kg), with lower amounts of Cu (249 mg/kg), Mg (296 mg/kg), Mn (29 mg/kg), Na (331 mg/kg), Ni (12 mg/kg) and Zn (185 mg/kg). The presence of high concentration of Fe is also highlighted by the intense red colour of the catalyst, obtained after 220 min of steady-state combustion and deposition on alumina (see Appendix C). The amount of each metal deposited on the catalyst was always lower than the original amount in the sewage sludge (e.g., Fe in the sludge was 14170 mg/kg).

3.2 Surface area, pore volume and pore diameter of fresh catalysts

Figure 41 shows the N_2 adsorption-desorption isotherms obtained for the seven catalysts used in this Thesis. According to the 1985 IUPAC classification of physisorption isotherms, the catalysts used in this work can be classified based on their specific pore structure, as evidenced by the characteristic shape of their adsorption isotherm and relative hysteresis loops. HZSM-5 and HY catalysts exhibit a type IV physisorption isotherm, characterized by a concave curve in the region of low P/P_0, followed by a hysteresis loop in the high-pressure region (starting at P/P_0=0.65 for HZSM-5 and at P/P_0=0.45 for HY). This behaviour is associated a significant microporous structure – typical of zeolites – and with the capillary condensation of gas within mesopores (20-500 Å). γ-Al_2O_3 exhibits a type V isotherm, with a convex curve at low pressure (suggesting the absence of

significant microporous structure) followed by a type-H2 hysteresis loop, probably due to a more complex pore structure compared to zeolites. Similar considerations can be extended to the two γ-Al_2O_3-based catalysts, even though a small difference in the hysteresis loop's shape can be observed, probably induced by impregnation.

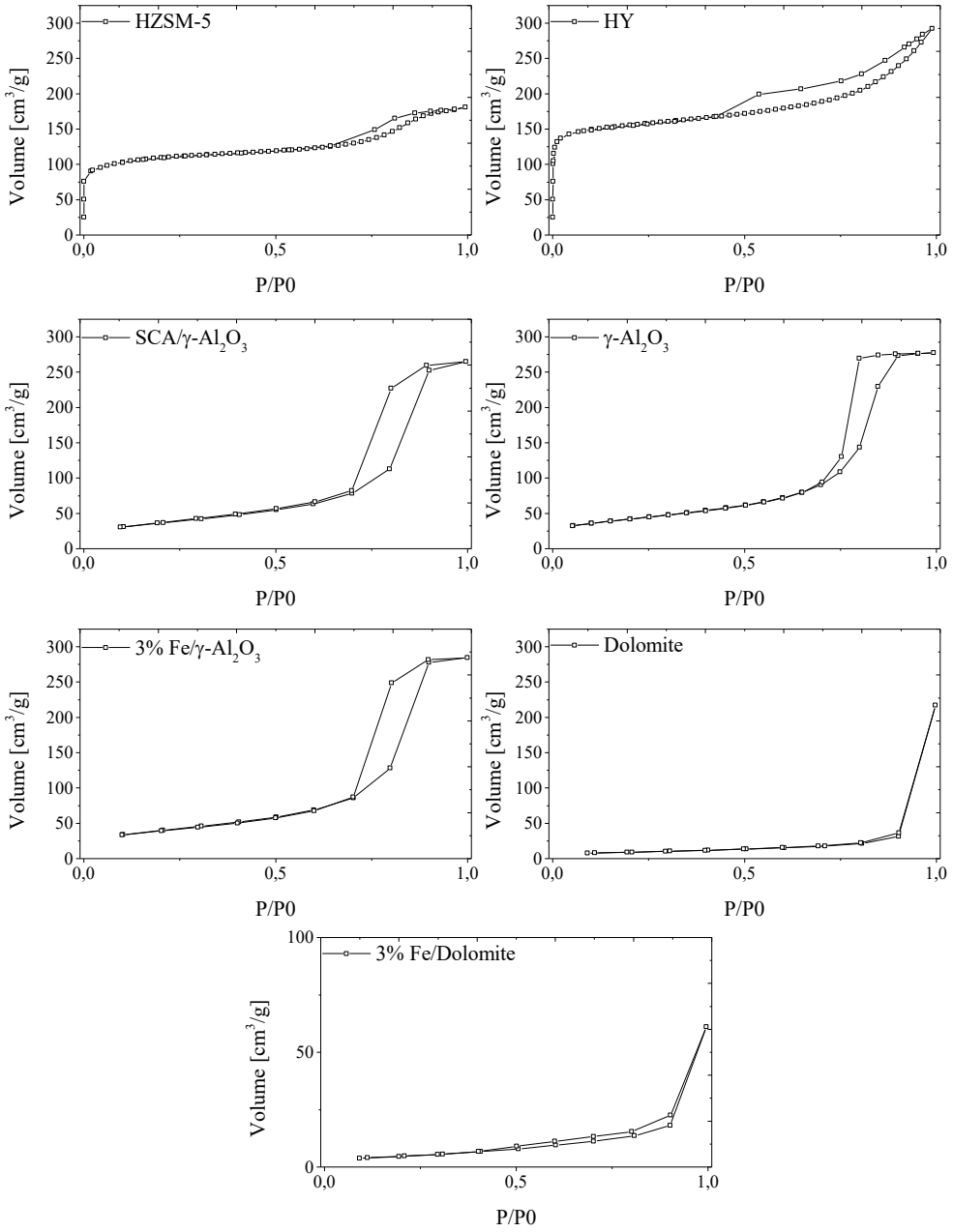

Figure 41: N_2 adsorption-desorption isotherms of the catalysts used in this work.

Dolomite and Fe/dolomite catalysts are characterized by a type III isotherm, typical of materials with weak gas-solid interactions, with negligible hysteresis loop. A similar result was found by Duffy et al. (2006), who confirmed that calcination is favourable to improve porosity in dolomite due to CO_2 ejection during the heating process.

Table 16 summarizes the physical properties of the catalysts used in this Thesis, including BET specific surface area, micropore area, mesopore volume and mean pore diameter of the catalyst.

Table 16: Physical properties of the catalysts used in this work.

Catalyst	BET [m^2/g]	A_{micro} [m^2/g]	V_{meso} [cm^3/g]	D_{pore} [Å]	$D_{catalyst}$ [4][mm]
HZSM-5	400	152.3	0.137	75	1.5
HY	595	448.1	0.263	97	1.5
SCA/ γ-Al_2O_3	131	-	0.433	156	1
γ-Al_2O_3	149	-	0.455	122	1
3%Fe/ γ-Al_2O_3	141	-	0.472	156	1
Dolomite	33	2.93	0.328	24	0.4-0.8
3%Fe/dolomite	18	0.63	0.093	29	0.4-0.8

In agreement with the shape of N_2 adsorption-desorption isotherms, HZSM-5 and HY zeolite-based catalysts present a significant microporous structure, as evidenced by the micropore area (152.3 and 448.1 m^2/g, respectively). The HY catalyst is based on clay as binder, while the HZSM-5 is based on alumina, and is characterized by a smaller average pore diameter (7.5 nm). The data confirmed the specifications of the manufacturer about the high BET surface area of the catalysts.

γ-Al_2O_3 has a substantially lower BET surface area compared to zeolites (149 m^2/g) and the micropore structure is negligible. Similarly, SCA/ γ-Al_2O_3 and 3% Fe/ γ-Al_2O_3 have a slightly lower surface area compared to pure alumina (131 and 141 m^2/g), probably due to the impregnation/deposition of the metal on them. No significant differences were found among the three γ-Al_2O_3 – based catalysts in terms of pore volume and pore size.

Finally, dolomite after calcination has a very low surface area (33 m^2/g) compared to other catalysts, has some micropores but is mostly a mesoporous material. Iron impregnation resulted in a further reduction of surface area (18 m^2/g) compared to calcined dolomite, with a substantial reduction in overall porosity. These characteristics drastically limited the catalytic activity of this 3% Fe/dolomite catalyst.

3.3 Acidity and basicity of fresh catalysts

The NH_3 and CO_2-TPD profiles obtained for the different catalyst samples are reported in Figure 42, together with the amount of total acidity evaluated by

[4] Catalyst particle size was chosen as a compromise between satisfactory catalytic activity (with limited mass transfer resistance) and acceptable operative pressure drop withing the pyrolysis system.

integration of the TCD signal (Table 17). The catalysts are characterized by significant differences in terms of both acidity and acidic site distribution. HZSM-5 exhibits a broad TPD profile that extends over a wide temperature range. Distinct peaks at low (≈120°C), medium (≈230°C) and high (≈430°C) temperatures can be easily recognised, with an overall acidity of 1.577 mmol $NH_3/g_{catalyst}$, the highest among the catalysts investigated. In particular, the acidic site strength distribution revealed that weak, medium and strong acidic sites accounted for the 29.4%, 49.7% and 20.9% of the total, respectively. The shape of the TPD profile is widely observed in the literature for HZSM-5 based catalysts (e.g., Iisa et al., 2016a). HY catalyst has a predominant desorption peak at low temperature, implying the presence of weak acidic sites, with a total acidity of only 0.244 mmol $NH_3/g_{catalyst}$. This is also justified by the higher Si/Al ratio of HY (100) compared to HZSM-5 (40). The SCA/ γ-Al_2O_3 catalyst has a lower acidity compared to HY (0.192 mmol $NH_3/g_{catalyst}$) but a little contribution by average acidic sites can be acknowledged. This is caused by the presence of AAEMs on the surface of the catalyst, as demonstrated by the results of ICP-MS conducted (Coppola et al., 2015)

γ-Al_2O_3 exhibits desorption peaks at higher temperatures than HY and SCA/ γ-Al_2O_3, with the principal peak at 450°C. This indicates the presence of medium and strong acid sites. The overall acidity (0.980 mmol $NH_3/g_{catalyst}$) is considerable and reflects the known acidity of alumina, mostly coming from the presence of Lewis sites and, to a lesser extent, to superficial Brønsted sites (Cheng et al., 2016). The TPD profile of Fe/ γ-Al_2O_3 catalyst is similar to that of pure γ-Al_2O_3, but with a lower peak intensity and a bigger contribution of average and weak acidic sites. The presence of 3% Fe modified the acidic sites distribution, reducing the proportion of strong sites and limiting their accessibility. Nevertheless, the overall acidity was calculated to be 1.299 mmol $NH_3/g_{catalyst}$, suggesting that the presence of the metal, its dispersion and its oxidation state contribute to the acidic properties of alumina.

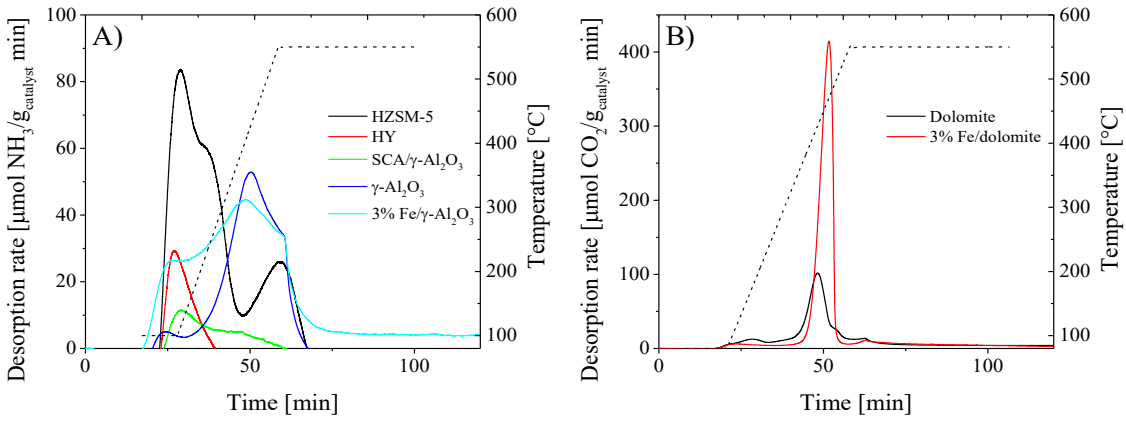

Figure 42: TPD-NH_3 (A) and TPD-CO_2 (B) profiles for the catalysts investigated in this work.

The TPD-CO_2 profile of dolomite shows a peak at around 400°C. On the other hand, 3% Fe/dolomite exhibits a more selective and intense peak at 420°C,

without contributions from lower temperature peaks, like in the case of calcined dolomite. This can be explained by the range of temperature selected for the desorption (25-550°C), in which dolomite does not eject all the CO_2, as shown in Figure 110 (Appendix F).

Table 17: Acidity and basicity of catalysts measured by TPD-NH_3 and TPD-CO_2.

Catalyst	TCD area	mmol $^5NH_3/g_{catalyst}$	Acidic sites
HZSM-5	0.622	1.577	W/M/S
HY	0.116	0.244	W
Sludge SCA/ γ-Al_2O_3	0.109	0.192	W
γ-Al_2O_3	0.413	0.980	M/S
3%Fe/ γ-Al_2O_3	0.387	1.299	M/S
Catalyst	**TCD area**	**mmol $CO_2/g_{catalyst}$**	
Dolomite	3.258	1.307	
3%Fe/Dolomite	1.794	2.368	

3.4 Scanning Electron Microscopy of fresh catalysts

Figure 43 shows the SEM images for selected fresh catalyst samples. The HZSM-5 catalyst was observed as cylindrical extrudates. At higher magnification, its surface was found to be made of small, irregular crystals with a high degree of porosity between them. The SCA/γ-Al_2O_3 support material consisted of uniform, spherical particles. The surface of these spheres was granular and composed of fine, densely packed particles, indicating a porous structure.

The 3% Fe/γ-Al_2O_3 catalyst also consisted of spherical particles, but its surface showed significant cracking and larger pores compared to the original support. These changes are likely due to the iron impregnation and heating process. The calcined dolomite appeared as irregular, angular particles of different sizes. Its surface was rough and porous, with some visible layered features. The 3% Fe/dolomite sample was covered with small, well-dispersed particles, which are believed to be the iron oxide.

[5] The calculation of total acidity (basicity) is the result of i) integration of the TCD signal vs time to obtain the TCD total area; ii) conversion of TCD area into mol of probe molecule by response factor and iii) normalization on the catalyst mass.

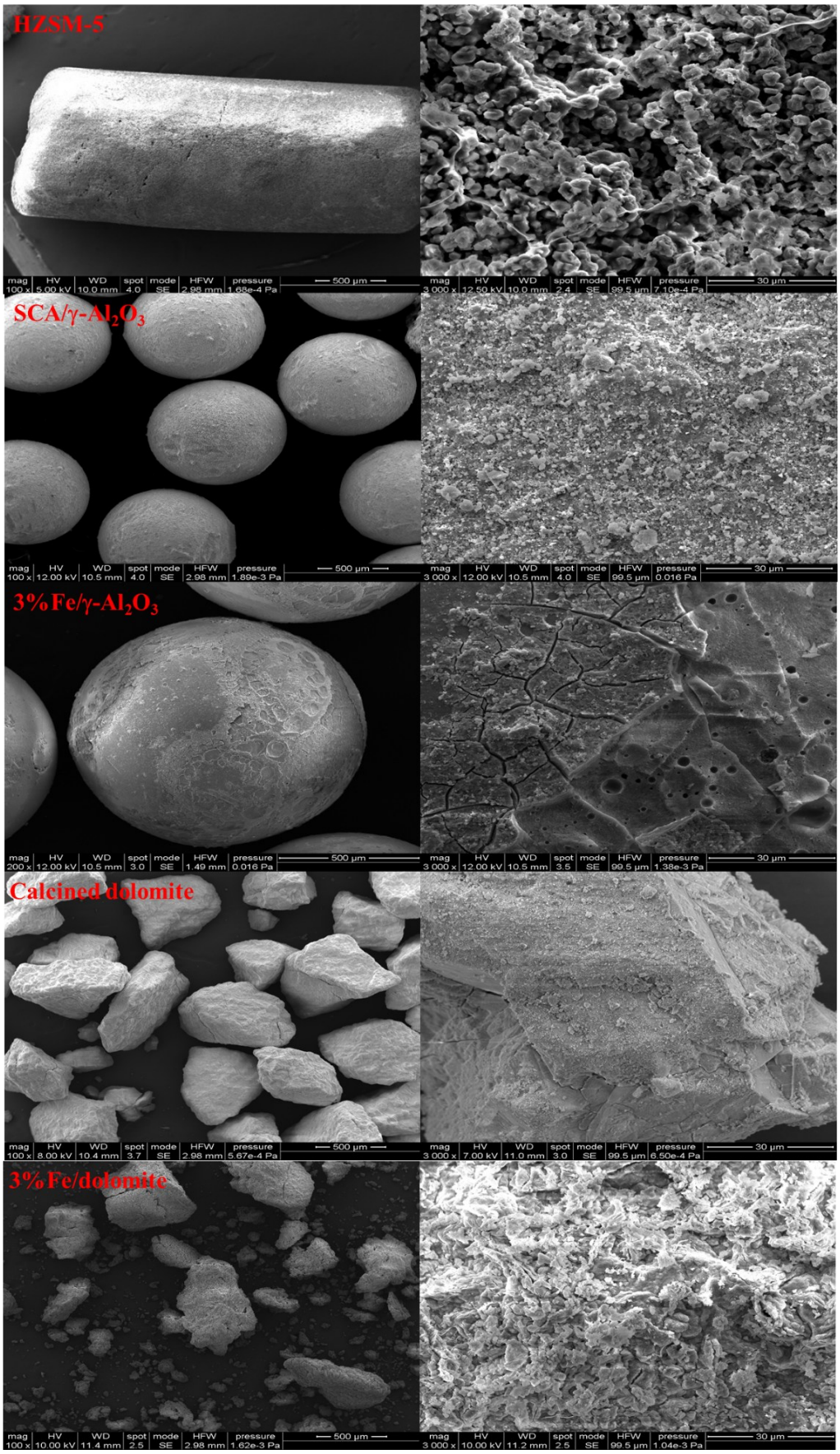

Figure 43: SEM images of fresh catalysts with 100x (left) and 3000x (right) magnification.

Chapter 4

Pyrolysis and in-line catalytic cracking of Olive Stone on ZSM-5

The results obtained in the experimental campaign on OS catalytic pyrolysis carried out in plant P1 are reported in the following sections. More specifically, the investigation aimed at evaluating the influence of the operating conditions (space-time, primary pyrolysis temperature and cracking temperature) on the distribution of pyrolysis products (char, coke, bio-oil and gas) and on the characteristics of the upgraded bio-oil to identify suitable conditions for selective production of value-added chemical families (aromatics, phenolics).

4.1 Effect of space-time

The effect of catalyst space-time, expressed as $g_{catalyst}\cdot min/g_{OS}$, on product yield distribution, the physicochemical properties of the resulting bio-liquid, and the extent of catalyst deactivation, including structural and textural deterioration was investigated in an experimental campaign using a HZSM-5 zeolite catalyst.

The space-time was varied between 0 $g_{catalyst}\cdot min/g_{OS}$ (representing non-catalytic thermal cracking) and 28 $g_{catalyst}\cdot min/g_{OS}$ (corresponding to the maximum catalyst mass that could be accommodated in the 40 mL fixed-bed reactor). All the experiments have been performed with a fixed volume of 40 mL of bed (catalyst + inert), and space-time has been changed by changing the amount of catalyst loaded in the reactor. To keep constant the bed height, coarse sand has been mixed with the catalyst. Ensuring a constant bed height by dilution with inert sand eliminates hydrodynamic variables and allows to isolate the effects of the catalyst mass (i.e., space-time). In all these experiments, the temperature of both the pyrolysis reactor and the fixed-bed catalytic reactor have been set to 500°C. Biomass feed rate and nitrogen flowrate have been set to 1 g min^{-1} and 800 NL h^{-1} throughout the experimental campaign, respectively. The results obtained from the ex-situ catalytic pyrolysis of olive stone are shown in Figure 44.

The distribution of products is significantly affected by the space-time, i.e. the amount of catalyst loaded in the reactor. In the baseline case (τ= 0 $g_{catalyst}$·min/g_{OS}) – meaning that the second-stage reactor is filled with coarse inert sand – the pyrolysis vapours produced in the spouted-bed reactor underwent non-catalytic thermal cracking exclusively. In these conditions, the yield of liquid product was maximum, 65.4 wt% of which 52.4% organics and 13.0% water. This result is in line with those obtained by Fernandez et al. (2021) during the pyrolysis of pine wood at 500°C in a spouted-bed reactor. The cracking of pyrolysis vapours intensifies as they come in contact with the catalyst's surface and this behaviour is enhanced with increasing space-time. For this reason, organics yield linearly decreases with increasing space-time, going from 52.4% for pure thermal cracking to 17.4% for higher space-time (τ=28 $g_{catalyst}$·min/g_{OS}). Conversely, water yield increases from 13.0% to 28.2%. This trend is consistent with numerous studies on the catalytic pyrolysis of various biomass feedstocks, including corn stover (Liu et al., 2017; Zhang et al., 2016a) and wheat straw (Hernando et al., 2016).

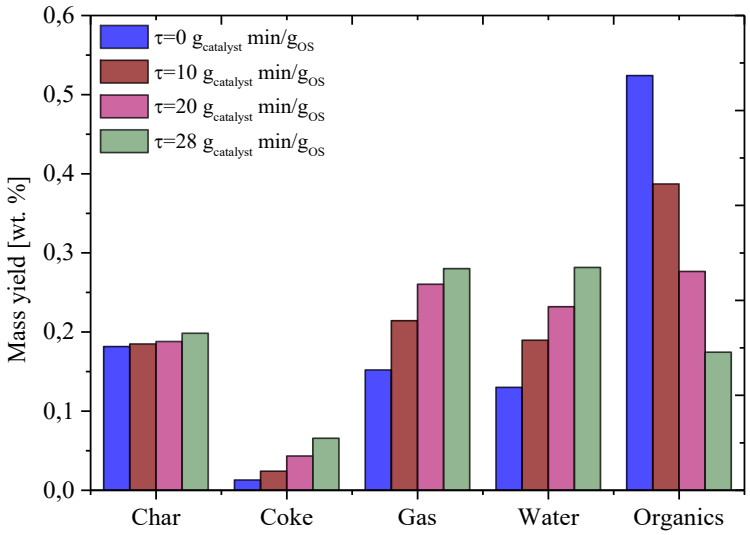

Figure 44: Effect of catalyst space-time on the mass yields of the main product fractions. Conditions: $T_{pyrolysis}$=$T_{cracking}$=500°C.

The gas yield also increases with increasing space-time as a consequence of decarbonylation, decarboxylation, hydrocracking and ketonization reactions, which are all part of the complex mechanism of biomass fast pyrolysis and catalytic cracking over zeolite catalysts. In the case of the cracking reactor loaded with inert sand, the gas yield is 15.2 wt.%, and it increases up to 28.0 wt.% at higher space-time. As expected, the yield of solid char is not influenced by the change in space-time of the catalytic reactor – see the discussion in Section 2.6.6 - and is always slightly less than 20% (between 18.2 wt.% and 19.8 wt.%). Moreover, Hernando et al. (2016) found a similar result in the catalytic fast pyrolysis of wheat straw in a two-stage downdraft fixed-bed reactor.

The value of char yield obtained is also in complete agreement with the proximate analysis of olive stone, from which the fixed carbon content of the olive stone was determined to be 19.5 wt.% (as-received basis). The consistency

of the char yield across all experiments, and its agreement with the fixed carbon content of the feedstock (19.5 wt.%), provides a validation for test repeatability in the ex-situ configuration.

The total coke yield increased linearly with space-time, which can be attributed to both the larger catalyst surface area available for deposition (Liu et al., 2017) increased by the presence of a higher amount of catalyst and the promotion of condensation reactions at longer residence times (Meng et al., 2007). In the range of space-time considered, coke yield increases from 1.3 wt.% to 6.6 wt.%. Carlson et al. (2011) observed that reducing WHSV – thus increasing space-time – increased coke yield from 20 to 37% during the catalytic pyrolysis of pine wood sawdust in a bubbling fluidized-bed reactor. However, the trend of decreasing coke content (wt.% on catalyst) with increasing catalyst-to-biomass ratio, as reported by Hernando et al. (2016), was not observed in this study, potentially due to differences in feedstock composition.

In summary, the trends observed for product yields are widely confirmed in the literature for the catalytic fast pyrolysis of biomass. For instance, Pütün (2010) observed a reduction in liquid yield from 42% to 30% when catalyst amount was increased from 5 to 20% during in-situ catalytic fast pyrolysis of cotton seeds at 550°C using a tubular fixed-bed reactor. Similarly, gas yield increased from 20 to 30% and char yield from 20 to 26%. This observation is consistent with the present work, where the total solid yield (char + coke) increases with space-time.

Similarly, Castello et al. (2019) observed an increase in gas yield from 21.7% to 26.7% during the ex-situ catalytic pyrolysis of pine wood using commercial ZSM-5 (Si/Al=3) and Na_2O/γ-Al_2O_3. Water yield increased from 13.7% to 24.4% and coke yield increased from 0.0% to 8.6% when increasing the catalyst/biomass ratio. The char yield was not significantly affected by change in space-time. The trends are also confirmed by Iisa et al. (2016a) and (2016b) during the in-situ and ex-situ catalytic fast pyrolysis of pine wood. Finally, Hernando et al. (2016) also demonstrated that increasing the catalyst/biomass ratio from to 0.4 to 2.8 g leads to an increase in the yield of gas, water and coke, while the yield of organics decreased.

The N_2-free volume composition of the permanent gas product from the catalytic pyrolysis of olive stone and the mass yields of single gas-phase compounds are shown in Figure 45-A and 45-B. The production of carbon dioxide and carbon monoxide increases with increasing space-time (Figure 45-B) since decarbonylation and decarboxylation reactions are dominant during pyrolysis vapours catalytic cracking due to the thermal degradation of carbonyl and carboxyl functionalities in holocellulose and lignin (responsible for the production of CO_2), while the rupture of C–O–C and C–O bonds lead to the formation of CO. The H_2 generation is associated to the cleavage of C–H bonds and aromatic groups (Couhert et al., 2009).

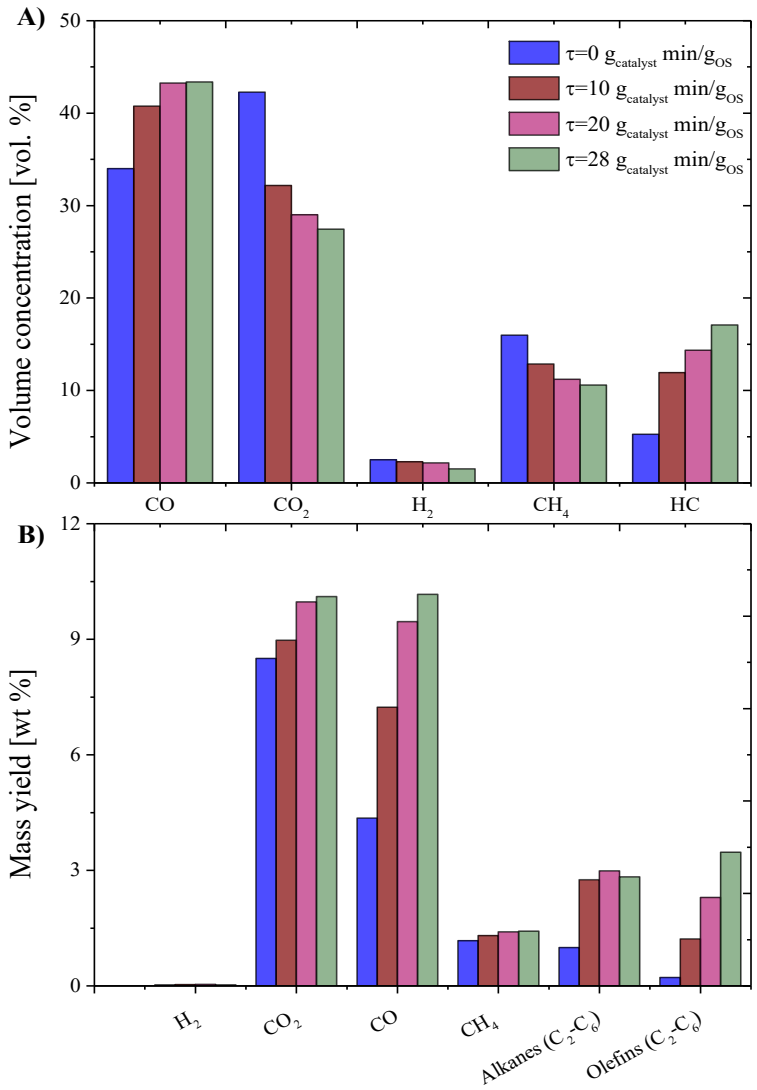

Figure 45: N_2-free composition of pyro-gas (A) and yields of single gas-phase species (B) as function of space-time.

More specifically, CO_2 yield increases from 8.50 wt.% to 10.11 wt.% when going from pure thermal cracking to the maximum space-time of τ=28 $g_{catalyst}$·min/g_{OS}, while CO yield increases from 4.35 wt.% to 10.16 wt.%. The higher increase in CO yield compared to CO_2 suggests that decarbonylation of carbonyl groups in aldehydes and ketones may be the preferential pathway followed during upgrading (Paasikallio et al., 2017; Carlson et al., 2009). The results are in line with the findings of Wang et al. (2022), who reported that dehydration is the primary deoxygenation route at low catalyst loadings, while decarbonylation becomes dominant as catalyst contact increases. Methane yield only slightly increases with space-time, from 1.17 wt.% to 1.42 wt.%. Finally, an increase in light olefin production from 0.21 wt.% to 3.47 wt.% is observed when space-time goes from 0 to 28 $g_{catalyst}$·min/g_{OS}. C_1-C_4 light hydrocarbons are known to be the primary cracking product over HZSM-5 for many model compounds (Chang & Silvestri, 1977). Light olefins can be the result of dehydration of light alcohols at low temperature (Gayubo et al., 2004a). Although hydrogen yield increased with space-time, its contribution to the total mass balance was negligible (<0.05 wt.%), in agreement with previous reports (Williams &

Nugranad, 2000; Paasikallio et al., 2017; Stephanidis et al., 2011a). The volumetric composition data in Figure 45-A are important for the energetic valorization of the pyrolysis gas: they revealed an interesting shift in the gas-phase makeup. The concentration of light hydrocarbons (alkanes and olefins) increases with space-time (Williams and Nugranad, 2000). In the same range, the concentration of CO increases from 31.18 wt.% to 43.37 wt.%, while concentrations of CO_2 and CH_4 decrease. This occurs because, as space time increases, the total gas volume also increases, leading to a dilution effect. Consequently, the relative fractions of CO_2 and CH_4 decline, since their formation rates do not rise as sharply as that of CO.

The effect of space-time on the quality of bio-oil is illustrated in Figure 46. As anticipated, the presence of an acid catalyst such as HZSM-5 impacts not only the total bio-oil yield but also its molecular composition, driven by a complex interplay of decarbonylation, decarboxylation, ketonization, cracking, aromatization, oligomerization, and other secondary transformations. GC-MS peak areas were used to describe relative abundances, allowing semi-quantitative interpretation since peak area scales approximately with concentration of analytes. The optimization of space-time – i.e., the amount of catalyst available for vapours upgrading – is critical because it directly governs the extent of vapour-catalyst contact and thus the competition between desired and undesired reactions. The presence of the catalyst acts in a different way on different classes of compounds. For instance, it was observed that the concentration of aldehydes, ketones, furans, sugars and organic acids – mainly derived from the decomposition of cellulose and hemicellulose fractions of olive stone – decreases with space-time and are significantly converted when the amount of catalyst is sufficiently high, as also reported by Hernando et al. (2016) and Paasikallio et al. (2017). Cellulose undergoes dehydration to yield primary anhydrosugars, releasing water as a by-product. Acid catalysis converts these sugars toward furan derivatives via dehydration, decarbonylation, and decarboxylation. Successively, these furans can rearrange and oligomerize into aromatic hydrocarbons via the “hydrocarbon pool” mechanism (Yildiz et al., 2016). A similar reduction in organic acids, ketones, furans, and anhydrosugars was reported by Arabiourrutia et al. (2024) for bio-oil obtained from corncob pyrolysis at different catalyst-to-biomass ratios at 450°C. Aldehydes and ketones are known to be easily dehydrated over acidic catalysts in parallel to cracking and aromatization reactions (Adjaye & Bakhshi, 1995).

In parallel, the catalytic cracking of light oxygenated molecules (such as acetic acid, small aldehydes, ketones and alcohols) can be responsible for the formation of light hydrocarbons (Chang and Silvestri, 1977). The high water yield observed using HZSM-5 and the almost total absence of alcohols in the resulting bio-oils, suggest that the zeolite exhibits strong dehydration activity. Low molecular weight alcohols are likely converted on the catalyst’s acid sites to produce water and an olefin. According to the literature (Adjaye & Bakhshi, 1995; Chiang & Bhan, 2010), the process begins with the protonation of the alcohol forming a cation, followed by the elimination of water; subsequently, the

carbocation or an alkoxide adsorbed on the acid site regenerates the site by desorbing as an olefin. Moreover, most of the alcohols may also take part in alkylation-cyclization-aromatization reactions to produce aromatic hydrocarbons (Adjaye & Bakhshi, 1995). Reducing the content of organic acids and sugars is advantageous for bio-oil storage and upgrading since these compounds contribute to lowering bio-oil pH and increasing corrosiveness (Bakar & Titiloye, 2013).
Levoglucosan – the major product of cellulose thermal decomposition and consistently the dominant sugar detected (Naqvi et al., 2014) -is completely converted (from 4.1% to 0.0%) when space-time reaches the maximum of τ=28 $g_{catalyst}$·min/g_{OS}. The reduction of anhydrosugars share finds confirmation in the work of Hernando et al. (2016), Zhang et al. (2016a) and, more recently, in the work of Arabiuourrutia et al. (2024) in corncob pyrolysis. Similarly, the concentration of furan compounds (above all furfural, 2-furanmethanol, 2(5H)-furanone) decreases from 9.3% to 3.5% with increasing space-time, with a corresponding increase in the yield of aromatic compounds (monoaromatic hydrocarbons and oxygenated monoaromatics). The decrease of sugar concentration appears to be linked to the corresponding increase in aromatics, which can be produced by cyclization-dehydrogenation or Diels-Alder condensation of light olefins with furans and other light oxygenates (Dorado et al., 2015; Cheng et al., 2012; Dai et al., 2020). However, contradictory observations in the literature, such as increased furan and acid formation with higher catalyst-to-biomass ratios (Naqvi et al., 2014), highlight the need for feedstock-specific catalyst optimization. Furthermore, excessive space-time can favour coke formation, partly through polymerization of furan derivatives (Zhang et al., 2014), which decreases catalyst lifetime and increases regeneration costs.

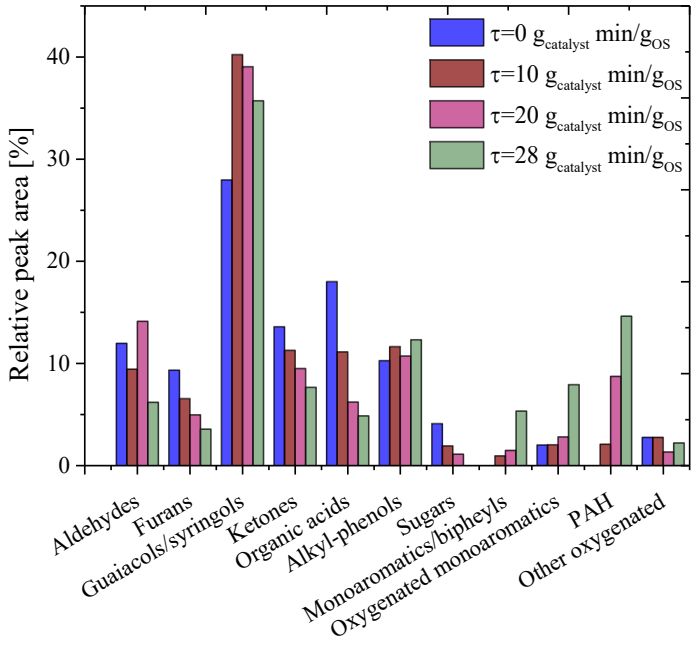

Figure 46: Effect of space-time on the chemical family distribution in the upgraded bio-oil. Pyrolysis and cracking temperature held constant at 500°C.

Phenolic compounds are predominantly produced by catalytic cracking of lignin oligomers via hydrogenolysis and hydrodeoxygenation reactions (Olcese et

al., 2013). Methoxy-phenols present a non-monotonic trend with a maximum guaiacols/syringols content of 40.2% when space-time is τ=10 $g_{catalyst}\cdot min/g_{OS}$. Typical methoxyphenols detected by means of GCMS are 2-methoxy-phenol (guaiacol), creosol, 2,6-dimethoxy-phenol (syringol), trans-isoeugenol and 2-methoxy-4-vinylphenol, as also reported by Patwardhan et al. (2011) for the pyrolysis of pure lignin. Lignin-derived units, such as syringols, are not readily converted over ZSM-5 catalysts due to the stable nature of aromatic ether bonds (Gayubo et al., 2004a, Yu et al., 2012; Mihalcik et al., 2011), unless more severe reaction conditions—such as higher catalytic temperatures or longer space-times—are applied (Liu et al., 2020). Gayubo et al. (2004a) confirmed the low reactivity of phenolic compounds, with the main products being light hydrocarbons and traces of carbon oxides.

Alkyl-phenols (phenol, methyl-phenols, catechol) are even less affected by change in space-time, with a mean concentration of 11.2±0.7 %. Phenols and aldehydes are known to be quite stable products over HZSM-5 and therefore they are the main precursors of coke (Gayubo et al., 2004a; Gayubo et al., 2004b) together with olefins and PAHs (Wang et al., 2022). When alkyl-phenols react over zeolite catalysts, isomerization is a preferred route, producing a spectrum of molecules with the same atomic composition but different chemical structures (Pujro et al., 2021; Adjaye & Bakhshi, 1995).

In general, diffusional limitations restrict the conversion of bulky molecules within the zeolite pores, favouring secondary reactions that lead to coke formation on the catalyst surface and, consequently, its deactivation (Liu et al., 2020). The elemental analysis of bio-oil samples never detected the presence of N-containing compounds, which in turn was not detected in the starting biomass itself.

These trends are in agreement with the general mechanism of biomass fast pyrolysis on acid catalysts (Yildiz et al., 2016), in which reactive intermediate compounds (i.e., furans, ketones, acids…) are consumed to favour the production of end products like coke, olefins and aromatics (especially PAHs produced by the condensation of monoaromatics). Aromatization reactions within the zeolite's pore can convert alcohols, furans and sugars into aromatics (Qi and Fan, 2019), with PAH yield sharply increasing with higher space-time of HZSM-5 (Liu et al., 2017). While PAHs were not detected during the non-catalytic experiment, their concentration increased steadily with space-time from 2.09% to 14.62%. The presence of HZSM-5 favours the formation of both monoaromatic hydrocarbons and oxygenated aromatics, with a marked increase observed when the space-time was raised from 20 to 28 $g_{catalyst}\cdot min/g_{OS}$.

The increased presence of multi-ring aromatics (phenanthrenes, anthracenes) at high space-times (Paasikallio et al., 2017) indicates that secondary condensation is promoted by the greater availability of acidic sites—enhancing aromatic content but also increasing heavy fraction and coke yield (see Appendix B).Since Brønsted acid sites are generally more effective than Lewis's acid sites in catalysing aromatization reactions (Cai et al., 2020), careful design of pore architecture, as well as the strength and spatial distribution of acid sites, is essential to optimize selectivity toward aromatic compounds.

4.2 Effect of pyrolysis temperature

While the catalytic stage dictates the final product upgrading, the initial pyrolysis temperature fundamentally defines the composition of the vapor stream fed to the catalyst. This chapter systematically isolates the effect of the primary pyrolysis temperature (450-600°C) to understand how the initial thermal decomposition of olive stone dictates the final product distribution and bio-oil quality under constant catalytic cracking conditions. As a preliminary investigation, single-stage pure thermal pyrolysis at 500°C and ex-situ catalytic fast pyrolysis of OS ($T_{pyrolysis}$=$T_{cracking}$=500°C, 0 $g_{catalyst}$·min/g_{OS}) were compared. Results clearly demonstrated that the presence of the second step (acting as *thermal cracking reactor*) did not significantly influence product distribution (e.g., gas yield 15.82 vs 15.20%, water yield 14.61% vs 13.0%, bio-oil yield 52.87 vs. 52.4% for single-stage pure thermal and 2-stage configurations, respectively). Therefore, any significant change in product yields can be ascribed to the presence of the catalyst, since thermal cracking contribution is negligible at least below 500°C.

Figure 47 illustrates the effect of the pyrolysis temperature on product distribution during ex-situ catalytic pyrolysis of olive stone biomass over commercial HZSM-5. All tests have been performed using a space-time of 20 $g_{catalyst}$·min/g_{OS} and setting the temperature of the catalytic reactor at 500°C and keeping constant all the other process parameters – i.e., nitrogen flowrate, catalytic bed volume and biomass feed rate.

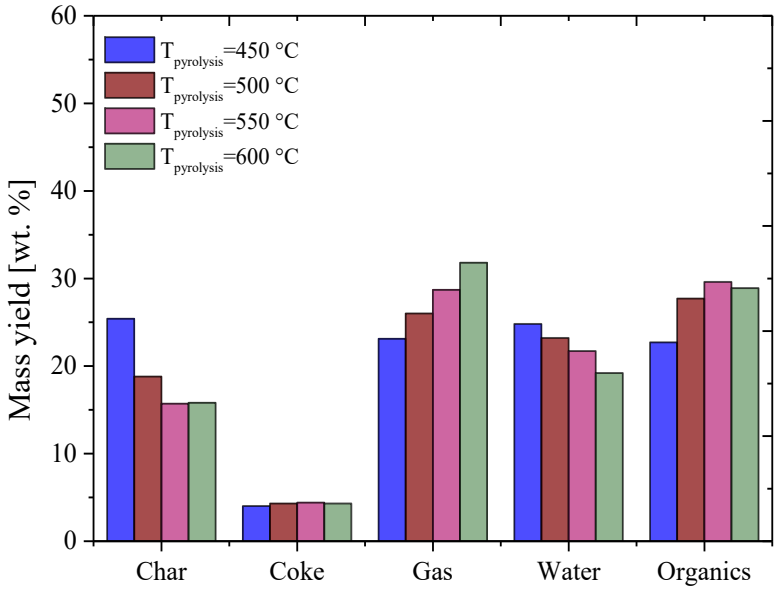

Figure 47: Effect of pyrolysis temperature on the mass yields of the main product fractions. Conditions: $T_{cracking}$=500°C, τ=20 $g_{catalyst}$ min/g_{OS}.

As the pyrolysis temperature increases from 450 °C to 600 °C, the gaseous fraction rises from 23.1 wt.% at 450 °C to 31.8 wt.% at 600 °C, reflecting enhanced secondary cracking of primary pyrolysis vapours and accelerated

β-scission reactions on the Brønsted acid sites of the HZSM-5 catalyst. For what concerns the composition of the gas phase (Figure 48), the major products are carbon monoxide and carbon dioxide in all the investigated temperature range (450-600°C). The concentration of CH_4 increases with temperature and its concentration is comparable to that of other light hydrocarbons produced during the process (ethylene, ethane, propylene, butenes), which show a maximum at 550°C. Finally, hydrogen was produced in rather small amounts – with a maximum of 5.7% vol. at 600°C. The observed behaviour is in agreement with a more extensive cracking of the larger organic molecules present in the vapours, leading to the formation of smaller molecules, including light hydrocarbons and H_2 (Uddin et al., 2014).

Considering the mass yield of single gas-phase compounds (Figure 48-B), it is possible to nota that CO production is deeply influenced by pyrolysis temperature, while CO_2 levels are quite stable at ≈10 wt.%. Williams and Nugranad (2000) also found that the increase in CO was more pronounced compared to CO_2.

The concurrent increase in CO and H_2 yields, coupled with the decrease in water yield, suggests the possibility of in-situ steam reforming or gasification reactions occurring within the pyrolysis reactor (Hernando et al., 2016) and shows that decarbonylation and decarboxylation reactions are favoured at higher pyrolysis temperatures, while the extent of dehydration reactions becomes comparatively less significant, as also reported by Hernando et al., (2016).

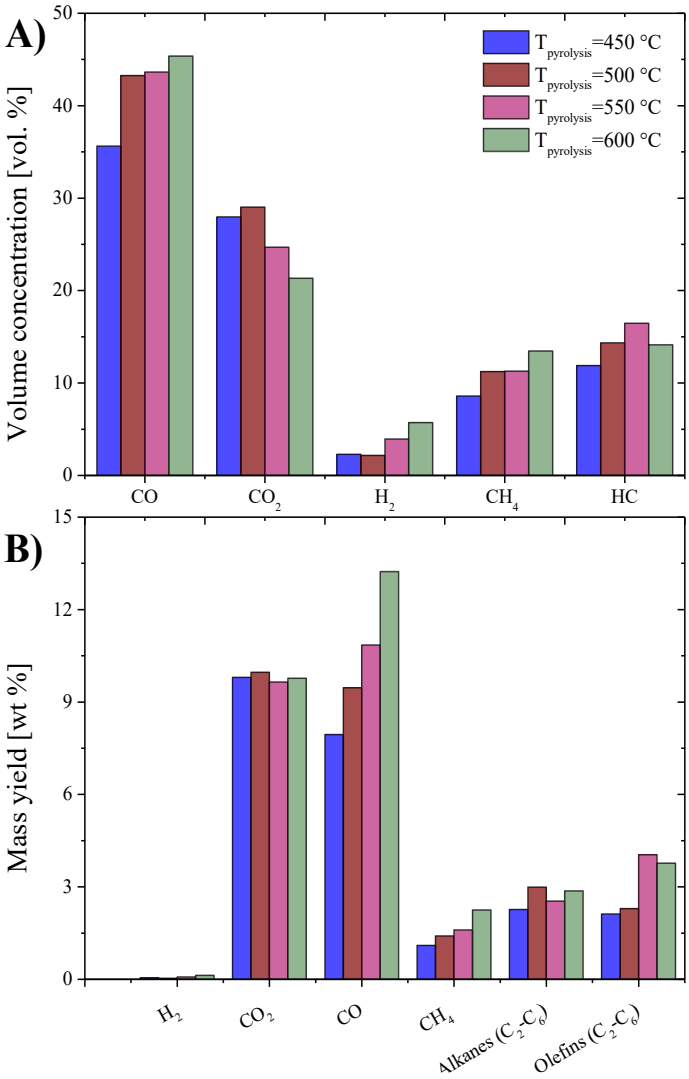

Figure 48: N_2-free composition of pyro-gas (A) and yields of single gas-phase species (B) as function of pyrolysis temperature.

Shifting the attention to the liquid fraction, the pyrolytic water yield declines (from 24.8 wt.% to 19.2 wt.%) with increasing pyrolysis temperature, as also observed by Hernando et al. (2016) during non-catalytic fast pyrolysis of wheat straw in the 475-600°C range. On the other hand, the organic liquid yield exhibited a maximum at 550°C, before declining slightly at 600°C. Between 450 and 550°C, biomass devolatilization is favoured by increasing temperature producing condensable vapours, but when temperature is increased further, excessive thermal secondary cracking reduces bio-oil yield, as also observed by Liu et al., (2017) during the two-stage fast microwave-assisted pyrolysis of corn stover.

The effect of pyrolysis temperature on the composition of the oil recovered after catalytic upgrading is detailed in Figure 49.

The amount of aldehydes initially increases, then sharply decreases as the pyrolysis temperature is increased, a trend attributed to their thermal instability under elevated temperatures more than to catalytic activity (Gayubo et al., 2004b). As temperature rises, aldehydes are increasingly subjected to secondary reactions

such as decarbonylation, decarboxylation, and polymerization, yielding lighter hydrocarbons, CO, CO_2, or other compounds. For instance, acetaldehyde can undergo decarbonylation to produce methane and carbon monoxide or be converted to C_{6+} olefins, C_{4+} paraffins and trimethyltrioxane (Gayubo et al., 2004b), while larger aldehydes may participate in aldol condensation, generating more complex molecules that can subsequently crack or polymerize at high temperatures.

A similar behaviour is observed also for furans. They have a reduced thermal stability as temperature increases, undergoing ring-opening and fragmentation reactions that lead to the formation of permanent gases and smaller oxygenated compounds. Consequently, compounds such as furfural, 2-furanmethanol and 2(5H)-furanone were completely degraded at 600°C. Organic acids, such as acetic acid, are prone to decarboxylation at higher pyrolysis temperatures, producing methane and CO_2, while dehydration plays a minor role and decarbonylation is negligible, especially at lower temperatures. Acetic acid, for instance, shows low reactivity below 400 °C, but it can first be converted into acetone and subsequently into olefins when the temperature is >400°C (Gayubo et al., 2004b). The further decomposition of aldehydes, furans and organic acids is in agreement with the change in the gas composition and the observed increase of CO, CO_2 and methane with increasing temperature.

The concentration of ketones increases with pyrolysis temperature, from 9.2% to 13.2%. The increase in ketones likely arises from competing reaction rates, their formation via ketonization of carboxylic acids and their degradation by cracking or aldol condensation. Since ketonization of carboxylic acids is a dominant pathway on zeolites and accelerates at high temperatures (Boekaerts & Sels, 2021), it is possible that formation of ketones from the acid precursors in the pyrolysis vapours is faster than their subsequent conversion, resulting in progressive ketone accumulation in bio-oil.
The concentration of anhydrous sugars (predominantly levoglucosan) rises from 1.0% at 450 °C to 2.6% at 600 °C.
The observed increase in levoglucosan with pyrolysis temperature has been observed (Shen et al., 2011). Its production is associated with cellulose pyrolysis and follows a competitive reaction pathway between levoglucosan production and its further cracking. The rate of the primary depolymerization reaction to form levoglucosan increases more steeply with temperature than the rate of its secondary degradation in the 450-600°C range investigated, with a consequent increase in levoglucosan yield in the range 500-580°C before declining (Shen & Gu, 2009a).

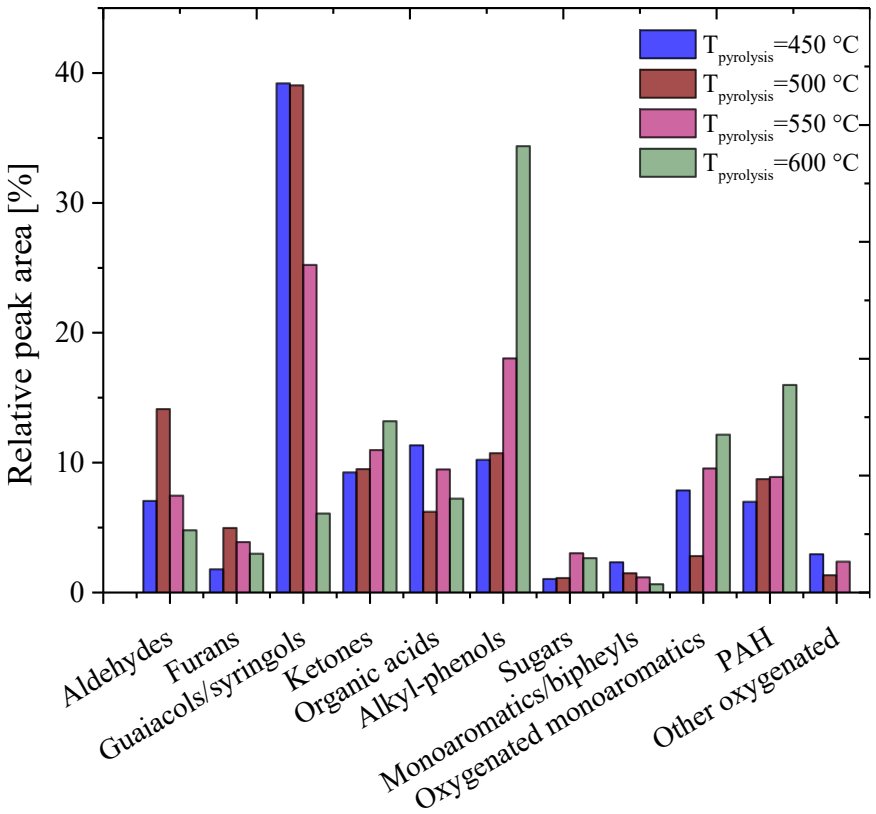

Figure 49: Effect of primary pyrolysis temperature on the chemical family distribution in the upgraded bio-oil. Cracking temperature held constant at 500°C and space-time of 20 $g_{catalyst}$ min/g_{OS}.

At low temperatures (e.g., 450–500 °C), a high concentration of methoxyphenols (guaiacols and syringols) in the bio-oil, which are oligomeric derivatives of lignin, is observed. With increasing pyrolysis temperature, simultaneous thermal cracking and demethoxylation reactions of guaiacols and syringols favour the production of simpler alkylphenols, whose collective relative abundance increases steadily from 10.2% to 34.4%. It has been demonstrated that the pyrolysis of phenolic compounds, such as guaiacol and vanillin, proceeds through a radical mechanism involving the homolytic cleavage of C–C and C–O bonds; therefore, higher temperatures are required to break these high-energy bonds (Shin et al., 2001; Nguyen et al., 2016). For instance, the concentration of guaiacol was reduced from 2.6% to 0.2%, while that of trans-isoeugenol from 7.86 to 1.56%. Correspondingly, an increase in the yield of phenol (from 1.07% to 3.13%) and catechol (from 2.74% to 7.71%) was observed.

This aligns with the findings of Afifi et al. (1996), who observed that in the presence of hydrogen-donor species—commonly found in bio-oils (Pujro et al., 2021)—guaiacol is converted into catechol, phenol, and anisole. This pathway is particularly relevant, as the primary pyrolysis vapours are inherently rich in such hydrogen-donor species (e.g., alcohols, acids), thus facilitating these specific conversion routes at higher temperatures. Simultaneously, the cleavage of C–C bonds in the side chains of alkyl-phenols can also occur, yielding simpler phenols and hydrocarbons. The demethoxylation of many phenolic compounds (guaiacol, methylguaiacol, syringol, eugenol and others) has been verified (Saidi et al.,

2014). Thus, syringol can be demethoxylated to produce guaiacol and then phenol with a two-step hydrogenation (Pujro et al. 2021; Yang et al., 2017).

Regarding the production of aromatic compounds, a decrease in the concentration of monoaromatics and biphenyls is observed, from 2.3% to 0.6%, with a corresponding increase in oxygenated aromatics (from 7.8% to 12.1%) and PAHs, whose concentration doubles from 6.99% to 15.98% as the pyrolysis temperature increases from 450 °C to 600 °C. Likely the higher concentration of reactive, unstable species (like furan-derivatives and aldehydes) produced at higher pyrolysis temperatures provides a richer pool of precursors for cyclization and aromatization reactions on the catalyst surface, leading to the observed increase in naphthalenes and indenes. The main contribution to PAHs production is given by naphthalenes, whose relative abundance increases from 4.06% to 8.03% when the pyrolysis temperature rises from 450 °C to 600 °C. The second most relevant contributors are indene derivatives, increasing from 0.37% to 4.09%, while anthracenes production does not appear to be significantly affected by pyrolysis temperature under the operating conditions investigated (mean % peak area ≈1.3±0.4 %). A similar increase in oxygenated aromatics and PAHs under these conditions was also reported by Iisa et al. (2017).

Also char yield is influenced by pyrolysis temperature. More in detail, as the pyrolysis temperature increases from 450 °C to 600 °C, the char yield decreases. The higher char yield at lower temperature is attributed to incomplete primary thermal devolatilization of the biomass (Williams and Nugranad, 2000; Eom et al., 2013). At higher temperature, devolatilization and - to a lesser extent - char gasification reactions (e.g., $C+H_2O \rightarrow CO+H_2$ and $C+CO_2 \rightarrow 2CO$) are favoured and lead to increased yields of permanent gases such as CO and CO_2 (Di Blasi et al., 1999). Similar results in terms of char yield were found by Imran et al. (2016) during the *in-situ* flash pyrolysis of wood fibres in the presence of HZSM-5.

Pyrolysis temperature influenced the physiochemical properties of the biochar samples in terms of carbon content, specific surface area, mean pore diameter and surface morphology.

The TGA analysis of char samples obtained at different pyrolysis temperature (450, 500, 550 and 600°C) revealed, as expected, a decrease in the volatile matter (from 36.1% to 28.1%) and a corresponding increase in fixed carbon content (from 56.9% to 64.8%) and the decrease of both the O/C and H/C ratios with pyrolysis temperature (Figure 55-B). The temperature of primary pyrolysis also affects the physical properties of the char. The samples generally exhibited a very low surface area (<1 m^2/g) while the opening of higher porosity (surface area of 22.7 m^2/g) was promoted only for the sample obtained at 600°C. It should be noted that, since the duration of each pyrolysis test was fixed to 45 min, the resulting properties of the char should be only ascribed to the operating temperature of the pyrolyser.

The temperature also influenced the portioning of metals present in the ashes. Since metals ions can replace H^+ in the structure of the zeolite via ion-exchange (Lin et al., 2022), it is important to limit their interaction with the catalyst. The concentration of primary and trace metals in biochar samples produced ad different pyrolysis temperature is illustrated in Figure 50. A natural concentration effect is observed for most metals with increasing pyrolysis temperature, due to the higher extent of devolatilization. K and Ca, the most abundant metals in raw olive stone, are found in biochar samples with concentration in the 5000-10000 ppm and 2000-4000 ppm range, respectively. All other primary metals are typically present with lower concentrations (<700 ppm), and trace metals are well below 30 ppm.

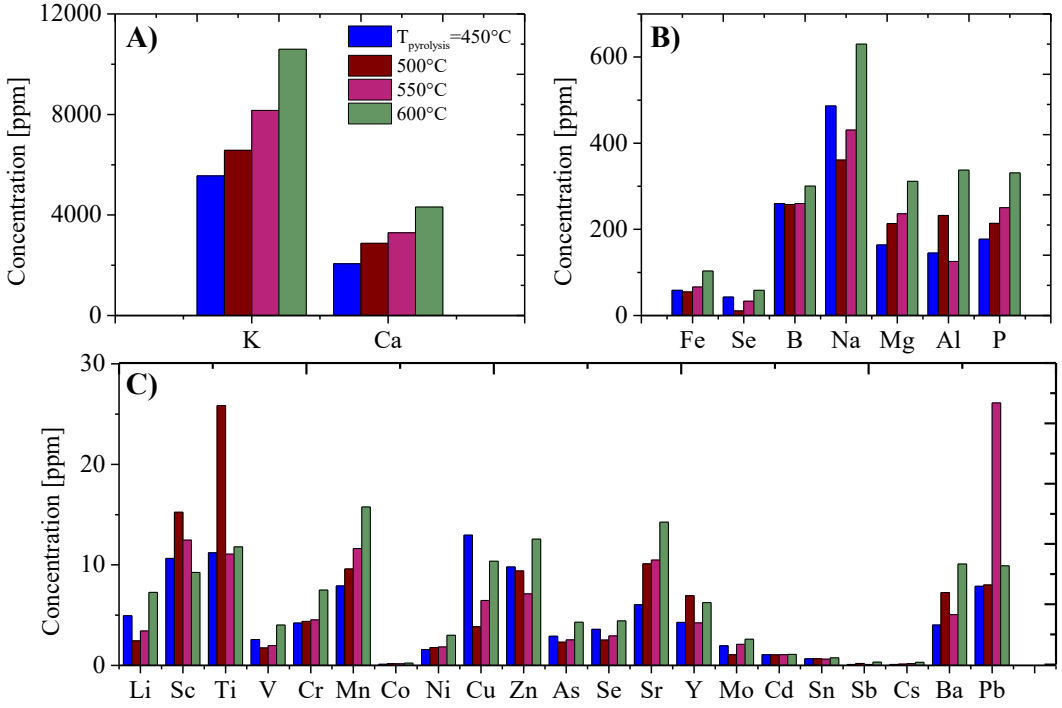

Figure 50: High (A), medium (B) and trace (C) concentration metal distribution from ICP-MS in char samples at different pyrolysis temperature.

By performing a mass balance on primary metals, it is possible to estimate the amount of sequestered metal in biochar compared to the metal in the feed. Results for selected metals are reported in Figure 51 as a function of pyrolysis temperature. Around 80-90% of K entering the pyrolysis system is retained in the biochar, with a non-monotonic trend with a minimum at 500°C. Similarly, Ca retention is between 70-90%. Follows Mg with 65-75% retention.

Finally, P and Fe are the least sequestered metals in biochar (45-60% and 30-45%, respectively). A more detailed analysis on metal content in bio-oil and on the surface of the catalyst would be needed to close the mass balance and to understand where else these metals accumulate in the system.

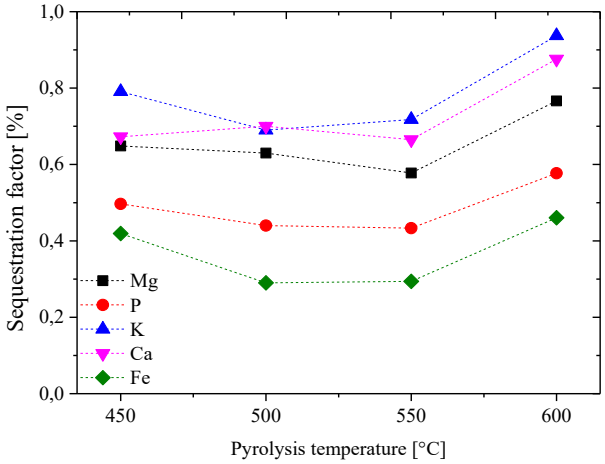

Figure 51: Effect of pyrolysis temperature on sequestration of selected metals in biochar.

Under the worst-case hypothesis that metals not sequestered in biochar are all reposited on the surface of the catalyst during reaction, it follows that Fe preferably is retained on the catalyst, as also observed by Mullen et al. (2013).

Finally, coke deposition on the catalyst remains relatively low and nearly constant (4–4.4 wt.%), suggesting that the amount of coke is determined by the operative conditions in the catalytic stage (T=500°C, τ=20 $g_{catalyst}$ min/g_{OS}), more than the composition of the incoming vapours, in agreement with that reported by Liu et al. (2017).

4.3 Effect of cracking temperature

This section systematically investigates the effect of temperature of the catalytic stage (400-550°C) on the extent of deoxygenation, product selectivity, and the ultimate quality of the bio-oil, while holding primary pyrolysis conditions constant. An HZSM-5 zeolite catalyst has been used for the experimental campaign.

Figure 52 illustrates the effect of cracking temperature on the product yield distribution during the ex-situ catalytic fast pyrolysis of olive stone. During all experiments, the pyrolysis temperature was set to 500°C and the catalyst space-time was 20 $g_{catalyst}$·min/g_{OS}.

Given that the pyrolysis step is not influenced by the operating conditions of the catalytic step, the solid char yield is basically constant (≈19.0±0.5 wt.%), in agreement with the trend observed in Section 4.1 for the effect of space-time and reported by Hernando et al. (2016). Minor deviations from the mean value are attributable to inaccuracies in weighing the solid residue and to slight errors during manual continuous feeding. The char yield aligns well with the feedstock's fixed-carbon content of 19.5% measured from TGA.

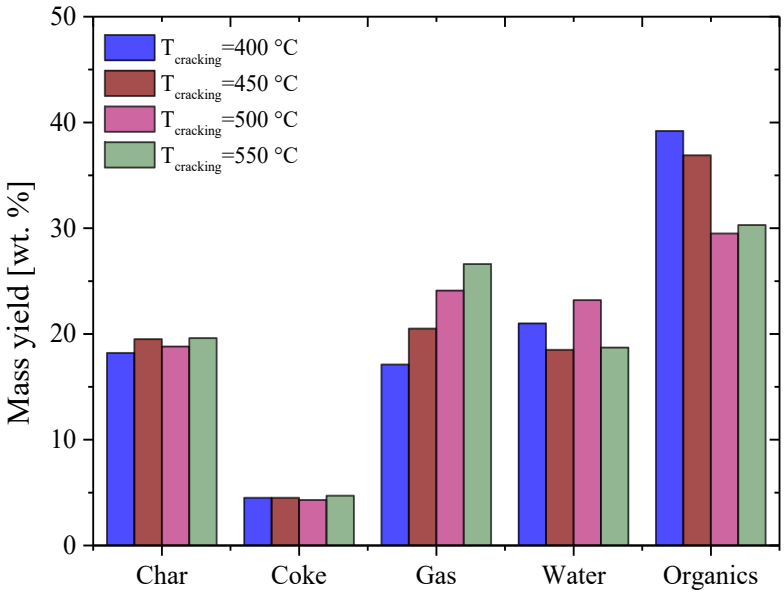

Figure 52: Effect of cracking temperature on the mass yields of the main product fractions. Conditions: $T_{pyrolysis}$=500°C, τ=20 $g_{catalyst}$ min/g_{OS}.

Higher cracking temperatures enhanced the catalyst's activity, leading to an increase in gas yield and water content at the expense of organics. The water yield did not exhibit a clear tendency to increase, with a mean value of 20.4±1.7 wt.% (see Hernando et al., 2016), despite the volumetric water content of the resulting bio-liquid is increasing- as discussed in Section 4.4. Similarly, the coke yield was scarcely influenced by the change in the cracking temperature and the mean values obtained (4.5±0.1 wt% yield with respect to biomass feed and 10 $\%_{coke}/g_{catalyst}$) are in excellent agreement with the literature. For instance, 5.2 wt% coke was obtained by Aho et al. (2008) during catalytic pyrolysis of pine wood in a fluidized bed reactor while Zhang et al. (2009) found a coke yield of 8.4 wt%

during corncob catalytic fast pyrolysis in the presence of ZSM-5. Finally, a coke yield of 3.8 wt% was achieved by Mante & Agblevor (2011) in hybrid poplar wood pyrolysis and 2.87 wt.% by Stephanidis et al. (2011b) for beech wood. Interestingly, Pütün et al (2009) found that coke content on ZSM-5 decreases with catalyst bed temperature in the 350-500°C range but using a dual fixed-bed reactor apparatus. Similarly, Wang et al. (2014) reported a comparable reduction in coke yield in their study on the catalytic pyrolysis of hybrid poplar using a two-stage microreactor system.

The yield of organics is reduced by increasing the temperature of the catalytic step due to the faster decomposition of primary pyrolysis vapour into permanent gases (CO, CO_2, CH_4 and light hydrocarbons) and light oxygenated molecules. This trend was observed also by Liu et al. (2017) for the two-stage microwave-assisted catalytic pyrolysis of corn stover and by Pütün et al. (2009) during the catalytic upgrading of olive residue-derived pyrolysis vapours in a dual fixed-bed reactor.

As regards the composition of the gaseous product, carbon monoxide (CO) and carbon dioxide (CO_2) are the most abundant compounds, with lower amounts of methane (CH_4), light alkanes and light olefins (Figure 53-A and 53-B). It is interesting to note that the yield of CO_2 is not significantly influenced by the cracking temperature (≈9.5±0.3 wt%), while CO yield systematically increases in the 400-550°C range, going from 5.12 wt.% to 11.48 wt.%. The higher sensitivity of CO yield to cracking temperature, and the quite stable CO_2 yield, suggest that catalytic decarbonylation is the dominant temperature-dependent deoxygenation pathway in the second stage, whereas decarboxylation is less affected by the catalytic conditions and likely occurs primarily during initial pyrolysis. According to Hernando et al. (2016), higher cracking temperatures favour decarbonylation and decarboxylation reactions, while slowing dehydration. Moreover, the hydrocarbon yield increases with cracking temperature, as higher temperatures facilitate the cleavage of long aliphatic side chains from phenolic compounds (Bhoi et al., 2020). For example, CH_4 can be produced through the demethoxylation of pyrolysis vapours followed by subsequent reduction (Liu et al., 2014a).

H_2 is always the less abundant product in all experiments, with yields ranging from 0.03 wt.% when $T_{cracking}$=400°C to 0.08 wt.% when $T_{cracking}$=550°C . Similar results in terms of gas production were reported by Hernando et al. (2016) for wheat straw pyrolysis.

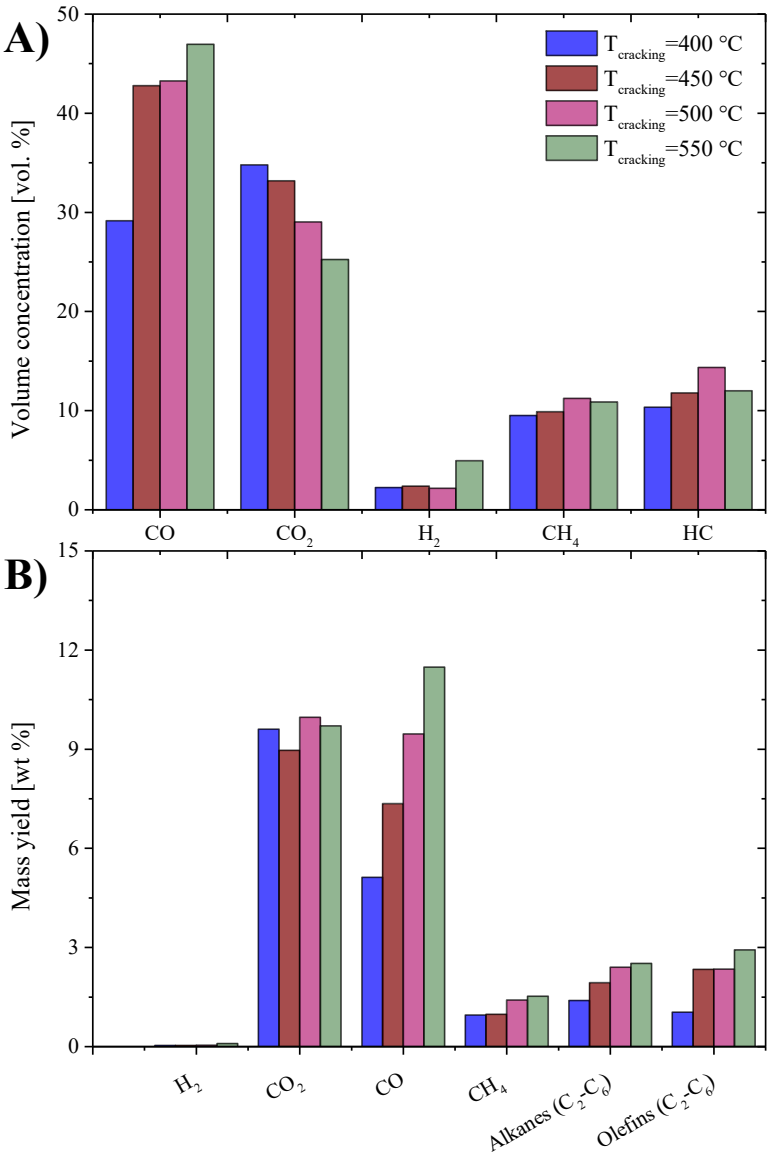

Figure 53: N_2-free composition of pyro-gas (A) and yields of single gas-phase species (B) as function of cracking temperature.

Increasing the cracking temperature in the catalytic stage decreases the concentration of nearly all families of oxygenated compounds, namely aldehydes, furans, ketones, organic acids (Figure 54). Increasing the cracking temperature appears to be as beneficial, as increasing the space-time, to reduce light oxygenates like aldehydes, ketones and organic acids. Aldehydes and ketones can react via ketonization and aldol condensation to produce bigger molecules (Asadieraghi et al., 2015), but at higher temperature decarbonylation and decarboxylation reaction are favoured.

In particular, it has been suggested that the pore structure of HZSM-5 may promote decarbonylation of ketones (Wang et al., 2015b) by enabling the involved species to adsorb in close proximity (Pujro et al., 2021). The mechanism involves the adsorption of the C=O group onto the acid site of the zeolite via an O–Al interaction. The surrounding acidic sites facilitate the cleavage of C–C bonds thanks to electron migration next to the C atom in the C=O bond, producing

adsorbed alkyl radical species and adsorbed CO, which are subsequently released (Wang et al., 2015b; Pujro et al., 2021).

As reported by Hernando et al. (2016), increasing the cracking temperature leads to a decrease of organic acids in the oil, and especially of acetic acid (whose relative peak area decreased from 10.66% to 2.83% as the cracking temperature was raised from 400°C to 550°C), which undergoes ketonization to produce acetone and then is converted to olefins and aromatics (Gayubo et al., 2004b). Similarly, propanoic acid was completely degraded at 550°C and butanoic acid was not observed.

The cracking of lignin oligomers produced in the first reactor is enhanced by increasing the temperature of the catalytic stage, resulting in a higher yield of alkylphenols (from 6.52% to 18.66%) at the expense of methoxyphenols, whose concentration decreases from 31.65% to 26.68%. At temperatures above 450 °C, the demethoxylation and demethylation of guaiacols and syringols to form alkylphenols appear to be promoted (Wang et al., 2015a). Nevertheless, the effect of cracking temperature on alkyl-phenol production is less pronounced than that of pyrolysis temperature, indicating that the primary thermal decomposition of olive stones plays a more significant role in vapor composition than the catalytic step in this context. Specifically, a 150°C increase in pyrolysis temperature led to a ~24% increase in alkylphenols (from 10.2% to 34.4%), whereas the same temperature delta in the cracking stage yielded only a ~12% (from 6.52% to 18.66%). This result suggests that primary thermal decomposition, rather than secondary catalytic upgrading, is the dominant step controlling the initial formation of phenolic structures.

The concentration of hydrocarbons—particularly monoaromatic hydrocarbons and polycyclic aromatic hydrocarbons (PAHs)—increases with rising catalytic temperature. Increasing temperature is beneficial to the selectivity of aromatic hydrocarbons and oxygenated aromatics (Hernando et al., 2016, Liu et al., 2017). It is commonly accepted that bulky oxygenated molecules such as phenols are cracked on the outside of the catalyst structure (external acidic sites) producing smaller fragments, while the conversion of light derivatives into aromatics happens within the pores of the zeolite (Liu et al., 2020). This concept helps explain our observations: large methoxyphenols (e.g., syringols) from lignin likely undergo initial cracking on the external surface of the HZSM-5, breaking down into smaller, less bulky alkylphenols. These smaller phenolic molecules can then potentially enter the zeolite micropores to be further deoxygenated and converted into aromatic hydrocarbons. At higher temperatures, aromatic intermediates can undergo further alkylation, cyclization, and dehydrogenation, leading to larger, more condensed ring systems. This process is a known pathway to coke formation, suggesting that the observed PAH increase is a direct precursor to the catalyst deactivation. The PAHs increase with temperature from 0.43% at 400°C to 8.19% at 550°C, and this is related to the coke deposition on the catalyst's surface. As previously discussed regarding pyrolysis temperature, naphthalenes

constitute the largest fraction of PAHs (about 64% of all PAHs at 550°C). Additionally, anthracenes and indenes were found at higher concentrations with increasing temperature, representing roughly 26% and 1.8% of total PAHs.

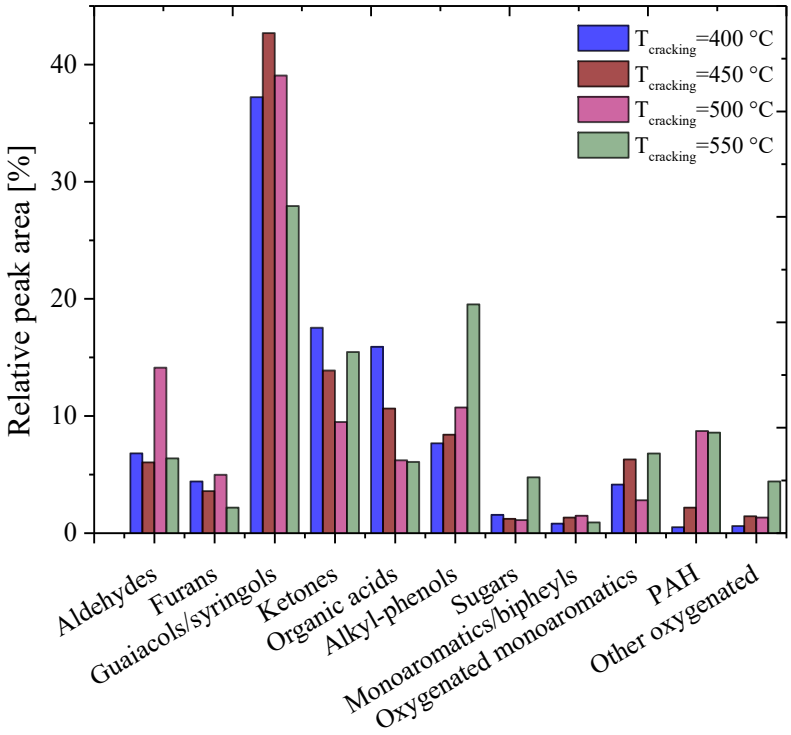

Figure 54: Effect of cracking temperature on the chemical family distribution in the upgraded bio-oil. Pyrolysis temperature held constant at 500°C and space-time of 20 $g_{catalyst}$ min/g_{OS}.

4.4 Discussion

Figure 55 and 56 illustrates the effect of the operating conditions on the elemental molar composition of the resulting char and bio-oil samples. The composition of the char is, as expected, independent of the space-time and cracking temperature since the char is produced in the primary reactor and is not affected by the conditions in the downstream catalytic reactor (Figure 55-A and C). This aspect confirms the repeatability of the experimental tests. On the other hand, increasing the pyrolysis temperature results in char samples with improved composition, as evidenced by an increase in carbon content from 78.74% at $T_{pyrolysis}$=450°C to 87.87% at $T_{pyrolysis}$=600°C. Although its high carbon content makes it a good solid fuel potentially capable of thermally co-sustaining the process, its porosity confers high value for applications such as soil fertilization, due to its ability to reduce the leaching of essential nutrients (Bhoi et al., 2020). Other potential uses, including as activated carbon or catalytic support, have also been explored in the literature (Dada et al., 2023).

Looking at Figure 56, it is evident that both space-time and the temperature of the catalytic stage are responsible for increasing the water concentration in the condensed pyrolysis oil. This phenomenon can be explained in terms of the greater contribution of decarbonylation, decarboxylation, and dehydration reactions of the pyrolysis vapours when the operating conditions of the catalytic

stage are more severe. Conversely, increasing the temperature of the pyrolysis stage leads to a reduction in the water content of the resulting oil. A higher pyrolysis temperature promotes, already during the thermal decomposition of biomass, the production of permanent gases at the expense of organic vapours, which are characterized by a different composition upon contact with the catalyst. Since the catalytic bed conditions in this test series were kept constant (500 °C and τ = 20 min), the reduction in water content is also attributable to the lower contribution of dehydration reactions.

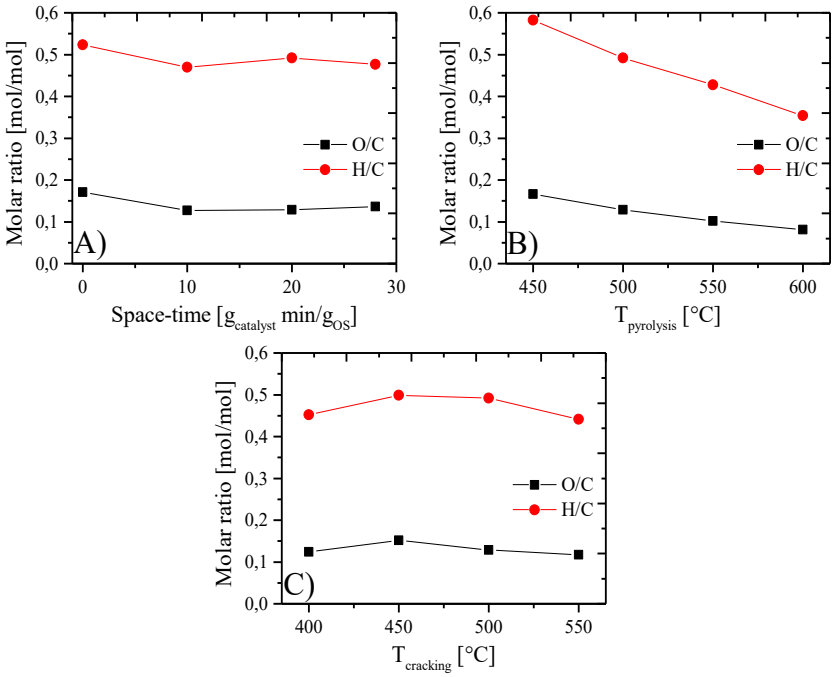

Figure 55: Effect of space time (A), pyrolysis temperature (B) and cracking temperature (C) on the elemental composition of solid char.

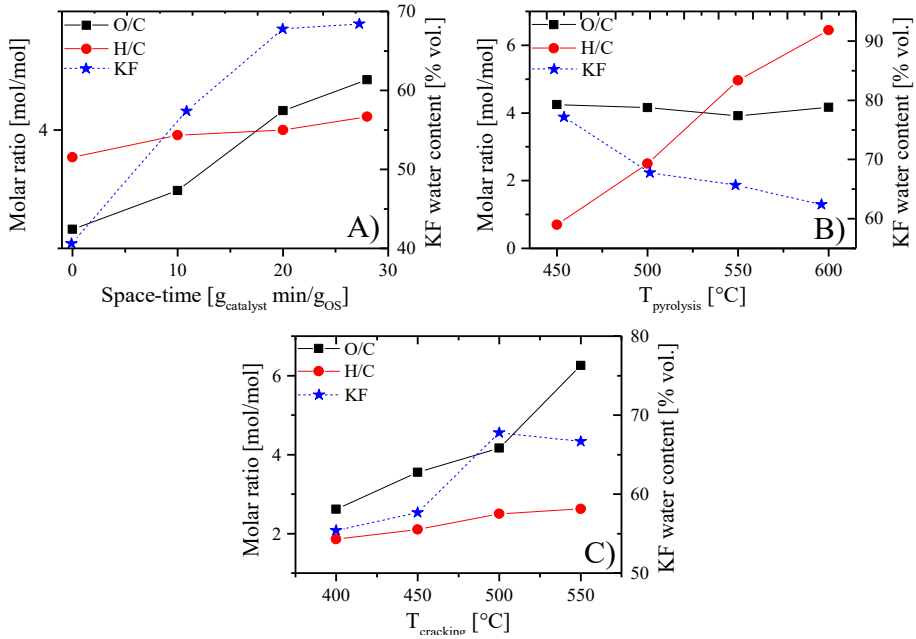

Figure 56: Effect of space time (A), pyrolysis temperature (B) and cracking temperature (C) on the water-free molar composition of the aqueous fraction of bio-oil.

One of the key aspects in catalytic pyrolysis is reducing the oxygen content in bio-oil, as it represents one of the main factors limiting its use as a high-grade fuel due to its low energy density (Gollakota et al., 2016). However, it is not only the overall oxygen content that is critical, but also the specific forms (i.e., functional groups) in which oxygen is present in the bio-oil. Acids, aldehydes, ketones, and sugars are known to be reactive compounds that contribute to instability in pyrolysis oils (Oasmaa et al., 2011; Cai et al., 2021). The preceding sections have described how, through the use of the HZSM-5 catalyst and the proper balance of key operating parameters—space-time, pyrolysis temperature, and catalytic cracking temperature—it is possible to affect the bio-oil composition. In Figure 57 the effect of space-time, pyrolysis temperature and cracking temperature on the oxygenated compound content of bio-oil has been compared.

The O/C molar ratio of the organic fraction in the condensed bio-oil appears to increase with both space-time and cracking temperature, which at first glance contradicts expectations. In the fractional condensation process following the catalytic reactor the carbon-rich, energy-dense fraction condenses first at ambient temperature, while a secondary set of condensers at 0°C collects an aqueous fraction of the bio-oil. The elemental analysis is performed on the "as-condensed" raw bio-oil. Due to its limited volume, samples of the heavy fraction could not be analysed.

This limitation notwithstanding, these results do not contradict the recognized deoxygenation capability of HZSM-5. Supporting evidence includes increased formation of carbon oxides and water—evidence of oxygen (and carbon) removal—and an increased proportion of non-oxygenated compounds at the expense of oxygenated species in the bio-oil. Deoxygenation is incomplete but evident, and its extent grows with harsher catalytic conditions, as can be appreciated by the results in Figure 57, reporting the change in % area from GCMS associated to oxygenated compounds as a function of the operating parameters. The results show that space-time is the most important parameter for improving bio-oil upgrading, as it reduces the amount of oxygenated compounds more significantly than the cracking temperature, which appears to have only a limited effect. Pyrolysis temperature does not significantly influence the deoxygenation of bio-oil under the experimental conditions investigated in this work. Unfortunately, direct comparison with literature values is not straightforward. Christoforou et al. (2018) reported a reduction in oxygen content in upgraded bio-oil compared to the experiment without catalyst (from 37.06% to 26.80%) during pyrolysis of olive mill solid waste. Similarly, Iliopoulou et al. (2012) reported that, in the presence of ZSM-5 as catalyst, the bio-oil yield decreased to 21 wt% compared to 37 wt% in the non-catalytic test, while the oxygen content was simultaneously reduced from 40% to 31%. Veses et al. (2015) reported a reduction of oxygen content from 30% in the non-catalytic test to 22% in the presence of HZSM-5.

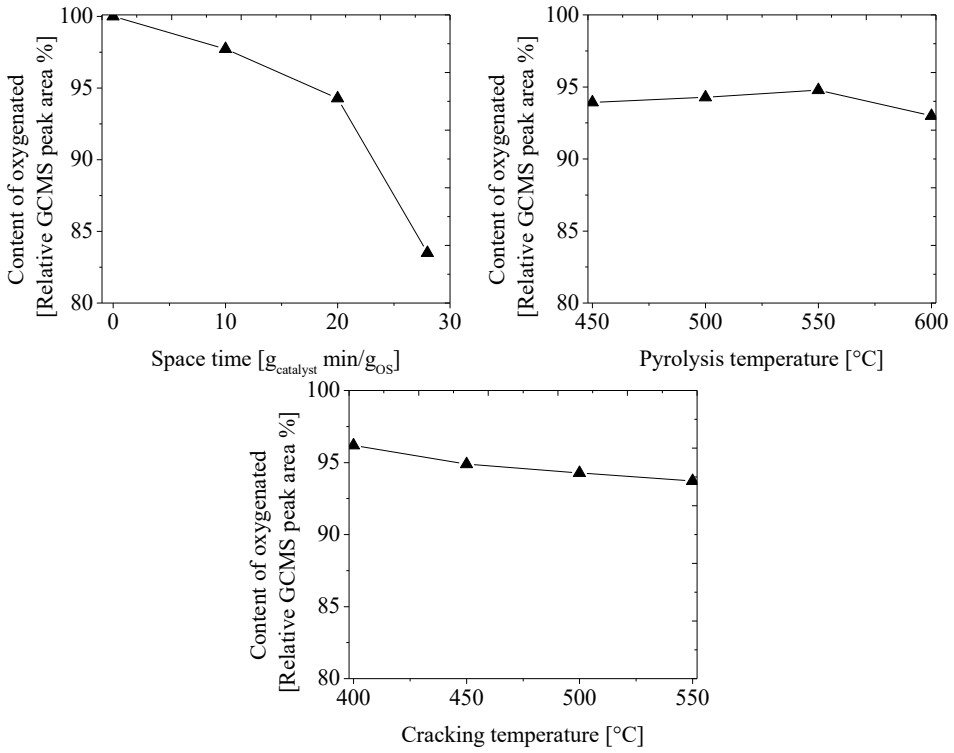

Figure 57: Effect of space-time, pyrolysis temperature and cracking temperature on the oxygenated compound content of bio-oil (relative GCMS peak area).

4.5 Effect of operating parameters on catalyst deactivation

The process parameters not only influence the product distribution – as explored in previous paragraphs – but also dictate the rate and severity of catalyst deactivation. To clarify how catalyst samples behave in different conditions, the carbonaceous deposits on HZSM-5's surface were characterized by Temperature Programmed Oxidation (TPO). This technique provided insights into the distinction of different coke fractions.

Coke deposition on zeolite-based catalyst during catalytic fast pyrolysis of biomass has been widely studied in the literature. For instance, Luna-Murillo et al. (2018) recently investigated catalyst deactivation via coke deposition during *ex-situ* CFP of pine wood and cellulose at 500°C employing different techniques, namely X-ray diffraction (XRD), porosimetry, SEM-EDX, FTIR spectroscopy, NH_3-TPD and NMR. They found that small-oxygenated molecules act as coke precursors within the pores (via ring-condensation reactions), while bulky lignin-derived oligomers are mainly responsible for the formation of external thermal coke. Oxygenate volatiles serve as coke precursors with different level of reactivity and the reaction paths towards coke formation typically include aldol condensation, ketonization, dehydration, hydrogen transfer and polymerization reactions (Lin et al., 2022). In terms of reactivity, it has been found that aldehydes and phenols are the most active in coke deposition (Gayubo et al., 2004a and 2004b). Phenolic compounds are known to have low reactivity on HZSM-5;

therefore they can undergo oligomerization and dehydration (loss of water) and produce coke on the external surface of the catalyst (Lin et al., 2022). From temperature programmed oxidation (TPO) analysis, different peaks associated with different kinds of coke can be identified. For instance, Fan et al. (2017) observed a bimodal DTG curve from the TPO of spent zeolite samples, recalling the common distinction between a soft or "thermal" coke (type I coke) burning at lower temperatures, and a hard or "catalytic" coke (type II coke) burning at higher temperatures. Coke deposition is a ubiquitous phenomenon that cannot be completely inhibited, but some strategies have been acknowledged to limit catalyst deactivation by coking:

1. Tuning catalyst's pore structure and acidity distribution (Cai et al., 2020).
2. Co-feeding of H-rich donors (e.g., methanol, water), as reported by Lin et al. (2022).

Results from TPO of spent HZSM-5 samples operated in different conditions of space-time, pyrolysis temperature and cracking temperature are illustrated in Figure 58. The curves exhibit a quite wide distribution with two distinct peaks: a predominant one at lower temperature (460–500 °C) and a smaller one at higher temperature (550–600 °C). This bimodal structure is commonly reported in the literature for the TPO of coke deposited on HZSM-5 zeolites (Gauybo et al., 2004c). The presence of two peaks is the evidence that combustion of carbonaceous deposits of different nature is occurring: a low-temperature coke (type I coke), which is less structured and more volatile, and a high-temperature "catalytic" coke (type II coke), which is more graphitized and aromatic in character (Fan et al., 2017). It can be observed that all combustion events are completed at approximately 700 °C.

It was hypothesized that higher space-time should result in higher total coke yield because of the higher surface area available (higher mass of catalyst), but lower specific carbon content ($\%_{coke}/g_{catalyst}$) due to a progressive dilution effect. Nevertheless, the effect of space-time was found to be negligible within the range investigated in this work, as the TPO profiles are almost identical. This observation is consistent with the similar coke contents measured for these samples, approximately 10.3±0.5 wt%. This can also be related the arbitrary choice of the sample.

In contrast, the temperatures of both the primary pyrolysis stage and the catalytic upgrading stage had a pronounced influence on the shape of the TPO profiles. The pyrolysis temperature affects coke deposition by determining the initial composition of the pyrolysis vapours coming from the spouted-bed reactor. As the pyrolysis temperature (first stage) increases from 450 °C to 600 °C, an enhancement in the low-temperature peak (Type I coke) is observed, together with a less pronounced increase in the high-temperature peak (Type II coke). Interestingly, the profiles obtained at 550 °C and 600 °C show a clear shift of the first peak compared with those recorded at lower temperatures, suggesting a

higher reactivity of the coke originating from pyrolysis vapours generated at higher temperature. This trend can be attributed to the progressively increasing contribution of the purely thermal pathway, which favours the formation of more amorphous coke, relative to the catalytic pathway as the pyrolysis temperature increases.

The effect of the cracking temperature is twofold. On the one hand, a distinct increase in the low-temperature peak (Type I coke) is observed with increasing temperature. In addition, the TPO curves become narrower — particularly on the low-temperature side — and the amount of coke combusted below 400 °C becomes negligible for the sample treated at a cracking temperature of 550 °C. This behavior can be attributed to an increased tendency of coke to graphitize as the reaction temperature rises. Zhang et al. (2014) reported experiments of catalytic conversion of furan (which is found as intermediate product) over HZSM-5 at different temperatures, confirming the different nature of thermal and catalytic coke and suggesting that cracking temperature is a fundamental parameter that controls the degree of aromaticity of coke compounds. Nevertheless, no substantial difference was observed in the coke content of the samples obtained at different cracking temperature (about 10 wt.%).

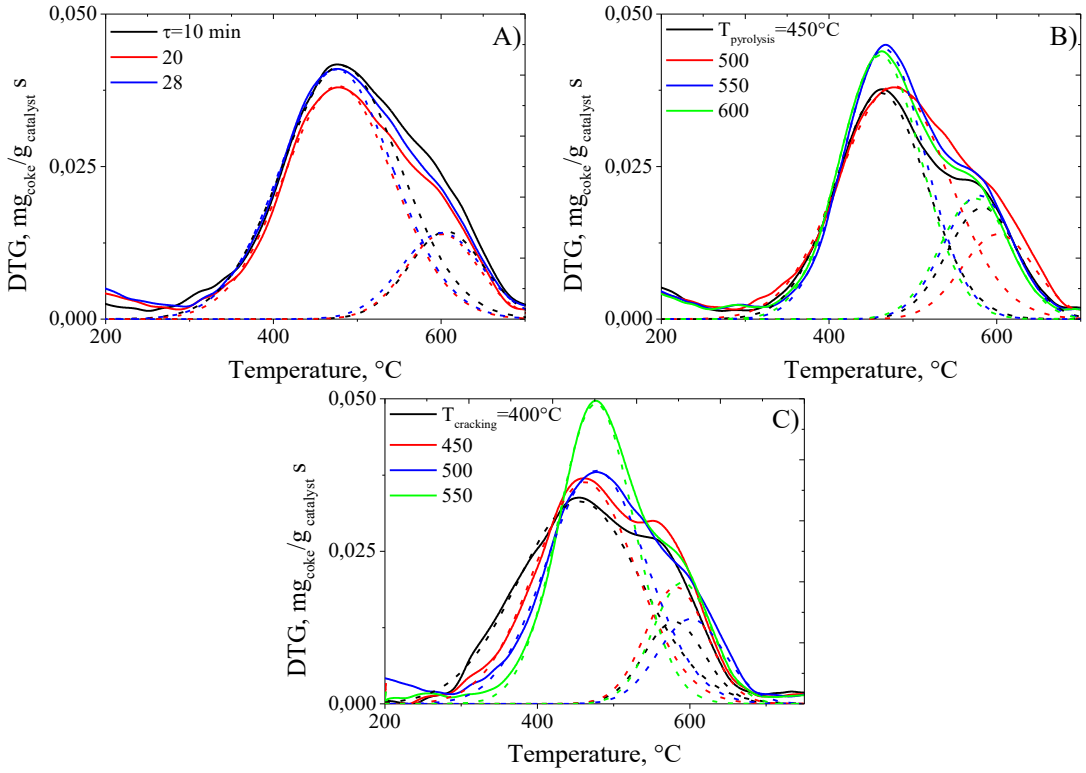

Figure 58: Effect of space-time (A), pyrolysis temperature (B) and cracking temperature (C) on coke deposition on HZSM-5.

The deposition of coke on the catalyst surface is responsible for the bocking and/or neutralization of its active sites, reducing its activity. In order to understand how the deterioration of the catalyst's acidic properties can be correlated to the

loss in activity and to the operating conditions, TPD-NH_3 was performed on the spent catalyst samples.

Figure 59-A shows the effect of space time on the TPD-NH_3 for spent HZSM-5 samples. The total acidity of the catalyst is reduced from 1.58 mmol NH_3/g to 1.42, 1.23 and 1.33 mmol NH_3/g at τ=10, 20 and 28 $g_{catalyst}$ min/g_{OS}, respectively. As a result of the catalytic pyrolysis, some of the acidic sites have been blocked/ covered by carbonaceous deposits, thus reducing the acidity. The shape of the desorption profile is not appreciably modified after reaction, and peaks can still be identified suggesting that the coke coverage does not occur preferentially on specific acid sites.

Nevertheless, no clear trend can be highlighted between total acidity and catalyst space-time, also due to the fact that catalyst deactivation by coke deposition is not homogeneous throughout the catalyst bed but follows and axial profile, therefore depends on the specific catalyst particles constituting the sample.

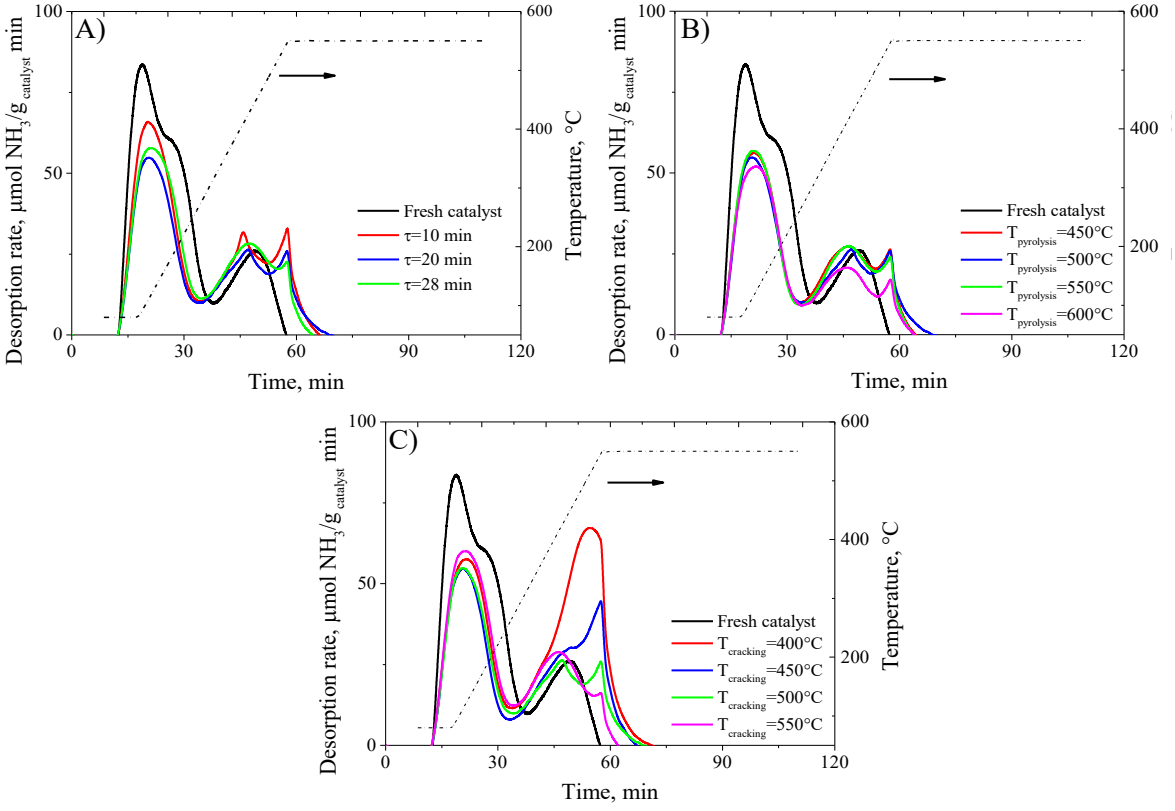

Figure 59: Effect of space-time (A), pyrolysis temperature (B) and cracking temperature (C) on acidity deterioration of HZSM-5.

Similar considerations can be derived for spent HZSM-5 samples operating at different pyrolysis temperatures - i.e., the temperature of the first reactor - and different cracking temperatures (Figure 59-B and 59-C).

In all the measurements it is possible to distinguish a second peak at high temperature. The intensity of these peaks is not influenced by the space time used in the test, while increases with decreasing pyrolysis temperature and cracking

temperature. From further experiment (see Figure 109 in Appendix F) carried out without ammonia adsorption steps it is possible to assume that these peaks are not associated with the desorption of ammonia, but likely with heavy condensed species which desorb during the process. The negligible differences in terms of acidity reduction of catalyst operating at different space-time, pyrolysis temperature and cracking temperature suggests that the reduction of acidic sites has reached a plateau value already after 45 min of reaction. In the presence of water – which is the case of pyrolysis vapours due to intrinsic biomass moisture and dehydration reactions – irreversible dealumination of HZSM-5 can be observed already at 450°C (Gayubo et al., 2004a).

Regeneration of the catalyst via coke oxidation and further acidity measurement would be able to ascertain the degree of irreversibility of the deactivation process.

The results obtained from N_2 adsorption-desorption cycles for spent HZSM-5 samples are reported in Figure 60 in terms of surface area and pore volume. As expected, all samples show a decrease in specific surface area and pore volume compared to the fresh catalyst, mainly as a result of coke deposition. The physical properties of deactivated samples are dependent on the specific operating conditions during the test. For instance, samples used in tests at different space-time (A) present a slightly-increasing trend of surface area and pore volume with space-time. This can be explained by the fact that using higher amounts of catalyst in the bed results in a lower deactivation per unit mass due to the lower local concentration of coke precursors, thus slowing coke formation. In addition, since deactivation is not homogeneous across the catalyst bed, samples retrieved from tests at higher space-time are more likely to include less-deactivated particles.

Increasing the temperature of the pyrolysis step resulted in a decrease in external surface area and an increase of micropore area (B). No significant effect was observed on the pore volume of the samples. Finally, the effect of cracking temperature (C) on the physical properties of spent HZSM-5 showed a more marked trend. More in detail, the sample tested at 400°C experienced the highest deactivation, and increasing the operating temperature resulted in an increase in surface area (both external and of micropores) and of pore volume. This can be explained by the higher deposition of condensed species on the surface of the catalyst, which can limit N_2 adsorption on the sample. Micropore volume experiences the highest reduction compared to the value of fresh catalyst in all operating conditions, suggesting that coke is primarily deposited in these pores. This is in agreement with that reported by Fan et al. (2017). In contrast, Heracleous et al. (2019) observed a more marked reduction in macro- and mesopore volume during catalytic pyrolysis of oak in a fluidized bed/fixed bed system. The difference may be ascribed to the presence of ZrO_2 in their catalyst, which can modify the coke formation pathway.

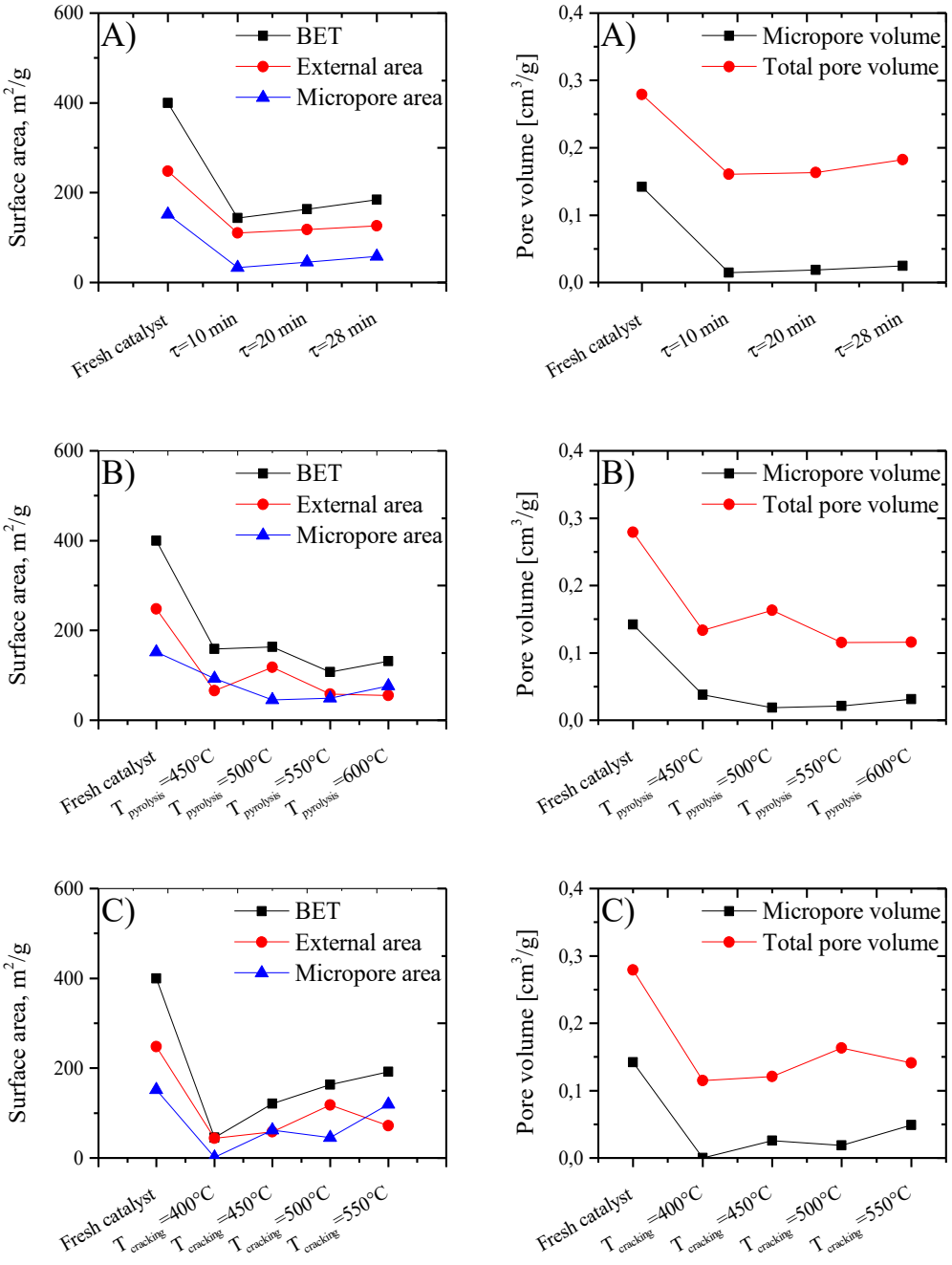

Figure 60: Effect of space-time (A), pyrolysis temperature (B) and cracking temperature (C) on physical properties deterioration of HZSM-5 (TOS= 0.75 h for all experimental runs).

Chapter 5

Comparative catalyst screening for ex-situ CFP of olive stone

This chapter presents a comparative performance evaluation of seven distinct catalysts for the in-line catalytic cracking of pyrolysis volatiles from olive stone fast pyrolysis. As previously detailed, the catalysts selected for the test are two zeolites with different porosity and acidity (HZSM-5 and HY), two Fe-based homemade catalysts (3% Fe/ γ-Al_2O_3 and 3% Fe/dolomite) and the high-surface γ-Al_2O_3 and calcined dolomite used as support for the iron-based catalysts. The last catalyst was prepared recovering the metal of the ashes of sewage sludge combustion (SCA/ γ-Al_2O_3). The rationale of this choice lies in the opportunity to investigate and identify low-cost materials to achieve pyrolysis vapours upgrading, limiting the use of noble and expensive metals and, preferably, taking advantage of otherwise waste end-life materials. The catalyst systems have been chosen to evaluate the effect of the most important properties involved in the upgrade of pyrolysis oil. More specifically, HZSM-5 would maximize aromatics and gas yield due to its strong acidity and shape selectivity and has been considered as a benchmark for comparison, since it is extensively studied for the catalytic pyrolysis of biomass and plastics. The HY zeolite has been chosen to evaluate the contribution of shape-selectivity. Having larger pore dimensions compared to HZSM-5, HY allows larger intermediate molecules to access the pore structure (Qiu et al., 2022a), but it also facilitates their polymerization into coke (Cai et al., 2020).

The potential of γ-Al_2O_3 as acidic catalyst for the catalytic fast pyrolysis of olive stone was highlighted by Recio Ruiz et al. (2023) and Brachi et al. (2022) in a fixed-bed reactor and in a fluidized-bed reactor, respectively. The Lewis acid sites on the surface of γ-Al_2O_3 catalyse the dehydration and cracking of pyrolysis vapours, facilitating the transformation of heavier oxygenated molecules into lighter compounds, water, and non-condensable gases (Tian et al., 2022). Fe-

based catalysts would enhance deoxygenation through redox-mediated pathways like steam reforming of oxygenates.

Moreover, Iliopoulou et al. (2023) demonstrated that Fe/γ-Al_2O_3 catalysts with varying metal loadings (10% and 20%) consistently resulted in lower organic yields and increased water production, favouring the formation of permanent gases. A higher metal loading enhanced the catalytic effect compared to the non-catalytic reaction.

The last two catalysts tested in this experimental campaign—calcined dolomite and a 3 wt.% Fe/dolomite catalyst—have also received attention in the specialized literature for their ability to reduce organic acids in bio-oil (Encinar et al., 2008; Taralas & Kontominas, 2006; Prabhakara et al., 2021a; Li et al., 2023a; Ly et al., 2018; Xu et al., 2022; Valle et al., 2019; Arabiuourrutia et al., 2024; Prabhakara et al., 2021b). The effectiveness of dolomite for tar conversion during apricot stone steam gasification was confirmed by Hu et al., (2006).

5.1 Effect of catalyst on product yields and composition

The screening of catalysts has been carried out fixing the operating conditions of the pyrolysis and cracking units. More specifically, the adopted conditions are: $T_{pyrolysis}$=$T_{cracking}$=500°C and space-time of 20 $g_{catalyst}$ min/g_{OS}.

The result of catalysts screening is reported in Figure 61 in terms of mass yield of solid char, coke deposited on the surface of the catalyst, permanent gases and pyrolysis liquid, i.e., pyrolytic water and organics. As it is possible to see in Figure 61, HZSM-5 zeolite exhibits the highest activity in pyrolysis vapor cracking, as indicated by the highest gas and water yields – 26.0 wt% and 23.2 wt%, respectively- among the catalysts examined, coupled with the lowest yield of organic compounds (27.7 wt%) in agreement with literature data (Qiu et al., 2022a; Cai et al., 2020) and previous results on this Thesis.

HY demonstrated lower catalytic activity than ZSM-5 with respect to decarbonylation and decarboxylation (gas production), as well as dehydration (water production). The gas yield reached 19.1 wt.%, while the water yield was slightly lower than that obtained with HZSM-5 (21.0 wt.%). As a result, the yield of organic compounds was comparatively higher (37.4 wt.%).

Shifting the focus to the results obtained from testing alumina and the two alumina-based catalysts (SCA/γ-Al_2O_3 and 3%Fe/γ-Al_2O_3), it can be observed that the yield of permanent gases increases in the order 3%Fe/γ-Al_2O_3> Al_2O_3 > SCA/γ-Al_2O_3, with corresponding values of 17.6 wt.%, 16.0 wt.%, and 15.3 wt.%, respectively. The three catalysts exhibit similar behavior in terms of pyrolysis water yield, with a slightly higher value for Fe/γ-Al_2O_3 (21.2 wt.%) compared to pure alumina (20.2 wt.%) and the SCA/γ-Al_2O_3 catalyst (20.5 wt.%). The yield of organics was maximum for the SCA/γ-Al_2O_3 catalyst (41.1 wt.%). The addition of iron to an alumina support generally results in a further reduction in liquid bio-oil yield and an increase in gas production compared to the use of pure alumina, as reported by Iliopoulou et al. (2023).

No significant differences were found between HY and HZSM-5 in terms of coke yield (3.9 wt.% vs. 4.3 wt.%, respectively), despite the higher surface area of HY (600 m^2/g) compared to HZSM-5 (400 m^2/g). This result contrasts with the findings reported by Aho et al. (2008) for the *in-situ* catalytic pyrolysis of pine wood in a fluidized bed reactor at 450°C. In their comparison of various zeolites (β, HY, ZSM-5, and mordenite), they observed that the coke yield for HY was significantly higher than that for HZSM-5 (16.7 wt.% vs. 5.2 wt.%). They reported a similar trend for the coke content within the zeolite structure, expressed as weight percent of coke per gram of catalyst, which was 39.9 wt.% for HY and only 16.3 wt.% for HZSM-5. Similarly, Valle et al. (2022) reported that, at equal space-time, the coke content was higher for HY than for HZSM-5 during bio-oil conversion in a two-stage catalytic cracking system at 450 °C. The differences observed can be ascribed to the different value of the temperature adopted or the biomass/catalyst ratio used in our tests.

The coking behaviour did not significantly differ when γ-Al_2O_3 is loaded with Fe compared to pure γ-Al_2O_3. The coke yield was 4.5 wt.% in the first case and 5.0 wt.% in the second case. The same result was found by Iliopoulou et al. (2023) while testing 10%Fe/γ-Al_2O_3 and 20%Fe/γ-Al_2O_3 for the catalytic pyrolysis of OMWWS (olive mill wastewater sludge). The lowest coke yield among the alumina-based catalysts was obtained with SCA/γ-Al_2O_3 (4.0 wt.%). Direct comparison with literature is challenging, as studies using waste-derived sludge ash as a catalyst for biomass pyrolysis are scarce.

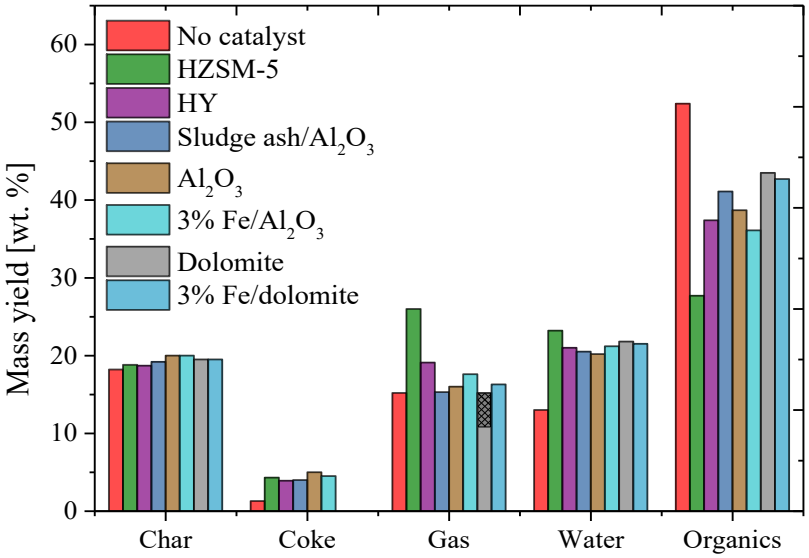

Figure 61: Effect of catalyst type on product yield distribution ($T_{pyrolysis}$=$T_{cracking}$=500°C and τ=20 g_{cat} min/g_{OS}).

Notably, the coke yield for dolomite and 3% Fe/dolomite is negligible compared to the average coke yields for zeolite-based (4.1 wt.%) and alumina-based catalysts (4.5 wt.%). This behavior can be attributed to several factors, including the lower specific surface area of dolomitic catalysts relative to zeolites and alumina, as well as the absence of delocalized acid sites on the surface,

which—as previously noted—are responsible for promoting chemical reactions that lead to the nucleation and agglomeration of coke structures (Wan et al., 2016; Liu et al., 2020). Encinar et al. (2008) observed that the use of dolomite as a catalyst for the cracking of pyrolysis vapours is feasible and leads to a marked decrease in oil yield, accompanied by a corresponding increase in permanent gas production. During catalytic pyrolysis of olive oil waste in a two-stage pyrolysis system, char yield was ≈23.6 wt.% which is in line with the results found in this work (≈19.5 wt.%). Similarly, Taralas and Kontominas (2006) reported that calcined dolomite is effective for tar cracking during the catalytic pyrolysis of exhausted olive husks. They found that increasing the catalyst space-time and/or the catalytic temperature led to higher gas yields at the expense of tar formation.

The gas yields obtained with the two dolomitic catalysts were 15.2 wt.% and 16.3 wt.%, respectively. Notably, calcined dolomite has a CO_2 capture capacity during the pyrolysis process (dark grey area in dolomite gas yield), as also evidenced by the gas composition data presented in Figures 62 and 63. The presence of Fe on the dolomite support substantially inhibited the CO_2 capture capabilities of the material. The yield of water is higher compared to the non-catalytic test (21.8 wt.% vs 13.0 wt.%), as a consequence of the intensification of dehydration reactions (Ly et al., 2018).

The composition of the gas fraction obtained from the catalytic pyrolysis process with different catalysts is reported in Figure 62, both in terms of nitrogen-free volumetric composition (A) and mass yield (B). HZSM-5 is the most active catalyst in terms of decarbonylation (CO production) and the generation of light paraffinic and olefinic hydrocarbons. The CO yield obtained with HZSM-5 is 9.46 wt.%, more than double that of the non-catalytic case (4.35 wt.%). The production of light alkanes and light olefins reaches 2.98 wt.% and 2.29 wt.%, respectively, both significantly higher than in the non-catalytic case (0.99 wt.% and 0.21 wt.%). Methane production was slightly increased compared to the non-catalytic test (1.40 wt.% vs 1.17 wt.%), while H_2 yield is similar and negligible (0.03 wt.% vs 0.02 wt.%).

The HY zeolite also shows good activity in decarboxylation and decarbonylation under the operating conditions studied (8.79 wt% of CO_2 compared to 7.26 wt% of CO). Similarly to what occurs with HZSM-5, the increase in CO production compared to the non-catalytic case is greater than the corresponding increase in CO_2. This represents a trade-off in terms of bio-oil deoxygenation and a drawback in terms of carbon efficiency. In fact, the high CO yields obtained with HZSM-5 imply that a significant amount of carbon is also removed from the bio-oil, hindering the selective removal of oxygen (Shi et al., 2023). Oxygen removal as CO_2 is the most desirable pathway for improving the quality of the resulting oil (Imran et al., 2018). HY produced more methane than HZSM-5 (1.64 wt.%), but the yields of light alkanes and light olefins were not significantly higher than in the non-catalytic test.

The results obtained for the pure γ-Al_2O_3, 3%Fe/ γ-Al_2O_3, and SCA/γ-Al_2O_3 show that in terms of CO_2 production, the three catalysts exhibited similar

performance, with 3%Fe/ γ-Al_2O_3 generating the highest CO_2 yield (10.72 wt%). The iron-based catalysts produced a higher amount of CO_2, further suggesting greater decarboxylation activity. Iron also promotes both the steam reforming of oxygenated compounds present in the pyrolysis vapours with water vapor (originating both from the moisture in the initial biomass and from dehydration reactions), producing CO and H_2 according to the following equation (Czernik et al., 2002; Quan et al., 2017, Hu & Lu, 2010):

$$C_nH_mO_k + (n-k)H_2O \rightarrow nCO + \left(n + \frac{m}{2} - k\right)H_2 \quad [15]$$

and the water–gas shift (WGS) reaction, which converts CO into CO_2:

$$CO + H_2O \leftrightarrow CO_2 + H_2 \quad [16]$$

According to the occurrence of these two reactions, the amount of hydrocarbons is quite totally depressed and an increase in H_2 production is observed. Iliopoulou et al. (2023) reached the same conclusion while studying different Fe- and Mn-based catalysts supported on alumina, silica, and magnesia for the catalytic pyrolysis of olive mill wastes. Transition metals (e.g., Ni, Co, Fe) and noble metals (e.g., Pt, Pd, Ru, Rh) supported on metal oxides such as Al_2O_3, TiO_2, and ZrO_2 are well known for their steam reforming and dehydrogenation activity, which promotes H_2 production (Bhoi et al., 2020; Kan et al., 2020; Liu et al., 2014a; Wang et al., 2022; Qiu et al., 2022b).

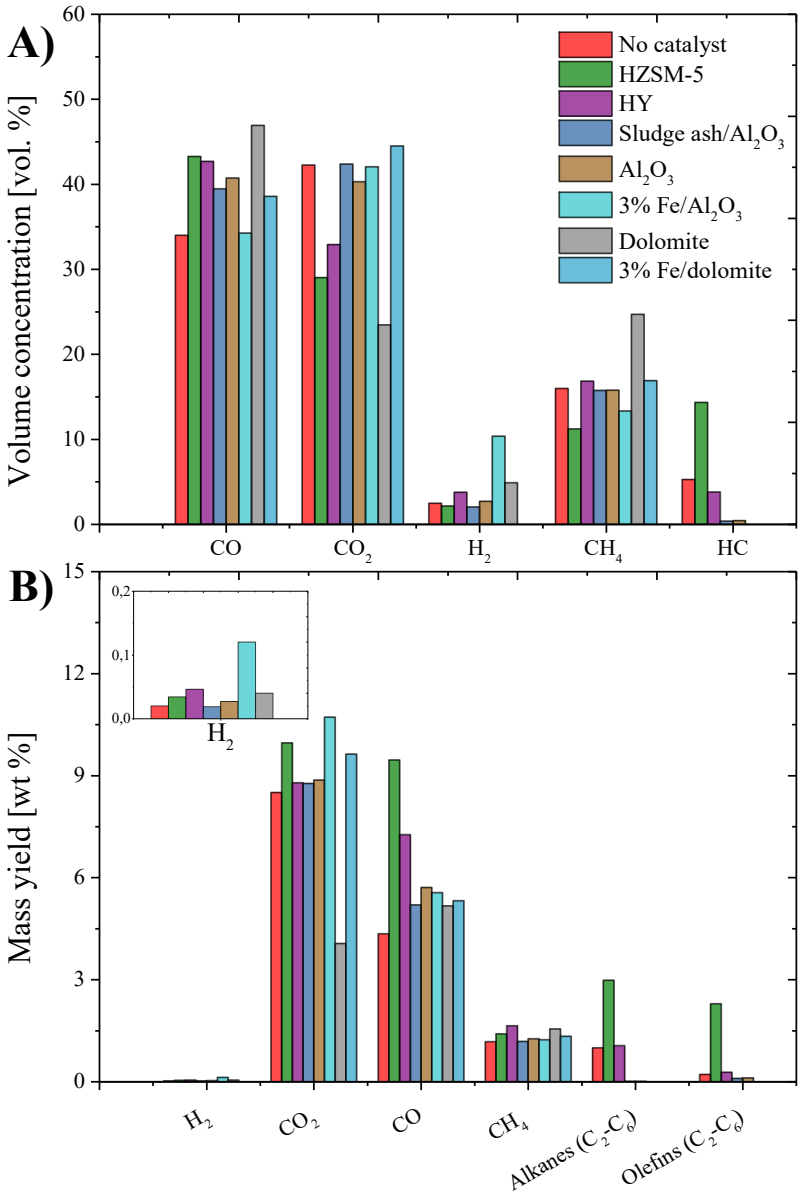

Figure 62: N_2-free composition of pyro-gas (A) and yields of single gas-phase species (B) as function of catalyst type.

Regarding decarbonylation activity, all three catalysts increased CO production compared to the non-catalytic case, with pure alumina achieving the highest yield (5.71 wt.%). Notably, the 3%Fe/γ-Al_2O_3 catalyst showed a stronger tendency to produce hydrogen (0.12 wt.%) than the SCA/γ-Al_2O_3 catalyst (0.02 wt.%) and pure alumina (0.027 wt.%), in agreement with its bifunctional nature (acidic-redox).

A notable effect of calcined dolomite, particularly in the presence of steam, is the increase in H_2 concentration in the produced gas (Prabhakara et al., 2021a; Li et al., 2023a) and the reduction in CO_2 yield. This behaviour can be attributed to the dual role of dolomite as both a catalyst for the water-gas shift (WGS) reaction ($CO + H_2O \leftrightarrow CO_2 + H_2$) and a CO_2 reactive sorbent. The in-situ CO_2 capture by the CaO component of dolomite shifts the WGS equilibrium toward enhanced H_2

production (Prabhakara et al., 2021a). This transient phenomenon of CO_2 capture and WGS catalysis is clearly illustrated by the concentration profiles of the main permanent gases (CO, CO_2, CH_4, and H_2) during the tests with dolomite and 3%Fe/dolomite, as shown in Figure 63-A and 63-B. Hydrogen production is non-steady, with a peak at the initial reaction time (t = 0) followed by a gradual decrease until it is completely suppressed after approximately 15 minutes. Simultaneously, the measured CO_2 concentration is less than 0.1% at the beginning of the reaction, due to the CO_2 capture capacity of the fresh dolomite, which progressively becomes saturated over time. Once the dolomite becomes fully saturated, the H_2 produced is converted into CO and H_2O, resulting in a decline in hydrogen concentration. A similar, though much faster and less pronounced CO_2 capture-release cycle was observed for the Fe/dolomite catalyst, due to the reduced CO_2 capture capacity caused by the presence of the iron loading (Figure 63-B). The same CO_2 capture phenomenon was reported by Valle et al. (2019) during bio-oil upgrading using calcined dolomite as a low-cost basic catalyst. During the first 1.5 h of reaction, they recorded a very low CO_2 concentration and a high, decreasing hydrogen concentration during the dolomite carbonation period.

The use of dolomite would therefore be advantageous also in limiting CO_2 emissions in the pyrolysis gas, improving its combustion characteristics and calorific value. Clearly, for this to occur, it is necessary to use a sufficient amount of catalyst to prevent complete saturation during the reaction, or alternatively, to implement in-situ catalyst regeneration cycles. The use of such sorbents is central to "sorption-enhanced" processes, e.g., sorption-enhanced gasification (Boon, 2023; Dou et al., 2019).

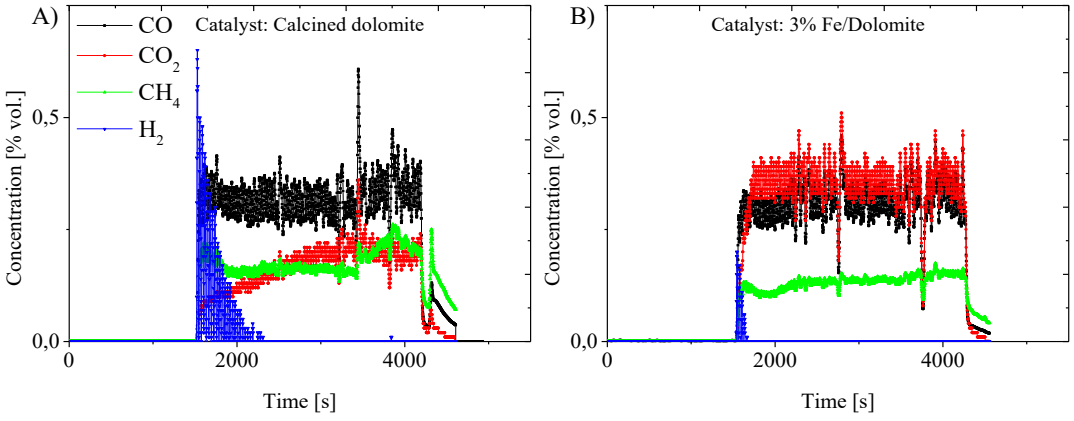

Figure 63: Time evolution of permanent gases during test with dolomite (A) and 3% Fe/dolomite catalyst (B)

Dolomite is subject to deactivation through both coke deposition and carbonation (Valle et al., 2019). The active CaO component reacts with the CO_2 produced during pyrolysis to form inactive $CaCO_3$ (carbonation). This process saturates the basic sites of the catalyst, thereby reducing its activity for ketonization and deoxygenation reactions (Valle et al., 2019). The catalyst can be

regenerated by heating it to high temperatures (e.g., >800 °C) to decompose $CaCO_3$ back into CaO, thereby releasing the captured CO_2 (Chen et al., 2021).

As previously reported, the different catalysts significantly alter the composition of bio-oil, reflecting changes in reaction pathways during upgrading of volatiles. The H/C and O/C ratio of the bio-oil produced in the different tests (Figure 64-A) have been evaluated performing elemental analysis, together with the water concentration determined by Karl Fischer titration. The H/C molar ratio was not significantly affected by the choice of catalyst, while a strong effect on the O/C ratio (ranging between 5.0 and 18.1) was observed. The O/C ratio is linked to the KF-determined water content, confirming that the oxygen removed from the oil is partly recovered in the form of water (dehydration of oxygenates).

pH measurements have also been carried out on bio-oil samples (Figure 64-B). Despite being an easy measurement, it has a limited validity since many compounds in bio-oil which contribute to acidity are not soluble in water and vice versa. A robust measurement would be the total acid number (TAN), that is a measure of the amount of KOH to neutralize 1 g of sample (mg KOH/g_{oil}).

The results revealed that all bio-oil samples produced were highly acidic, with values ranging between 2 and 3. A weak correlation was observed between pH and the content of organic acids, expressed semi-quantitatively as area % in GC–MS analysis; specifically, higher concentrations of organic acids corresponded to lower pH values. Based on these measurements, it can be concluded that HZSM-5 promotes a partial reduction in the organic acid content of the bio-oil, increasing the pH to approximately 3. In contrast, all other catalysts yielded oils with lower pH values.

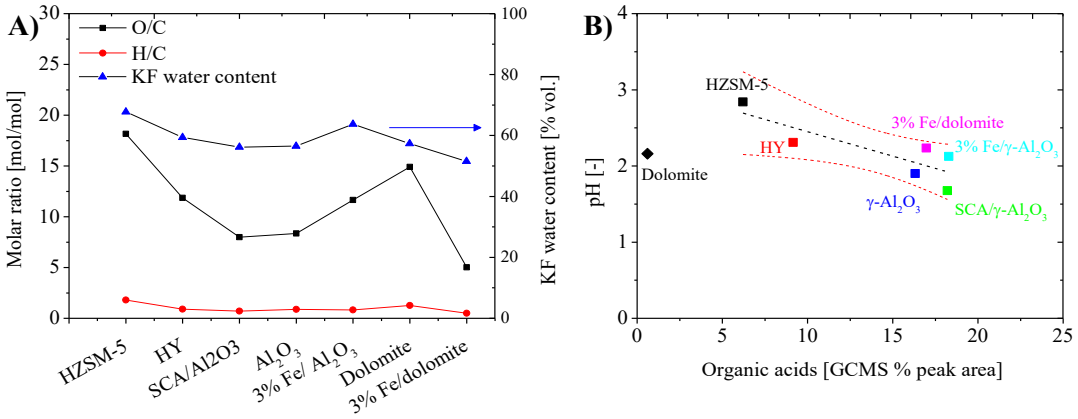

Figure 64: Molar composition (A) and pH (B) of the aqueous fraction of bio-oil including water as a function of catalyst type.

As previously reported, the different nature of the catalysts, both in terms of physical properties (such as porosity and pore structure) and functionalities (acidic catalysts, basic catalysts, catalysts with redox effects), significantly influences both the yield and the composition of the bio-oil. Figure 65 shows the bio-oil composition obtained with the different catalysts, expressed as relative abundance of each compound evaluated from GCMS data. The data confirm the capacity of

HZSM-5 zeolite to reduce the content of light oxygenated species (e.g., organic acids, aldehydes, ketones, furans, and anhydrosugars) while simultaneously promoting the production of aromatic compounds (both oxygenated and non-oxygenated) and PAHs compared to the non-catalytic reaction. HY zeolite is effective in deoxygenating pyrolysis vapours but is less selective for aromatic hydrocarbons compared to HZSM-5, in agreement with that reported by Zhang et al. (2016b). It tends to produce a higher proportion of aliphatic hydrocarbons and a wider range of oxygenated compounds, although the overall oxygen content is reduced (Liu et al., 2014a). HY also can effectively reduce the content of acids in bio-oil (Liu et al., 2014a). The HY also promotes the formation of PAHs and totally reduces the presence of sugars but strongly enhances the production of alkylphenols.

HY zeolite, due to the bigger pore size compared to HZSM-5, favoured the conversion of methoxyphenols into alkyl-phenols by alkylation and deoxygenation in agreement with that reported by Valle et al. (2022). Diffusional limitations of bulky oxygenated molecules are therefore reduced due to the bigger pore size and to the straight pore structure compared to HZSM-5.

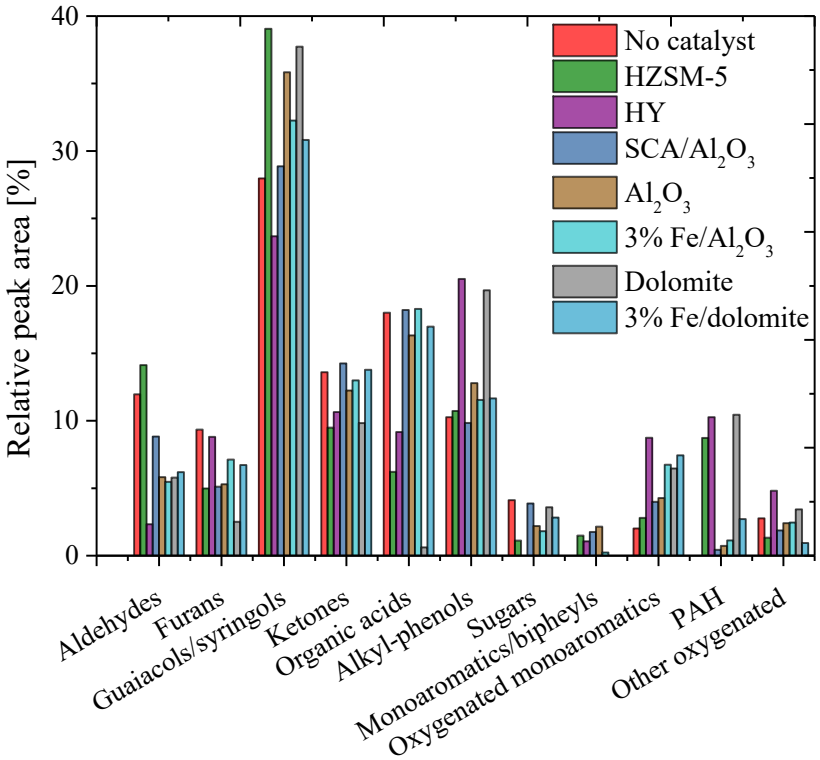

Figure 65: Effect of catalyst type on bio-oil composition ($T_{pyrolysis}$=$T_{cracking}$=500°C and τ=20 g_{cat} min/g_{OS}).

None of the three alumina-based catalysts (SCA/γ-Al_2O_3, pure γ-Al_2O_3, and 3%Fe/ γ-Al_2O_3) were able to reduce the acid content in the bio-oil compared to the non-catalytic case, even if the presence of Lewis acidic sites should promote the conversion of organic acids into ketones (Cheng et al., 2016; Qiu et al., 2022b). The reduction in aldehyde and furan content was much more pronounced than that of ketones. The 3%Fe/γ-Al_2O_3 catalyst reduced the aldehyde content to 4.90% compared to 10.10% in the non-catalytic test, while SCA/γ-Al_2O_3 had a

less marked effect (7.70%). The 3%Fe/γ-Al_2O_3 catalyst shows the highest catalytic activity for degradation of anhydrosugars. The three γ-Al_2O_3-based catalysts promote the formation of oxygenated aromatics and show a very limited effect in PAH formation.

High effectiveness in removing acidic compounds—such as acetic acid—has been observed for dolomite. In fact, the concentration of organic acids in the bio-oil obtained using dolomite is only 0.53%. Its effect is also higher compared to that observed for HZSM-5. This property of dolomite was also reported by Valle et al. (2019) and Prabhakara et al. (2021a). This property is particularly advantageous, as it significantly reduces the oil's corrosiveness (Valle et al., 2019). One of the suggested mechanisms involves acid neutralization by the basic sites (CaO, MgO) present in dolomite, followed by ketonization reactions that convert carboxylic acids into ketones (Valle et al., 2019; Arabiourrutia et al., 2024). Nevertheless, the concentration of ketones did not increase compared to the non-catalysed experiment. Carboxylic acids can be converted into hydrocarbons through decarboxylation (Ding et al., 2018; Ly et al., 2018) in the presence of basic catalysts. Among the catalysts investigated in the study, dolomite led to the higher total phenol content (50.13%, of which 17.18% alkyl-phenols and the rest methoxyphenols), which is interesting for potential recovery of valuable phenolics for innovative applications; for example, alkylphenols serve as key precursors for detergents, antioxidants, fuel and lubricant additives, and as partial substitutes in phenolic resins, as reported by Pinheiro Pires et al. (2019).

Dolomite also facilitates the transformation of heavy phenolic compounds (e.g., syringols and guaiacols) into lighter, less oxygenated alkylphenols (Valle et al., 2019; Prabhakara et al., 2021a). This occurs via demethoxylation and dealkylation reactions, which reduce both the oxygen content and structural complexity of the phenolic fraction, thereby enhancing the overall quality of the bio-oil.

However, this positive result was offset by the significant formation of PAHs, a yield comparable to that of the zeolite catalysts. It is also noteworthy that, while in the case of HZSM-5 the main polyaromatic compounds are naphthalene derivatives (with some phenanthrene derivatives and traces of indenes and anthracenes), in the case of HY and dolomite the main component is represented by both oxygenated and non-oxygenated indene derivatives (66.7% of the total PAHs for HY, and 58.4% in the case of dolomite), with naphthalenes ranking second in relative abundance. No phenanthrene- or anthracene-derived compounds were detected in the tests with dolomite. The addition of iron to the dolomite support promotes the formation of furans and ketones compared to dolomite alone but dramatically suppressed the deacidification capability of the catalyst. The complete loss of deacidification activity observed is supported by the results obtained from TPO analysis, in which it is observed that CO_2 capture capability of Fe/dolomite is depressed due to the adding of iron, which covers basic CaO sites responsible for CO_2 capture.

Comparison of XRD spectra between calcined dolomite and Fe/dolomite catalyst has revealed the presence of non-homogeneously distributed iron oxides on the

catalyst's surface. These can be responsible for the (partial) covering of the basic sites of the dolomite support already during preparation and calcination, making it passive towards deacidification but active for gas-phase reactions. This explains why, despite the presence of a dolomite support, the catalyst did not reduce the organic acid content in the bio-oil.

Preliminary results from the Folin-Ciocâlteu assay for phenol quantification are reported in Appendix F. The TPC (Total Phenolic Content) of the bio-oil samples were plotted against the Total Phenolic Area (TPA), i.e., the sum of area of all compounds from GC-MS with at least one phenolic functional group. No clear correlation has been observed. Future work will be aimed at the systematization of the method to establish a quantitative measurement of phenols in bio-oil.

5.2 Catalyst deactivation

Coke deposition

The temperature programmed oxidation (TPO) profiles of spent catalyst samples are reported in Figure 66. All the catalysts presented mass loss-associated peaks below 700°C, excluding the two dolomite-based catalysts. The HZSM-5 and HY catalysts are characterized by wider DTG curves compared to alumina-based catalysts. As previously discussed, HZSM-5 presents a bimodal curve, with peaks associated to type I and type II coke. All the other catalysts present a monomodal DTG curve. For the two zeolites, the highest peak is located at around 500°C. A second peak for HZSM-5 is located at 600°C. These results are in line with the different nature of the catalysts in terms of internal pore structure and acidity. The high acidity of HZSM-5 (Bronsted sites) coupled with the microporous structure leads to high coke formation via ring-condensation reaction. The HY has a low acidity and bigger pores, leading to the formation of bigger coke molecules but with less graphitic character, meaning that they can burn at a slightly lower temperature.

The three γ-Al_2O_3-based catalysts exhibited only one peak, located at 450°C for pure γ-Al_2O_3 and SCA/ γ-Al_2O_3, and at 370°C for 3% Fe/ γ-Al_2O_3. The absence of the high temperature shoulder peak suggests a lower degree of graphitization of the coke. Alumina mainly possesses Lewis's acid sites, which are less effective than zeolites in promoting deep aromatization reactions, but they remain active in primary cracking. As a result, a fraction of heavy pyrolysis vapours is not completely converted and tends to deposit on the external surface and within mesopores as type I coke. Given the absence of a microporous structure, there is no diffusion-limited combustion within the pores, and all the coke can burn at virtually the same temperature. The shape of the DTG profile for the 3% Fe/ γ-Al_2O_3 catalyst is in agreement with that reported by He et al. (2020).

The two peaks observed for dolomite and Fe/dolomite are explained by the different chemistry of these catalysts. The high peak at high temperature (700-800°C) is associated with the thermal decomposition of $CaCO_3$ that is formed

during reaction (carbon capture). The low temperature peak can be associated to the release of bond-water at lower temperature, probably due to the presence of $Ca(OH)_2$ and $Mg(OH)_2$. The lower peak observed in the case of Fe/dolomite at 700°C confirms that the presence of Fe reduced the capability of dolomite to capture CO_2, as previously discussed.

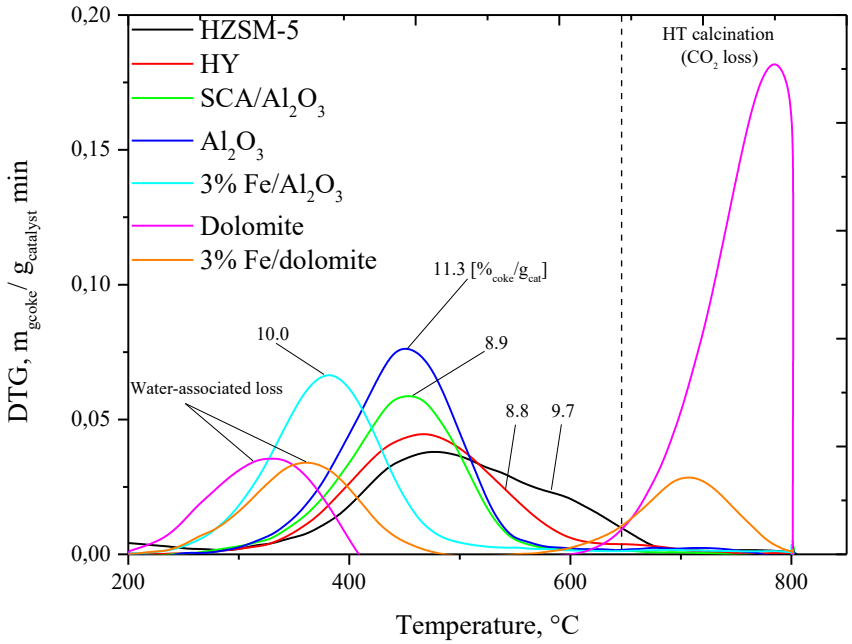

Figure 66: TPO profiles and total coke content of spent catalyst samples.

Physical properties deterioration

As a result of the combined influence of thermal effects (prolonged exposure to the reaction temperature) and catalytic effects (coke deposition on the catalyst surface), a deterioration of the catalysts' physical properties – and therefore activity (Fan et al., 2017)- was observed. As discussed in the literature (e.g., Bartholomew, 2001; Guisnet et al., 1997), during catalytic cracking of pyrolysis vapours, heavy organic molecules and coke precursors (such as aromatics, olefins, and heavy phenolics) adsorb onto the catalyst surface and undergo polymerization. The resulting carbonaceous deposits physically obstruct pore access, particularly within the micropores, leading to a measurable loss of surface area and pore volume. The rapidity of this decline indicates that coking is a primary and fast-acting deactivation mechanism under the investigated conditions.

Porosimetric analysis has been carried out on fresh and used catalyst in order to evaluate the behaviour of catalyst deactivation. Since all the tests had the same duration (TOS=45 min), differences in terms of porosimetry are only due to the nature of the catalyst itself, and how the catalyst interacts with the reaction environment. The analysis has been performed in terms of comparison of specific

surface area, pore volume, and average pore diameter (Figure 67). A significant reduction in BET surface area was observed for the two zeolite-based catalysts, more specifically a reduction of 58.0% and 36.8% (compared to the surface area of fresh catalyst) is obtained for HZSM-5 and HY, respectively. For HZSM-5, micropore volume decrease from 0.142 cm^3/g to 0.019 cm^3/g, while for HY from 0.189 cm^3/g to 0.021 cm^3/g. Mesopore volume decreased from 0.137 cm^3/g to 0.093 cm^3/g for HZSM-5 and from 0.263 cm^3/g to 0.225 cm^3/g for HY. Analysis of mesopore and micropore volume reduction suggests that coke deposition starts primarily within the micropores, as their volume decreases to a much greater extent than that of the mesopores. Subsequently, coke accumulates along the internal pore walls, progressively narrowing the pore entrances and reducing the average pore diameter (Figure 67-C). This evidence confirms that coking is not limited to the external surface but involves diffusion of coke precursors deep into the pore network, including the micropores, making it a pervasive phenomenon. For the sake of comparison, Mullen et al. (2018) reported only a negligible decrease in BET surface area, from 368 to 350 m^2/g, for HZSM-5 pellets (2 mm) during in-situ catalytic fast pyrolysis of eucalyptus wood in a fluidized-bed reactor (test duration not specified). In contrast, Heracleous et al. (2019) observed a more pronounced loss in textural properties for a 10 wt% ZrO_2/ZSM-5 catalyst (3 mm diameter, 5-6 mm length) during ex-situ catalytic fast pyrolysis of oak. In their study, the BET surface area decreased from 303 to 255 m^2/g after 20 min and stabilized at ~250 m^2/g after 40 min, while the mesopore volume declined from 0.38 to 0.32 cm^3/g. The different result can be ascribed to the higher operating temperature used in this work and to the different formulation of the catalyst, and – to a lesser extent – to granulometry.

The γ-Al_2O_3-based catalysts exhibited a mesoporous structure ($V_{micropore} << V_{mesopore}$) and did not undergo significant reduction in terms of surface area in 45 min of reaction. Nevertheless, mesopore volume decrease of 16.6%, 21.6% and 27.3% were registered for γ-Al_2O_3, 3% Fe/γ-Al_2O_3 and SCA/γ-Al_2O_3, respectively. The lowest mesopore volume reduction registered for pure γ-Al_2O_3 suggests that impregnation of metals (or catalytic ashes) on its surface accelerates its deterioration.

Dolomite and 3% Fe/dolomite experienced negligible change in BET surface area and a reduction of 73.5% and 75.1% in mesopore volume, respectively. Unlike zeolites or alumina, dolomite is not a porous material with high surface area. Its catalytic activity derives primarily from surface chemistry (basic CaO and MgO sites), rather than from textural properties. Accordingly, the reaction mechanism occurs on the external surface rather than within a porous network. Deactivation calcined dolomite and 3% Fe/dolomite is therefore not mainly associated with pore blockage, but more with surface coking, whereby a carbonaceous layer covers the external active sites, and carbonation (Valle et al., 2019).

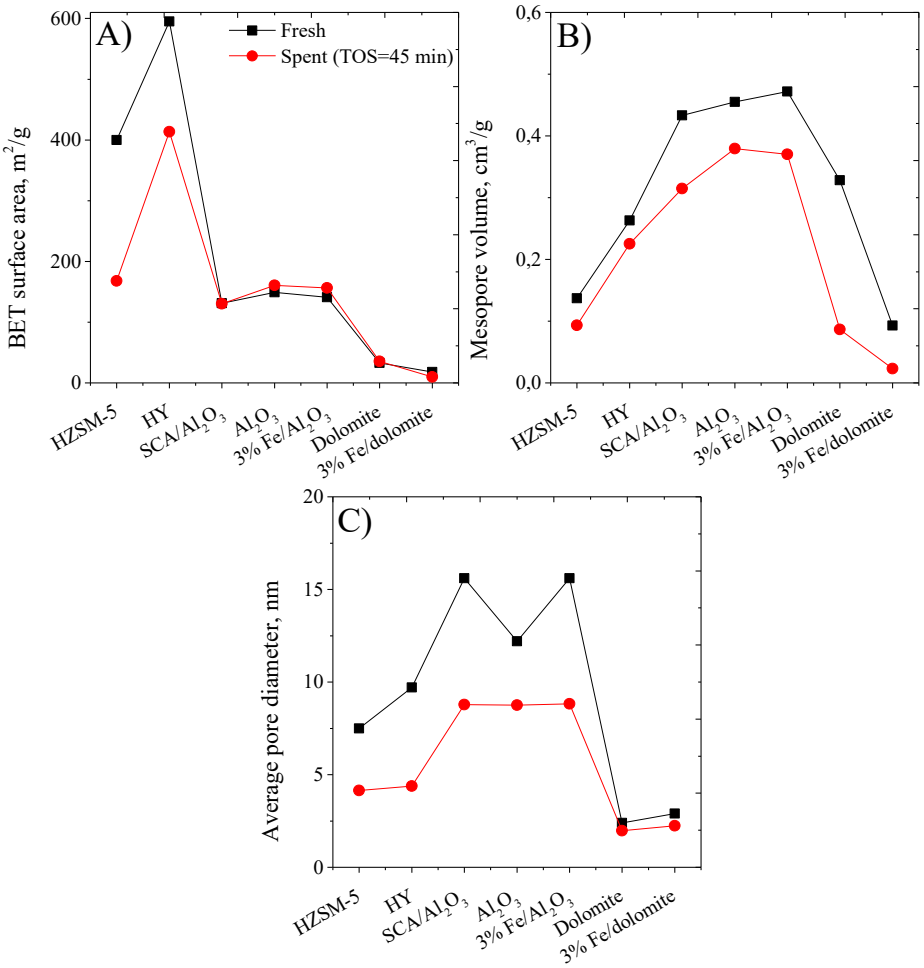

Figure 67: BET surface area (A), mesopore volume (B) and average pore diameter (C) of fresh and spent catalyst samples.

Chapter 6

Pyrolysis and ex-situ catalytic cracking of polyolefin-derived pyrolysis volatiles on HZSM-5

This experimental campaign has been conducted at the University of the Basque Country (Spain) using the experimental apparatus P2. The feedstock consisted in a mixture of polyolefins (50% HDPE, 40% LDPE, 10% PP) and the catalyst was a commercial HZSM-5.

6.1 Effect of space-time on product distribution in experiments with fresh catalyst

The effect of space-time on the distribution of different fractions of products when the catalyst is at 100% activity has been initially evaluated. To ensure stable, steady-state operation, experimental data were collected after 5-10 minutes on stream. This interval is considered representative of initial catalyst activity (TOS ≈ 0 h) with negligible deactivation.

For this set of experiments, the temperature of the pyrolysis stage (conical spouted-bed reactor) has been fixed to 500°C, the temperature of the cracking step (fixed-bed catalytic reactor) was 500°C and the N_2 flowrate was 10 L min^{-1}. The volume of the catalytic bed was always 30 mL, and the amount of catalyst has been modified to obtain the values of τ= 8 – 10 – 12 – 15 and 20 $g_{catalyst}$ min/$g_{plastic}$. Space-time is the inverse of WHSV (weight hourly space velocity) and serves as a key parameter representing the contact time between the reactant vapours and the catalyst.

The effect of space-time on the mass yields of different fractions of products at "zero-time" is illustrated in Figure 68. The results are expressed as $g_{product}/100g_{plastic}$. As a general trend, it can be observed that increasing space-time results in the monotonic increase in the mass yield of light alkanes (C_1-C_4) and

BTX aromatics (benzene, toluene, xylenes) and a corresponding decrease in the gasoline and diesel fractions.

At the lowest space-time investigated (τ= 8 $g_{catalyst}$ min/$g_{plastic}$), there was a significant production of diesel range hydrocarbons and waxes, implying non-complete conversion of the incoming polyolefins during the process. For higher values of space-time, the diesel fraction was consumed due to cracking reactions that convert these compounds into lighter products, including olefins and aromatics (Lopez et al., 2017b).

The results demonstrate the high cracking activity of the HZSM-5 catalyst. Indeed, heavier molecules were consistently converted into lighter compounds with higher commercial interest, such as aromatic hydrocarbons (BTX) and light olefins. The yield of the gasoline fraction was reduced from 5.8 wt% when space-time was 8 $g_{catalyst}$ min/$g_{plastic}$ to 2.0 wt% at τ = 20 $g_{catalyst}$ min/$g_{plastic}$, while the diesel fraction yield decreased sharply from 22.2 wt% to 0.47 wt%.

A non-monotonic trend in the yield of light olefins is observed. It started from 58.37 wt% at τ=8 $g_{catalyst}$ min/$g_{plastic}$, reaching a maximum value of 77.12 wt% for τ=10 $g_{catalyst}$ min/$g_{plastic}$ and then decreasing to 65.74 wt% for τ=20 $g_{catalyst}$ min/$g_{plastic}$. This non-monotonic trend confirms that that the interaction between pyrolysis vapours and acidic sites of the catalyst is governed by competing pathways, and it includes cyclic reactions that can reduce light olefins' production in favour of other species, such as BTX, according to the "hydrocarbon pool" mechanism. Indeed, it has been observed that although an increase in space-time is generally favourable for the production of light olefins, an excessive increase can trigger undesired secondary reactions, including hydrogen transfer (converting olefins into alkanes) or oligomerization and aromatization, which lead to the formation of heavier compounds (Dong et al., 2022).

This explanation is further supported by the consistent and concurrent increase in the yield of BTX (from 8.59 wt% to 21.77 wt%) and light alkanes (from 4.34 wt% to 7.52 wt%) with the increase in space-time from 8 to 20 $g_{catalyst}$ min/$g_{plastic}$. Therefore, an improvement in the contact between the catalyst and the pyrolysis vapours favours secondary reactions leading to cyclization and condensation of light olefins to produce monoaromatics.

It is known that the HZSM-5 catalyst is suitable for the production of light hydrocarbons (C_1-C_4), especially olefins (Elordi et al., 2009; Elordi et al., 2011a; Artetxe et al., 2013; Artetxe et al., 2012; Mastral et al., 2006). Thus, Artetxe et al. (2012) obtained a maximum yield of light olefins of 62.9 wt% during the in-line catalytic cracking of HDPE pyrolysis vapours in a two-stage pyrolysis system at 550°C. San Miguel et al. (2009) found that the presence of HZSM-5 resulted in the production of light hydrocarbons (up to 53 wt% when the catalytic temperature was 475°C), especially C_3-C_4 olefins, during the ex-situ catalytic pyrolysis of waste PE in a batch + fixed-bed reactor system. Elordi et al. (2009) reported a 70 wt% yield in light olefins for fresh HZSM-5 during the in-situ

catalytic pyrolysis of HDPE in a spouted-bed reactor, then reducing to 58 wt% after 6 h of continuous reaction.

The same process has been previously explored by Artetxe et al. (2012) and (2013) using HDPE as plastic feed and a homemade HZSM-5 catalysts agglomerated with alumina and bentonite. Given that the plastic mixture used in this work is predominantly composed of polyethylene (90%), these results are directly comparable to studies using pure HDPE. While trends in light alkanes and aromatics are similar, light olefins presented an increasing trend with space-time, probably because the maximum in olefins' production was not reached in that range. These results demonstrate that the process can be tuned to selectively maximize either light olefins (at an optimal space-time) or monoaromatics (at longer space-times). As discussed by Artetxe et al. (2012), the efficiency of the process relies in the short residence time in both the pyrolysis stage and the cracking step, which helps minimize undesirable secondary cracking reactions.

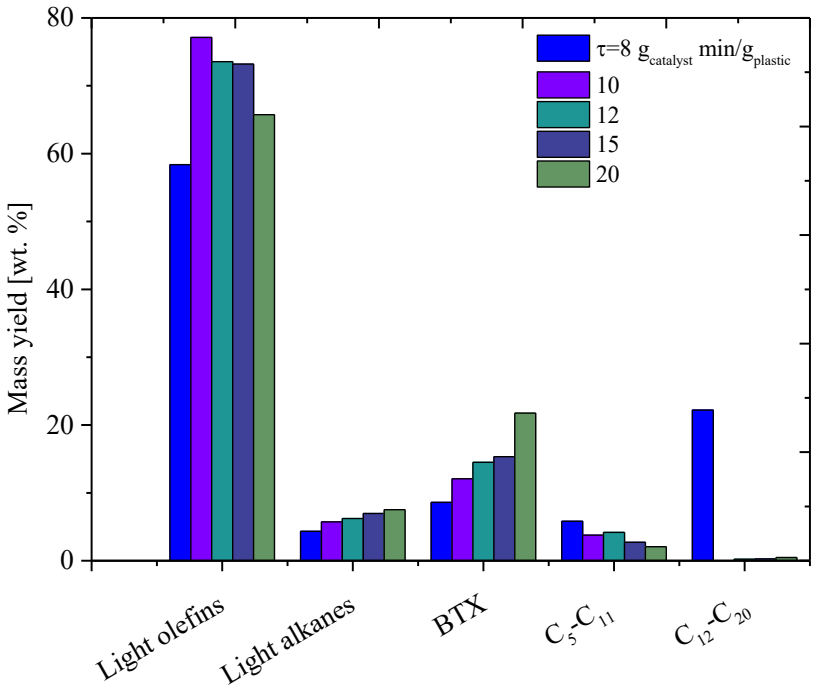

Figure 68: Effect of space-time on the yield of different fractions of products at 500°C.

Elordi et al. (2011a) explored the continuous catalytic cracking of HDPE in a spouted-bed reactor by feeding 1 g/min of plastic in a 30 g HZSM-5 bed, following an "in-situ" configuration. At 500°C, mass yields of light olefins, light alkanes, non-aromatics C_5-C_{11}, monoaromatics, and C_{12}-C_{20} of 57.8 wt%, 14.8 wt%, 15.4 wt%, 10.9 wt% and 1.2 wt% were reported by Elordi et al. (2011a), respectively. Considering the differences between the two reaction configurations and the characteristics of the catalysts used (commercial vs. homemade), it can be concluded that the product composition can be more easily tuned in a two-stage process (in-line) compared to the "in-situ" one. At the same reaction temperature

of 500°C, the in-line configuration allowed to maximize the production of selected products by changing space-time (e.g., light olefins at τ= 10 $g_{catalyst}$ min/$g_{plastic}$ or BTX at maximum τ). The results show that the production of light olefins can be maximized at a space-time of 10 $g_{catalyst}$ min/$g_{plastic}$, above which secondary reactions lead to a progressive reduction.

The activity of HZSM-5 for the catalytic cracking of polyolefins-derived pyrolysis vapours is also highlighted by the results reported in Figure 69. By looking at the process from a macroscopic perspective, i.e., considering the relative proportions of the gaseous and liquid products, it can be concluded that the yield of gases can be maximized by choosing an appropriate value for the space-time, that is the same for the maximization of light olefins. Under conditions of completer wax conversion (τ> 10 $g_{catalyst}$ min/$g_{plastic}$), the total liquid yield stabilized at approximately 20-25 wt%. Similar results were reported by Artetxe et al. (2012) during the ex-situ catalytic pyrolysis of HDPE in a two-stage system. Using an HZSM-5 zeolite with Si/Al = 30, they obtained a gas yield of 72.2 wt% and a liquid yield of 27.8 wt%. Likewise, Yu et al. (2020) reported gas yields of 77.66 wt%, 81.3 wt%, and 85.4 wt% during the in-situ pyrolysis of HDPE in a fixed-bed quartz tube reactor with a plastic/zeolite ratio of 2, using HZSM-5 zeolites with Si/Al ratios of 27, 80, and 150, respectively.

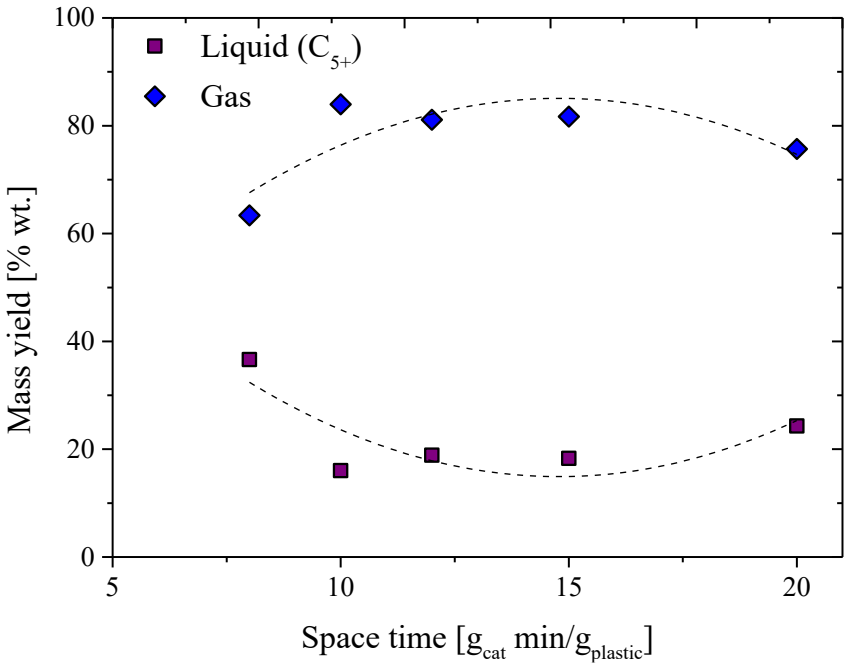

Figure 69: Effect of space-time on total gas and liquid yield at 500°C.

The effect of space-time on the distribution of C_1-C_4 compounds is shown in Figure 70. While the yield of methane and C_2 hydrocarbons increases with increasing space-time, C_3 and C_4 compounds pass through a maximum. In particular, the maximum yield of C_3 and C_4 compounds is obtained once again at τ= 10 $g_{catalyst}$ min/$g_{plastic}$, since the total yield of light alkanes increased

monotonically, whereas the total light olefin yield exhibited a maximum. Moreover, the C_2 fraction is composed by ethane and ethylene, with ethylene being the only light olefin whose yields steadily increases with τ. The yields of individual compounds in the gas phase, distinguished between C_1-C_4 alkanes (left axis) and C_2-C_4 olefins (right axis), are illustrated in Figure 71. Hydrogen is the least abundant compound in the gas phase, and its yield slightly increases from 0.24 wt% to 0.86 wt% going from 8 to 20 $g_{catalyst}$ min/g $_{plastic}$. Following the "hydrocarbon pool" mechanism, hydrogen is a co-product of aromatization reactions, such as the dehydrogenation of cyclic intermediates.

The increase in H_2 yield with space-time is, in fact, related to and justified by the analogous increase in monoaromatics (BTX), as shown in Figure 68.

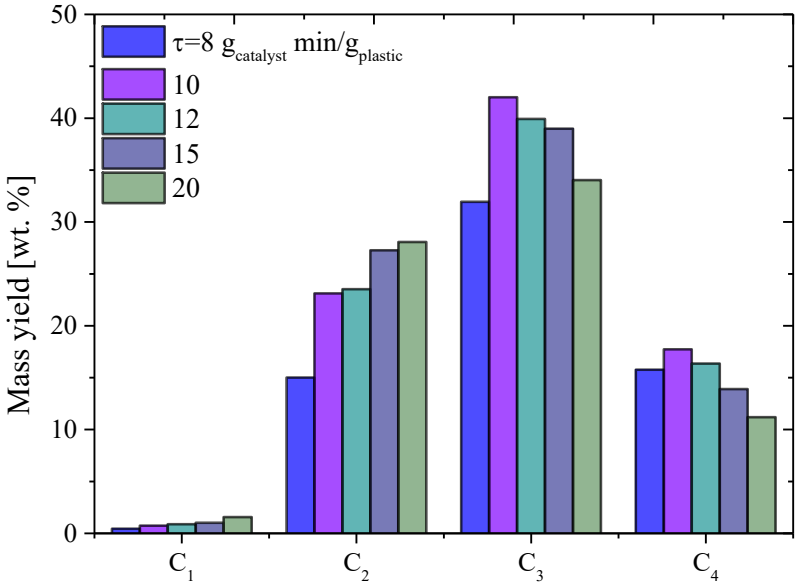

Figure 70: Effect of space-time on product yields of light hydrocarbons at 500°C.

Single light alkanes (methane, ethane, propane and butane) exhibit a consistent increase in yield with increasing space-time. In more detail, when space-time increases from 8 to 20 $g_{catalyst}$ min/g $_{plastic}$, methane yield goes from 0.44 wt% to 1.56 wt%, ethane yield goes from 0.53 wt% to 1.26 wt%, propane yield goes from 2.73 wt% to 4.96 wt% and butane from 1.09 wt% to 1.29 wt%.

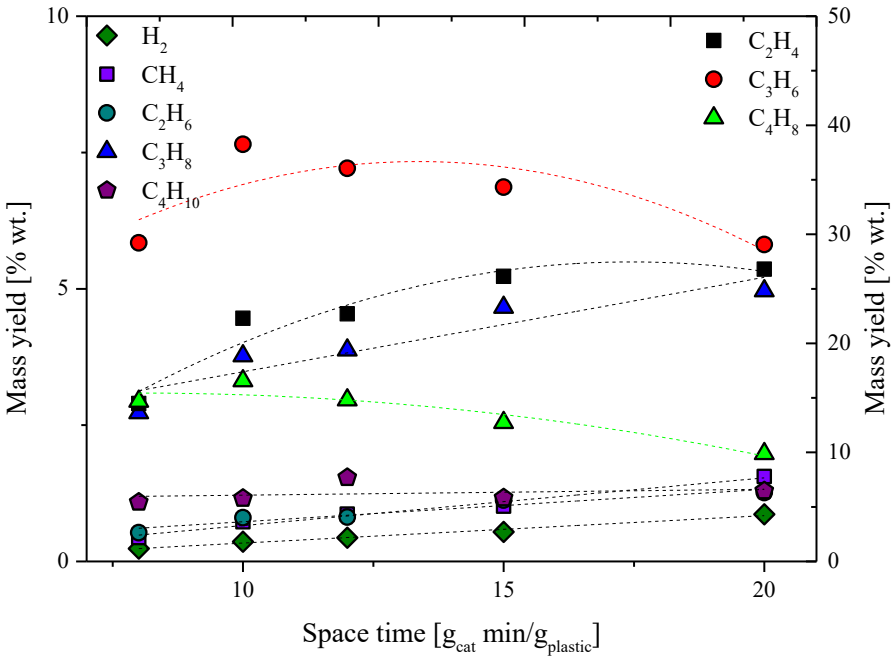

Figure 71: Detailed effect of space-time on yield of single gas-phase compounds at 500°C.

On the other hand, single light olefins – except for ethylene – show a non-monotonic trend passing through a maximum, in agreement with the trend previously discussed for light olefins. Specifically, the maximum mass yields of propylene and butenes are of 38.25 wt% and 16.56 wt% respectively, and they are obtained when τ=10 $g_{catalyst}$ min/$g_{plastic}$. Differently, ethylene concentration steadily increased from 14.48 wt% at τ=8 $g_{catalyst}$ min/$g_{plastic}$ to 26.80 wt% at τ=20 $g_{catalyst}$ min/$g_{plastic}$. This could be due to ethylene being a final product of severe cracking (β-scission of larger carbenium ions) that is less reactive in oligomerization compared to propylene and butenes (Corma & Iborra, 2006). These trends are consistent with Elordi et al. (2011a), who reported selectivities of 29% propylene, 21% butenes, and 10% ethylene during in-situ catalytic pyrolysis of HDPE.

Figure 72 illustrates the effect of space-time on the distribution of products belonging to the gasoline fraction, i.e., C_5-C_{11} hydrocarbons including monoaromatics, ordered according to the number of carbon atoms. When space-time increases, the yields of C_6, C_7 and C_8 increase whereas those of C_5 and C_9-C_{11} decrease. In particular, C_5 fraction –mostly olefins - goes from the maximum of 3.91 wt% to 1.6 wt% when space-time is 20 $g_{catalyst}$ min/$g_{plastic}$. C_9-C_{11} represent a very small fraction of the gasoline product (0.82 wt% at τ=8 $g_{catalyst}$ min/$g_{plastic}$, and only 0.33 wt% at τ=20 $g_{catalyst}$ min/$g_{plastic}$) obtained using this commercial zeolite. Compounds with 6, 7 and 8 carbon atoms, among which BTX make up the majority in terms of yield, have monotonic increasing trends with space-time, exactly as for BTX.

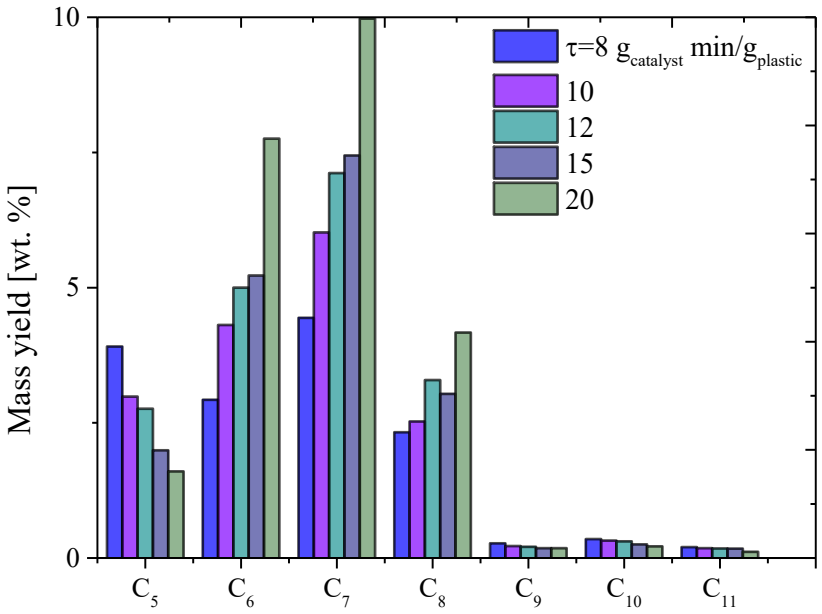

Figure 72: Effect of space-time on product yields of gasoline fraction.

The trends observed in Figure 72 could be associated to the improvement of cracking of high-molecular weight alkanes and olefins to produce light hydrocarbons (saturated and unsaturated) and the simultaneous increase in aromatic production.

Given the importance of BTX in the chemical market as fundamental building blocks, their production via thermochemical processing of (waste) plastic is of outstanding importance. The yield of single BTX is reported in Figure 73. As commented in the previous section, BTX yield is favoured by an increase in the space-time in the range investigated in this Thesis. This increasing trend is observed for each of the individual monoaromatic compounds: benzene, toluene, and the xylene isomers. Toluene is the most abundant compound of the BTX fraction, followed by benzene and, lastly, by xylenes. The selectivity[6] to benzene slightly increases with space-time, from 25.1% when τ= 8 $g_{catalyst}$ min/g $_{plastic}$, to 35.0% when τ= 20 $g_{catalyst}$ min/g $_{plastic}$. In contrast, the selectivity towards toluene within the BTX fraction remained relatively constant at approximately 46-47% across the range of space-times investigated. Overall, higher space-times favour aromatization within the gasoline fraction, shifting selectivity towards BTX monoaromatics while reducing C_5 olefins and heavier C_9–C_{11} species.

[6] selectivity is defined as the ratio between the mass of desired product (e.g., benzene) over the total product mass (total BTX).

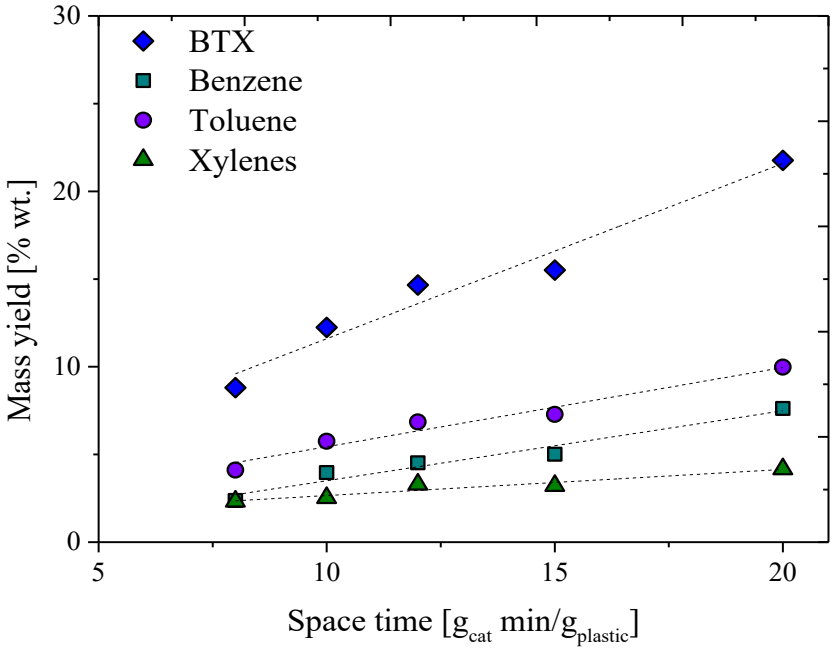

Figure 73: Effect of space-time on the yield of monoaromatics (BTX) at 500°C.

6.2 Catalyst stability during in-line catalytic cracking of polyolefins

This Section includes results related to the deactivation of commercial HZSM-5 during in-line catalytic cracking of pyrolysis vapours from polyolefins. It is generally accepted that catalyst deactivation in cracking processes can occur mainly due to thermal sintering or coke deposition. In our experimental campaign the temperature effects on deactivation are negligible due to the efficient control of cracking temperature during the reaction. Therefore, the main cause of activity decline over time is the deposition of carbonaceous matter onto the catalyst's surface and inside the pores (coking), favoured by the polymerization of aromatics and olefins.

The investigation has been realized by setting the pyrolysis reactor at 500°C, and changing the operating conditions of the cracking reactor, i.e., cracking temperature and space-time. Three different experiments were conducted in the following conditions:

1. Deactivation at $T_{cracking}$=500°C and τ= 15 $g_{catalyst}$ min/$g_{plastic}$
2. Deactivation at $T_{cracking}$=500°C and τ= 10 $g_{catalyst}$ min/$g_{plastic}$
3. Deactivation at $T_{cracking}$=450°C and τ= 10 $g_{catalyst}$ min/$g_{plastic}$

This experimental design allows for the individual effects of cracking temperature and space-time on catalyst deactivation to be systematically evaluated. First, the effect of time on stream (TOS) on the yields of different products has been investigated for the three experimental conditions listed above.

Then, the effect of space-time and cracking temperature on the severity of catalyst's deactivation has been discussed. Finally, samples of spent catalyst have been fully characterized to understand how deactivation influences the deterioration of physical properties (especially porosity) and coke deposition.

Since a fixed-bed reactor was used for catalytic cracking, both the deterioration of surface properties and deposition of coke were not homogeneous along the catalyst bed but followed an axial profile. In this way it was possible to distinguish between coke deposition caused by waxes and by coke precursors like olefins and aromatics. This aspect has been previously highlighted by Artetxe et al. (2012; 2013), who divided the catalyst bed into three different layers to shed light on the severity of deactivation along the fixed bed. According to the methodology adopted by Artetxe and coworkers, the bed has been divided into two distinct layers by interposing a steel wire mesh. Therefore, it was possible to individually characterize the two layers. The total duration of the reactions is 4 h, corresponding to 240 g of plastic mixture fed to the reactor. Samples of spent catalyst were taken and characterized after 1 h, 2 h and 4 h.

Figures 74-77 illustrate the evolution with reaction time (time on stream) of the main products coming from catalytic cracking of pyrolysis volatiles at 500°C and using a space-time of 15 $g_{catalyst}$ min/g $_{plastic}$. As previously, the products were divided into light olefins (C_2-C_4), light alkanes (C_1-C_4), monoaromatics (BTX), gasoline range liquid (C_5-C_{11}, excluding BTX) and heavier liquid product, including waxes (C_{12+}). The amount of coke produced during the process was always negligible in comparison with the amount of plastics fed to the reactor in each experiment (around 200 mg for 240 g of plastic mixture).

Under these conditions (500°C, τ = 15 $g_{catalyst}$ min/$g_{plastic}$), the catalyst exhibited high stability over 4 h of operation, as evidenced by the relatively constant yields of light olefins, light alkanes, and the bulk liquid fractions (Figure 74). Nevertheless, a small decrease in BTX can be observed over time. The same trend was also found by Elordi et al. (2009) highlighting the good resistance to deactivation exhibited by ZSM-5, attributed to its unique pore structure, which sterically hinders the progression of coke precursors into polyaromatic compounds (Lopez et al., 2017b). A slight deactivation of the catalyst is observed in the early stages of the reaction, and it could be attributed to the coverage of strong acid sites by coke deposits, as reported by Elordi et al. (2009).

The results are also in agreement with Elordi et al. (2011b) who observed that deactivation of HZSM-5 was not significant up to a TOS of 15 h even during the in-situ catalytic pyrolysis of HDPE in a spouted-bed reactor. These findings confirm that the present results are in line with prior studies demonstrating the high stability of HZSM-5 under catalytic pyrolysis conditions.

Additional experiments at lower space-time and lower cracking temperature (Appendix A) exhibited comparable trends, except for the experiments at 450°C, in which clear incipient deactivation of the catalyst can be observed.

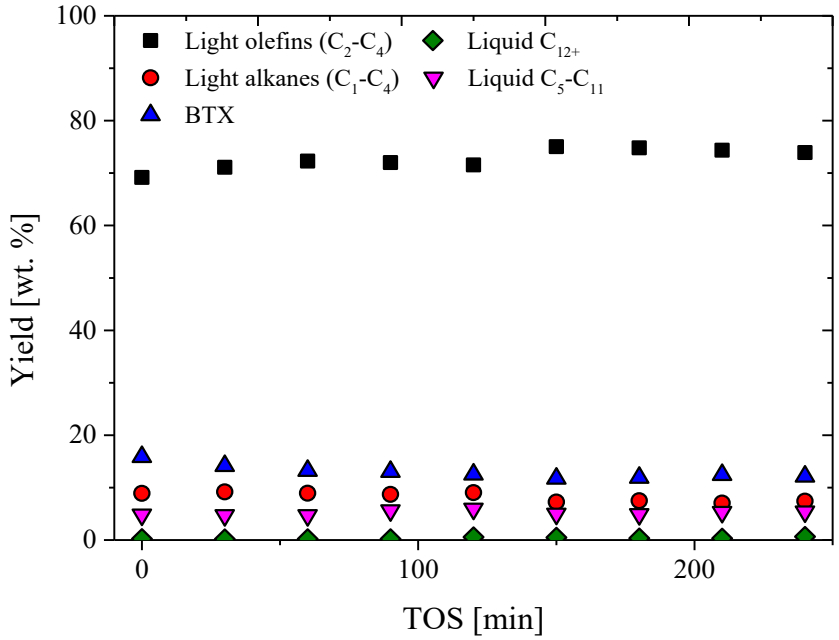

Figure 74: Time evolution of product class yields at 500°C, τ= 15 $g_{catalyst}$ min/$g_{plastic}$.

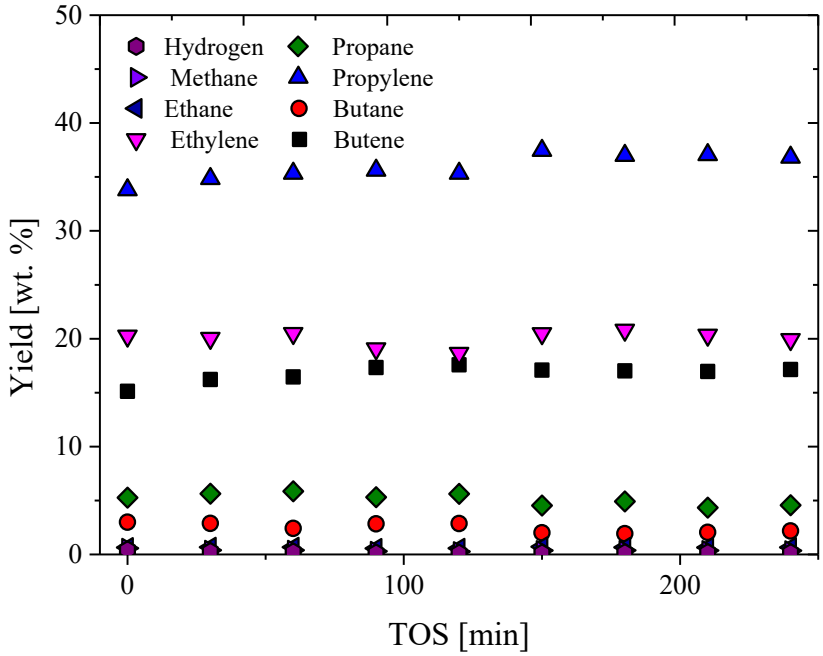

Figure 75: Time evolution of gas-phase yields at 500°C, τ= 15 $g_{catalyst}$ min/$g_{plastic}$.

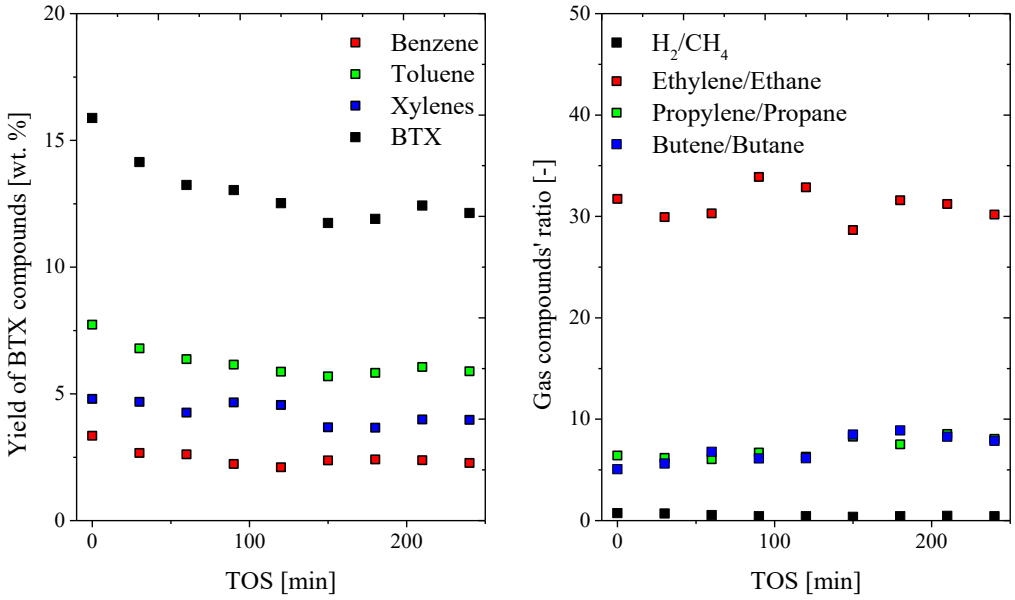

Figure 76: Effect of TOS on yield of BTX (A) and of gas-phase ratios (B) during the deactivation of HZSM-5 at 500°C, τ=15 $g_{catalyst}$ min/g $_{plastic}$.

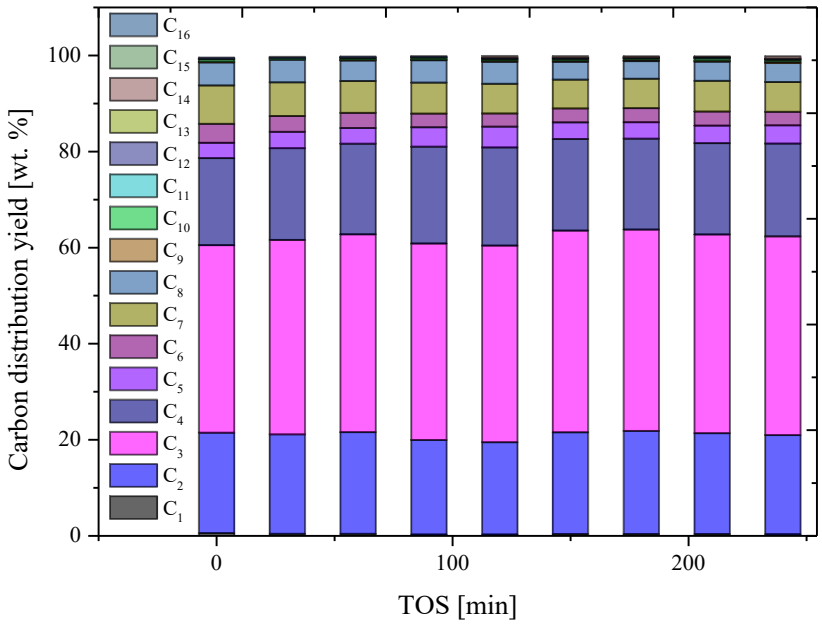

Figure 77: Time evolution of product distribution (process conditions: 500°C, τ= 15 $g_{catalyst}$ min/g $_{plastic}$).

A comparison of the light olefin yields found under the three experimental conditions investigated is shown in Figure 78. Light olefins yield slightly changed with space-time, in particular increased (from ≈70 to ≈75 wt%) when space-time went from 15 to 10 $g_{catalyst}$ min/g $_{plastic}$, in complete agreement with the results shown for yields at "zero time", where τ= 10 $g_{catalyst}$ min/g $_{plastic}$ represented the optimum for C_2-C_4 olefin production. In both cases, catalyst deactivation was negligible, and the yield of light olefins was quite constant up to TOS= 4 h.

On the other hand, when cracking temperature was set to 450°C, light olefin yields substantially decreased (59.7 wt% at zero time) compared to 500°C. Moreover, catalyst deactivation was considerably more severe in this case, given the lower temperature (450°C) combined with a lower space-time (10 $g_{catalyst}$ min/$g_{plastic}$). Results clearly indicate that cracking temperature is a stronger tuning parameter for the optimization of the process and to reduce catalyst deactivation.

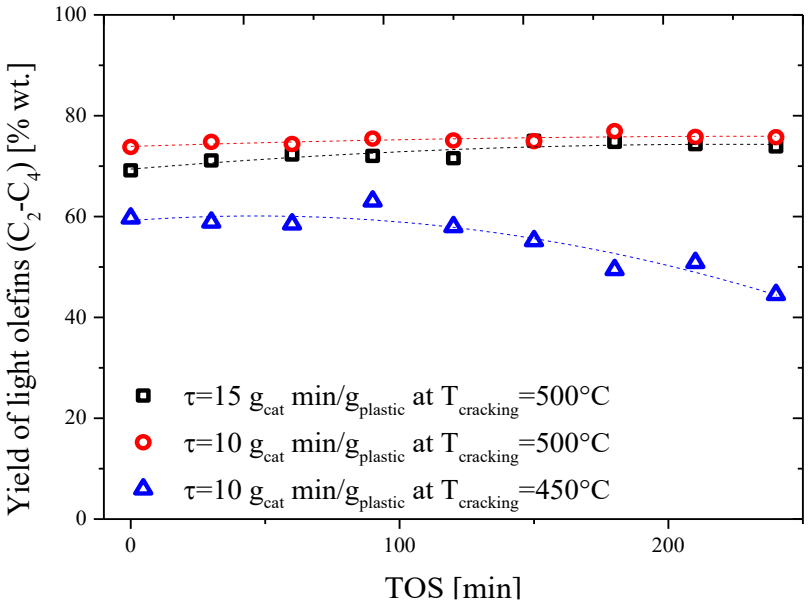

Figure 78: Effect of TOS on the yield of light olefins in different operating conditions.

Similarly, the time evolution of light alkanes is shown in Figure 79. In all the experimental conditions investigated in this work, light alkanes yield decreases with TOS at the same rate. The trends reported are in agreement with results shown for the study at "zero time", given that light alkanes are more abundant when space-time is higher at a fixed cracking temperature. When τ= 15 $g_{catalyst}$ min/$g_{plastic}$ at 500°C, light alkanes yield went from 8.9 wt% at zero time to 7.4 wt% after 4 h of reaction; on the other hand, when τ= 10 $g_{catalyst}$ min/$g_{plastic}$, it went from 7.26 wt% to 5.17 wt% after 4 h. Results also suggest that light alkanes production is slightly higher at 450°C compared to 500°C. This is in line with the conclusion from Artetxe et al (2012; 2013), who investigated the effect of cracking temperature on the yield of products from HDPE catalytic pyrolysis. Using a homemade HZSM-5 catalyst (Si/Al_2O_3=30, similar to this study) and working with τ= 8 $g_{catalyst}$ min/$g_{plastic}$, they found a maximum yield of light alkanes of 12.6 wt% at 450°C at "zero time" condition. By comparison, using a commercial HZSM-5 catalyst with τ= 10 $g_{catalyst}$ min/$g_{plastic}$, the yield of light alkanes was 10.99 wt% at 450°C and 7.26 wt% at 500°C.

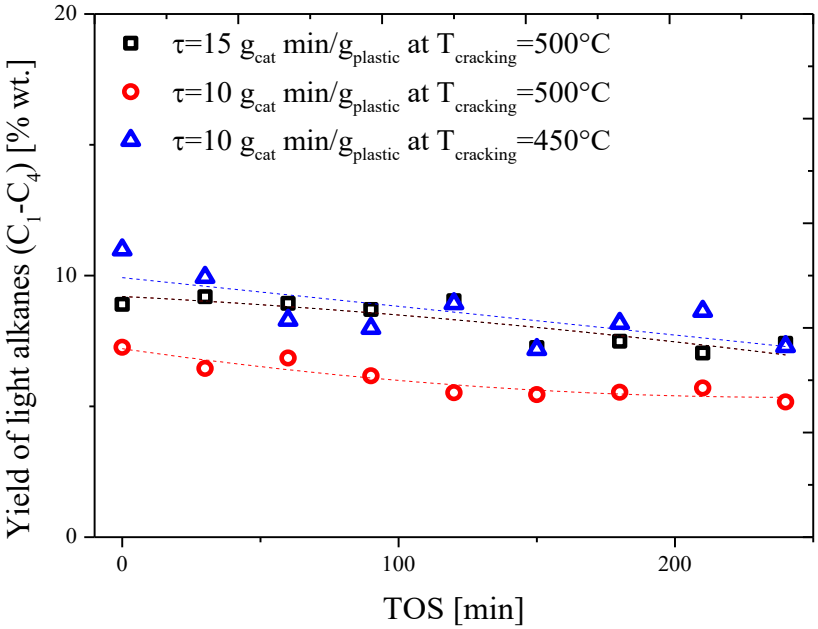

Figure 79: Effect of TOS on the yield of light alkanes in different operating conditions.

The yield of BTX as a function of time on stream in illustrated in Figure 80. A monotonic decrease in yield can be observed in all the experimental conditions investigated, suggesting that , with increasing TOS, aromatic compounds trapped into the pores of the catalyst may react via condensation and polymerization reactions leading to deposition of carbonaceous residues, in agreement with the fact that light olefins and aromatics represent the most important coke precursors in the catalytic pyrolysis on zeolites, as reported by Ibañez et al. (2014).

At 500°C, the BTX yield went from 15.88 wt% at zero time to 12.13 wt% after 4 h of steady state reaction with τ= 15 $g_{catalyst}$ min/$g_{plastic}$. A further reduction of the space-time to τ= 10 $g_{catalyst}$ min/$g_{plastic}$ led to a reduction in BTX yield, from 11.58 wt% to 8.32 wt% at TOS= 4 h.

The effect of cracking temperature at fixed space-time showed counterintuitive results. Using a space-time of τ= 10 $g_{catalyst}$ min/$g_{plastic}$, a reduction of cracking temperature from 500°C to 450°C resulted in an increase of BTX yield. Specifically, at 450°C, the yield of BTX started from 12.85 wt% and decreased to 9.63 wt% after 4 h. Instead, Artetxe et al. (2012; 2013) reported that using a homemade HZSM-5 (Si/Al=30) with τ= 8 $g_{catalyst}$ min/$g_{plastic}$, the yield of aromatics always increases with cracking temperature between 350°C and 550°C.

The higher yield of BTX observed at 450°C compared to 500°C can be justified taking into account the nature itself of the pyrolysis feedstock. The current study utilized a mixed polyolefin stream comprising 50% HDPE, 40% LDPE, and 10% PP by weight. It is well established that LDPE and PP generate pyrolysis vapours richer in branched hydrocarbons and light olefins, both of which exhibit increased reactivity under catalytic conditions (Wakayama & Matsuhashi, 2005). These species are more susceptible to secondary transformations—such as overcracking and coke formation—particularly at elevated temperatures. As a consequence, the vapor mixture entering the catalytic

bed at 500 °C likely undergoes competitive reactions, probably enhanced by high temperatures, that favoured the formation of gaseous products and coke precursors at the expense of BTX intermediates, thereby reducing the overall selectivity toward target monocyclic aromatics. A second relevant factor pertains to the employed space-time. In the present work, a value of 10 $g_{catalyst}$ min/g $_{plastic}$ was used, in contrast to the 8 $g_{catalyst}$ min/g $_{plastic}$ adopted by Artetxe et al. (2012; 2013). While increased space-time generally enhances the extent of vapor–catalyst contact and, hence, conversion, at higher temperatures it may also intensify undesired overcracking phenomena.

This interpretation is consistent with the experimentally observed increase in light olefins and corresponding decrease in light paraffins at 500 °C. Paradoxically, despite exhibiting a higher extent of catalyst deactivation via coking, the experiments conducted at 450 °C resulted in slightly superior BTX yields. This observation suggests that milder thermal conditions may promote more selective aromatization routes from light olefins and alkanes, while concurrently minimizing secondary transformations that compromise aromatic product stability. The different result could also be ascribed to a methodological difference used to quantify aromatics in the two works. Specifically, Artetxe (2013) quantified total aromatics—including both monocyclic (BTX) and polycyclic aromatic hydrocarbons (PAHs)—whereas the present analysis focuses exclusively on BTX. It is therefore plausible that, at 500 °C, total aromatic yield increases via further cyclization and condensation reactions, resulting in higher PAH formation. Under such conditions, BTX intermediates may undergo ring fusion or oligomerization to yield heavier aromatic species, thereby accounting for the reduced BTX selectivity observed in this study despite higher overall catalytic activity.

At 500°C the cracking of pyrolysis vapours can furthermore fragment intermediate olefins – from which aromatics are obtained via cyclization-dehydrogenation reactions – into light gases (C_1-C_4). For instance, Park et al. (1999) found that raising the temperature from 450°C to 500°C led to a reduction in aromatics (in relative wt% of the liquid phase) from 23.4 to 19.5.

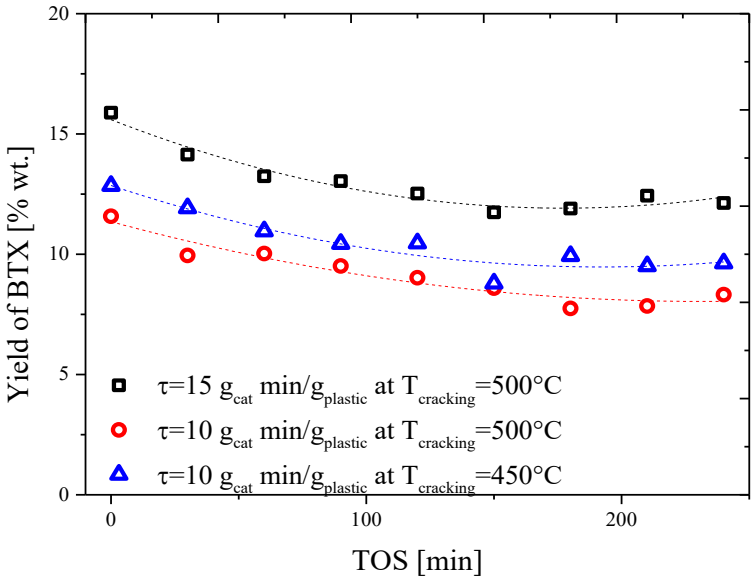

Figure 80: Effect of TOS on the yield of BTX in different operating conditions.

The yield of single monoaromatic compounds (namely, benzene, toluene and xylenes) is reported in Figure 81 as a function of TOS. At fixed cracking temperature of 500°C, the increase in space-time determines an increase in benzene, toluene and xylene yields. On the other hand, at a fixed space-time of τ= 10 $g_{catalyst}$ min/g $_{plastic}$, an increase in cracking temperature from 450°C to 500°C results in a small increase in benzene yield and a corresponding decrease in xylenes yield. The decrease in xylenes was more significant than the decrease in benzene. Therefore, given that toluene yield was practically not affected by the change in temperature, this resulted in an overall increase of BTX at lower temperature.

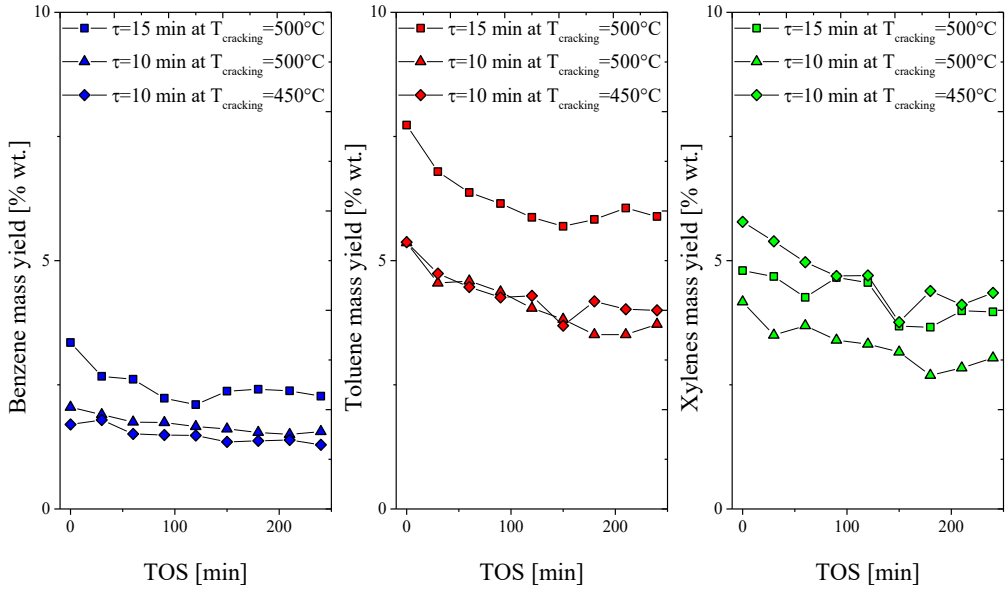

Figure 81: Effect of TOS on the yield of single BTX in different operating conditions.

In conclusion, a comparison of product distribution obtained from 4 h continuous steady-state reaction in different operating conditions is reported in Figure 82. The C_1-C_4 fraction accounts for the 81.66% of the exit stream at 500°C when τ= 15 $g_{catalyst}$ min/$g_{plastic}$, and 81.08% when τ= 10 $g_{catalyst}$ min/$g_{plastic}$. This suggests that catalyst deactivation is minimal in these operating conditions, and catalytic cracking of heavier molecules into light compounds (especially light olefins and alkanes) is significant even after 4 h of reaction. In the above-mentioned space-time conditions at 500°C, only minor changes in the distribution of the liquid fraction (C_{5+}) can be observed.

When τ= 10 $g_{catalyst}$ min/$g_{plastic}$ and the cracking temperature is reduced to 450°C, the catalyst suffers more deactivation due to unfavourable cracking conditions. Lower temperatures reduce the activity of zeolite pores resulting in a lower cracking of heavy compounds. After 4 h of reaction, the C_1-C_4 fraction only represented 51.88% of the exit stream. The liquid fraction, on the other hand, represented the 48.03 % in weight. Overall, catalyst stability was preserved at 500°C regardless of space-time, whereas at 450°C deactivation was significant, shifting the product distribution from gases (≈82 wt%) to liquids (≈48 wt%). These results demonstrate that cracking temperature is the dominant parameter controlling both deactivation and selectivity.

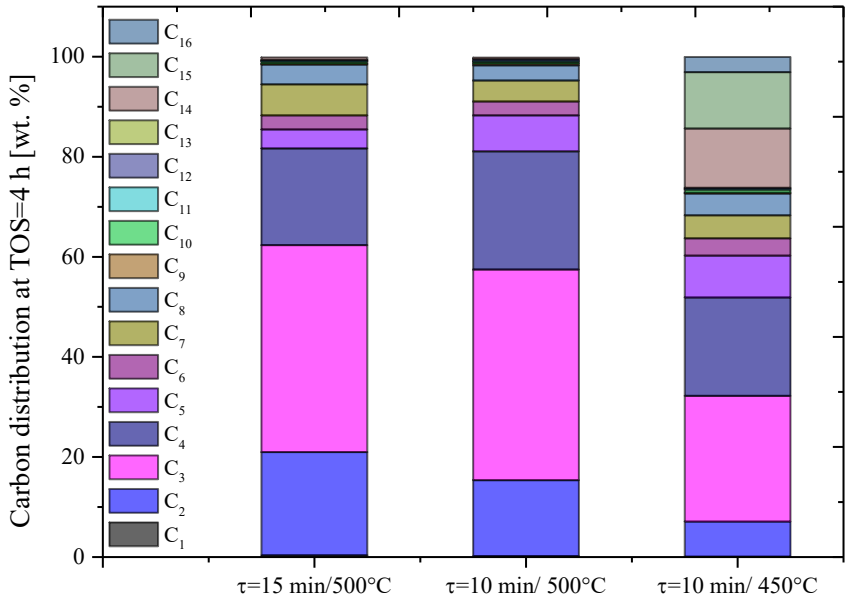

Figure 82: Comparison of product distribution after 4 h of reaction in different operating conditions.

6.3 Catalyst deactivation

The characterization of spent HZSM-5 catalyst samples collected at various times-on-stream (TOS) was performed with the aim of investigating the progressive deterioration of their morphological and catalytic properties to establish correlations between catalyst deactivation mechanism and operating parameters. The analysis considers the influence of reaction duration, axial location within the reactor (i.e., first or second catalytic bed), and operating conditions, including reaction temperature and space-time.

To evaluate the physical properties of the spent catalyst samples, nitrogen adsorption–desorption measurements were performed. Figures 83 and 84 illustrate the influence of time-on-stream (TOS) on key textural properties of the catalyst—namely, the BET surface area, micropore volume, and mesopore volume—under different reaction conditions. All measured properties exhibited a progressive decline with increasing TOS, characterized by a pronounced initial drop within the first 2 hours of reaction, followed by stabilization at approximately 4 hours. This trend is explained by the slight but progressive deactivation of the catalyst due to coke deposition.

When the cracking temperature is set to 500°C and the space-time is τ= 15 $g_{catalyst}$ min/$g_{plastic}$, the BET specific surface area of the catalyst in the first section of the catalytic bed is reduced from 401.9 m^2/g to 372.6 m^2/g after 4 h of reaction, which is a reduction of 7.3%. The second catalytic bed also appears to suffer the same deterioration (9.8%). Similarly, a reduction in micropore volume of 6.3% and of mesopore volume of 7.3% can be observed for the first catalytic bed after 4 h of reaction. The second catalytic bed had 11.3% and 7.3%, respectively. No significant difference was observed between the first and second catalytic bed in terms of morphological deterioration in these operating conditions. Elordi et al. (2011b) also observed a clear deterioration of catalyst properties after 15 h of HDPE catalytic pyrolysis in a spouted-bed reactor. More in detail, the surface area was reduced by 19% while the micropore area was reduced by 15%. Similarly, Castaño et al. (2012) reported a similar decrease in BET surface area and micropore area for HDPE and PP after 1600 min of operation

When the space-time is reduced to τ= 10 $g_{catalyst}$ min/$g_{plastic}$, a significant difference between the two catalytic beds can be observed. The BET surface area of the first catalytic bed decreases by 13.9% at TOS= 4 h, while the second catalytic bed decreases by 7.9%. It should be also noted that the first catalytic bed experiences a worse deterioration when τ= 10 $g_{catalyst}$ min/$g_{plastic}$ compared to the case of τ= 15 $g_{catalyst}$ min/$g_{plastic}$, in agreement with the higher coke deposition registered (see Section 6.4). Micropore volume of the first and second catalytic bed was reduced from 0.142 cm^3/g to 0.124 and 0.132 cm^3/g, respectively. Mesopore volume was reduced from 0.137 cm^3/g to 0.115 and 0.125 cm^3/g.

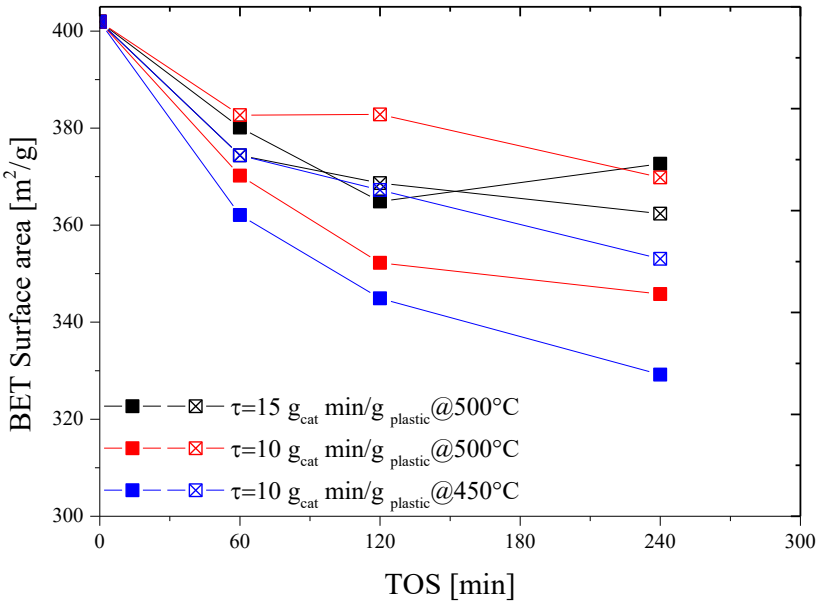

Figure 83: Reduction of BET specific surface area of HZSM-5 in different operating conditions (filled squares refer to 1st catalytic bed).

Finally, when cracking temperature was lowered to 450°C at fixed space-time of τ= 10 $g_{catalyst}$ min/$g_{plastic}$, the most severe deterioration was found. BET surfaces area diminished by 18.1% for the first catalytic bed and by 12.1% for the second. Similarly, micropore volume decreased to 0.116 cm^3/g and to 0.123 cm^3/g for the first and second catalytic bed, respectively. The mesopore volume decrease to 0.126 and to 0.122 cm^3/g after 4 h or reaction.

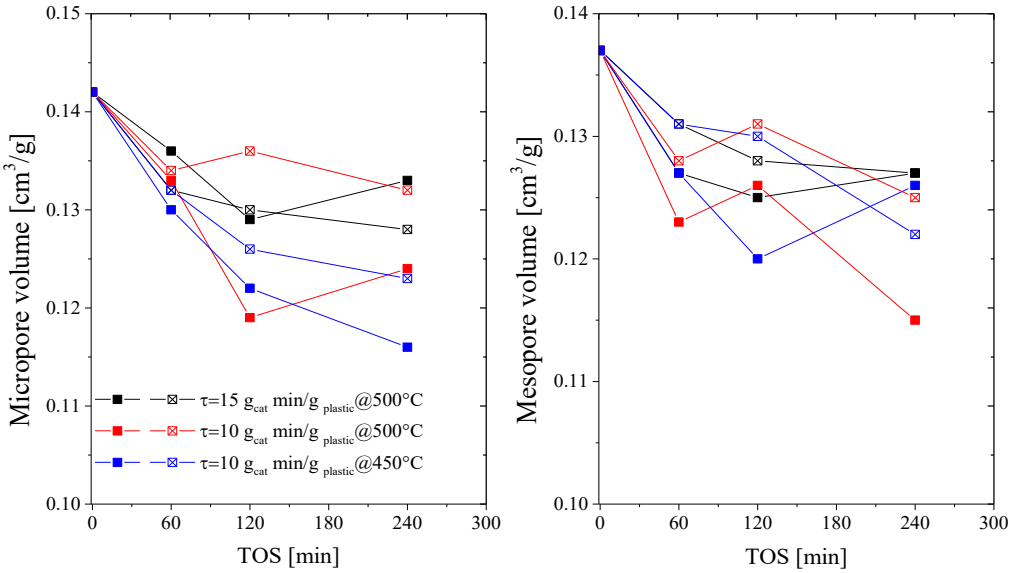

Figure 84: Reduction of micropore and mesopore volume of HZSM-5 in different operating conditions (filled squares refer to 1st catalytic bed).

As expected, the first catalyst bed consistently experiences more pronounced deactivation than the second, given the fact that it directly meets pyrolysis waxes coming from the spouted-bed reactor. Overall, deterioration severity followed the

order τ=15/500°C < τ=10/500°C < τ=10/450°C, consistent with coke-driven blockage of micropores and preferential loss of strong acid sites. This aspect is also confirmed by the analysis of N_2-adsorption-desorption reported in Appendix A, where the curves for both the first and second catalytic bed follow the same trend. These results are in agreement with those reported by Artetxe (2013) related to the deterioration of physical properties of a HZSM-5 zeolite catalyst agglomerated with alumina and bentonite.

Effect of reaction time on the TPD profiles of the spent catalyst samples compared to the fresh are illustrated in Figure 85. Specifically, the ammonia desorption rate profile of spent catalysts is significantly lower compared to the fresh one, suggesting that interaction with pyrolysis volatiles and coke deposits reduces the activity of acidic sites. Fresh catalyst has a total acidity of 1.577 mmol $NH_3/g_{catalyst}$, while spent catalyst sample only registered values of 0.706, 0.744 and 0.492 mmol $NH_3/g_{catalyst}$ after 1, 2 and 4 h (Figure 86-A).

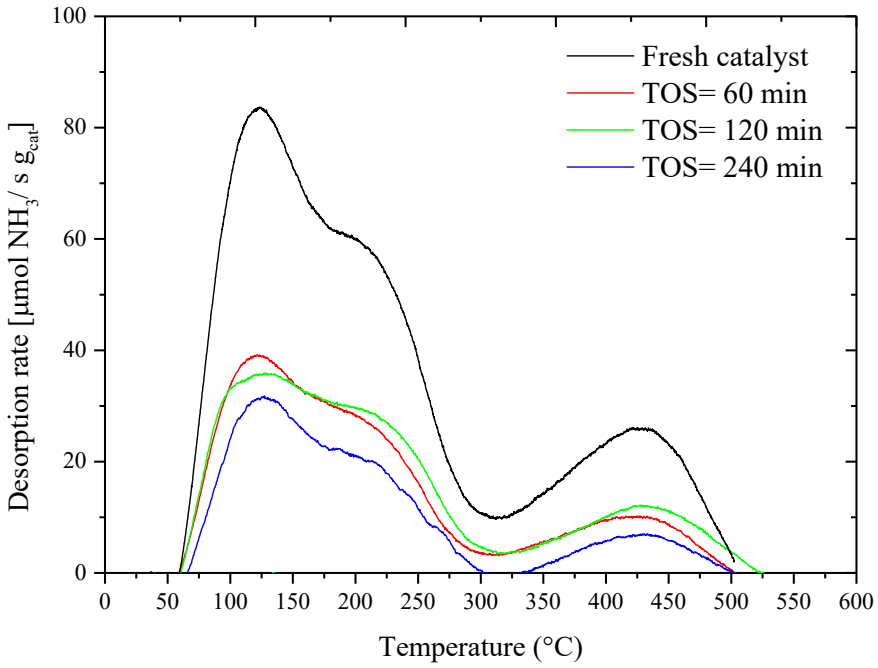

Figure 85: Effect of TOS on acidity of the first catalytic bed. Conditions were: $T_{pyrolysis}$=500°C, $T_{cracking}$=450°C, τ=10 $g_{catalyst}$ min/$g_{plastic}$.

The reduction in acidity involves all acidic sites (weak, middle and strong), but as a consequence of reaction time, weak and mean acidic sites increase their share. For instance, while the fresh catalyst had 29.4%, 49.7% and 20.9% of weak, mean and strong acid sites, respectively, after a TOS=4h, the relative shares became 39.9%, 46.5% and 13.6% (Figure 86-B).

The reduction of the acidity of HZSM-5 was also reported by Castaño et al. (2012). The authors demonstrated that strong acid sites were the first to disappear – being prone to deactivation by coke deposition (Marcilla et al., 2007), leaving behind medium and weak acid sites, with the overall acidity progressively decreasing with time on stream.

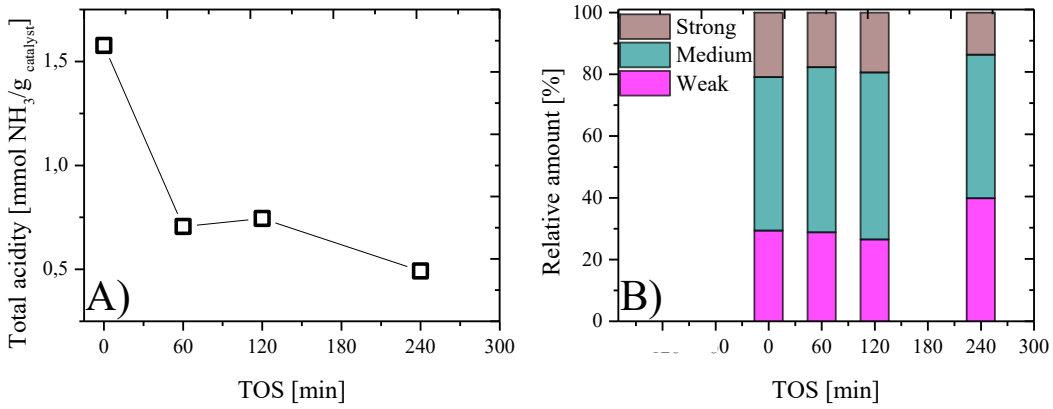

Figure 86: Effect of TOS on total acidity (A) and acidic sites distribution (B) for the first catalytic bed. Conditions were: $T_{pyrolysis}$=500°C, $T_{cracking}$=450°C, τ=10 $g_{catalyst}$ min/$g_{plastic}$.

6.4 Coke deposition and characterization

During pyrolysis, zeolitic catalysts tend to undergo deactivation—at varying rates—due to the deposition of carbonaceous material on both the external and internal surfaces of the catalyst. Coke formation is the result of a series of chemical reactions (including oligomerization, condensation, cyclization, and hydrogen transfer) that lead to the production of higher molecular weight or hydrogen-deficient species (Guisnet & Magnoux, 2001). The rate of coke deposition and its chemical nature are intrinsically linked to the type of plastic feedstock, operating conditions, reactor type and the physicochemical properties of the catalyst itself (Thangaraj & Lee, 2025). Coke deposition on spent catalyst samples has been investigated by Temperature Programmed Oxidation (TPO) using a *T.A. Instruments TGA Q5000* according to the procedure previously reported.

Figure 87 illustrates the evolution of coke yield on the catalyst surface as a function of time on stream (TOS) in the three different sets of operating conditions investigated in this Thesis.

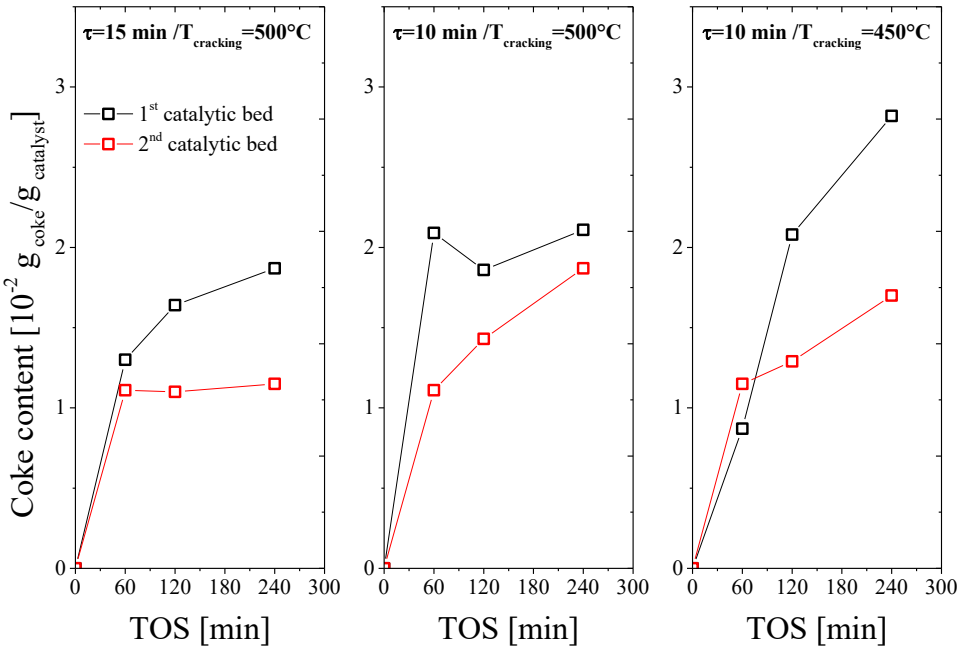

Figure 87: Coke deposition on the first (black markers) and second (red markers) catalytic beds as a function of TOS under three different process conditions.

Independently of the space-time (10 or 15 $g_{catalyst}$ min/$g_{plastic}$) and of cracking temperature (450°C or 500°C), the first catalytic bed experiences a more pronounced deposition of coke compared to the second one. A similar behaviour has been reported by Artetxe et al. (2012; 2013) They propose that in the first section, the catalytic bed is in direct contact with primary pyrolysis waxes, which act as coke precursors (Ibánez et al., 2014). The second catalytic bed is somehow shielded by the first one with respect to waxes but has also been in contact with

other coke precursor species (e.g., light olefins and aromatics) can be responsible for coke deposition (Thangaraj & Lee, 2025; Aguayo et al., 2011).

The amount of coke deposited after 4h of continuous reaction is quite small compared to the mass of the catalyst totally loaded in the reactor. In absolute terms, the process yields around 200 mg of coke for 240 g of plastic fed to the reactor, giving an overall coke yield of the process (mass of coke/mass of plastic fed) <0.1 % wt. The maximum amount was 2.82% wt. for the first catalytic bed and was obtained at 450°C and 10 $g_{catalyst}$ min/$g_{plastic}$. It is generally accepted that the typical three-dimensional structure of ZSM-5 contributes to its chemical stability, facilitating the migration of coke precursors toward the exterior of the zeolite, from where they are then removed by the high nitrogen flow used during the pyrolysis process (Castaño et al., 2011). Moreover, its shape selectivity and acidity favour monomolecular cracking reactions over bimolecular ones, which are mainly responsible for oligomerization, cyclization, and condensation of olefins leading to coke formation (Guisnet & Magnoux, 2001).

Moreover, while at 500°C the coke yield approaches a steady value on time on stream, at 450°C it still increases at TOS= 4h.

Figure 88 shows the results from the temperature programmed oxidation of spent catalyst samples – and of the carbonaceous deposits on the surface – for different operating conditions in terms of space-time (τ=10 and 15 min) and cracking temperature ($T_{cracking}$= 450°C and 500°C). The differential thermogravimetric data (DTG) were plotted as a function of temperature and parametric in the TOS. Especially for catalyst samples which experienced longer reaction time (TOS= 4 h), the DTG curve presents -at least - two different peaks, associated with maximum coke combustion rate. The first peak is located in the 450-490°C range, while the second peak is located in the 560-600°C range, with small differences among the operating conditions investigated in this work. The bimodal DTG profile for HZSM-5 is consistent with the findings of Elordi et al. (2011b), who observed a similar profile when comparing the deactivation behavior of three zeolites (HZSM-5, HY and Hβ) with different framework structures.

The DTG curves have been deconvoluted by means of a multi-peak Gaussian fitting procedure (4 parameter fitting, Levenberg Marquardt iteration method) in order to obtain the single contribution of the distinct peaks associated with to the different types of coke known in the literature (type I and type II coke). This procedure is commonly done in the pertinent literature (Ibáñez et al., 2014; Elordi et al., 2012a; Castaño et al., 2012). The literature on the characterization of coke deposits on acidic catalysts is vast, and there is general agreement on the distinction between two different types of coke, different in chemical nature (more or less poly-aromatic), composition (H/C content) and position within the catalyst's structure. In particular, coke deposited within accessible pores (meso- and macropores) can be easily reached by oxygen and burn at lower temperature, while coke in micropores reacts more slowly due to O_2 diffusional limitations.

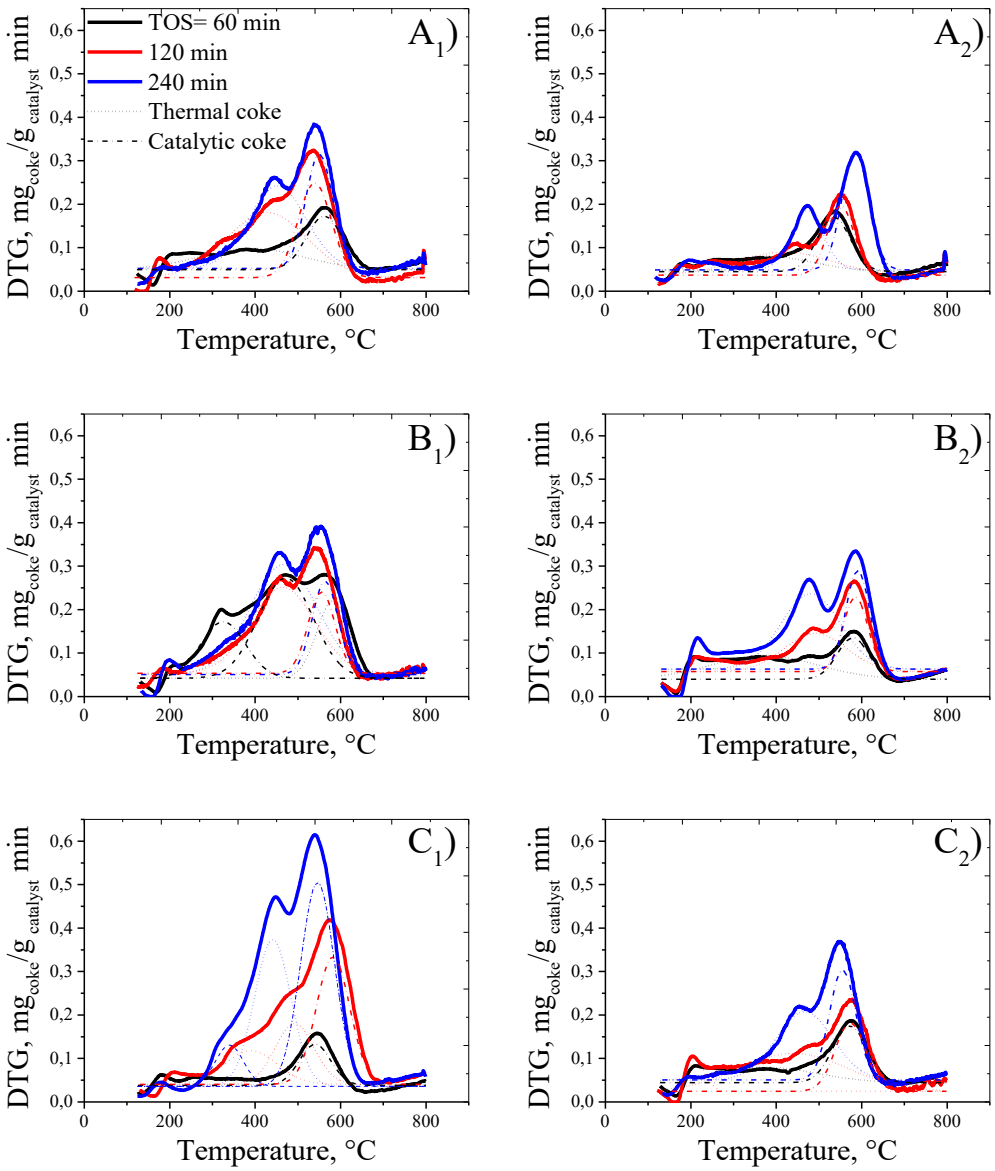

Figure 88: TPO results for coke characterization in different operating conditions: 15 min/500°C (A), 10 min/500°C (B) and 10 min/450°C (C). Left pictures are related to the first catalytic bed, while right pictures to the second catalytic bed.

Type I coke is characterized by higher H/C and is burned – as previously anticipated - at generally lower temperatures, while type II coke is a highly-condensed polyaromatic carbon residue with higher combustion temperature (Bauer & Karge, 2007). Another important difference between the two types of coke is related to the chemical nature. Type I coke compounds are produced by the oligomerization, condensation and alkylation of pyrolysis vapours and are therefore the result of direct retention of waxes and other heavy compounds in the mesoporous zeolite structure (Artetxe, 2013).

At higher temperatures reactions such as cyclization, cracking and hydrogen transfer become important for type II coke compounds in the micropores of the zeolite and lead towards heavy polyaromatic compounds (Guisnet & Magnoux,

2001). It is worth noticing that type I coke is reversible, meaning that it can be fully removed by mild oxidative regeneration without permanent damage to the zeolite framework (Daligaux et al., 2021); type II coke is irreversible due to its high stability. Even after regeneration, which requires higher temperature compared to coke I, it leaves behind irreversible loss of micropore volume and surface area due to pore collapse, dealumination or permanent obstruction (Thangaraj & Lee, 2025; Daligaux et al., 2021). Coke content always increases with increasing TOS for both the catalyst beds; with type I coke growing faster than type II coke ("catalytic" coke).

Figure 89 shows, for the three experimental conditions analyzed in this Thesis, the evolution over reaction time of the two main types of carbonaceous deposits found on the catalyst surface, represented by the two distinct peaks in the graphs of Figure 88, i.e., thermal coke (coke I) and catalytic coke (coke II). The yields of coke I and coke II were obtained from the deconvolution of the peaks in the DTG curves of Figure 88. It can be observed that, in each of the operating conditions investigated, the content of thermal coke (coke I) increases over time more rapidly than catalytic coke (coke II).

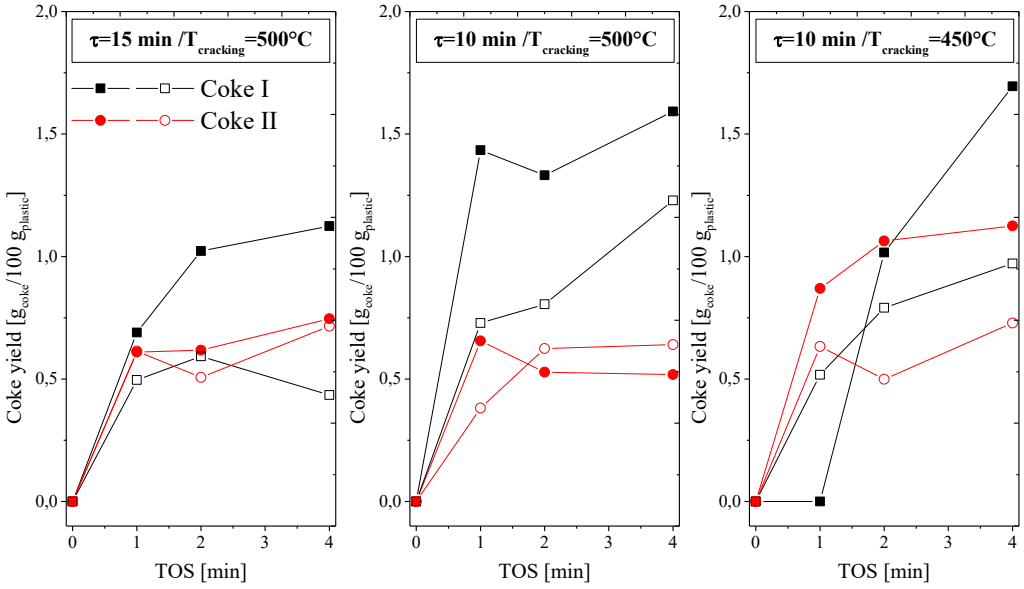

Figure 89: Time evolution of type I coke and type II coke on HZSM-5 as function of the operating conditions. Filled markers refer to the first catalytic bed, while hollow markers to the second.

In conclusion, this investigation into the deactivation of HZSM-5 during the ex-situ catalytic cracking of polyolefin vapours unequivocally identifies cracking temperature as the most important parameter governing catalyst stability and performance. While the catalyst demonstrated high resilience at 500°C, a reduction in temperature to 450°C induced rapid and severe deactivation. Characterization of the spent catalyst revealed that this deactivation is primarily driven by the physical blockage of the catalyst's pore structure by Type I coke, which originates from the condensation of heavy, uncracked pyrolysis vapours.

Operating at 500°C is therefore crucial, not only for maximizing the yield of valuable light olefins but, more importantly, for ensuring these coke precursors are effectively cracked, thereby preserving catalyst activity and extending its operational lifetime. These findings underscore that for ex-situ polyolefin upgrading, maintaining a sufficiently high catalytic temperature is the most critical strategy for mitigating deactivation and achieving a stable, continuous process.

Conclusions and future perspectives

Climate change, extreme weather events and energy insecurity constitute an emergency state that requires a general effort to promote the complete revision of the paradigm of our energy production, development, storage, and distribution from a centralized, fossil fuel-based model to a decentralized and diversified one. In this context, the research and development of alternative and clean sources of fuels and chemicals is of primary importance. The use of bioenergy represents one of the possible strategies to reply to this reclaim. On the other hand, the advancement of alternative energy sources cannot be separated from the management of waste streams and by end-user products such as plastics, and it becomes essential to integrate the necessity to produce alternative and clean fuel sources with waste management.

This PhD work moves in the context of the thermo-catalytic valorization of waste streams as alternative carbon sources. More specifically, the conversion of waste plastics and lignocellulosic biomass (i.e., carbon from biogenic and non-biogenic source) for the production of carbon-efficient fuels or valuable chemicals has been investigated in order to try to overcome the challenges still open in this frame, such as the limited understanding of the complex mechanism of catalytic upgrading of pyrolysis vapours on catalysts of different nature, the necessity to develop new, efficient and stable catalysts for the process and to prevent coke deposition and deactivation.

With this goal in mind, two-stage catalytic fast pyrolysis has been studied using an ad hoc developed spouted-bed reactor for the pyrolysis step coupled with an in-line catalytic fixed-bed reactor for volatiles upgrading. The process has been investigated for the valorization of a biogenic carbon source (olive stone biomass) and a mixture of polyolefin plastics (HDPE, LDPE and PP). The pyrolysis system can operate at steady state, giving insights on the valorization of plastic and lignocellulosic biomass.

A first experimental campaign was meant to explore the performance of a commercial HZSM-5 catalyst (Si/Al=40) for the catalytic cracking of polyolefin-derived volatiles into valuable light olefins and aromatics (especially industrially relevant BTX) with the aim to optimize the operating conditions to maximize the production of light olefins and BTX. The effect of catalyst contact time - or WHSV - at fixed pyrolysis and cracking temperature (500°C for both reactors) at zero-time conditions, i.e., fresh catalyst with negligible deactivation, has been evaluated, highlighting that the catalyst is able to completely convert the waxes derived from polyolefin pyrolysis and that the selective maximization of either light olefins or BTX can be achieved depending on the applied contact time.

Catalyst stability and deactivation under different operating conditions (contact time of 10 and 15 $g_{catalyst}$ min/$g_{plastic}$ with a cracking temperature of 500°C and contact time of 10 $g_{catalyst}$ min/$g_{plastic}$ at 450°C) up to a time on stream (TOS) of 4 h has been assessed, showing that the temperature of the catalytic stage is the most important parameter to control catalyst deactivation. The deterioration of catalyst properties due to deactivation as a function of axial position within the bed has been also elucidated. Temperature-programmed oxidation (TPO), acidity measurements via TPD-NH_3, and porosimetric analysis of the spent catalyst (BET surface area and pore volume via N_2 physisorption) have been carried out to provide further insights into the deactivation mechanisms of the zeolite. Results suggest that the catalyst exhibited good stability and negligible deactivation at 500 °C while more pronounced signs of deactivation and coke deposition were observed at 450 °C.

The same HZSM-5 catalyst was thereafter used for olive stone valorization in a similar two-stage pyrolysis system. Olive stone, which represents an important and valuable residue from the olive oil industry (particularly widespread in the Mediterranean basin), thanks to its chemical composition, low ash content, and ease of handling, is an excellent candidate for thermo-catalytic conversion through pyrolysis, turning it into a resource no longer destined for disposal.

The effect of the main operating conditions, i.e., temperature of the pyrolysis stage, temperature of the cracking reactor and contact time, on the product yield distribution, on the quality of the resulting bio-liquid and on the deactivation of the catalyst at constant TOS were thoroughly investigated. All the parameters had remarkable influence on the productivity and composition of bio-oil, with contact time being the controlling one. Increasing contact time and cracking temperature resulted in lower bio-oil yield, higher water content and higher gas production. Moreover, the catalyst showed discrete activity towards decarbonylation and dehydration more than decarboxylation, leading to high CO concentration in the gas phase and improved oil composition (less light reactive oxygenated, more aromatics). Results from the characterization of spent catalyst samples revealed that coke deposition is more severe compared to the case of plastic pyrolysis (around 10 wt. % $_{coke}$/$g_{catalyst}$ after 45 min compared to less than 3 wt.% in 240 min), and catalyst deactivation – both in terms of physical properties and acidity deterioration - becomes evident already after 45 min of reaction.

Finally, a screening of different catalysts (HY zeolite, SCA/γ-Al_2O_3, γ-Al_2O_3, 3%Fe/γ-Al_2O_3, dolomite and 3% Fe/dolomite) was conducted by comparing the performance of the catalysts at fixed pyrolysis and cracking temperatures (500°C) and using a space-time of 20 $g_{catalyst}$ min/g_{OS}. The experimental campaign allowed to isolate the effect of the catalysts on the properties of the resulting bio-oil in terms of composition, acidity, and phenolic content, and correlate their performance with their formulation and properties. HZSM-5 remains the benchmark for maximizing deoxygenation and producing aromatic hydrocarbons, albeit with higher coke and gas yields. Dolomite is unequivocally superior for

deacidification, drastically reducing organic acids and producing a less corrosive bio-oil, moreover it acts as CO_2 trap, producing a better-quality pyro-gas. Dolomite also produced a high content of phenols, making it a promising candidate for a process targeting the recovery of valuable phenolic chemicals. Other low-cost catalysts exhibited lower activity, and more work is needed to explore their potential.

In conclusion, this work:

1. Gave insights on the upgrading of pyrolysis volatiles from non-biogenic (plastic) waste and lignocellulosic biomass in two-stage continuous reactor systems.
2. Clarified the effect of operating conditions for the maximization of light olefins and BTX yield (from polyolefin plastics) and of phenolics and aromatic hydrocarbons (from olive stone).
3. Explored catalyst deactivation in different operating conditions, suggesting correlations among coke deposition, acidity loss and surface area deterioration.
4. Investigated possible low-cost alternative catalysts to be used in the process of olive-stone valorization.

These results highlight the necessity of a feedstock-specific approach, in which catalyst selection and process configuration are tailored to the chemical nature of the raw material.

Further research into real post-consumer plastic waste utilization as feedstock would increase our knowledge of the impact of heterogeneous composition and impurities on product distribution, process stability and catalyst deactivation. Moreover, since HZSM-5 was not significantly deactivated during this study, longer time-on-stream experiments are required to better elucidate coke formation mechanisms and deactivation kinetics on an industrial time-scale.

As for olive stone valorization, improvements in the condensation system of pyrolysis vapours are needed to achieve a more comprehensive characterization of condensable products and to improve mass balance closure. Further research should focus on the development and testing of alternative catalysts, including metal-modified zeolites. Since biomass-derived volatiles are more prone to coke deposition on zeolites, it is necessary to realize systematic studies of catalyst deactivation, and assessment of regeneration and reuse under prolonged operating conditions.

The co-pyrolysis of olive stone and hydrogen-rich polyolefins presents a promising research direction at the intersection of biomass valorization and plastic waste management. However, further investigation is required to fully understand the interaction between biomass and plastic-derived volatiles. Key areas of focus include enhancing hydrogen transfer reactions, suppressing coke formation, and reducing oxygen content in the bio-oil. Additionally, optimizing blending ratios, reactor configurations, and integrating these processes within a circular economy

framework are critical for improving the sustainability and efficiency of the process.

Additional challenges include the development of selective separation strategies for targeted compounds from pyrolysis oils, the exploration of catalytic upgrading configurations beyond fixed-bed reactors to approach industrially relevant conditions, and the implementation of techno-economic and life cycle assessments to evaluate the competitiveness and environmental impact of the proposed process.

Appendices

Appendix A

Time evolution of product class yields during fast pyrolysis and in-line catalytic cracking of polyolefins

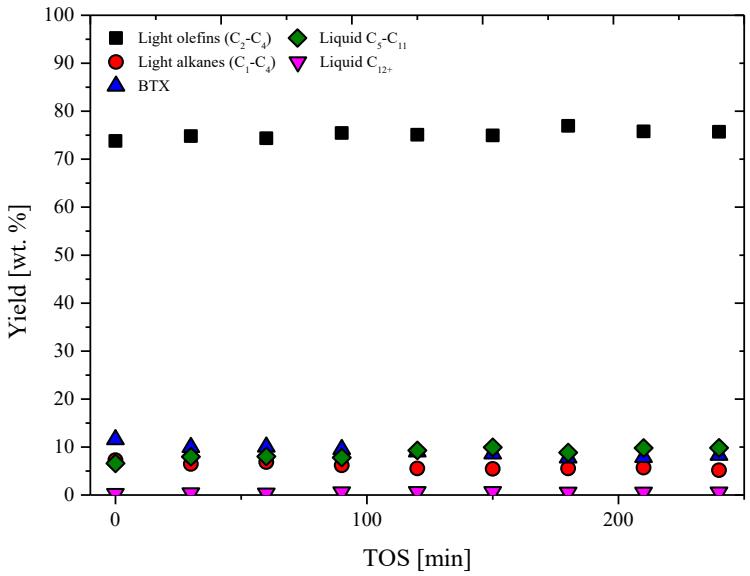

Figure 90: Time evolution of product class yields at 500°C, τ= 10 $g_{catalyst}$ min/$g_{plastic}$.

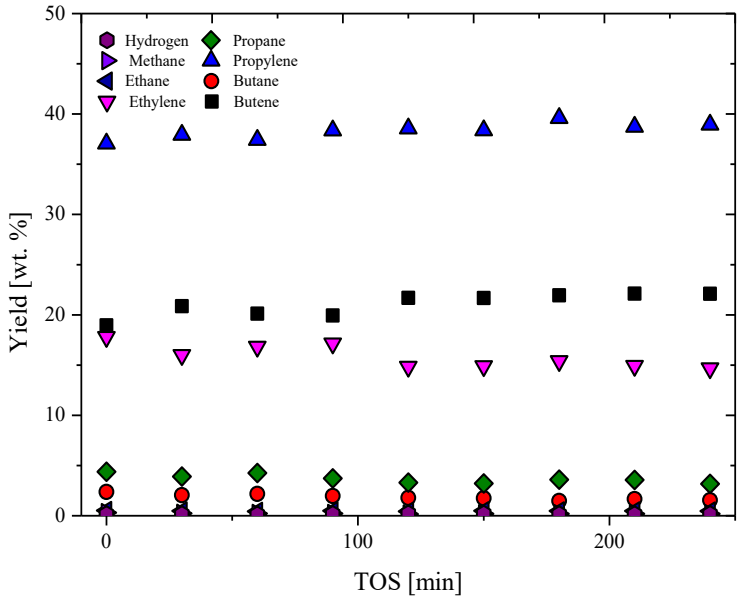

Figure 91: Time evolution of gas-phase yields at 500°C, τ= 10 $g_{catalyst}$ min/$g_{plastic}$.

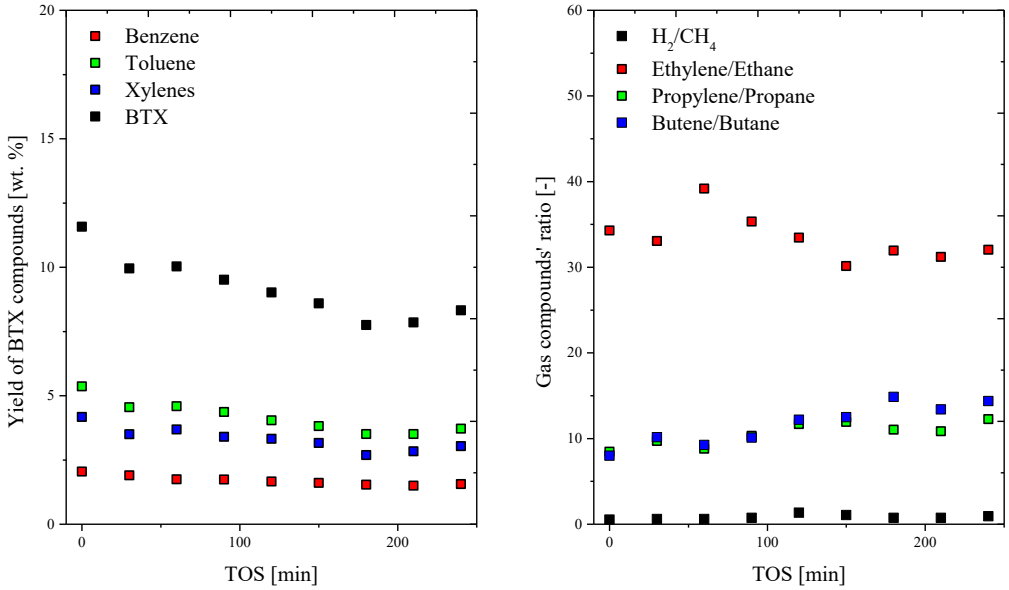

Figure 92: Effect of TOS on yield of BTX (A) and of gas-phase ratios (B) during the deactivation of HZSM-5 at 500°C, τ=10 $g_{catalyst}$ min/$g_{plastic}$.

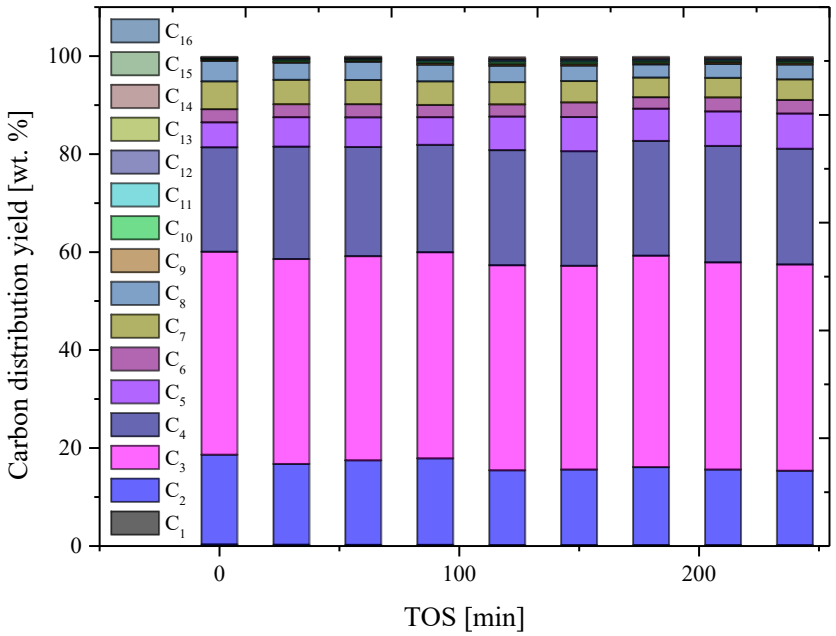

Figure 93: Time evolution of product distribution (process conditions: 500°C, τ= 10 $g_{catalyst}$ min/$g_{plastic}$).

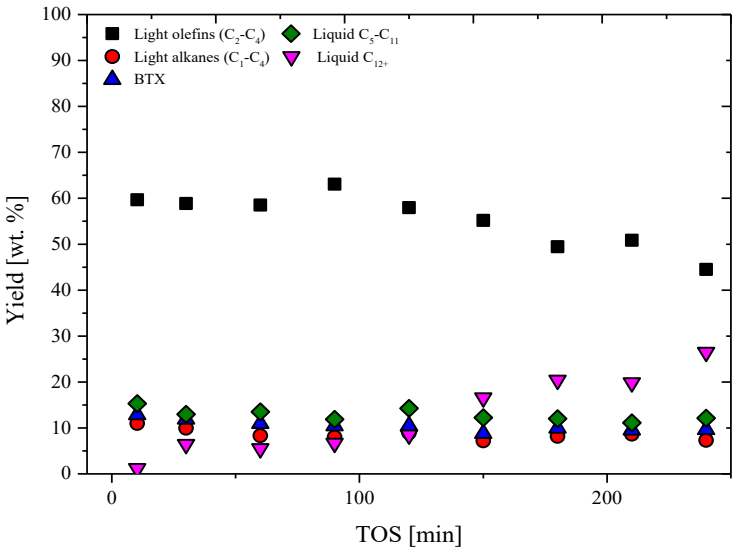

Figure 94: Time evolution of product class yields at 450°C, τ= 10 $g_{catalyst}$ min/$g_{plastic}$.

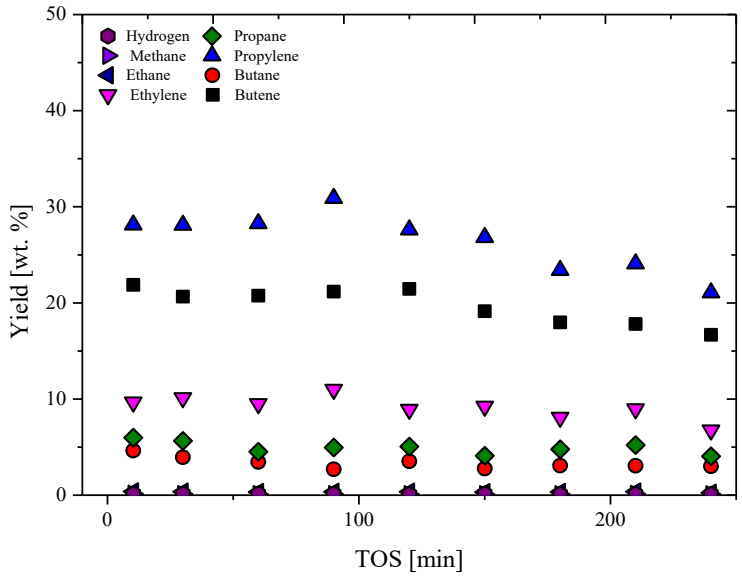

Figure 95: Time evolution of gas-phase yields at 450°C, τ= 10 $g_{catalyst}$ min/$g_{plastic}$.

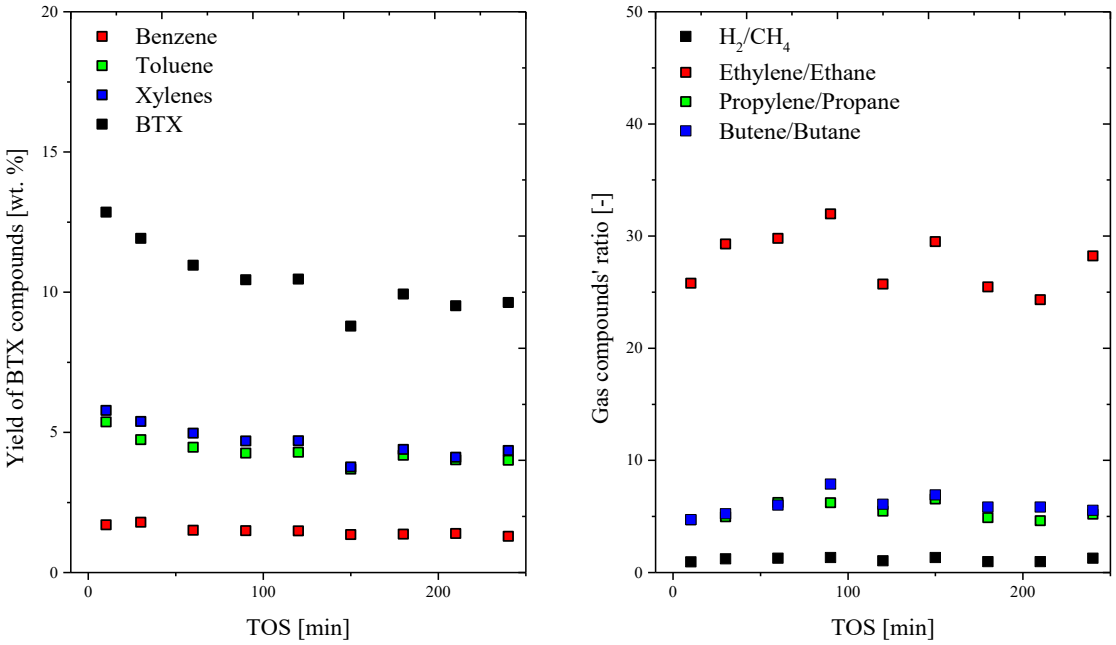

Figure 96: Effect of TOS on yield of BTX (A) and of gas-phase ratios (B) during the deactivation of HZSM-5 at 450°C, τ=10 $g_{catalyst}$ min/$g_{plastic}$.

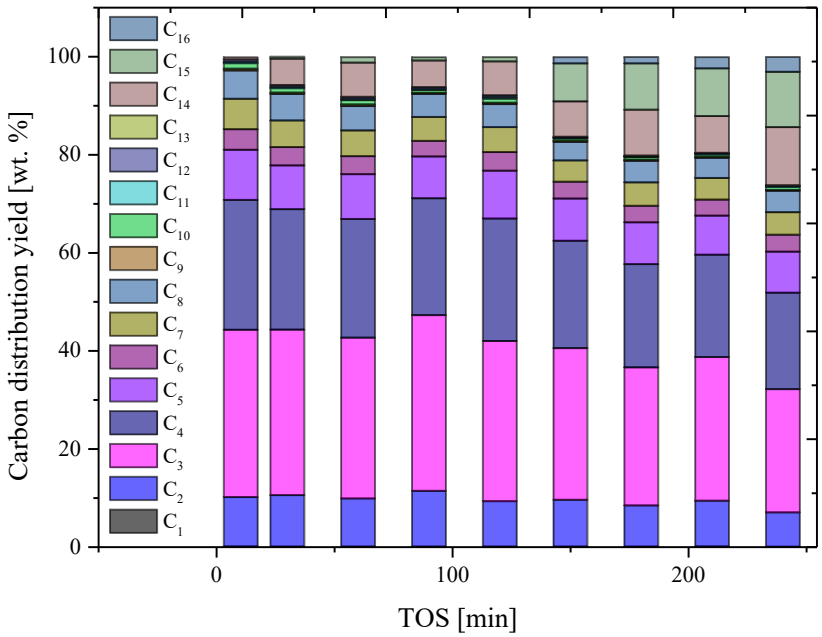

Figure 97: Time evolution of product distribution (process conditions: 450°C, τ= 10 $g_{catalyst}$ min/$g_{plastic}$).

Deterioration of physical properties of spent catalyst during fast pyrolysis and in-line catalytic cracking of polyolefins

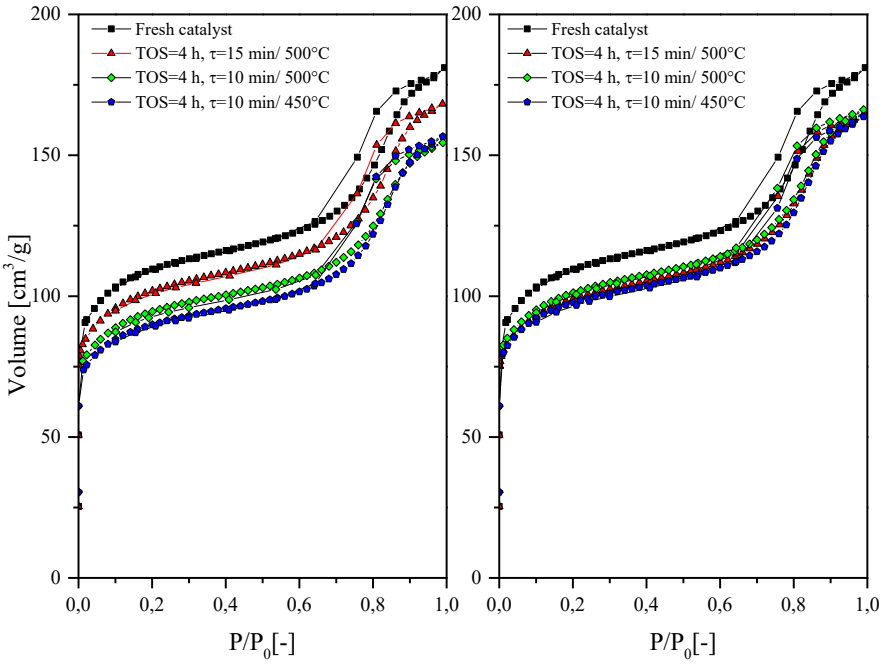

Figure 98: N_2-adsorption curves of fresh and spent HZSM-5 in first (A) and second (B) catalytic bed.

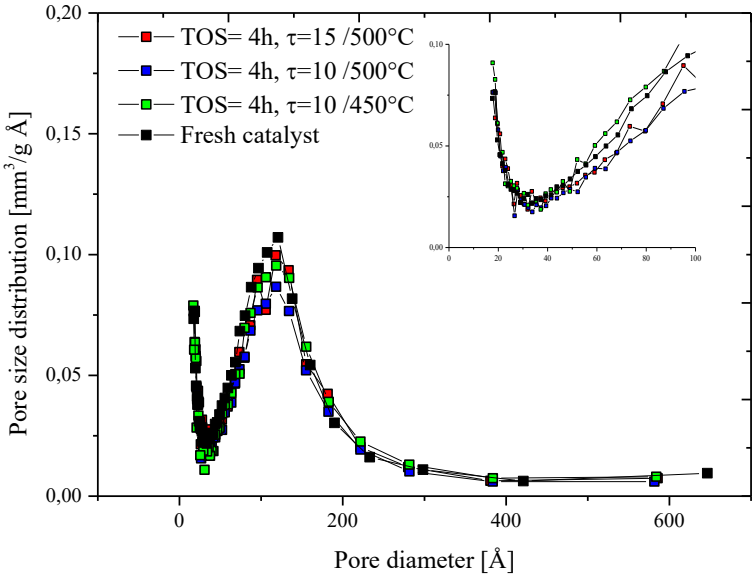

Figure 99: Pore size distribution of fresh and spent HZSM-5 from the first catalytic bed.

Appendix B

Effect of space-time on bio-oil composition during fast pyrolysis and in-line catalytic cracking of olive stone pyrolysis vapours: GCMS comparison

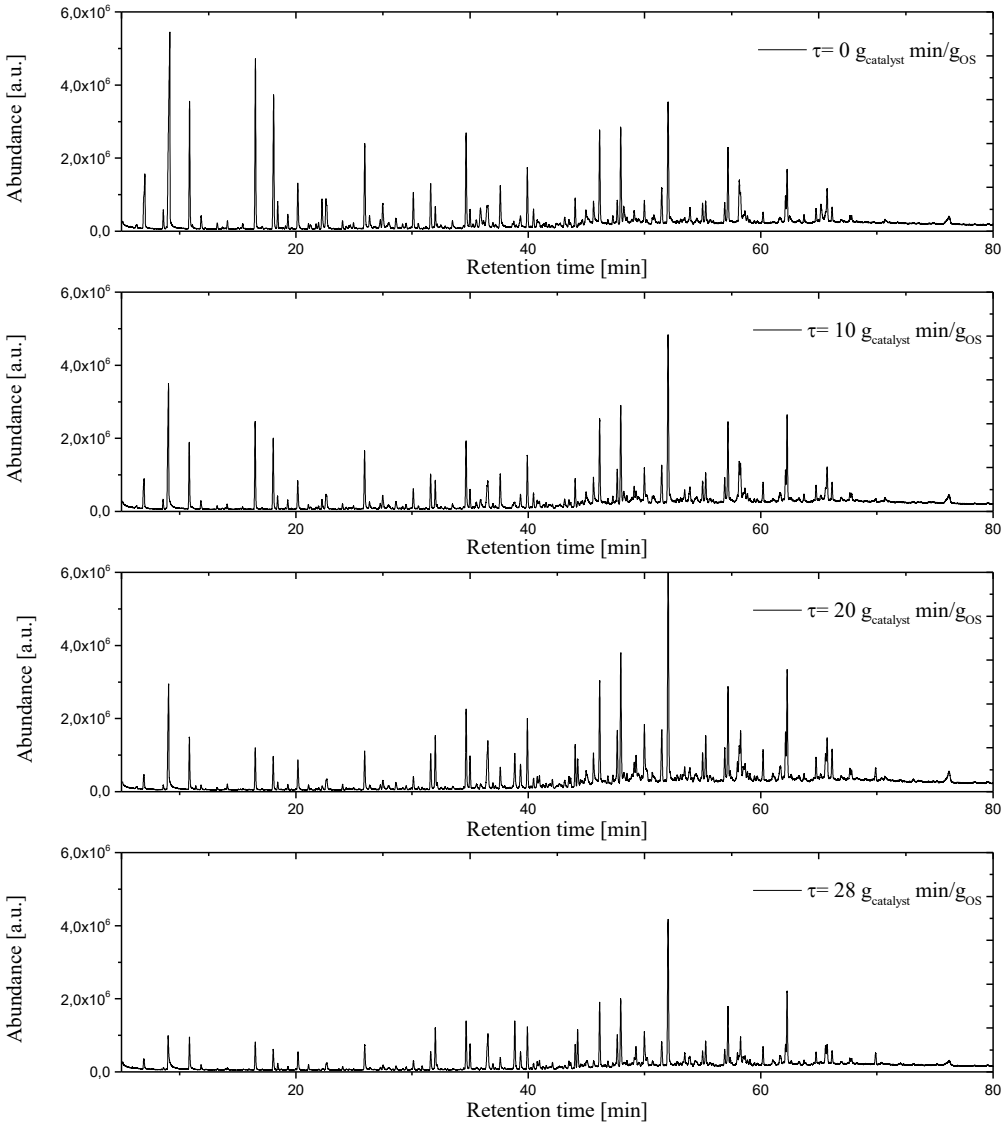

Figure 100: Effect of space-time on bio-oil chromatogram by GCMS.

Effect of space-time on the yield of specific bio-oil compounds

Table 18: Effect of space-time on bio-oil composition (semi-quantitative, %relative peak area).

Compounds	*τ=0 $g_{catalyst}$ min/ g_{OS}*	*τ=10 $g_{catalyst}$ min/ g_{OS}*	*τ=20 $g_{catalyst}$ min/ g_{OS}*	*τ=28 $g_{catalyst}$ min/ g_{OS}*
Organic acids	**15,14**	**9,69**	**5,41**	**4,42**
Acetic acid	9,01	5,58	3,49	2,62
Propanoic acid	0,23	0,17	0,13	0,10
Butanoic acid	0,07	-	-	-
Aldehydes	**10,10**	**8,22**	**12,30**	**5,60**
Succindialdehyde	4,08	2,61	0,89	1,10
Benzaldehyde, 3-hydroxy-	0,18	0,26	0,97	0,45
4-Hydroxy-2-methoxycinnamaldehyde	1,67	2,19	-	1,15
Ketones	**11,43**	**9,82**	**8,27**	**6,95**
2-Propanone, 1-hydroxy-	3,38	2,12	1,20	1,59
1,2-Cyclopentanedione	2,69	-	1,11	-
1,2-Cyclopentanedione, 3-methyl-	1,37	1,31	-	0,96
Furans	**7,85**	**5,71**	**4,33**	**2,90**
Furfural	1,46	1,13	0,88	0,97
2-Furanmethanol	0,99	0,44	0,14	-
2(5H)-Furanone	1,00	0,71	0,36	0,38
Phenols	**32,14**	**45,19**	**43,37**	**43,97**
Alkyl-phenols	**8,63**	**10,14**	**9,34**	**11,19**
Phenol	0,71	1,03	1,44	2,07
Phenol, 2-methyl-	0,59	0,66	0,92	1,26
Catechol	1,23	1,89	2,17	0,73
Guaiacols/syringols	**23,51**	**35,05**	**34,03**	**32,78**
Phenol, 2-methoxy-	2,98	2,58	2,17	2,47
Creosol	1,80	1,92	1,87	2,09
2-Methoxy-4-vinylphenol	3,18	3,60	3,27	-
Phenol, 2,6-dimethoxy-	2,97	3,83	3,85	3,66
trans-Isoeugenol	4,21	6,89	8,06	8,51
Sugars	**3,45**	**1,67**	**0,97**	**0,00**
Levoglucosan	2,53	1,67	0,97	-
Aromatics	**1,69**	**2,59**	**3,73**	**12,03**
Monoaromatics/biphenyl	0,00	0,82	1,29	4,84
Oxygenated monoaromatics	1,69	1,77	2,44	7,19
PAH	**0,00**	**1,82**	**7,60**	**13,29**
Naphtalenes	-	1.56	5,25	9,17
Phenanthrenes	-	0.26	1,23	0,81
Indenes	-	-	0,51	1,40
Anthracenes	-	-	0,50	1,54
Other compounds	**2,32**	**2,40**	**1,15**	**1,67**
Not identified	**15,88**	**12,89**	**12,87**	**9,17**

Effect of pyrolysis temperature on bio-oil composition during fast pyrolysis and in-line catalytic cracking of olive stone pyrolysis vapours: GCMS comparison

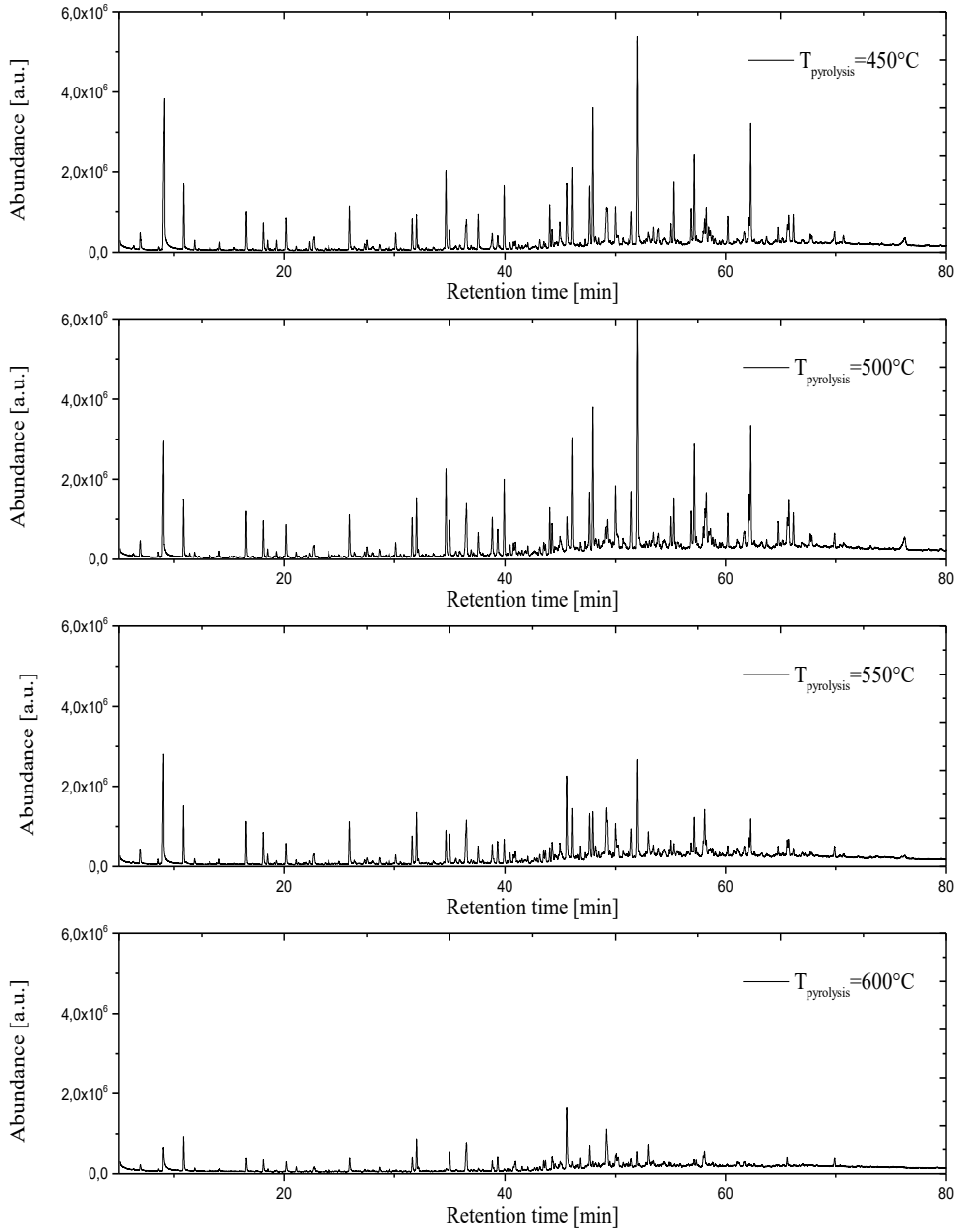

Figure 101: Effect of pyrolysis temperature on bio-oil chromatogram by GCMS.

Effect of pyrolysis temperature on the yield of specific bio-oil compounds

Table 19: Effect of pyrolysis temperature on bio-oil composition (semi-quantitative, %relative peak area).

Compounds	$T_{pyrolysis}$=450°C	$T_{pyrolysis}$ =500°C	$T_{pyrolysis}$ =550°C	$T_{pyrolysis}$ =600°C
Organic acids	**9,80**	**9,69**	**8,52**	**6,23**
Acetic acid	7,48	5,58	5,26	4,08
Propanoic acid	0,23	0,17	0,18	0,22
Butanoic acid	0,00	0,00	0,00	0,00
Aldehydes	**6,10**	**8,22**	**6,70**	**4,10**
Succindialdehyde	0,94	2,61	1,28	0,00
Benzaldehyde, 3-hydroxy-	0,28	0,26	0,70	0,50
4-Hydroxy-2-methoxycinnamaldehyde	1,04	2,19	0,79	0,00
Ketones	**8,00**	**9,82**	**9,86**	**11,36**
2-Propanone, 1-hydroxy-	1,82	2,12	1,92	3,13
1,2-Cyclopentanedione	-	-	1,81	-
1,2-Cyclopentanedione, 3-methyl-	1,05	1,31	0,35	1,54
Furans	**1,54**	**5,71**	**3,49**	**2,57**
Furfural	0,31*	1,13	0,91	0,00
2-Furanmethanol	0,30	0,44	0,16	0,00
2(5H)-Furanone	0,43	0,71	0,40	0,00
Phenols	**42,75**	**45,19**	**38,92**	**34,84**
Alkyl-phenols	**8,84**	**10,14**	**16,22**	**29,61**
Phenol	1,07	1,03	1,97	3,13
Phenol, 2-methyl-	0,68	0,66	1,16	1,79
Catechol	2,74	1,89	4,42	7,71
Guaiacols/syringols	**33,91**	**35,05**	**22,70**	**5,23**
Phenol, 2-methoxy-	2,61	2,58	1,41	0,25
Creosol	1,97	1,92	0,99	0,32
2-Methoxy-4-vinylphenol	2,66	3,60	2,40	1,07
Phenol, 2,6-dimethoxy-	4,57	3,83	2,15	0,74
trans-Isoeugenol	7,86	6,89	4,29	1,56
Sugars	**0,89**	**1,67**	**2,72**	**2,27**
Levoglucosan	0,89	1,67	2,72	2,27
Aromatics	**8,82**	**2,59**	**9,64**	**11,01**
Monoaromatics/biphenyl	2,02	0,82	1,05	0,54
Oxygenated monoaromatics	6,80	1,77	8,59	10,47
PAH	**6,05**	**7,60**	**8,00**	**13,77**
Naphtalenes	4,06	5,25	5,16	8,03
Phenanthrenes	0,00	1,23	0,00	0,00
Indenes	0,37	0,51	1,48	4,09
Anthracenes	1,62	0,50	1,36	1,65
Other compounds	**2,55**	**1,15**	**2,14**	**0,00**
Not identified	**13,50**	**8,36**	**10,01**	**13,85**

Effect of cracking temperature on bio-oil composition during fast pyrolysis and in-line catalytic cracking of olive stone pyrolysis vapours: GCMS comparison

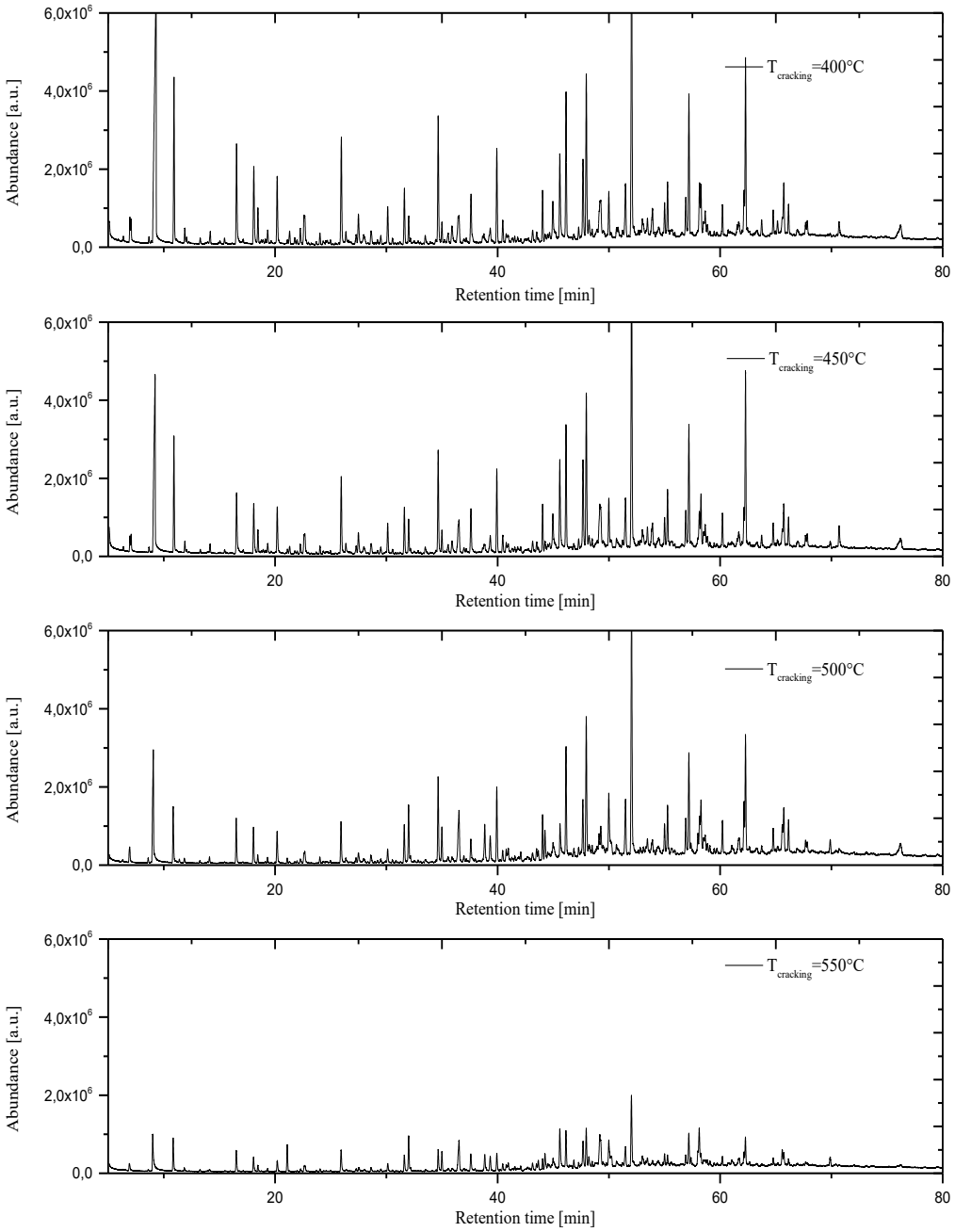

Figure 102: Effect of cracking temperature on bio-oil chromatogram by GCMS.

Effect of cracking temperature on the yield of specific bio-oil compounds

Table 20: Effect of cracking temperature on bio-oil composition (semi-quantitative, %relative peak area).

Compounds	$T_{cracking}$=400°C	$T_{cracking}$=450°C	$T_{cracking}$=500°C	$T_{cracking}$=550°C
Organic acids	**13,52**	**9,33**	**9,69**	**5,81**
Acetic acid	10,66	6,78	5,58	2,83
Propanoic acid	0,25	0,20	0,17	0,00
Butanoic acid	0,00	0,00	0,00	0,00
Aldehydes	**5,80**	**5,30**	**8,22**	**6,10**
Succindialdehyde	1,77	1,49	2,61	n.d.
Benzaldehyde, 3-hydroxy-	0,20	0,28	0,26	0,26
4-Hydroxy-2-methoxycinnamaldehyde	1,42	1,22	2,19	n.d.
Ketones	**14,91**	**12,18**	**9,82**	**14,77**
2-Propanone, 1-hydroxy-	3,03	2,55	2,12	2,37
1,2-Cyclopentanedione	2,35	2,05		1,03
1,2-Cyclopentanedione, 3-methyl-	1,21	1,24	1,31	0,14
Furans	**3,75**	**3,15**	**5,71**	**2,07**
Furfural	1,42	1,25	1,13	n.d.
2-Furanmethanol	0,34	0,26	0,44	0,20
2(5H)-Furanone	0,76	0,71	0,71	0,41
Phenols	**38,17**	**44,83**	**45,19**	**45,34**
Alkyl-phenols	**6,52**	**7,37**	**10,14**	**18,66**
Phenol	0,56	0,81	1,03	2,69
Phenol, 2-methyl-	0,38	0,54	0,66	1,40
Catechol	1,87	2,50	1,89	3,36
Guaiacols/syringols	**31,65**	**37,46**	**35,05**	**26,68**
Phenol, 2-methoxy-	2,64	2,77	2,58	1,81
Creosol	1,97	2,18	1,92	1,30
2-Methoxy-4-vinylphenol	2,97	3,10	3,60	n.**d.**
Phenol, 2,6-dimethoxy-	3,70	4,23	3,83	3,27
trans-Isoeugenol	7,19	8,74	6,89	6,15
Sugars	**1,32**	**1,06**	**1,67**	**4,55**
Levoglucosan	1,32	1,06	1,67	3,34
Aromatics	**4,21**	**6,69**	**2,59**	**7,37**
Monoaromatics/biphenyl	0,69	1,17	0,82	0,87
Oxygenated monoaromatics	3,52	5,52	1,77	6,50
PAH	**0,43**	**1,90**	**7,60**	**8,19**
Naphtalenes	0,31	0,89	5,25	5,47
Phenanthrenes	0,00	0,00	1,23	n.**d.**
Indenes	0,12	0,30	0,51	0,15
Anthracenes	0,00	0,61	0,50	2,12
Other compounds	**2,93**	**3,31**	**1,15**	**1,36**
Not identified	**14,96**	**12,25**	**8,36**	**4,44**

Effect of catalyst type on bio-oil composition during fast pyrolysis and in-line catalytic cracking of olive stone pyrolysis vapours: GCMS comparison

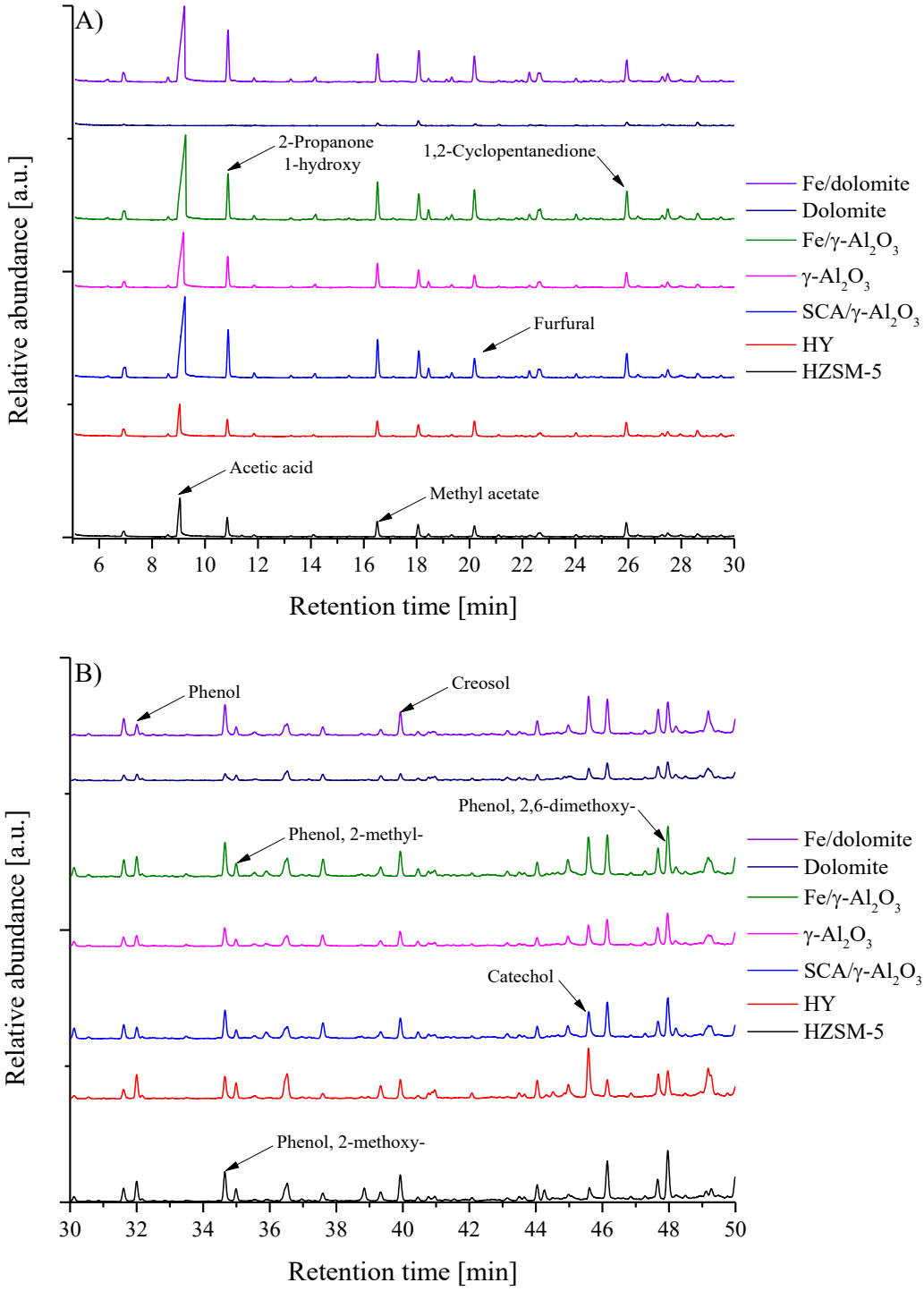

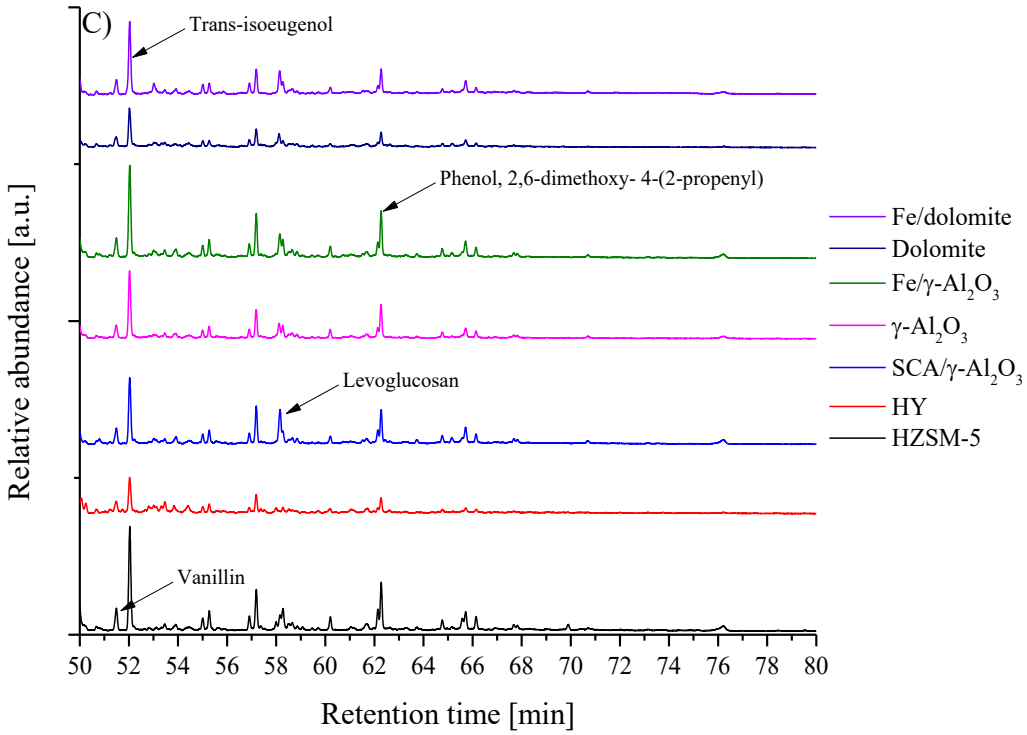

Figure 103: Effect of catalyst on bio-oil chromatogram by GCMS.

Effect of catalyst the yield of specific bio-oil compounds

Table 21: Effect of catalyst type on bio-oil composition (semi-quantitative, %relative peak area).

Compounds	*No-catalyst*	*HZSM-5*	*HY*	*SCA/ γ-Al_2O_3*	*γ-Al_2O_3*	*3%Fe/ γ-Al_2O_3*	*Dolomite*	*3%Fe/ Dolomite*
Organic acids	**15,14**	**9,69**	**5,91**	**16,13**	**14,90**	**17,23**	**0,53**	**15,36**
Acetic acid	9,01	5,58	3,92	11,96	10,01	11,52	-	11,98
Propanoic acid	0,23	0,17	0,17	0,32	0,34	0,37	-	0,44
Butanoic acid	0,07	-	-	0,12	0,11	0,14	-	0,18
Aldehydes	**10,10**	**8,22**	**4,30**	**7,70**	**5,10**	**4,90**	**5,10**	**5,60**
Succindialdehyde	4,08	2,61	1,44	2,32	1,87	1,89	1,01	2,73
Benzaldehyde, 3-hydroxy-	0,18	0,26	0,41	0,19*	0,21*	0,05*	1,07	0,27*
4-Hydroxy-2-methoxy-cinnamaldehyde	1,67	2,19	-	1,25	1,42	0,15	2,08	1,30
Ketones	**11,43**	**9,82**	**8,78**	**11,92**	**11,14**	**11,81**	**8,58**	**12,47**
2-Propanone, 1-hydroxy-	3,38	2,12	1,71	3,44	3,04	2,79	-	3,81
1,2-Cyclopentanedione	2,69	-	1,71	2,09	-	-	-	-
1,2-Cyclopentanedione, 3-methyl-	1,37	1,31	-	-	1,08	-	-	-
Furans	**7,85**	**5,71**	**8,25**	**4,53**	**4,58**	**6,11**	**2,18**	**6,07**
Furfural	1,46	1,13	1,84	1,68	1,48	2,18	-	2,34
2-Furanmethanol	0,99	0,44	-	0,58	0,27	0,40	0,22	0,83
2(5H)-Furanone	1,00	0,71	0,57	0,81	0,73	0,86	0,29	0,90
Phenols	**32,14**	**45,19**	**40,47**	**34,28**	**41,10**	**37,62**	**50,13**	**38,45**
Alkyl-phenols	**8,63**	**10,14**	**20,28**	**8,71**	**9,91**	**9,95**	**17,18**	**10,55**
Phenol	0,71	1,03	2,59	0,85	1,16	1,32	1,14	0,86
Phenol, 2-methyl-	0,59	0,66	1,69	0,69	0,71	0,78	1,00	0,69
Catechol	1,23	1,89	6,22	2,22	2,97	2,68	2,90	3,80
Guaiacols/syringols	**23,51**	**35,05**	**20,19**	**25,57**	**31,19**	**27,67**	**32,95**	**27,90**
Guaiacol	2,98	2,58	2,68	2,40	2,13	2,36	1,60	2,68
Creosol	1,80	1,92	2,17	1,64	1,60	1,70	1,25	1,89
2-Methoxy-4-vinylphenol	3,18	3,60	-	2,63	3,14	2,62	-	3,03
Syringol	2,97	3,83	3,41	3,29	3,76	3,46	3,60	2,84
trans-Isoeugenol	4,21	6,89	3,95	5,22	7,42	6,18	7,68	6,03
Sugars	**3,45**	**1,67**	**0,10**	**3,07**	**1,90**	**1,55**	**3,13**	**2,55**
Levoglucosan	2,53	1,67	0,10	3,07	1,90	1,55	3,13	2,08
Aromatics	**1,69**	**2,59**	**13,27**	**4,84**	**6,72**	**6,09**	**5,63**	**6,73**
Monoaromatics biphenyl	-	0,82	0,69	1,48	1,85	0,46	-	-
Oxygenated monoaromatics	1,69	1,77	12,58	3,36	4,87	5,63	5,63	6,73
PAH	**0,00**	**7,60**	**8,55**	**0,36**	**1,28**	**1,24**	**9,12**	**2,45**
Naphtalenes	-	5,25	2,74	0,36	0,62	1,05	3,79	0,38
Phenanthrenes	-	1,23	0,10	-	0,07	-	-	-
Indenes	-	0,51	5,71	-	0,59	0,19	5,33	0,40
Anthracenes	-	0,50	-	-	-	-	-	-
Other compounds	**2,32**	**1,15**	**2,29**	**1,57**	**2,08**	**2,96**	**2,99**	**0,84**
Not identified	**15,88**	**8,36**	**8,08**	**15,60**	**11,20**	**10,49**	**12,61**	**9,48**

Appendix C

Optical microscope images of fresh catalysts (Leica DM 2700 m)

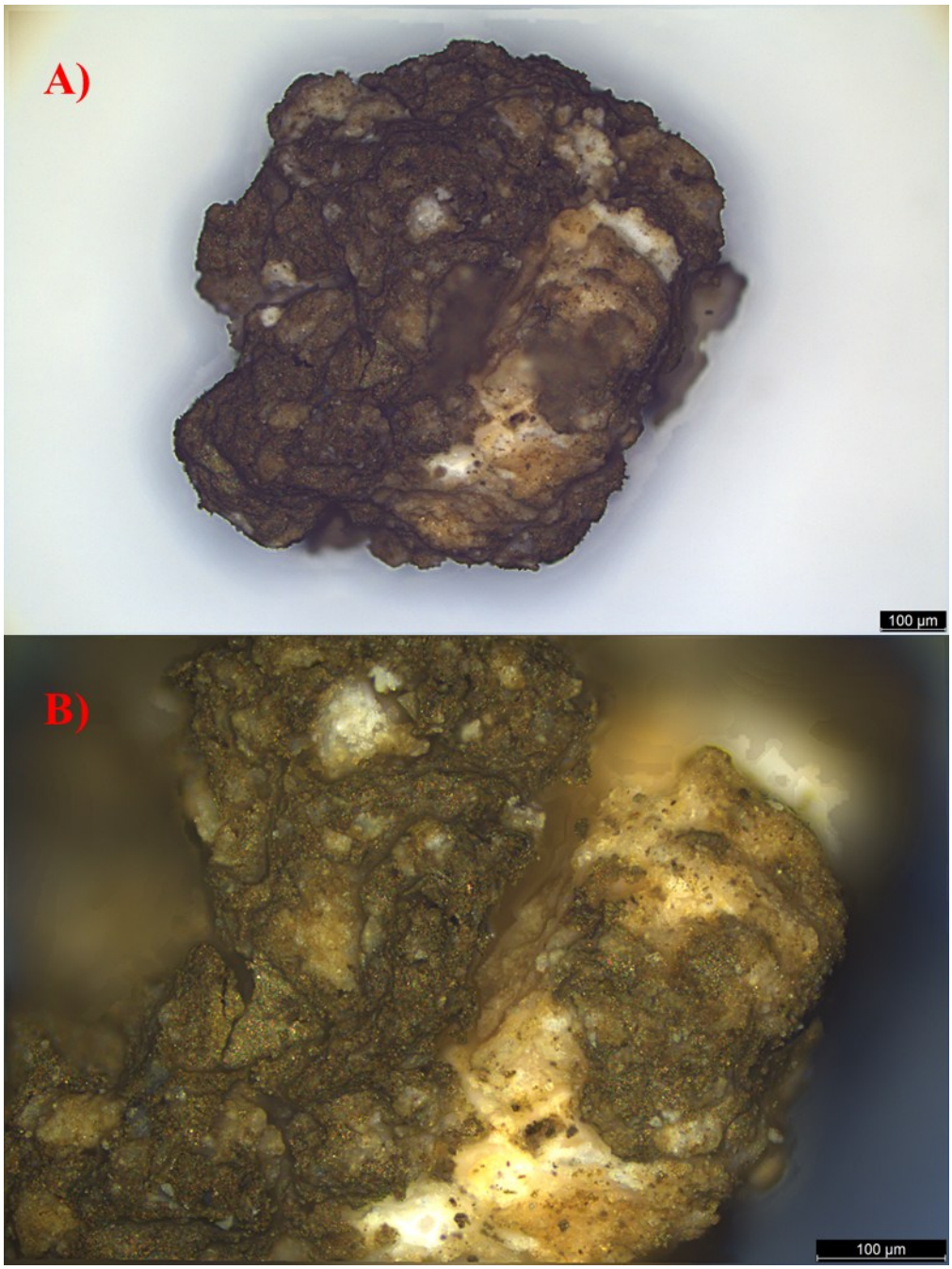

Figure 104: 3% Fe/dolomite catalyst, entire particle (A) and region of poor Fe deposition (B).

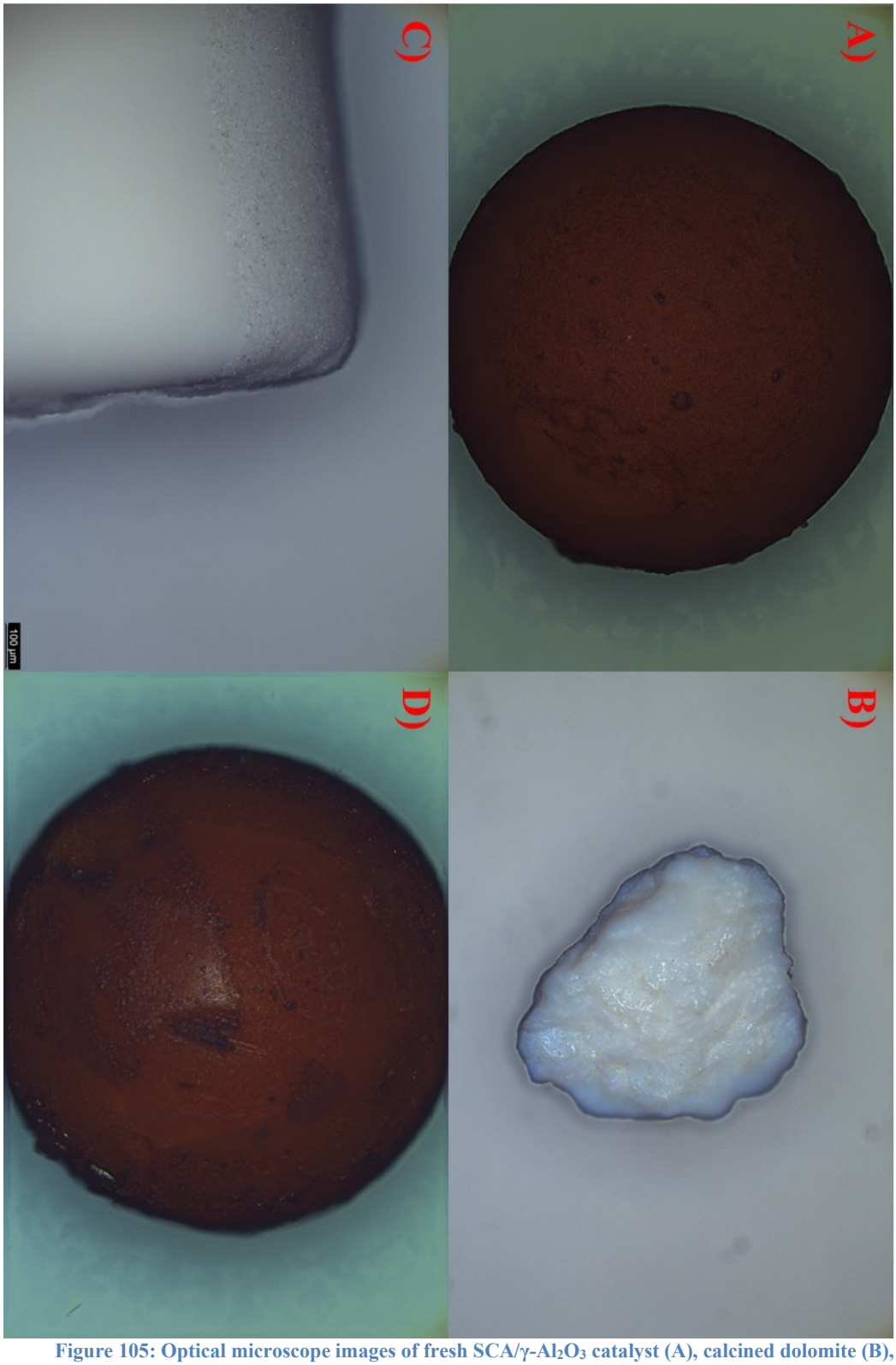

Figure 105: Optical microscope images of fresh SCA/γ-Al_2O_3 catalyst (A), calcined dolomite (B), HZSM-5 (C) and 3%Fe/ γ-Al_2O_3 (D).

Appendix D

Protocol for total phenol quantification in bio-oil samples with Folin-Ciocâlteu assay by Swita et al. (2022)

1. Preparation of Guaiacol Calibration Curve

1.1. Preparation of Guaiacol Stock Solution (Stock 1)

A concentrated guaiacol stock solution (approximately 1.5% w/w) was prepared by accurately weighing 0.0750 g of guaiacol into a tared 20 mL scintillation vial (labelled 'STOCK 1'). Subsequently, 6.25 mL (approximately 4.925 g) of acetone was added via micropipette. The vial was immediately capped to minimize acetone volatilization, and the precise mass of added acetone was recorded. This step is critical due to the volatile nature of acetone and the small quantities involved.

1.2. Preparation of Guaiacol Standard Solutions (S1-S5)

Five guaiacol standard solutions (S1-S5) were prepared by serial dilution from Stock 1 using 20 mL scintillation vials (Figure 106). Each vial was tared with its cap before additions, and the masses of all added components were meticulously recorded.

•Standard S5: Approximately 0.50 g of Stock 1 was added to a tared vial, followed by 4.90 g of acetone.

•Standard S4: Approximately 0.75 mL of S5 was added to a tared vial, followed by 0.25 mL of acetone.

•Standard S3: Approximately 0.50 mL of S5 was added to a tared vial, followed by 0.25 mL of acetone.

•Standard S2: Approximately 0.25 mL of S5 was added to a tared vial, followed by 0.75 mL of acetone.

•Standard S1: Approximately 0.1 mL of S5 was added to a tared vial, followed by 0.9 mL of acetone.

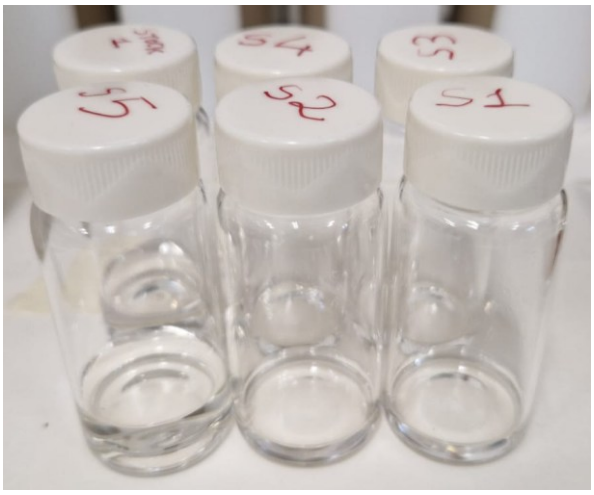

Figure 106: Standard guaiacol solutions.

2. Folin-Ciocâlteu Assay on Standard Solutions (S1-S5)

The Folin-Ciocâlteu assay was performed on each standard solution (S1-S5) in separate 20 mL scintillation vials (labelled S1-FC to S5-FC). Each vial was tared with its cap before additions, and the masses of all added reagents were recorded.

For each standard (S1-S5):

- 100 µL of deionized water was added to the tared vial.
- 200 µL of Folin-Ciocâlteu reagent was subsequently added.
- 100 µL of the respective guaiacol standard solution (S1, S2, S3, S4, or S5) was introduced.

The mixture was agitated and allowed to react for 5 minutes. 600 µL of a 20% (w/v) anhydrous sodium carbonate (Na_2CO_3) aqueous solution was added. The solution was then allowed to cool at room temperature for 2 hours. Alternatively, to reduce reaction time, samples could be incubated in a 45 °C water bath for 30 minutes, followed by cooling to room temperature before analysis (Figure 107)

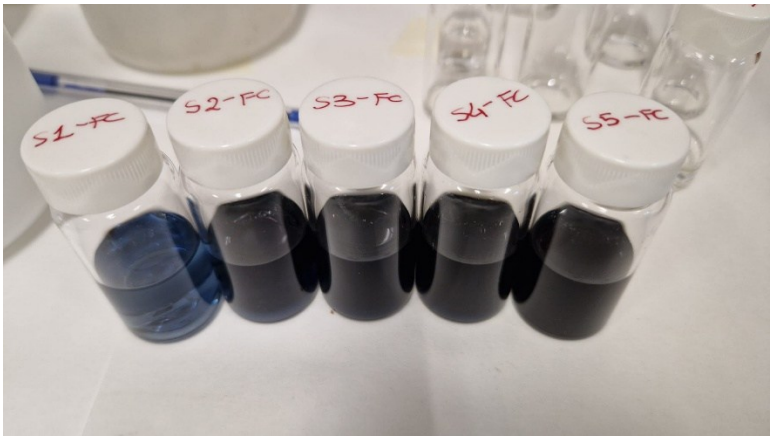

Figure 107: F-C assay on standard guaiacol solutions.

3. Preparation and Analysis of Blank Sample

A blank sample was prepared in a 20 mL scintillation vial (labelled 'BLANK') to account for reagent background absorbance. The vial was tared with its cap before additions, and all masses were recorded.

- Approximately 10 mL of deionized water was added.
- 200 µL of Folin-Ciocâlteu reagent was added.
- 100 µL of acetone was introduced.

The mixture was agitated and allowed to react for 5 minutes. 600 µL of a 20% (w/v) anhydrous sodium carbonate (Na_2CO_3) aqueous solution was added. The solution was then allowed to incubate at room temperature for 2 hours. As an alternative, the blank could be heated in a 45 °C water bath for 30 minutes, followed by cooling to room temperature prior to analysis.

4. UV-Vis Spectrophotometric Analysis

Following the reaction period, appropriate aliquots of the treated standard solutions (S1-FC to S5-FC) and the blank were transferred to separate cuvettes. Absorbance measurements were performed using a UV-Vis spectrophotometer set at 765 nm. For each sample, a minimum of three absorbance readings were taken, and the mean value was reported. Blank-corrected absorbance values were obtained by subtracting the blank absorbance from the sample absorbances. It is noted that the guaiacol calibration curve typically exhibits a second-order polynomial relationship for absorbance values between 0.1 and 1.5.

5. Analysis of Bio-Oil Sample

5.1. Preparation of Bio-Oil Stock Solution (Sol. A)

A concentrated bio-oil stock solution (Sol. A) was prepared by weighing approximately 0.3 g of bio-oil into a tared 20 mL scintillation vial (labelled 'Sol. A'). Subsequently, 10 mL of acetone was added, and the mass of added acetone was recorded. The bio-oil sample was thoroughly homogenized prior to preparation to ensure representativeness.

5.2. Preparation of Diluted Bio-Oil Solution (Sol. B)

A diluted bio-oil solution (Sol. B) was prepared by adding approximately 0.4 mL of Sol. A to a tared 20 mL scintillation vial (labelled 'Sol. B'), followed by 0.6 mL of acetone. The mass of added acetone was recorded.

Note on Absorbance Range: The absorbance of the bio-oil sample (Sol. B) should ideally fall between 0.2 and 0.9. If the absorbance is below 0.2, a more concentrated Sol. B should be prepared. Conversely, if the absorbance exceeds 0.9, further dilution of Sol. B with acetone is required before proceeding with the Folin-Ciocâlteu assay.

6. Folin-Ciocâlteu Assay on Bio-Oil Sample (Sol. B)

The Folin-Ciocâlteu assay was performed on the diluted bio-oil solution (Sol. B) in a 20 mL scintillation vial (labelled 'Sol. B-FC'). The vial was tared with its cap before additions, and all masses were recorded.

- Approximately 10 mL of deionized water was added to the tared vial.
- 200 µL of Folin-Ciocâlteu reagent was subsequently added.
- 60 µL of Sol. B was introduced.

The mixture was agitated and allowed to react for 5 minutes. 600 µL of a 20% (w/v) anhydrous sodium carbonate (Na_2CO_3) aqueous solution was added. The solution was then allowed to incubate at room temperature for 2 hours. Alternatively, to reduce reaction time, the sample could be incubated in a 45 °C water bath for 30 minutes, followed by cooling to room temperature before analysis.

7. UV-Vis Spectrophotometric Analysis of Bio-Oil Sample

Following the reaction period, an appropriate aliquot of the treated bio-oil solution (Sol. B-FC) was transferred to a cuvette. Absorbance measurements were

performed using a UV-Vis spectrophotometer set at 765 nm. A minimum of three absorbance readings were taken, and the mean value was reported. The blank absorbance was subtracted to obtain the blank-corrected absorbance.

Preparation of 20% (w/v) Sodium Carbonate Solution

A 20% (w/v) sodium carbonate solution was prepared by dissolving 20 grams of anhydrous sodium carbonate (Na_2CO_3) in distilled water. The solution was quantitatively transferred to a 100 mL volumetric flask, and the volume was adjusted to 100 mL with distilled water. The solution was gently stirred until complete dissolution of the sodium carbonate was achieved.

Appendix E

Hydrodynamics of the flat-base spouted bed reactor

The operating conditions of the flat-base spouted-bed reactor have been the result of careful experimentation on the hydrodynamics to guarantee stable spouted regime and avoid dead volumes, i.e. motionless portions of the bed usually located at the bottom. Experiments were conducted at both ambient and pyrolysis temperatures (500°C), using silica sand of different particle size (0.3-0.45 mm, 0.45-0.6 mm and 0.6-0.8 mm) and with different bed height (3 cm, 4 cm, 5 cm and 6 cm). The main conclusions are here summarised:

1. The pressure drop profile reflects typical characteristics of spouted-bed reactors in typical pyrolysis conditions (Figure 108-A)
2. It is possible to keep steady-state stable spouted regime at 500°C
3. With the appropriate choice of gas velocity, it is possible to reduce dead volume and obtain complete conversion of biomass particles[7]
4. The minimum spouting velocity (U_{ms}) is linear with the height of the bed (Figure 108-B)

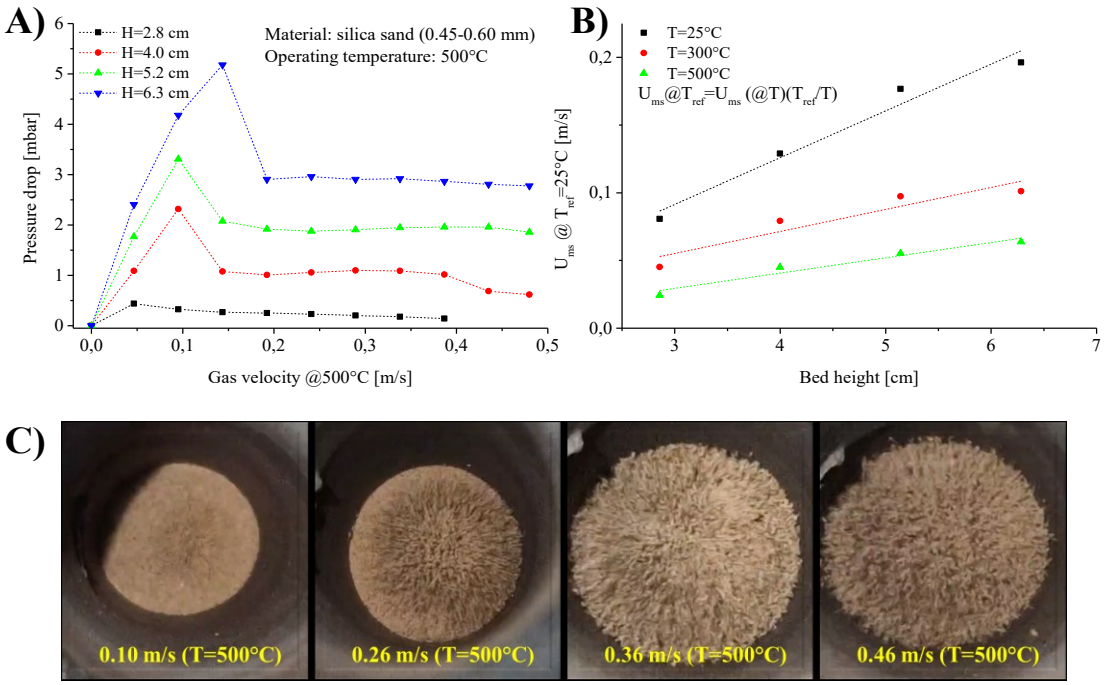

Figure 108: Pressure drop vs. superficial velocity profiles in pyrolysis conditions (A); effect of temperature and bed height on Ums (B); evolution of spouted regime with increasing gas superficial velocity (C).

[7] Several preliminary tests at 500°C have been conducted using different biomass (particularly olive stone and spruce wood pellets) to verify this statement. It was observed that at low gas velocities some biomass particles were not completely pyrolyzed, while uniform char particles were obtained at higher gas velocity ($U \approx 2.5U_{ms}$) probably due to the vigorous mixing reaching most of the sand bed (Figure 108-C).

Appendix F

Supplementary characterization results

- Figure 109 illustrates the results obtained from TPD of a spent HZSM-5 sample (operated at $T_{cracking}$=400°C). It can be observed that a high temperature peak is found during simple heating of the sample to 550°C (without preliminary NH_3 adsorption). This peak is associated with heavy organics condensed on the surface of the catalyst during pyrolysis, which are released with heating.

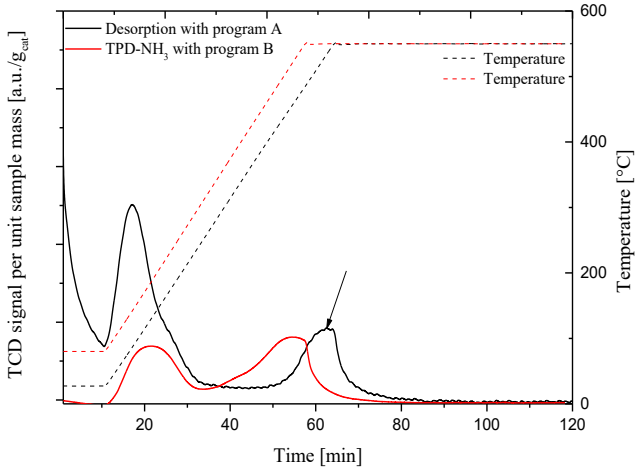

Figure 109: High-temperature peak associated with heavy condensed species during TPD of HZSM-5. Program A is heating in inert atmosphere to 550°C. Program B is pretreatment (400°C, He) + NH_3 adsorption at 25°C + heating to 550°C.

- The results from TG-MS (Thermogravimetry-Mass Spectroscopy) for the spent dolomite and Fe/dolomite catalysts is illustrated in Figure 110. From the MS profiles of CO_2, H_2O and CO it is possible to confirm that the peak obtained at 400°C is not associated with coke combustion, but to loss of water from the mineral structure of dolomite. The main weight losses are associated to CO_2 (above 600°C) and also to CO in the case of Fe/dolomite.

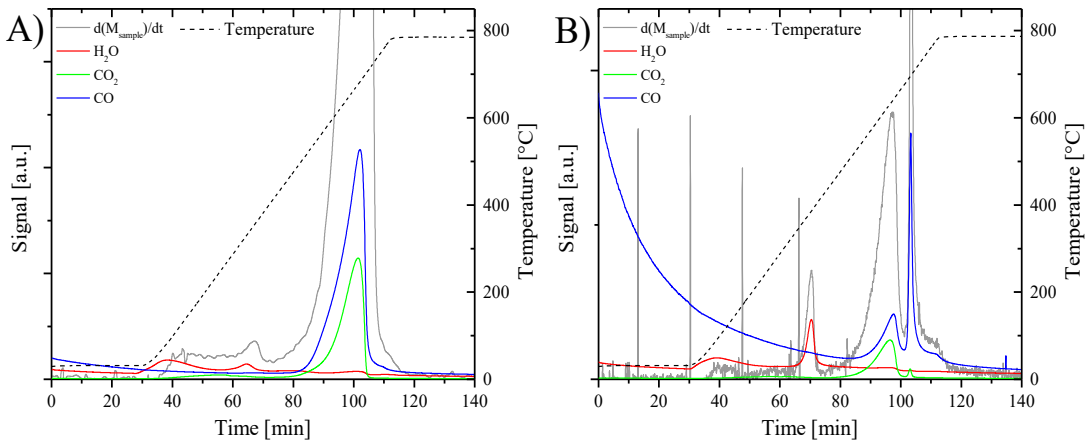

Figure 110: TG-MS results for spent dolomite (A) and Fe/dolomite (B) catalyst.

- Preliminary results on the quantification of phenols in bio-oil with the Folin-Ciocâlteu assay are reported in Figure 111.

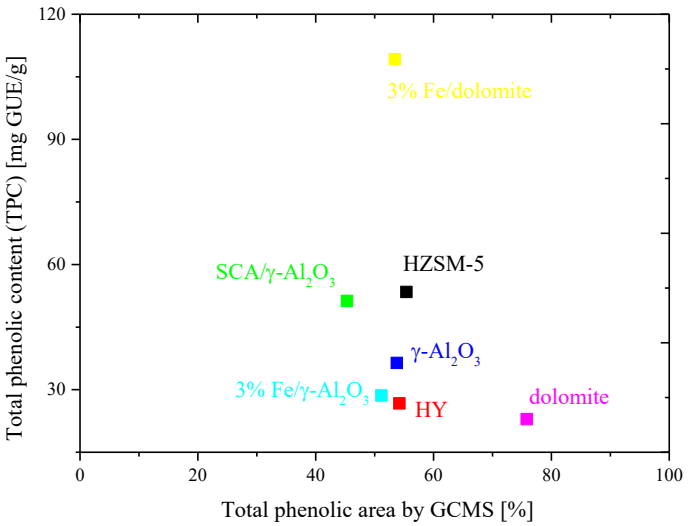

Figure 111: Total phenolic content of bio-oil samples obtained with different catalysts. Conditions were: $T_{pyrolysis}=T_{cracking}=500°C$, $\tau=20\ g_{catalyst}$ min/g_{OS}.

References

Abbas-Abadi, M. S., Haghighi, M. N., & Yeganeh, H. (2013). Evaluation of pyrolysis product of virgin high density polyethylene degradation using different process parameters in a stirred reactor. Fuel processing technology, 109, 90-95.

Achilias, D. S., Roupakias, C., Megalokonomos, P., Lappas, A. A., & Antonakou, E. V. (2007). Chemical recycling of plastic wastes made from polyethylene (LDPE and HDPE) and polypropylene (PP). Journal of hazardous materials, 149(3), 536-542.

Adams, P., Bridgwater, T., Lea-Langton, A., Ross, A., & Watson, I. (2018). Biomass conversion technologies. In Greenhouse gas balances of bioenergy systems (pp. 107-139). Academic Press.

Adeniyi, A. G., Otoikhian, K. S., & Ighalo, J. O. (2019). Steam reforming of biomass pyrolysis oil: a review. International Journal of Chemical Reactor Engineering, 17(4), 20180328.

Adjaye, J. D., & Bakhshi, N. N. (1995). Catalytic conversion of a biomass-derived oil to fuels and chemicals I: Model compound studies and reaction pathways. Biomass and Bioenergy, 8(3), 131-149.

Afifi, A. I., Chornet, E., Thring, R. W., & Overend, R. P. (1996). The aryl ether bond reactions with H-donor solvents: guaiacol and tetralin in the presence of catalysts. Fuel, 75(4), 509-516.

Agblevor, F. A., Abdellaoui, H., Halouani, K., & Beis, S. H. (2017). Pyrolytic conversion of olive mill wastewater sludge to biofuels using red mud as catalyst. Int J Energy Power Eng, 6(6), 108.

Agblevor, F. A., Besler, S., & Evans, R. J. (1994). Inorganic compounds in biomass feedstock: Their role in char formation and effects on the quality of fat pyrolysis oils. In proceedings of biomass pyrolysis oil properties and combustion meeting edited by Milne, TA, M Estes Park, National Renewable Energy Laboratory, Golden, CO. NREL-CP-430-7215,, 77-89, September 26-28.

Agbor, V. B., Cicek, N., Sparling, R., Berlin, A., & Levin, D. B. (2011). Biomass pretreatment: fundamentals toward application. Biotechnology advances, 29(6), 675-685.

Agilent 8890/8850 Gas Chromatograph Operation Manual. © Agilent Technologies, Inc. 2024

Aguayo, A. T., Castaño, P., Mier, D., Gayubo, A. G., Olazar, M., & Bilbao, J. (2011). Effect of cofeeding butane with methanol on the deactivation by coke of a HZSM-5 zeolite catalyst. Industrial & engineering chemistry research, 50(17), 9980-9988.

Ahmad, I., Khan, M. I., Ishaq, M., Khan, H., Gul, K., & Ahmad, W. (2013). Catalytic efficiency of some novel nanostructured heterogeneous solid catalysts in pyrolysis of HDPE. Polymer Degradation and Stability, 98(12), 2512-2519.

Ahmadi, E., Coralli, I., Torri, C., Facchin, A., Rombolà, A. G., Zangheri, M., ... & Fabbri, D. (2025). Analytical pyrolysis of fir sawdust, olive stone and sewage sludge in molten carbonate salts. Journal of Analytical and Applied Pyrolysis, 107144.

Aho, A., Kumar, N., Eränen, K., Salmi, T., Hupa, M., & Murzin, D. Y. (2008). Catalytic pyrolysis of woody biomass in a fluidized bed reactor: influence of the zeolite structure. Fuel, 87(12), 2493-2501.

Akubo, K., Nahil, M. A., & Williams, P. T. (2019). Aromatic fuel oils produced from the pyrolysis-catalysis of polyethylene plastic with metal-impregnated zeolite catalysts. Journal of the energy institute, 92(1), 195-202.

Al-Farraji, A., Marsh, R., & Steer, J. (2017). A comparison of the pyrolysis of olive kernel biomass in fluidised and fixed bed conditions. Waste and Biomass Valorization, 8, 1273-1284.

Ali, S., Garforth, A., Harris, D. H., & Shigeishi, R. A. (2003). Polymer waste recycling over used catalysts. Surfactant science series, 108, 295-328.

Alvarez, J., Lopez, G., Amutio, M., Bilbao, J., & Olazar, M. (2014). Bio-oil production from rice husk fast pyrolysis in a conical spouted bed reactor. Fuel, 128, 162-169.

Amutio, M., Lopez, G., Artetxe, M., Elordi, G., Olazar, M., & Bilbao, J. (2012). Influence of temperature on biomass pyrolysis in a conical spouted bed reactor. Resources, Conservation and Recycling, 59, 23-31.

Antal, M. J. J., & Varhegyi, G. (1995). Cellulose pyrolysis kinetics: the current state of knowledge. Industrial & engineering chemistry research, 34(3), 703-717.

Antal, M. J., Varhegyi, G., & Jakab, E. (1998). Cellulose pyrolysis kinetics: revisited. Industrial & engineering chemistry research, 37(4), 1267-1275.

Arabiourrutia, M., Bensidhom, G., Bolanos, M., Trabelsi, A. B. H., & Olazar, M. (2024). Catalytic pyrolysis of date palm seeds on HZSM-5 and dolomite in a pyroprobe reactor in line with GC/MS. Biomass Conversion and Biorefinery, 14(2), 2799-2818.

Arabiourrutia, M., Elordi, G., Olazar, M., & Bilbao, J. (2017). Pyrolysis of polyolefins in a conical spouted bed reactor: a way to obtain valuable products (pp. 285-304). London, UK: IntechOpen.

Argyle, M. D., & Bartholomew, C. H. (2015). Heterogeneous catalyst deactivation and regeneration: a review. Catalysts, 5(1), 145-269.

Arnold, S., Moss, K., Henkel, M., & Hausmann, R. (2017). Biotechnological perspectives of pyrolysis oil for a bio-based economy. Trends in Biotechnology, 35(10), 925-936.

Arregi, A., Seifali Abbas-Abadi, M., Lopez, G., Santamaria, L., Artetxe, M., Bilbao, J., & Olazar, M. (2020). CeO2 and La2O3 promoters in the steam reforming of polyolefinic waste plastic pyrolysis volatiles on Ni-based catalysts. ACS Sustainable Chemistry & Engineering, 8(46), 17307-17321.

Artetxe Uria, Maite (2013). Producción de olefinas a partir de polietileno por pirólisis y craqueo en línea (Doctoral dissertation, Universidad del País Vasco-Euskal Herriko Unibertsitatea).

Artetxe, M., Lopez, G., Amutio, M., Elordi, G., Bilbao, J., & Olazar, M. (2012). Light olefins from HDPE cracking in a two-step thermal and catalytic process. Chemical Engineering Journal, 207, 27-34.

Artetxe, M., Lopez, G., Amutio, M., Elordi, G., Bilbao, J., & Olazar, M. (2013). Cracking of high density polyethylene pyrolysis waxes on HZSM-5 catalysts of different acidity. Industrial & Engineering Chemistry Research, 52(31), 10637-10645.

Asadieraghi, M., Daud, W. M. A. W., & Abbas, H. F. (2015). Heterogeneous catalysts for advanced bio-fuel production through catalytic biomass pyrolysis vapor upgrading: a review. RSC Advances, 5(28), 22234-22255.

Bakar, M. S. A., & Titiloye, J. O. (2013). Catalytic pyrolysis of rice husk for bio-oil production. Journal of analytical and applied pyrolysis, 103, 362-368.

Barbarias, I., Artetxe, M., Arregi, A., Alvarez, J., Lopez, G., Amutio, M., & Olazar, M. (2015). Catalytic cracking of HDPE pyrolysis volatiles over a spent FCC catalyst. Chem. Eng, 43, 1-6.

Barbarias, I., Lopez, G., Artetxe, M., Arregi, A., Bilbao, J., & Olazar, M. (2018). Valorisation of different waste plastics by pyrolysis and in-line catalytic steam reforming for hydrogen production. Energy Conversion and Management, 156, 575-584.

Barreiro, D. L., Prins, W., Ronsse, F., & Brilman, W. (2013). Hydrothermal liquefaction (HTL) of microalgae for biofuel production: state of the art review and future prospects. Biomass and bioenergy, 53, 113-127.

Bartholomew, C. H. (2001). Mechanisms of catalyst deactivation. Applied Catalysis A: General, 212(1-2), 17-60.

Bhoi, P. R., Ouedraogo, A. S., Soloiu, V., & Quirino, R. (2020). Recent advances on catalysts for improving hydrocarbon compounds in bio-oil of biomass catalytic pyrolysis. Renewable and Sustainable Energy Reviews, 121, 109676.

Boekaerts, B., & Sels, B. F. (2021). Catalytic advancements in carboxylic acid ketonization and its perspectives on biomass valorisation. Applied Catalysis B: Environmental, 283, 119607.

Boon, J. (2023). Sorption-enhanced reactions as enablers for CO2 capture and utilisation. Current Opinion in Chemical Engineering, 40, 100919.

Boskovic, G., & Baerns, M. (2004). Catalyst deactivation. In Basic principles in applied catalysis (pp. 477-503). Berlin, Heidelberg: Springer Berlin Heidelberg.

Brachi, P., Migliaccio, R., Ganda, E. T., Urciuolo, M., Ruoppolo, G., Coppola, A., ... & Salatino, P. (2022). Strategies to Improve Quality and Yield of Pyrolysis Bio-oils. Chemical Engineering Transactions, 92, 469-474.

Brethauer, S., & Studer, M. H. (2015). Biochemical conversion processes of lignocellulosic biomass to fuels and chemicals–a review. Chimia, 69(10), 572-572.

Bridgwater, A. V. (2012). Review of fast pyrolysis of biomass and product upgrading. Biomass and bioenergy, 38, 68-94.

Bridgwater, A. V., Meier, D., & Radlein, D. (1999). An overview of fast pyrolysis of biomass. Organic geochemistry, 30(12), 1479-1493.

Bridgwater, T. (2018). Challenges and opportunities in fast pyrolysis of biomass: Part I. Johnson Matthey Technology Review, 62(1), 118-130.

Brown, R. C. (Ed.). (2019). Thermochemical processing of biomass: conversion into fuels, chemicals and power. John Wiley & Sons.

Bunting, B. G., & Boyd, A. C. (2012). An Evaluation of Pyrolysis Oil Properties and Chemistry As Related to Process and Upgrade Conditions with Special Consideration to Pipeline Shipment. Oak Ridge National Lab.(ORNL), Oak Ridge, TN (United States). Fuels, Engines and Emissions Research Center (FEERC).

Butt, J. (2012). Activation, deactivation, and poisoning of catalysts. Elsevier.

Caballero, B. M., López-Urionabarrenechea, A., Pérez, B., Solar, J., Acha, E., & de Marco, I. (2020). Potentiality of "orujillo"(olive oil solid waste) to produce hydrogen by means of pyrolysis. International Journal of Hydrogen Energy, 45(40), 20549-20557.

Cai, J., He, Y., Yu, X., Banks, S. W., Yang, Y., Zhang, X., ... & Bridgwater, A. V. (2017). Review of physicochemical properties and analytical characterization of lignocellulosic biomass. Renewable and sustainable energy reviews, 76, 309-322.

Cai, J., Rahman, M. M., Zhang, S., Sarker, M., Zhang, X., Zhang, Y., ... & Fini, E. H. (2021). Review on aging of bio-oil from biomass pyrolysis and strategy to slowing aging. Energy & Fuels, 35(15), 11665-11692.

Cai, R., Pei, X., Pan, H., Wan, K., Chen, H., Zhang, Z., & Zhang, Y. (2020). Biomass catalytic pyrolysis over zeolite catalysts with an emphasis on porosity and acidity: a state-of-the-art review. Energy & Fuels, 34(10), 11771-11790.

Campanati, M., Fornasari, G., & Vaccari, A. (2003). Fundamentals in the preparation of heterogeneous catalysts. Catalysis today, 77(4), 299-314.

Carlson, T. R., Cheng, Y. T., Jae, J., & Huber, G. W. (2011). Production of green aromatics and olefins by catalytic fast pyrolysis of wood sawdust. Energy & Environmental Science, 4(1), 145-161.

Carlson, T. R., Jae, J., Lin, Y. C., Tompsett, G. A., & Huber, G. W. (2010). Catalytic fast pyrolysis of glucose with HZSM-5: The combined homogeneous and heterogeneous reactions. Journal of Catalysis, 270(1), 110-124.

Carlson, T. R., Tompsett, G. A., Conner, W. C., & Huber, G. W. (2009). Aromatic production from catalytic fast pyrolysis of biomass-derived feedstocks. Topics in Catalysis, 52(3), 241-252.

Castaño, P., Elordi, G., Ibañez, M., Olazar, M., & Bilbao, J. (2012). Pathways of coke formation on an MFI catalyst during the cracking of waste polyolefins. Catalysis Science & Technology, 2(3), 504-508.

Castano, P., Elordi, G., Olazar, M., Aguayo, A. T., Pawelec, B., & Bilbao, J. (2011). Insights into the coke deposited on HZSM-5, Hβ and HY zeolites during the cracking of polyethylene. Applied Catalysis B: Environmental, 104(1-2), 91-100.

Castello, D., He, S., Ruiz, M. P., Westerhof, R. J., Heeres, H. J., Seshan, K., & Kersten, S. R. (2019). Is it possible to increase the oil yield of catalytic pyrolysis of biomass? A study using commercially-available acid and basic catalysts in ex-situ and in-situ modus. Journal of analytical and applied pyrolysis, 137, 77-85.

Cen, Z., Han, X., Lin, L., Yang, S., Han, W., Wen, W., ... & Han, B. (2024). Upcycling of polyethylene to gasoline through a self-supplied hydrogen strategy in a layered self-pillared zeolite. Nature Chemistry, 1-10.

Chang, C. D., & Silvestri, A. J. (1977). The conversion of methanol and other O-compounds to hydrocarbons over zeolite catalysts. Journal of catalysis, 47(2), 249-259.

Chang, S. H. (2023). Plastic waste as pyrolysis feedstock for plastic oil production: a review. Science of The Total Environment, 877, 162719.

Channiwala, S. A., & Parikh, P. P. (2002). A unified correlation for estimating HHV of solid, liquid and gaseous fuels. Fuel, 81(8), 1051-1063.

Chen, D., Cen, K., Zhuang, X., Gan, Z., Zhou, J., Zhang, Y., & Zhang, H. (2022). Insight into biomass pyrolysis mechanism based on cellulose, hemicellulose, and lignin: Evolution of volatiles and kinetics, elucidation of reaction pathways, and characterization of gas, biochar and bio-oil. Combustion and Flame, 242, 112142.

Chen, N.Y., Degnan Jr, T.F., Koenig, L.R. (1986). Liquid fuel from carbohydrates. Chem Tech, 506-11.

Chen, X., Liu, Z., Li, S., Xia, S., Cai, N., Chen, W., ... & Chen, H. (2021). Catalytic pyrolysis of biomass to produce aromatic hydrocarbons over calcined dolomite and ZSM-5. Energy & Fuels, 35(20), 16629-16636.

Chen, Z., Erwin, B. J., & Che, L. (2024). Recycling waste polyethylene into fuels over Fe/USY catalyst: Evaluation on the catalytic activities of varied iron states. Fuel, 363, 131007.

Cheng, S., Wang, Y., Gao, N., Takahashi, F., Li, A., & Yoshikawa, K. (2016). Pyrolysis of oil sludge with oil sludge ash additive employing a stirred tank reactor. Journal of Analytical and Applied Pyrolysis, 120, 511-520.

Cheng, Y. T., & Huber, G. W. (2012). Production of targeted aromatics by using Diels–Alder classes of reactions with furans and olefins over ZSM-5. Green Chemistry, 14(11), 3114-3125.

Chiang, H., & Bhan, A. (2010). Catalytic consequences of hydroxyl group location on the rate and mechanism of parallel dehydration reactions of ethanol over acidic zeolites. Journal of Catalysis, 271(2), 251-261.

Christoforou, E. A., Fokaides, P. A., Banks, S. W., Nowakowski, D., Bridgwater, A. V., Stefanidis, S., ... & Lappas, A. A. (2018). Comparative study on catalytic and non-catalytic pyrolysis of olive mill solid wastes. Waste and Biomass Valorization, 9(2), 301-313.

Chu, S., Subrahmanyam, A. V., & Huber, G. W. (2013). The pyrolysis chemistry of a β-O-4 type oligomeric lignin model compound. Green chemistry, 15(1), 125-136.

Ciddor, L., Bennett, J. A., Hunns, J. A., Wilson, K., & Lee, A. F. (2015). Catalytic upgrading of bio-oils by esterification. Journal of Chemical Technology & Biotechnology, 90(5), 780-795.

Coppola, A., Chirone, R., Solimene, R., Ruoppolo, G., Urciuolo, M. Sewage sludge fluidized bed combustion for CLC oxygen carriers production. Proceedings of the 22nd International Conference on Fluidized Bed Conversion: June 14-17, 2015, Turku, Finland.

Corma, A., & Iborra, S. (2006). Oligomerization of alkenes. Catalysts for fine chemical synthesis: microporous and mesoporous solid catalysts, 4, 125-140.

Corma, A., & Orchillés, A. V. (2000). Current views on the mechanism of catalytic cracking. Microporous and mesoporous materials, 35, 21-30.

Corma, A., Huber, G. W., Sauvanaud, L., & O'connor, P. (2007). Processing biomass-derived oxygenates in the oil refinery: Catalytic cracking (FCC) reaction pathways and role of catalyst. Journal of Catalysis, 247(2), 307-327.

Cortazar, M., Alvarez, J., Lopez, G., Amutio, M., Artetxe, M., Bilbao, J., & Olazar, M. (2023). Syngas production by bio-oil steam gasification in a fountain confined conical spouted bed reactor. Fuel, 345, 128228.

Couhert, C., Commandre, J. M., & Salvador, S. (2009). Is it possible to predict gas yields of any biomass after rapid pyrolysis at high temperature from its composition in cellulose, hemicellulose and lignin?. Fuel, 88(3), 408-417.

Crocker, M. (Ed.). (2010). Thermochemical conversion of biomass to liquid fuels and chemicals. Royal Society of Chemistry.

Czernik, S., French, R., Feik, C., & Chornet, E. (2002). Hydrogen by catalytic steam reforming of liquid byproducts from biomass thermoconversion processes. Industrial & Engineering Chemistry Research, 41(17), 4209-4215.

Dabros, T. M., Stummann, M. Z., Høj, M., Jensen, P. A., Grunwaldt, J. D., Gabrielsen, J., ... & Jensen, A. D. (2018). Transportation fuels from biomass fast pyrolysis, catalytic hydrodeoxygenation, and catalytic fast hydropyrolysis. Progress in Energy and Combustion Science, 68, 268-309.

Dada, T. K., Sheehan, M., Murugavelh, S., & Antunes, E. (2023). A review on catalytic pyrolysis for high-quality bio-oil production from biomass. Biomass Conversion and Biorefinery, 13(4), 2595-2614.

Dai, L., Lata, S., Cobb, K., Zou, R., Lei, H., Chen, P., & Ruan, R. (2024). Recent advances in polyolefinic plastic pyrolysis to produce fuels and chemicals. Journal of Analytical and Applied Pyrolysis, 106551.

Dai, L., Wang, Y., Liu, Y., He, C., Ruan, R., Yu, Z., ... & Wu, Q. (2020). A review on selective production of value-added chemicals via catalytic pyrolysis of lignocellulosic biomass. Science of the Total Environment, 749, 142386.

Dai, L., Zhou, N., Lv, Y., Cobb, K., Cheng, Y., Wang, Y., ... & Ruan, R. (2021). Pyrolysis-catalysis for waste polyolefin conversion into low aromatic naphtha. Energy Conversion and Management, 245, 114578.

Daligaux, V., Richard, R., & Manero, M. H. (2021). Deactivation and regeneration of zeolite catalysts used in pyrolysis of plastic wastes—a process and analytical review. Catalysts, 11(7), 770.

Davidian, T., Guilhaume, N., Iojoiu, E., Provendier, H., & Mirodatos, C. (2007). Hydrogen production from crude pyrolysis oil by a sequential catalytic process. Applied Catalysis B: Environmental, 73(1-2), 116-127.

Del Pozo, C., Bartrolí, J., Alier, S., Puy, N., & Fàbregas, E. (2020). Production of antioxidants and other value-added compounds from coffee silverskin via pyrolysis under a biorefinery approach. Waste management, 109, 19-27.

del Remedio Hernández, M., García, Á. N., & Marcilla, A. (2007). Catalytic flash pyrolysis of HDPE in a fluidized bed reactor for recovery of fuel-like hydrocarbons. Journal of analytical and applied pyrolysis, 78(2), 272-281.

Demiral, İ., Şensöz, S. (2008). The effects of different catalysts on the pyrolysis of industrial wastes (olive and hazelnut bagasse). Bioresource Technology, Volume 99, Issue 17, Pages 8002-8007.

Denny, P. J., & Twigg, M. V. (1980). Factors determining the life of industrial heterogeneous catalysts. In Studies in surface science and catalysis (Vol. 6, pp. 577-599). Elsevier.

Di Blasi, C., Branca, C., Masotta, F., & De Biase, E. (2013). Experimental analysis of reaction heat effects during beech wood pyrolysis. Energy & fuels, 27(5), 2665-2674.

Di Blasi, C., Galgano, A., & Branca, C. (2019). Exothermic events of nut shell and fruit stone pyrolysis. ACS Sustainable Chemistry & Engineering, 7(9), 9035-9049.

Di Blasi, C., Signorelli, G., Di Russo, C., & Rea, G. (1999). Product distribution from pyrolysis of wood and agricultural residues. Industrial & Engineering Chemistry Research, 38(6), 2216-2224.

Dickerson, T., & Soria, J. (2013). Catalytic fast pyrolysis: a review. Energies, 6(1), 514-538.

Diebold, J., & Scahill, J. (1988). Production of primary pyrolysis oils in a vortex reactor.

Ding, K., Zhong, Z., Wang, J., Zhang, B., Fan, L., Liu, S., ... & Ruan, R. (2018). Improving hydrocarbon yield from catalytic fast co-pyrolysis of hemicellulose and plastic in the dual-catalyst bed of CaO and HZSM-5. Bioresource technology, 261, 86-92.

Dong, Z., Chen, W., Xu, K., Liu, Y., Wu, J., & Zhang, F. (2022). Understanding the structure–activity relationships in catalytic conversion of

polyolefin plastics by zeolite-based catalysts: a critical review. ACS catalysis, 12(24), 14882-14901.

Dorado, C., Mullen, C. A., & Boateng, A. A. (2015). Origin of carbon in aromatic and olefin products derived from HZSM-5 catalyzed co-pyrolysis of cellulose and plastics via isotopic labeling. Applied Catalysis B: Environmental, 162, 338-345.

Dou, B., Zhang, H., Song, Y., Zhao, L., Jiang, B., He, M., ... & Xu, Y. (2019). Hydrogen production from the thermochemical conversion of biomass: issues and challenges. Sustainable Energy & Fuels, 3(2), 314-342.

Duffy, A., Walker, G. M., & Allen, S. J. (2006). Investigations on the adsorption of acidic gases using activated dolomite. Chemical Engineering Journal, 117(3), 239-244.

Dwivedi, U., Naik, S. N., & Pant, K. K. (2021). High quality liquid fuel production from waste plastics via two-step cracking route in a bottom-up approach using bi-functional Fe/HZSM-5 catalyst. Waste Management, 132, 151-161.

Dyer, A. C., Nahil, M. A., & Williams, P. T. (2021). Catalytic co-pyrolysis of biomass and waste plastics as a route to upgraded bio-oil. Journal of the Energy Institute, 97, 27-36.

Elliott, D. C. (2007). Historical developments in hydroprocessing bio-oils. Energy & Fuels, 21(3), 1792-1815.

Elordi, G., Olazar, M., Artetxe, M., Castaño, P., & Bilbao, J. J. A. C. A. G. (2012a). Effect of the acidity of the HZSM-5 zeolite catalyst on the cracking of high density polyethylene in a conical spouted bed reactor. Applied Catalysis A: General, 415, 89-95.

Elordi, G., Olazar, M., Castano, P., Artetxe, M., & Bilbao, J. (2012b). Polyethylene cracking on a spent FCC catalyst in a conical spouted bed. Industrial & engineering chemistry research, 51(43), 14008-14017.

Elordi, G., Olazar, M., Lopez, G., Amutio, M., Artetxe, M., Aguado, R., & Bilbao, J. (2009). Catalytic pyrolysis of HDPE in continuous mode over zeolite catalysts in a conical spouted bed reactor. Journal of Analytical and Applied Pyrolysis, 85(1-2), 345-351.

Elordi, G., Olazar, M., Lopez, G., Artetxe, M., & Bilbao, J. (2011a). Product yields and compositions in the continuous pyrolysis of high-density polyethylene in a conical spouted bed reactor. Industrial & engineering chemistry research, 50(11), 6650-6659.

Elordi, G., Olazar, M., Lopez, G., Castaño, P., & Bilbao, J. (2011b). Role of pore structure in the deactivation of zeolites (HZSM-5, Hβ and HY) by coke in the pyrolysis of polyethylene in a conical spouted bed reactor. Applied Catalysis B: Environmental, 102(1-2), 224-231.

Encinar, J. M., González, J. F., Martínez, G., & González, J. M. (2008). Two stages catalytic pyrolysis of olive oil waste. Fuel Processing Technology, 89(12), 1448-1455.

Energy Institute - Statistical Review of World Energy (2025).

Eom, I. Y., Kim, J. Y., Lee, S. M., Cho, T. S., Yeo, H., & Choi, J. W. (2013). Comparison of pyrolytic products produced from inorganic-rich and demineralized rice straw (Oryza sativa L.) by fluidized bed pyrolyzer for future biorefinery approach. Bioresource technology, 128, 664-672.

Eschenbacher, A., Varghese, R. J., Delikonstantis, E., Mynko, O., Goodarzi, F., Enemark-Rasmussen, K., ... & Van Geem, K. M. (2022). Highly selective conversion of mixed polyolefins to valuable base chemicals using phosphorus-modified and steam-treated mesoporous HZSM-5 zeolite with minimal carbon footprint. Applied Catalysis B: Environmental, 309, 121251.

Evans, R. J., & Milne, T. A. (1987). Molecular characterization of the pyrolysis of biomass. Energy & Fuels, 1(2), 123-137.

Fagbemi, L., Khezami, L., & Capart, R. (2001). Pyrolysis products from different biomasses: application to the thermal cracking of tar. Applied energy, 69(4), 293-306.

Fan, Y., Cai, Y., Li, X., Yin, H., & Xia, J. (2017). Coking characteristics and deactivation mechanism of the HZSM-5 zeolite employed in the upgrading of biomass-derived vapors. Journal of industrial and engineering chemistry, 46, 139-149.

Farah, E., Atallah, E., Abu Tarboush, B. J., & Zeaiter, J. (2022). Pyrolysis of olive cake with catalytic upgrading of volatile products. Biomass Conversion and Biorefinery, 12(7), 2663-2675.

Fardhyanti, D. S., Imani, N. A. C., Damayanti, A., Mardhotillah, S. N., Afifudin, M., Mulyaningtyas, A., ... & Maulana, P. (2020, June). The separation of phenolic compounds from bio-oil produced from pyrolysis of corncobs. In AIP Conference Proceedings (Vol. 2243, No. 1, p. 020005). AIP Publishing LLC.

Fardhyanti, D. S., Megawati, Chafidz, A., Prasetiawan, H., Raharjo, P. T., Habibah, U., & Abasaeed, A. E. (2024). Production of bio-oil from sugarcane bagasse by fast pyrolysis and removal of phenolic compounds. Biomass Conversion and Biorefinery, 14(1), 217-227.

Farmer, T. J., & Mascal, M. (2015). Platform molecules. Introduction to chemicals from biomass, 89-155.

Faust, K., Denifl, P., & Hapke, M. (2023). Recent advances in catalytic chemical recycling of polyolefins. ChemCatChem, 15(13), e202300310.

Feng, Y., & Meier, D. (2017). Supercritical carbon dioxide extraction of fast pyrolysis oil from softwood. The Journal of Supercritical Fluids, 128, 6-17.

Fernandez, E., Cortazar, M., Santamaria, L., Artetxe, M., Amutio, M., Lopez, G., ... & Olazar, M. (2022a). Tuning pyrolysis temperature to improve the in-line steam reforming catalyst activity and stability. Process Safety and Environmental Protection, 166, 440-450.

Fernandez, E., Santamaria, L., Amutio, M., Artetxe, M., Arregi, A., Lopez, G., ... & Olazar, M. (2022b). Role of temperature in the biomass steam pyrolysis in a conical spouted bed reactor. Energy, 238, 122053.

Fernandez, E., Santamaria, L., Artetxe, M., Amutio, M., Arregi, A., Lopez, G., ... & Olazar, M. (2021). In line upgrading of biomass fast pyrolysis products using low-cost catalysts. Fuel, 296, 120682.

Fernandez-Akarregi, A. R., Makibar, J., Lopez, G., Amutio, M., & Olazar, M. (2013). Design and operation of a conical spouted bed reactor pilot plant (25 kg/h) for biomass fast pyrolysis. Fuel processing technology, 112, 48-56.

Figueirêdo, M. B., Hita, I., Deuss, P. J., Venderbosch, R. H., & Heeres, H. J. (2022). Pyrolytic lignin: a promising biorefinery feedstock for the production of fuels and valuable chemicals. Green Chemistry, 24(12), 4680-4702.

Frau, C., Ferrara, F., Orsini, A., & Pettinau, A. (2015). Characterization of several kinds of coal and biomass for pyrolysis and gasification. Fuel, 152, 138-145.

Ganda, E. T., Brachi, P., Urciuolo, M., Migliaccio, R., Coppola, A., Scala, F., ... & Ruoppolo, G. (2023). Catalytic pyrolysis of torrefied olive stone for production of potential petrochemical alternatives. Biofuels, Bioproducts and Biorefining, 17(2), 332-341.

García Martín, J. F., Cuevas, M., Feng, C. H., Álvarez Mateos, P., Torres Garcia, M., & Sánchez, S. (2020). Energetic valorisation of olive biomass: Olive-tree pruning, olive stones and pomaces. Processes, 8(5), 511.

Garcia, I., Lopez, G., Santamaria, L., Fernandez, E., Bilbao, J., Olazar, M., ... & Amutio, M. (2024). Biomass source influence on hydrogen production through pyrolysis and in line oxidative steam reforming. ChemSusChem, 17(20), e202400325.

Garcia-Nunez, J. A., Pelaez-Samaniego, M. R., Garcia-Perez, M. E., Fonts, I., Abrego, J., Westerhof, R. J. M., & Garcia-Perez, M. (2017). Historical developments of pyrolysis reactors: a review. Energy & fuels, 31(6), 5751-5775.

Garcia-Perez, M., Chaala, A., Pakdel, H., Kretschmer, D., & Roy, C. (2007). Characterization of bio-oils in chemical families. Biomass and Bioenergy, 31(4), 222-242.

Gayubo, A. G., Aguayo, A. T., Atutxa, A., Aguado, R., & Bilbao, J. (2004a). Transformation of oxygenate components of biomass pyrolysis oil on a HZSM-5 zeolite. I. Alcohols and phenols. Industrial & Engineering Chemistry Research, 43(11), 2610-2618.

Gayubo, A. G., Aguayo, A. T., Atutxa, A., Aguado, R., Olazar, M., & Bilbao, J. (2004b). Transformation of oxygenate components of biomass pyrolysis oil on a HZSM-5 zeolite. II. Aldehydes, ketones, and acids. Industrial & engineering chemistry research, 43(11), 2619-2626.

Gayubo, A. G., Aguayo, A. T., Atutxa, A., Prieto, R., & Bilbao, J. (2004c). Deactivation of a HZSM-5 zeolite catalyst in the transformation of the aqueous fraction of biomass pyrolysis oil into hydrocarbons. Energy & fuels, 18(6), 1640-1647.

Gollakota, A. R., Reddy, M., Subramanyam, M. D., & Kishore, N. (2016). A review on the upgradation techniques of pyrolysis oil. Renewable and Sustainable Energy Reviews, 58, 1543-1568.

Guisnet, M., & Magnoux, P. (2001). Organic chemistry of coke formation. Applied Catalysis A: General, 212(1-2), 83-96.

Guisnet, M., Magnoux, P., & Martin, D. (1997). Roles of acidity and pore structure in the deactivation of zeolites by carbonaceous deposits. In Studies in surface science and catalysis (Vol. 111, pp. 1-19). Elsevier.

Hani, F. F. B., & Hailat, M. M. (2016). Production of bio-oil from pyrolysis of olive biomass with/without catalyst. Advances in Chemical Engineering and Science, 6(04), 488.

Hansen, T. W., DeLaRiva, A. T., Challa, S. R., & Datye, A. K. (2013). Sintering of catalytic nanoparticles: particle migration or Ostwald ripening?. Accounts of chemical research, 46(8), 1720-1730.

Harmanos, H. L. (1997). Detectors and Data Handling in Modern Practice of Gas Chromatography, John Wiley & Sons, Inc., New York (1997).

Hasan, M. M., Rasul, M. G., Jahirul, M. I., & Khan, M. M. K. (2023). Characterization of pyrolysis oil produced from organic and plastic wastes using an auger reactor. Energy Conversion and Management, 278, 116723.

Hassanian-Moghaddam, D., Asghari, N., & Ahmadi, M. (2023). Circular polyolefins: advances toward a sustainable future. Macromolecules, 56(15), 5679-5697.

He, L., Hu, S., Yin, X., Xu, J., Han, H., Li, H., ... & Xiang, J. (2020). Promoting effects of Fe-Ni alloy on co-production of H2 and carbon nanotubes during steam reforming of biomass tar over Ni-Fe/α-Al2O3. Fuel, 276, 118116.

Hegedus, L.L.; McCabe, R.W. Catalyst Poisoning; Marcel Dekker: New York, NY, USA, 1984

Hennessy, W. (2010). Review of wood fuel testing standards (No. 10-11013). CRL Energy Report.

Heracleous, E., Pachatouridou, E., Hernández-Giménez, A. M., Hernando, H., Fakin, T., Paioni, A. L., ... & Lappas, A. A. (2019). Characterization of deactivated and regenerated zeolite ZSM-5-based catalyst extrudates used in catalytic pyrolysis of biomass. Journal of Catalysis, 380, 108-122.

Hernando, H., Jiménez-Sánchez, S., Fermoso, J., Pizarro, P., Coronado, J. M., & Serrano, D. P. (2016). Assessing biomass catalytic pyrolysis in terms of deoxygenation pathways and energy yields for the efficient production of advanced biofuels. Catalysis Science & Technology, 6(8), 2829-2843.

Hoang, A. T., Ong, H. C., Fattah, I. R., Chong, C. T., Cheng, C. K., Sakthivel, R., & Ok, Y. S. (2021). Progress on the lignocellulosic biomass pyrolysis for biofuel production toward environmental sustainability. Fuel Processing Technology, 223, 106997.

https://agriculture.ec.europa.eu/media/news/european-commission-launches-market-observatory-olive-oil-and-table-olives-sector-2024-11-11_en

https://plasticseurope.org/wp-content/uploads/2023/03/PE-PLASTICS-THE FACTS_FINAL_DIGITAL-1.pdf

Hu, G., Xu, S., Li, S., Xiao, C., & Liu, S. (2006). Steam gasification of apricot stones with olivine and dolomite as downstream catalysts. Fuel Processing Technology, 87(5), 375-382.

Hu, X., & Lu, G. (2010). Comparative study of alumina-supported transition metal catalysts for hydrogen generation by steam reforming of acetic acid. Applied Catalysis B: Environmental, 99(1-2), 289-297.

Hughes, R., Deactivation of Catalysts, San Diego: Academic Press, 1984

Hutchings, G. J., & Védrine, J. C. (2004). Heterogeneous catalyst preparation. In Basic principles in applied catalysis (pp. 215-258). Berlin, Heidelberg: Springer Berlin Heidelberg.

Ibáñez, M., Artetxe, M., Lopez, G., Elordi, G., Bilbao, J., Olazar, M., & Castaño, P. (2014). Identification of the coke deposited on an HZSM-5 zeolite catalyst during the sequenced pyrolysis–cracking of HDPE. Applied Catalysis B: Environmental, 148, 436-445.

Iisa, K., French, R. J., Orton, K. A., Budhi, S., Mukarakate, C., Stanton, A. R., ... & Nimlos, M. R. (2016a). Catalytic pyrolysis of pine over HZSM-5 with different binders. Topics in Catalysis, 59(1), 94-108.

Iisa, K., French, R. J., Orton, K. A., Dutta, A., & Schaidle, J. A. (2017). Production of low-oxygen bio-oil via ex situ catalytic fast pyrolysis and hydrotreating. Fuel, 207, 413-422.

Iisa, K., French, R. J., Orton, K. A., Yung, M. M., Johnson, D. K., ten Dam, J., ... & Nimlos, M. R. (2016b). In situ and ex situ catalytic pyrolysis of pine in a bench-scale fluidized bed reactor system. Energy & fuels, 30(3), 2144-2157.

Ilias, S., & Bhan, A. (2013). Mechanism of the catalytic conversion of methanol to hydrocarbons. Acs Catalysis, 3(1), 18-31.

Iliopoulou, E. F., Pachatouridou, E., Marianou, A. A., Michailof, C., Kalogiannis, K. K., & Lappas, A. A. (2023). Catalytic pyrolysis of olive mill wastes towards advanced bio-fuels and bio-chemicals using metal oxide catalysts. Catalysis Today, 420, 114151.

Iliopoulou, E. F., Stefanidis, S. D., Kalogiannis, K. G., Delimitis, A., Lappas, A. A., & Triantafyllidis, K. S. (2012). Catalytic upgrading of biomass pyrolysis vapors using transition metal-modified ZSM-5 zeolite. Applied Catalysis B: Environmental, 127, 281-290.

Imran, A., Bramer, E. A., Seshan, K., & Brem, G. (2016). Catalytic flash pyrolysis of biomass using different types of zeolite and online vapor fractionation. Energies, 9(3), 187.

Imran, A., Bramer, E. A., Seshan, K., & Brem, G. (2018). An overview of catalysts in biomass pyrolysis for production of biofuels.

Inaloo, E. B., & Saidi, M. (2023). Catalytic pyrolysis of olive pomace for biofuel production: application of metal oxide-modified zeolite catalysts. Biomass and Bioenergy, 177, 106947.

Jacobsson, S., & Johnson, A. (2000). The diffusion of renewable energy technology: an analytical framework and key issues for research. Energy policy, 28(9), 625-640.

Jakab, E., Faix, O., & Till, F. (1997). Thermal decomposition of milled wood lignins studied by thermogravimetry/mass spectrometry. Journal of Analytical and Applied Pyrolysis, 40, 171-186.

Jan, M. R., Shah, J., & Gulab, H. (2010a). Catalytic degradation of waste high-density polyethylene into fuel products using BaCO3 as a catalyst. Fuel processing technology, 91(11), 1428-1437.

Jan, M. R., Shah, J., & Gulab, H. (2010b). Degradation of waste high-density polyethylene into fuel oil using basic catalyst. Fuel, 89(2), 474-480.

Johansson, R., Hruby, S. L., Rass-Hansen, J., & Christensen, C. H. (2009). The hydrocarbon pool in ethanol-to-gasoline over HZSM-5 catalysts. Catalysis letters, 127(1), 1-6.

Juliastuti, S. R., Hisbullah, M. I., & Abdillah, M. (2018, March). High density Polyethylene plastic waste treatment with microwave heating pyrolysis method using coconut-shell activated carbon to produce alternative fuels. In IOP Conference Series: Materials Science and Engineering (Vol. 334, p. 012015). IOP Publishing.

Kan, T., Strezov, V., & Evans, T. J. (2016). Lignocellulosic biomass pyrolysis: A review of product properties and effects of pyrolysis parameters. Renewable and sustainable energy reviews, 57, 1126-1140.

Kan, T., Strezov, V., Evans, T., He, J., Kumar, R., & Lu, Q. (2020). Catalytic pyrolysis of lignocellulosic biomass: A review of variations in process factors and system structure. Renewable and Sustainable Energy Reviews, 134, 110305.

Karadağ, E., Bilge, S., Donar, Y. O., & Sinağ, A. (2022). Catalytic pyrolysis of olive oil residue to produce synthesis gas: the effect of bulk and nano metal oxides. Turkish Journal of Chemistry, 46(4), 1306-1315.

Kechagiopoulos, P. N., Voutetakis, S. S., Lemonidou, A. A., & Vasalos, I. A. (2006). Hydrogen production via steam reforming of the aqueous phase of bio-oil in a fixed bed reactor. Energy & fuels, 20(5), 2155-2163.

Kersten, S., & Garcia-Perez, M. (2013). Recent developments in fast pyrolysis of ligno-cellulosic materials. Current opinion in biotechnology, 24(3), 414-420.

Kostas, E. T., Durán-Jiménez, G., Shepherd, B. J., Meredith, W., Stevens, L. A., Williams, O. S., ... & Robinson, J. P. (2020). Microwave pyrolysis of olive pomace for bio-oil and bio-char production. Chemical Engineering Journal, 387, 123404.

Kumar, A., Chakraborty, J. P., & Singh, R. (2017). Bio-oil: the future of hydrogen generation. Biofuels, 8(6), 663-674.

Kunwar, B., Moser, B. R., Chandrasekaran, S. R., Rajagopalan, N., & Sharma, B. K. (2016). Catalytic and thermal depolymerization of low value post-consumer high density polyethylene plastic. Energy, 111, 884-892.

Lachos-Perez, D., Martins-Vieira, J. C., Missau, J., Anshu, K., Siakpebru, O. K., Thengane, S. K., ... & Bertuol, D. A. (2023). Review on biomass pyrolysis with a focus on bio-oil upgrading techniques. Analytica, 4(2), 182-205.

Lazzari, E., Schena, T., Primaz, C. T., da Silva Maciel, G. P., Machado, M. E., Cardoso, C. A. L., ... & Caramão, E. B. (2016). Production and

chromatographic characterization of bio-oil from the pyrolysis of mango seed waste. Industrial Crops and Products, 83, 529-536.

Lede, J., Panagopoulos, J., Li, H. Z., & Villermaux, J. (1985). Fast pyrolysis of wood: direct measurement and study of ablation rate. Fuel, 64(11), 1514-1520.

Lee, J., Yang, X., Cho, S. H., Kim, J. K., Lee, S. S., Tsang, D. C., ... & Kwon, E. E. (2017). Pyrolysis process of agricultural waste using CO2 for waste management, energy recovery, and biochar fabrication. Applied energy, 185, 214-222.

Lee, K. H., Jeon, S. G., Kim, K. H., Noh, N. S., Shin, D. H., Park, J., ... & Kim, G. T. (2003). Thermal and catalytic degradation of waste high-density polyethylene (HDPE) using spent FCC catalyst. Korean Journal of Chemical Engineering, 20, 693-697.

Lee, K. H., Noh, N. S., Shin, D. H., & Seo, Y. (2002). Comparison of plastic types for catalytic degradation of waste plastics into liquid product with spent FCC catalyst. Polymer Degradation and Stability, 78(3), 539-544.

Leibbrandt N H, Knoetze J H, Gorgens J F. Comparing biological and thermochemical processing of sugarcane bagasse: An energy balance perspective. Biomass and Bioenergy, 2011, 35: 2117–2126

Li, B., Mbeugang, C. F. M., Xie, X., Wei, J., Zhang, S., Zhang, L., ... & Liu, D. (2023a). Catalysis/CO2 sorption enhanced pyrolysis-gasification of biomass for H2-rich gas production: Effects of activated carbon, NiO active component and calcined dolomite. Fuel, 334, 126842.

Li, Y., Nahil, M. A., & Williams, P. T. (2023b). Pyrolysis-catalytic steam reforming of waste plastics for enhanced hydrogen/syngas yield using sacrificial tire pyrolysis char catalyst. Chemical Engineering Journal, 467, 143427.

Li, Y., Zhang, C., Liu, Y., Tang, S., Chen, G., Zhang, R., & Tang, X. (2017). Coke formation on the surface of Ni/HZSM-5 and Ni-Cu/HZSM-5 catalysts during bio-oil hydrodeoxygenation. Fuel, 189, 23-31.

Lin, F., Xu, M., Ramasamy, K. K., Li, Z., Klinger, J. L., Schaidle, J. A., & Wang, H. (2022). Catalyst deactivation and its mitigation during catalytic conversions of biomass. ACS Catalysis, 12(21), 13555-13599.

Lin, Y. H., Sharratt, P. N., Garforth, A. A., & Dwyer, J. (1998). Catalytic conversion of polyolefins to chemicals and fuels over various cracking catalysts. Energy & Fuels, 12(4), 767-774.

Lin, Y. H., Yang, M. H., Yeh, T. F., & Ger, M. D. (2004). Catalytic degradation of high density polyethylene over mesoporous and microporous catalysts in a fluidised-bed reactor. Polymer Degradation and Stability, 86(1), 121-128.

Lindfors, C., Kuoppala, E., Oasmaa, A., Solantausta, Y., & Arpiainen, V. (2014). Fractionation of bio-oil. Energy & fuels, 28(9), 5785-5791.

Liu, C., Wang, H., Karim, A. M., Sun, J., & Wang, Y. (2014a). Catalytic fast pyrolysis of lignocellulosic biomass. Chemical Society Reviews, 43(22), 7594-7623.

Liu, M., Zhuo, J. K., Xiong, S. J., & Yao, Q. (2014b). Catalytic degradation of high-density polyethylene over a clay catalyst compared with other catalysts. Energy & fuels, 28(9), 6038-6045.

Liu, R., Rahman, M. M., Sarker, M., Chai, M., Li, C., & Cai, J. (2020). A review on the catalytic pyrolysis of biomass for the bio-oil production with ZSM-5: Focus on structure. Fuel Processing Technology, 199, 106301.

Liu, S., Zhang, Y., Fan, L., Zhou, N., Tian, G., Zhu, X., ... & Ruan, R. (2017). Bio-oil production from sequential two-step catalytic fast microwave-assisted biomass pyrolysis. Fuel, 196, 261-268.

Liu, Y., Li, Z., Leahy, J. J., & Kwapinski, W. (2015). Catalytically upgrading bio-oil via esterification. Energy & Fuels, 29(6), 3691-3698.

Liu, Z., Quek, A., Hoekman, S. K., & Balasubramanian, R. (2013). Production of solid biochar fuel from waste biomass by hydrothermal carbonization. Fuel, 103, 943-949.

Lopez, G., Alvarez, J., Amutio, M., Mkhize, N. M., Danon, B., Van der Gryp, P., ... & Olazar, M. (2017a). Waste truck-tyre processing by flash pyrolysis in a conical spouted bed reactor. Energy conversion and management, 142, 523-532.

Lopez, G., Artetxe, M., Amutio, M., Bilbao, J., & Olazar, M. (2017b). Thermochemical routes for the valorization of waste polyolefinic plastics to produce fuels and chemicals. A review. Renewable and Sustainable Energy Reviews, 73, 346-368.

López, G., Olazar, M., Aguado, R., & Bilbao, J. (2010). Continuous pyrolysis of waste tyres in a conical spouted bed reactor. Fuel, 89(8), 1946-1952.

López, M. B., Blanco, C. G., Martínez-Alonso, A., & Tascón, J. M. D. (2002). Composition of gases released during olive stones pyrolysis. Journal of analytical and applied pyrolysis, 65(2), 313-322.

Luo, G., Suto, T., Yasu, S., & Kato, K. (2000). Catalytic degradation of high density polyethylene and polypropylene into liquid fuel in a powder-particle fluidized bed. Polymer Degradation and Stability, 70(1), 97-102.

Luo, Wang, Liao, & Cen. (2004). Mechanism study of cellulose rapid pyrolysis. Industrial & engineering chemistry research, 43(18), 5605-5610.

Ly, H. V., Lim, D. H., Sim, J. W., Kim, S. S., & Kim, J. (2018). Catalytic pyrolysis of tulip tree (Liriodendron) in bubbling fluidized-bed reactor for upgrading bio-oil using dolomite catalyst. Energy, 162, 564-575.

Magalhães, D., Gürel, K., Matsakas, L., Christakopoulos, P., Pisano, I., Leahy, J. J., ... & Trubetskaya, A. (2021). Prediction of yields and composition of char from fast pyrolysis of commercial lignocellulosic materials, organosolv fractionated and torrefied olive stones. Fuel, 289, 119862.

Makibar, J., Fernandez-Akarregi, A. R., Alava, I., Cueva, F., Lopez, G., & Olazar, M. (2011). Investigations on heat transfer and hydrodynamics under pyrolysis conditions of a pilot-plant draft tube conical spouted bed reactor. Chemical Engineering and Processing: Process Intensification, 50(8), 790-798.

Mansor, W. N. W., Razali, N. A., Abdullah, S., Jarkoni, M. N. K., Sharin, A. B. E., Abd Kadir, N. H., ... & Jalaludin, J. (2022, April). A Review of Plastic-derived Diesel Fuel as a Renewable Fuel for Internal Combustion Engines: Applications, Challenges, and Global Potential. In IOP Conference Series: Earth and Environmental Science (Vol. 1013, No. 1, p. 012014). IOP Publishing.

Mante, O. D., & Agblevor, F. A. (2011). Catalytic conversion of biomass to bio-syncrude oil. Biomass Conversion and Biorefinery, 1(4), 203-215.

Marcilla, A., Beltrán, M. I., & Navarro, R. (2007). Study of the deactivation process of HZSM5 zeolite during polyethylene pyrolysis. Applied Catalysis A: General, 333(1), 57-66.

Marcilla, A., Beltrán, M. I., & Navarro, R. (2009). Thermal and catalytic pyrolysis of polyethylene over HZSM5 and HUSY zeolites in a batch reactor under dynamic conditions. Applied Catalysis B: Environmental, 86(1-2), 78-86.

Martín, A. J., Mitchell, S., Mondelli, C., Jaydev, S., & Pérez-Ramírez, J. (2022). Unifying views on catalyst deactivation. Nature Catalysis, 5(10), 854-866.

Martín-Lara, M. A., Ronda, A., Blázquez, G., Pérez, A., & Calero, M. (2018). Pyrolysis kinetics of the lead-impregnated olive stone by non-isothermal thermogravimetry. Process Safety and Environmental Protection, 113, 448-458.

Masoum, S., Seifi, H., & Ebrahimabadi, E. H. (2013). Characterization of volatile components in Calligonum comosum by coupling gas chromatography-mass spectrometry and mean field approach independent component analysis. Analytical Methods, 5(18), 4639-4647.

Mastral, J. F., Berrueco, C., Gea, M., & Ceamanos, J. (2006). Catalytic degradation of high density polyethylene over nanocrystalline HZSM-5 zeolite. Polymer degradation and stability, 91(12), 3330-3338.

Mathur, K. B., & Epstein, N. (1974). Developments in spouted bed technology. The Canadian Journal of Chemical Engineering, 52(2), 129-144.

McKendry, P. (2002). Energy production from biomass (part 2): conversion technologies. Bioresource technology, 83(1), 47-54.

Meier, D., Schoell, S., & Klaubert, H. (2004). New ablative pyrolyser in operation in Germany. PyNe newsletter, 17(1).

Meng, X., Xu, C., & Gao, J. (2007). Coking behavior and catalyst deactivation for catalytic pyrolysis of heavy oil. Fuel, 86(12-13), 1720-1726.

Mihalcik, D. J., Mullen, C. A., & Boateng, A. A. (2011). Screening acidic zeolites for catalytic fast pyrolysis of biomass and its components. Journal of Analytical and Applied Pyrolysis, 92(1), 224-232.

Miskolczi, N., Angyal, A., Bartha, L., & Valkai, I. (2009). Fuels by pyrolysis of waste plastics from agricultural and packaging sectors in a pilot scale reactor. Fuel Processing Technology, 90(7-8), 1032-1040.

Miskolczi, N., Bartha, L., & Deák, G. (2006). Thermal degradation of polyethylene and polystyrene from the packaging industry over different

catalysts into fuel-like feed stocks. Polymer degradation and stability, 91(3), 517-526.

Miskolczi, N., Bartha, L., Deák, G., Jóver, B., & Kalló, D. (2004). Thermal and thermo-catalytic degradation of high-density polyethylene waste. Journal of Analytical and Applied Pyrolysis, 72(2), 235-242.

Mohan, D., Pittman Jr, C. U., & Steele, P. H. (2006). Pyrolysis of wood/biomass for bio-oil: a critical review. Energy & fuels, 20(3), 848-889.

Mondal, B. K., Guha, F., & Abser, M. N. (2023). Sol-gel derived Ti-doped mesoporous silica–alumina: An efficient catalyst to recover energy sources from environmental hazard waste plastics. Journal of Thermal Analysis and Calorimetry, 148(12), 5257-5270.

Montagnaro, F. (2024). Sustainable Energy Production Using Solid Materials. Springer Nature Switzerland, Imprint: Springer.

Mullen, C. A., & Boateng, A. A. (2013). Accumulation of inorganic impurities on HZSM-5 zeolites during catalytic fast pyrolysis of switchgrass. Industrial & Engineering Chemistry Research, 52(48), 17156-17161.

Mullen, C. A., Tarves, P. C., Raymundo, L. M., Schultz, E. L., Boateng, A. A., & Trierweiler, J. O. (2018). Fluidized bed catalytic pyrolysis of eucalyptus over HZSM-5: effect of acid density and gallium modification on catalyst deactivation. Energy & Fuels, 32(2), 1771-1778.

Nanda, S., Pattnaik, F., Borugadda, V. B., Dalai, A. K., Kozinski, J. A., & Naik, S. (2021). Catalytic and noncatalytic upgrading of bio-oil to synthetic fuels: an introductory review. Catalytic and Noncatalytic Upgrading of Oils, 1-28.

Naqvi, S. R., Uemura, Y., & Yusup, S. B. (2014). Catalytic pyrolysis of paddy husk in a drop type pyrolyzer for bio-oil production: The role of temperature and catalyst. Journal of Analytical and Applied Pyrolysis, 106, 57-62.

Nguyen, T. S., He, S., Lefferts, L., Brem, G., & Seshan, K. (2016). Study on the catalytic conversion of lignin-derived components in pyrolysis vapour using model component. Catalysis Today, 259, 381-387.

Oasmaa, A., & Czernik, S. (1999). Fuel oil quality of biomass pyrolysis oils state of the art for the end users. Energy & Fuels, 13(4), 914-921.

Oasmaa, A., Korhonen, J., & Kuoppala, E. (2011). An approach for stability measurement of wood-based fast pyrolysis bio-oils. Energy & Fuels, 25(7), 3307-3313.

Oasmaa, A., Sundqvist, T., Kuoppala, E., Garcia-Perez, M., Solantausta, Y., Lindfors, C., & Paasikallio, V. (2015). Controlling the phase stability of biomass fast pyrolysis bio-oils. Energy & Fuels, 29(7), 4373-4381.

OECD (2022), Global Plastics Outlook: Economic Drivers, Environmental Impacts and Policy Options, OECD Publishing, Paris, https://doi.org/10.1787/de747aef-en.

Olazar, M., Lopez, G., Amutio, M., Elordi, G., Aguado, R., & Bilbao, J. (2009). Influence of FCC catalyst steaming on HDPE pyrolysis product distribution. Journal of Analytical and Applied Pyrolysis, 85(1-2), 359-365.

Olazar, M., San Jose, M. J., Aguayo, A. T., Arandes, J. M., & Bilbao, J. (1992). Stable operation conditions for gas-solid contact regimes in conical spouted beds. Industrial & Engineering Chemistry Research, 31(7), 1784-1792.

Olcese, R., Bettahar, M. M., Malaman, B., Ghanbaja, J., Tibavizco, L., Petitjean, D., & Dufour, A. (2013). Gas-phase hydrodeoxygenation of guaiacol over iron-based catalysts. Effect of gases composition, iron load and supports (silica and activated carbon). Applied Catalysis B: Environmental, 129, 528-538.

Orozco, S., Lopez, G., Suarez, M. A., Artetxe, M., Alvarez, J., Bilbao, J., & Olazar, M. (2022). Oxidative fast pyrolysis of high-density polyethylene on a spent fluid catalytic cracking catalyst in a fountain confined conical spouted bed reactor. ACS Sustainable Chemistry & Engineering, 10(48), 15791-15801.

Osman, A. I., Mehta, N., Elgarahy, A. M., Al-Hinai, A., Al-Muhtaseb, A. A. H., & Rooney, D. W. (2021). Conversion of biomass to biofuels and life cycle assessment: a review. Environmental chemistry letters, 19, 4075-4118.

Paasikallio, V., Kalogiannis, K., Lappas, A., Lehto, J., & Lehtonen, J. (2017). Catalytic fast pyrolysis: influencing bio-oil quality with the catalyst-to-biomass ratio. Energy Technology, 5(1), 94-103.

Park, D. W., Hwang, E. Y., Kim, J. R., Choi, J. K., Kim, Y. A., & Woo, H. C. (1999). Catalytic degradation of polyethylene over solid acid catalysts. Polymer degradation and stability, 65(2), 193-198.

Patwardhan, P. R., Brown, R. C., & Shanks, B. H. (2011). Product distribution from the fast pyrolysis of hemicellulose. ChemSusChem, 4(5), 636-643.

Peacocke, G. V. C., & Bridgwater, A. V. (1994). Ablative plate pyrolysis of biomass for liquids. Biomass and Bioenergy, 7(1-6), 147-154.

Perego, C., & Villa, P. (1997). Catalyst preparation methods. Catalysis today, 34(3-4), 281-305.

Pérez, M., Dominguez-López, I., & Lamuela-Raventós, R. M. (2023). The chemistry behind the folin–ciocalteu method for the estimation of (poly) phenol content in food: Total phenolic intake in a mediterranean dietary pattern. Journal of agricultural and food chemistry, 71(46), 17543-17553.

Perkins, G., Bhaskar, T., & Konarova, M. (2018). Process development status of fast pyrolysis technologies for the manufacture of renewable transport fuels from biomass. Renewable and Sustainable Energy Reviews, 90, 292-315.

Petrov, N., Budinova, T., Razvigorova, M., Parra, J., & Galiatsatou, P. (2008). Conversion of olive wastes to volatiles and carbon adsorbents. Biomass and Bioenergy, 32(12), 1303-1310.

Pienihäkkinen, E., Lindfors, C., Ohra-Aho, T., & Oasmaa, A. (2022). Improving fast pyrolysis bio-oil yield and quality by alkali removal from feedstock. Energy & Fuels, 36(7), 3654-3664.

Pinheiro Pires, A. P., Arauzo, J., Fonts, I., Domine, M. E., Fernandez Arroyo, A., Garcia-Perez, M. E., ... & Garcia-Perez, M. (2019). Challenges and opportunities for bio-oil refining: A review. Energy & fuels, 33(6), 4683-4720.

Prabhakara, H. M., Bramer, E. A., & Brem, G. (2021a). Role of dolomite as an in-situ CO2 sorbent and deoxygenation catalyst in fast pyrolysis of beechwood in a bench scale fluidized bed reactor. Fuel Processing Technology, 224, 107029.

Prabhakara, H. M., Bramer, E., & Brem, G. (2021b). Biomass fast pyrolysis vapor upgrading over γ-alumina, hydrotalcite, dolomite and effect of Na2CO3 loading: a pyro probe GCMS study. Energies, 14(17), 5397.

Pujro, R., García, J. R., Bertero, M., Falco, M., & Sedran, U. (2021). Review on reaction pathways in the catalytic upgrading of biomass pyrolysis liquids. Energy & Fuels, 35(21), 16943-16964.

Pütün, A. E., Uzun, B. B., Apaydin, E., & Pütün, E. (2005). Bio-oil from olive oil industry wastes: Pyrolysis of olive residue under different conditions. Fuel Processing Technology, 87(1), 25-32.

Pütün, E. (2010). Catalytic pyrolysis of biomass: Effects of pyrolysis temperature, sweeping gas flow rate and MgO catalyst. Energy, 35(7), 2761-2766.

Putun, E., Uzun, B. B., & Putun, A. E. (2009). Rapid pyrolysis of olive residue. 2. Effect of catalytic upgrading of pyrolysis vapors in a two-stage fixed-bed reactor. Energy & Fuels, 23(4), 2248-2258.

Qi, X., & Fan, W. (2019). Selective production of aromatics by catalytic fast pyrolysis of furan with in situ dehydrogenation of propane. ACS Catalysis, 9(3), 2626-2632.

Qiu, B., Tao, X., Wang, J., Liu, Y., Li, S., & Chu, H. (2022a). Research progress in the preparation of high-quality liquid fuels and chemicals by catalytic pyrolysis of biomass: A review. Energy Conversion and Management, 261, 115647.

Qiu, B., Yang, C., Shao, Q., Liu, Y., & Chu, H. (2022b). Recent advances on industrial solid waste catalysts for improving the quality of bio-oil from biomass catalytic cracking: A review. Fuel, 315, 123218.

Quan, C., Xu, S., & Zhou, C. (2017). Steam reforming of bio-oil from coconut shell pyrolysis over Fe/olivine catalyst. Energy Conversion and Management, 141, 40-47.

Rasam, S., Azizi, K., Moraveji, M. K., Akbari, A., & Soria-Verdugo, A. (2022). Insights into the co–pyrolysis of olive stone, waste polyvinyl chloride and Spirulina microalgae blends through thermogravimetric analysis. Algal Research, 62, 102635.

Ratnasari, D. K., Nahil, M. A., & Williams, P. T. (2017). Catalytic pyrolysis of waste plastics using staged catalysis for production of gasoline range hydrocarbon oils. Journal of analytical and applied pyrolysis, 124, 631-637.

Recio-Ruiz, M. D. C., Ruiz-Rosas, R. R., Rosas-Martínez, J. M., Rodríguez-Mirasol, J., & Cordero-Alcántara, T. (2023). Catalytic fast pyrolysis of olive stone for bio-oil deoxygenation.

Remiro, A., Valle, B., Aguayo, A. T., Bilbao, J., & Gayubo, A. G. (2013). Steam reforming of raw bio-oil in a fluidized bed reactor with prior separation of pyrolytic lignin. Energy & fuels, 27(12), 7549-7559.

Ren, S., Ye, X. P., & Borole, A. P. (2017). Separation of chemical groups from bio-oil water-extract via sequential organic solvent extraction. Journal of Analytical and Applied Pyrolysis, 123, 30-39.

Rezaei, P. S., Shafaghat, H., & Daud, W. M. A. W. (2014). Production of green aromatics and olefins by catalytic cracking of oxygenate compounds derived from biomass pyrolysis: A review. Applied Catalysis A: General, 469, 490-511.

Richardson, J. T., & Richardson, J. T. (1989). Catalyst Development: How They Evolve. Principles of Catalyst Development, 41-48.

Rosbash, D. O. (1949). Preparation of Folin-Ciocalteu's Phenol Reagent. Am. J. Clin. Pathol, 19(297.10), 1093.

Rover, M. R., & Brown, R. C. (2013). Quantification of total phenols in bio-oil using the Folin–Ciocalteu method. Journal of Analytical and Applied Pyrolysis, 104, 366-371.

Sadeghbeigi, R. (2020). Fluid catalytic cracking handbook: An expert guide to the practical operation, design, and optimization of FCC units. Butterworth-Heinemann.

Saidi, M., Samimi, F., Karimipourfard, D., Nimmanwudipong, T., Gates, B. C., & Rahimpour, M. R. (2014). Upgrading of lignin-derived bio-oils by catalytic hydrodeoxygenation. Energy & Environmental Science, 7(1), 103-129.

Sakata, Y., Uddin, M. A., Muto, A., Kanada, Y., Koizumi, K., & Murata, K. (1997). Catalytic degradation of polyethylene into fuel oil over mesoporous silica (KFS-16) catalyst. Journal of Analytical and Applied Pyrolysis, 43(1), 15-25.

Salatino, P., Ruoppolo, G., Galia, A.,Montagnaro, F., Esposito, G., Russo, M.E., Barbanera, M. (2023). Stato e prospettive di sviluppo di processi per la valorizzazione di biomassa in filiera lunga. Editoriale scientifica, Napoli.

Salmiaton, A., & Garforth, A. A. (2011). Multiple use of waste catalysts with and without regeneration for waste polymer cracking. Waste management, 31(6), 1139-1145.

San Miguel, G., Serrano, D. P., & Aguado, J. (2009). Valorization of waste agricultural polyethylene film by sequential pyrolysis and catalytic reforming. Industrial & Engineering Chemistry Research, 48(18), 8697-8703.

Sánchez, F., & San Miguel, G. (2016). Improved fuel properties of whole table olive stones via pyrolytic processing. Biomass and Bioenergy, 92, 1-11.

Santamaria Moreno, L. (2019). Design and performance of Ni-based catalysts for the steam reforming of biomass fast pyrolysis volatiles (Doctoral dissertation, Universidad del País Vasco-Euskal Herriko Unibertsitatea).

Santamaria, L., Lopez, G., Arregi, A., Amutio, M., Artetxe, M., Bilbao, J., & Olazar, M. (2019). Stability of different Ni supported catalysts in the in-line steam reforming of biomass fast pyrolysis volatiles. Applied Catalysis B: Environmental, 242, 109-120.

Santos, R. M., Santos, A. O., Sussuchi, E. M., Nascimento, J. S., Lima, Á. S., & Freitas, L. S. (2015). Pyrolysis of mangaba seed: production and characterization of bio-oil. Bioresource Technology, 196, 43-48.

Saravanan, A., & Kumar, P. S. (2022). Biochar derived carbonaceous material for various environmental applications: Systematic review. Environmental Research, 214, 113857.

Satterfield, C. N. (1991). Heterogeneous catalysis in industrial practice.

Sehested, J. (2006). Four challenges for nickel steam-reforming catalysts. Catalysis Today, 111(1-2), 103-110.

Seo, Y. H., Lee, K. H., & Shin, D. H. (2003). Investigation of catalytic degradation of high-density polyethylene by hydrocarbon group type analysis. Journal of Analytical and Applied Pyrolysis, 70(2), 383-398.

Serrano, D. P., Aguado, J., Escola, J. M., & Rodríguez, J. M. (2005). Influence of nanocrystalline HZSM-5 external surface on the catalytic cracking of polyolefins. Journal of analytical and applied pyrolysis, 74(1-2), 353-360.

Shahbaz, M., Al-Ansari, T., Inayat, A., & Inayat, M. (2022). Technical readiness level of biohydrogen production process and its value chain. In Value-chain of biofuels (pp. 335-355). Elsevier.

Shahid, E. M., & Jamal, Y. (2011). Production of biodiesel: a technical review. Renewable and Sustainable Energy Reviews, 15(9), 4732-4745.

Sharifzadeh, M., Sadeqzadeh, M., Guo, M., Borhani, T. N., Konda, N. M., Garcia, M. C., ... & Shah, N. (2019). The multi-scale challenges of biomass fast pyrolysis and bio-oil upgrading: Review of the state of art and future research directions. Progress in Energy and Combustion Science, 71, 1-80.

Sharma, S. D., McLennan, K., Dolan, M., Nguyen, T., & Chase, D. (2013). Design and performance evaluation of dry cleaning process for syngas. Fuel, 108, 42-53.

Sharratt, P. N., Lin, Y. H., Garforth, A. A., & Dwyer, J. (1997). Investigation of the catalytic pyrolysis of high-density polyethylene over a HZSM-5 catalyst in a laboratory fluidized-bed reactor. Industrial & engineering chemistry research, 36(12), 5118-5124.

Shen, D. K., & Gu, S. (2009a). The mechanism for thermal decomposition of cellulose and its main products. Bioresource technology, 100(24), 6496-6504.

Shen, D. K., Gu, S., & Bridgwater, A. V. (2010). Study on the pyrolytic behaviour of xylan-based hemicellulose using TG–FTIR and Py–GC–FTIR. Journal of analytical and applied pyrolysis, 87(2), 199-206.

Shen, D., Xiao, R., Gu, S., & Luo, K. (2011). The pyrolytic behavior of cellulose in lignocellulosic biomass: a review. RSC advances, 1(9), 1641-1660.

Shen, J., Wang, X. S., Garcia-Perez, M., Mourant, D., Rhodes, M. J., & Li, C. Z. (2009b). Effects of particle size on the fast pyrolysis of oil mallee woody biomass. Fuel, 88(10), 1810-1817.

Shi, Z., Jin, Y., Svanberg, R., Han, T., Minidis, A. B., Ann-Sofi, K. D., ... & Yang, W. (2023). Continuous catalytic pyrolysis of biomass using a fluidized bed with commercial-ready catalysts for scale-up. Energy, 273, 127288.

Shin, E. J., Nimlos, M. R., & Evans, R. J. (2001). A study of the mechanisms of vanillin pyrolysis by mass spectrometry and multivariate analysis. Fuel, 80(12), 1689-1696.

Singleton, V. L., & Rossi, J. A. (1965). Colorimetry of total phenolics with phosphomolybdic-phosphotungstic acid reagents. American journal of Enology and Viticulture, 16(3), 144-158.

Slezak, R., Unyay, H., Szufa, S., & Ledakowicz, S. (2023). An extensive review and comparison of modern biomass reactors torrefaction vs. biomass pyrolizers—part 2. Energies, 16(5), 2212.

Smil, V. (2004). World history and energy. Encyclopedia of energy, 6, 549-561.

Stankovikj, F., McDonald, A. G., Helms, G. L., Olarte, M. V., & Garcia-Perez, M. (2017a). Characterization of the water-soluble fraction of woody biomass pyrolysis oils. Energy & Fuels, 31(2), 1650-1664.

Stankovikj, F., Tran, C. C., Kaliaguine, S., Olarte, M. V., & Garcia-Perez, M. (2017b). Evolution of functional groups during pyrolysis oil upgrading. Energy & Fuels, 31(8), 8300-8316.

Stephanidis, S. D., Kalogiannis, K. G., Iliopoulou, E. F., Lappas, A. A., & Pilavachi, P. A. (2011a). In-situ upgrading of biomass pyrolysis vapors: catalyst screening on a fixed bed reactor. Bioresource technology, 102(17), 8261-8267.

Stephanidis, S., Nitsos, C., Kalogiannis, K., Iliopoulou, E. F., Lappas, A. A., & Triantafyllidis, K. S. (2011b). Catalytic upgrading of lignocellulosic biomass pyrolysis vapours: effect of hydrothermal pre-treatment of biomass. Catalysis Today, 167(1), 37-45.

Suarez, M. A., Januszewicz, K., Cortazar, M., Lopez, G., Santamaria, L., Olazar, M., ... & Amutio, M. (2024). Selective H2 production from plastic waste through pyrolysis and in-line oxidative steam reforming. Energy, 131762.

Swita, M., Lemmon, T., Ma, R., Taylor, J., Padmaperuma, A. B., Olarte, M. V., ... & Ferrell III, J. R. (2022). Determination of Phenolic Groups in Bio-Oils Using Revised Folin-Ciocalteu Methods: Single Cuvette and Plate Reader. Laboratory Analytical Procedure (LAP), Issue Date: May 12, 2022 (No. NREL/TP-5100-82591; PNNL-SA-32722). National Renewable Energy Lab.(NREL), Golden, CO (United States); Pacific Northwest National Lab.(PNNL), Richland, WA (United States).

Taralas, G., & Kontominas, M. G. (2006). Pyrolysis of solid residues commencing from the olive oil food industry for potential hydrogen production. Journal of Analytical and Applied Pyrolysis, 76(1-2), 109-116.

Thangaraj, B., & Lee, Y. K. (2025). Review on recent development in catalytic cracking of waste polyolefins: Effect of zeolite-based catalysts and reaction parameters. Fuel, 380, 133220.

Titirici, M. M., White, R. J., Falco, C., & Sevilla, M. (2012). Black perspectives for a green future: hydrothermal carbons for environment protection and energy storage. Energy & Environmental Science, 5(5), 6796-6822.

Troiano, M., Ianzito, V., Solimene, R., Ganda, E. T., & Salatino, P. (2022). Fluidized bed pyrolysis of biomass: a model-based assessment of the relevance of heterogeneous secondary reactions and char loading. Energy & Fuels, 36(17), 9660-9671.

Trubetskaya, A., Von Berg, L., Johnson, R., Moore, S., Leahy, J. J., Han, Y., ... & Anca-Couce, A. (2023). Production and characterization of bio-oil from fluidized bed pyrolysis of olive stones, pinewood, and torrefied feedstock. Journal of Analytical and Applied Pyrolysis, 169, 105841.

Tursi, A. (2019). A review on biomass: importance, chemistry, classification, and conversion. Biofuel Research Journal, 6(2), 962-979.

Uddin, M. N., Daud, W. W., & Abbas, H. F. (2014). Effects of pyrolysis parameters on hydrogen formations from biomass: a review. Rsc Advances, 4(21), 10467-10490.

Uddin, M. N., Techato, K., Taweekun, J., Rahman, M. M., Rasul, M. G., Mahlia, T. M. I., & Ashrafur, S. M. (2018). An overview of recent developments in biomass pyrolysis technologies. Energies, 11(11), 3115.

Usino, D. O., Ylitervo, P., Moreno, A., Sipponen, M. H., & Richards, T. (2021). Primary interactions of biomass components during fast pyrolysis. Journal of Analytical and Applied Pyrolysis, 159, 105297.

Valle, B., García-Gómez, N., Remiro, A., Gayubo, A. G., & Bilbao, J. (2019). Cost-effective upgrading of biomass pyrolysis oil using activated dolomite as a basic catalyst. Fuel Processing Technology, 195, 106142.

Valle, B., Palos, R., Bilbao, J., & Gayubo, A. G. (2022). Role of zeolite properties in bio-oil deoxygenation and hydrocarbons production by catalytic cracking. Fuel Processing Technology, 227, 107130.

Vamvuka, D. (2011). Bio-oil, solid and gaseous biofuels from biomass pyrolysis processes—an overview. International journal of energy research, 35(10), 835-862.

Van Grieken, R., Serrano, D. P., Aguado, J., Garcıa, R., & Rojo, C. (2001). Thermal and catalytic cracking of polyethylene under mild conditions. Journal of Analytical and Applied Pyrolysis, 58, 127-142.

Varma, A. K., & Mondal, P. (2017). Pyrolysis of sugarcane bagasse in semi batch reactor: Effects of process parameters on product yields and characterization of products. Industrial Crops and Products, 95, 704-717.

Varma, A. K., Shankar, R., & Mondal, P. (2018). A review on pyrolysis of biomass and the impacts of operating conditions on product yield, quality, and upgradation. Recent advancements in biofuels and bioenergy utilization, 227-259.

Vassilev, S. V., Baxter, D., Andersen, L. K., & Vassileva, C. G. (2010). An overview of the chemical composition of biomass. Fuel, 89(5), 913-933.

Vassilev, S. V., Baxter, D., Andersen, L. K., Vassileva, C. G., & Morgan, T. J. (2012). An overview of the organic and inorganic phase composition of biomass. Fuel, 94, 1-33.

Vert, M., Doi, Y., Hellwich, K. H., Hess, M., Hodge, P., Kubisa, P., ... & Schué, F. (2012). Terminology for biorelated polymers and applications

(IUPAC Recommendations 2012). Pure and Applied Chemistry, 84(2), 377-410.

Veses, A., Puértolas, B., Callén, M. S., & García, T. (2015). Catalytic upgrading of biomass derived pyrolysis vapors over metal-loaded ZSM-5 zeolites: Effect of different metal cations on the bio-oil final properties. Microporous and Mesoporous Materials, 209, 189-196.

Wagenaar, B. M., Venderbosch, R. H., Carrasco, J., Strenziok, R., & Van der Aa, B. J. (2001). Rotating cone bio-oil production and applications. Progress in thermochemical biomass conversion, 1268-1280.

Wakayama, T., & Matsuhashi, H. (2005). Reaction of linear, branched, and cyclic alkanes catalyzed by Brönsted and Lewis acids on H-mordenite, H-beta, and sulfated zirconia. Journal of Molecular Catalysis A: Chemical, 239(1-2), 32-40.

Wan, S., & Wang, Y. (2014). A review on ex situ catalytic fast pyrolysis of biomass. Frontiers of Chemical Science and Engineering, 8, 280-294.

Wan, Z., Wu, W., Li, G. K., Wang, C., Yang, H., & Zhang, D. (2016). Effect of SiO2/Al2O3 ratio on the performance of nanocrystal ZSM-5 zeolite catalysts in methanol to gasoline conversion. Applied Catalysis A: General, 523, 312-320.

Wang, D., Czernik, S., & Chornet, E. (1998). Production of hydrogen from biomass by catalytic steam reforming of fast pyrolysis oils. Energy & Fuels, 12(1), 19-24.

Wang, D., Montané, D., & Chornet, E. (1996). Catalytic steam reforming of biomass-derived oxygenates: acetic acid and hydroxyacetaldehyde. Applied Catalysis A: General, 143(2), 245-270.

Wang, J., Cui, H., Wei, S., Zhuo, S., Wang, L., Li, Z., & Yi, W. (2010). Separation of biomass pyrolysis oil by supercritical CO2 extraction. Smart Grid and Renewable Energy, 1(02), 98-107.

Wang, K., Johnston, P. A., & Brown, R. C. (2014). Comparison of in-situ and ex-situ catalytic pyrolysis in a micro-reactor system. Bioresource technology, 173, 124-131.

Wang, S., Ru, B., Lin, H., Sun, W., & Luo, Z. (2015a). Pyrolysis behaviors of four lignin polymers isolated from the same pine wood. Bioresource technology, 182, 120-127.

Wang, Y., Akbarzadeh, A., Chong, L., Du, J., Tahir, N., & Awasthi, M. K. (2022). Catalytic pyrolysis of lignocellulosic biomass for bio-oil production: A review. Chemosphere, 297, 134181.

Wang, Z., Liu, S., Lin, W., & Song, W. (2015b). Influence of the Zeolite ZSM-5 on Catalytic Pyrolysis of Biomass via TG-FTIR. BioResources, 10(3), 4485-4497.

Wang, Z., Pan, Y., Dong, T., Zhu, X., Kan, T., Yuan, L., ... & Li, Q. (2007). Production of hydrogen from catalytic steam reforming of bio-oil using C12A7-O⁻-based catalysts. Applied Catalysis A: General, 320, 24-34.

Westlie, A. H., Chen, E. Y. X., Holland, C. M., Stahl, S. S., Doyle, M., Trenor, S. R., & Knauer, K. M. (2022). Polyolefin innovations toward

circularity and sustainable alternatives. Macromolecular rapid communications, 43(24), 2200492.

Wildschut, J., Mahfud, F. H., Venderbosch, R. H., & Heeres, H. J. (2009). Hydrotreatment of fast pyrolysis oil using heterogeneous noble-metal catalysts. Industrial & engineering chemistry research, 48(23), 10324-10334.

Williams, P. T., & Nugranad, N. (2000). Comparison of products from the pyrolysis and catalytic pyrolysis of rice husks. Energy, 25(6), 493-513.

Woolcock, P. J., & Brown, R. C. (2013). A review of cleaning technologies for biomass-derived syngas. Biomass and bioenergy, 52, 54-84.

Xu, T., Xu, J., & Wu, Y. (2022). Hydrogen-rich gas production from two-stage catalytic pyrolysis of pine sawdust with calcined dolomite. Catalysts, 12(2), 131.

Yang, H., Yan, R., Chen, H., Lee, D. H., & Zheng, C. (2007). Characteristics of hemicellulose, cellulose and lignin pyrolysis. Fuel, 86(12-13), 1781-1788.

Yang, L., Seshan, K., & Li, Y. (2017). A review on thermal chemical reactions of lignin model compounds. Catalysis Today, 298, 276-297.

Yel, E., Kalem, M., Göktepeli, G., Kurt, A. Ö., Ahmetli, G., & Önen, V. (2025). Catalytic co-pyrolysis of PET/PP plastics and olive pomace biomass with marble sludge catalyst. Turkish Journal of Analytical Chemistry, 7(1), 33-45.

Yildiz, G., Ronsse, F., Van Duren, R., & Prins, W. (2016). Challenges in the design and operation of processes for catalytic fast pyrolysis of woody biomass. Renewable and Sustainable Energy Reviews, 57, 1596-1610.

You, S., Ok, Y. S., Tsang, D. C., Kwon, E. E., & Wang, C. H. (2018). Towards practical application of gasification: a critical review from syngas and biochar perspectives. Critical Reviews in Environmental Science and Technology, 48(22-24), 1165-1213.

Yu, H., Li, F., He, W., Song, C., Zhang, Y., Li, Z., & Lin, H. (2020). Synthesis of micro–mesoporous ZSM-5 zeolite with microcrystalline cellulose as co-template and catalytic cracking of polyolefin plastics. RSC advances, 10(37), 22126-22136.

Yu, Y., Li, X., Su, L., Zhang, Y., Wang, Y., & Zhang, H. (2012). The role of shape selectivity in catalytic fast pyrolysis of lignin with zeolite catalysts. Applied Catalysis A: General, 447, 115-123.

Yuan, H., Li, C., Shan, R., Zhang, J., Wu, Y., & Chen, Y. (2022). Recent developments on the zeolites catalyzed polyolefin plastics pyrolysis. Fuel Processing Technology, 238, 107531.

Zacher, A. H., Olarte, M. V., Santosa, D. M., Elliott, D. C., & Jones, S. B. (2014). A review and perspective of recent bio-oil hydrotreating research. Green chemistry, 16(2), 491-515.

Zakzeski, J., Bruijnincx, P. C., Jongerius, A. L., & Weckhuysen, B. M. (2010). The catalytic valorization of lignin for the production of renewable chemicals. Chemical reviews, 110(6), 3552-3599.

Zeaiter, J. (2014). A process study on the pyrolysis of waste polyethylene. Fuel, 133, 276-282.

Zhang, B., Zhong, Z., Xie, Q., Liu, S., & Ruan, R. (2016a). Two-step fast microwave-assisted pyrolysis of biomass for bio-oil production using microwave absorbent and HZSM-5 catalyst. Journal of Environmental Sciences, 45, 240-247.

Zhang, H., Shao, S., Xiao, R., Shen, D., & Zeng, J. (2014). Characterization of coke deposition in the catalytic fast pyrolysis of biomass derivates. Energy & Fuels, 28(1), 52-57.

Zhang, H., Xiao, R., Huang, H., & Xiao, G. (2009). Comparison of non-catalytic and catalytic fast pyrolysis of corncob in a fluidized bed reactor. Bioresource technology, 100(3), 1428-1434.

Zhang, M., Hu, Y., Wang, H., Li, H., Han, X., Zeng, Y., & Xu, C. C. (2021). A review of bio-oil upgrading by catalytic hydrotreatment: Advances, challenges, and prospects. Molecular Catalysis, 504, 111438.

Zhang, X., Lei, H., Chen, S., & Wu, J. (2016b). Catalytic co-pyrolysis of lignocellulosic biomass with polymers: a critical review. Green Chemistry, 18(15), 4145-4169.

Zhou, C. H., Xia, X., Lin, C. X., Tong, D. S., & Beltramini, J. (2011). Catalytic conversion of lignocellulosic biomass to fine chemicals and fuels. Chemical Society Reviews, 40(11), 5588-5617.

List of publications

Ciccone, B., Murena, F., Ruoppolo, G., Urciuolo, M., & Brachi, P. (2024). Methanation of syngas from biomass gasification: Small-scale plant design in Aspen Plus. Applied Thermal Engineering, 122901.

Urciuolo, M., Migliaccio, R., Ciccone, B., Ruoppolo, G., de Folly d'Auris, A., Frisario, S., Panepinto, D., Premoli, G., Ruffino, B., Zanetti, M. (2025). Experimental Investigation on PFAS Degradation Through Municipal Sludge Combustion Processes. Applied Thermal Engineering, 127006

Ciccone, B., Scognamiglio, S., Landi, G., & Ruoppolo, G. (2024). Design and Performance of a Biomass-based Poly-generation System for Simultaneous DME and Power Production. Chemical Engineering Transactions, 109, 223-228.

Scognamiglio, S., Ciccone, B., Ruoppolo, G., & Landi, G. (2024). Design and Simulation of Methanol and Dimethyl Ether (DME) Production from Biomass-derived Syngas. Chemical Engineering Transactions, 109, 277-282.